

A Multiwavelength study of X-ray selected samples of star-forming galaxies

Thesis submitted for the degree of
Doctor of Philosophy
at the University of Leicester.

by

Andreas Zezas
X-ray Astronomy Group
Department of Physics and Astronomy
University of Leicester

March 2000

UMI Number: U550762

All rights reserved

INFORMATION TO ALL USERS

The quality of this reproduction is dependent upon the quality of the copy submitted.

In the unlikely event that the author did not send a complete manuscript and there are missing pages, these will be noted. Also, if material had to be removed, a note will indicate the deletion.



UMI U550762

Published by ProQuest LLC 2013. Copyright in the Dissertation held by the Author.
Microform Edition © ProQuest LLC.

All rights reserved. This work is protected against
unauthorized copying under Title 17, United States Code.



ProQuest LLC
789 East Eisenhower Parkway
P.O. Box 1346
Ann Arbor, MI 48106-1346

Declaration

I hereby declare that no part of this thesis has been previously submitted to this or any other University as part of the requirement for a higher degree. The work described herein was conducted by the undersigned except for contributions from colleagues as acknowledged in the text.

Part of the work presented in this thesis is published in the Monthly Notices of the Royal Astronomical Society.:

Sections 1 and 2 of Chapter 4 in

Zezas A., Georgantopoulos I. & Ward M.J., 1998, MNRAS, 301, 915

and Section 3 of Chapter 4 in

Zezas A., Georgantopoulos I. & Ward M.J., 1999, MNRAS, 308, 202

Also sections of the work described in Chapters 2 and 3 have been presented at various conferences and meetings.

Andreas Zezas

March 2000

Acknowledgements

Firstly I would like to thank my supervisor Martin Ward for his guidance and advice during the course of this work and also for suggesting this very exciting subject. Also I would like to thank Ioannis Georgantopoulos for the numerous discussions we had and all the ideas he shared with me. This work would have not been possible without the help of Gareth Griffiths and Dave Smith who introduced me to the world of the X-ray data reduction and Paul Hirst and Duncan Law-Green who showed me how to reduce optical and infrared spectroscopic data. I specially would like to thank Paul for not running away every time I was asking him about problems with IRAF, and other packages. I also would like to thank Paulina Lira for the very useful discussions we had. I am grateful to Mandie Burston who went through an earlier version of the thesis and corrected quite a few grammar mistakes.

Special thanks go to Almudena Alonso-Herrero and Lisa Kewley for helping us to obtain the optical spectroscopic data presented in chapter 2. I am grateful to Almudena for her warm hospitality during the three observing runs at Kitt Peak. Also I would like to apologise to Lisa for not being possible to assist her with the observing and help her for reducing the data she obtained.

Last, but certainly not least I would like to thank my parents for their support and encouragement all these years.

A multiwavelength study of X-ray selected samples of star-forming galaxies

Andreas Zezas

ABSTRACT

This thesis presents a multiwavelength study of two X-ray selected samples of star-forming galaxies. The first sample is defined by the cross-correlation of *ROSAT* source catalogues with the IRAS Faint Source Catalogue, the Markarian and the Kiso catalogues. The main objective of this project is to investigate whether X-ray luminous star-forming galaxies exist, and if so to quantify their properties. A number of star-forming galaxies with luminosities $> 10^{41}$ erg s^{-1} are found. Their X-ray luminosity can be explained in terms of a superwind and an X-ray binary component. Moreover, their multiwavelength properties are very similar to the properties of their lower luminosity counterparts. The second sample studied is drawn from the optical spectroscopic atlas of Ho, Filippenko & Sargent (1997a). It consists of 44 *bona-fide* star-forming galaxies which are observed either as targets or serendipitously with the *ROSAT* PSPC. The correlation between their X-ray emission and their emission in the optical, far-infrared and radio bands are studied. These correlations are used in order to probe the origin of their X-ray emission. Also a correlation between the star-formation rate and X-ray luminosity for star-forming galaxies is calculated. This is convolved with the evolution of star-formation rate with redshift in order to estimate the contribution of star-forming galaxies to the XRB. It is found that they can produce between 10% – 50% of the soft extragalactic (0.1-2.5keV) X-ray background. Finally, two examples of X-ray luminous starburst galaxies, namely Arp299 and NGC3310 are studied in detail using data from the *ROSAT* and *ASCA*. Their X-ray properties are similar to the X-ray properties of lower luminosity star-forming galaxies, suggesting that the same mechanisms are responsible for the X-ray emission of star-forming galaxies spanning three orders of magnitude in luminosity. Thirdly Holmberg-II which is an X-ray luminous dwarf star-forming galaxy is also studied. It is found that all of its X-ray emission arises from a single variable source. The fact that its X-ray luminosity is $\sim 10^{40}$ erg s^{-1} suggests that it could be a black-hole X-ray binary with a mass of $\sim 200 M_{\odot}$. This result together, with other recent studies, suggests that there might be a new class of X-ray binary systems with extremely high mass black-holes. If so, this raises intriguing questions concerning their formation and evolution. Finally, the potential of the new major X-ray observatories, XMM-Newton and *Chandra* is discussed in the light of the studies described in this thesis.

ΣΤΟΥΣ ΓΟΝΕΙΣ ΜΟΥ

Contents

1	Starburst galaxies: An introduction	1
1.1	Activity in galaxies	1
1.2	General properties of star-forming galaxies	5
1.2.1	Optical emission	7
1.2.2	Infrared and Radio emission	7
1.3	The X-ray emission	9
1.3.1	Discrete sources	12
1.3.2	X-ray binaries	13
1.3.3	Supernova remnants	15
1.3.4	Diffuse emission	17
1.4	The parameters of the star-formation	20
1.5	Star-forming galaxies at High Redshift	22
1.6	X-ray Background and star-forming galaxies	24
1.7	Motivation for this work	26
2	A search for X-ray luminous star-forming galaxies	27
2.1	Selection of the sample	27
2.2	The results of the cross-correlations	33

2.2.1	The IRAS samples	33
2.2.2	The Markarian samples	52
2.2.3	The KISO samples	64
2.3	Spectroscopic classifications	71
2.3.1	Observations and Data reduction	71
2.3.2	Spectroscopic classifications	75
2.4	The X-ray luminous star-forming galaxies	95
2.4.1	Starformation Rate	95
2.4.2	The origin of the X-rays	98
3	A soft X-ray survey of star-forming galaxies	106
3.1	Selection of the sample	107
3.2	Data reduction	108
3.3	Imaging analysis	110
3.3.1	X-ray measurements	132
3.3.2	Multiwavelength data	138
3.4	Correlations	139
3.4.1	Optical vs. X-ray emission	141
3.4.2	Infrared vs. X-ray emission	145
3.4.3	Radio vs. X-ray emission	150
3.5	The multiwavelength properties of star-forming galaxies - The origin of the soft X-ray emission	153
3.6	Implications for the soft X-ray background	154
3.6.1	Modelling	155
3.6.2	Starbursts vs. AGN	160

4	Study of selected X-ray luminous starburst galaxies¹	162
4.1	NGC3310	162
4.1.1	Overview	162
4.1.2	The data	163
4.1.3	Soft X-ray imaging	165
4.1.4	Spectral analysis	166
4.1.5	Discussion	171
4.2	Arp 299	174
4.2.1	Overview	174
4.2.2	The data	175
4.2.3	Soft X-ray imaging	176
4.2.4	X-ray spectroscopy	180
4.2.5	Discussion	183
4.3	UGC4305 (Holmberg II)	186
4.3.1	The <i>ROSAT</i> data	187
4.3.2	X-ray imaging	187
4.3.3	Variability	190
4.3.4	X-ray spectroscopy	191
4.3.5	Discussion	194
5	Conclusions and future work	198
5.1	An overview of the presented work	198
5.1.1	Do X-ray luminous star-forming galaxies exist ?	198
5.1.2	The properties of X-ray luminous starbursts	199
5.1.3	The link between X-rays and other wavelengths	200

5.1.4	The contribution of star-forming galaxies to the XRB	200
5.2	Future work	201
5.2.1	Surveys	201
5.2.2	High resolution imaging	202
5.2.3	High quality spectroscopy	203
References		206

List of Figures

1.1	Typical spectra of Seyfert 1 (top left), Seyfert 2 (top right), LINER (bottom left) and starburst nuclei (bottom right) (from Ho, Filippenko & Sargent 1997 <i>a</i>).	2
1.2	Two diagnostic diagrams from (from Veilleux & Osterbrock 1987). The short dashed lines are for H II region models for four different temperatures. The solid curve separates AGN from H II -type objects.	3
1.3	A sketch demonstrating the Unification scheme for AGN, (from Peterson 1997).	4
1.4	The mean SEDs of active (Sy2, LINER, starburst) and non-active (elliptical, spiral) galaxies. SBH and SBL refer to star-forming galaxies with high and low obscuration respectively (from Schmitt, Kinney, Calzetti & Storchi Bergmann 1997).	6
1.5	The spectrum of a typical WR galaxy (from Vacca & Conti 1992).	7
1.6	The contribution of the different components in the IR/sub-mm emission of the Galaxy. Dashed curve: cold dust; crosses: very cold dust; dotted curve: warm dust. (from Cox, Kruegel & Mezger 1986).	8
1.7	The radio/FIR spectrum of M82; from Condon (1992). The dot-dashed line shows the synchrotron component, whereas the dashed and the dotted lines show the free-free and dust components.	9
1.8	The radio-FIR correlation for normal galaxies (from Condon 1992).	9
1.9	The distribution of the X-ray luminosities of various classes of X-ray binaries in the Galaxy. For comparison the distribution of X-ray luminosity of binaries in the Magellanic clouds is also presented. (from van Paradijs & McClintock 1995).	14
1.10	The X-ray luminosity of X-ray binaries divided by the number of O type stars, in systems with different metallicities (from Griffiths & Padovani 1990).	15
1.11	ASCA spectrum of Vela-X1 at post-eclipse (top), pre-eclipse (middle) and eclipse (bottom), from Nagase, Zylstra, Sonobe, Kotani, Inoue & Woo (1994).	16
1.12	The ASCA SIS0 spectrum of Tycho SNR showing a wealth of emission lines.	16

1.13	A DSS image of M82 showing the superwind geometry and the positions of the SNRs detected in radio observations (from Strickland & Stevens 2000)	18
1.14	The evolution of the X-ray luminosity of the diffuse emission of a starburst which converts $10^8 M_{\odot}$ of gas to stars. The dashed line represents the emission from gas in the disk, and the dotted line is the emission from the halo. The total emission is shown by the solid line. The model in the top panel assumes a thick disk, whereas the one in the bottom panel assumes a thin disk (from Strickland & Stevens 2000)	19
1.15	The IMF of Miller & Scalo (1979) (crosses) and its revision by Scalo (1986) (points). The two lines represent the Salpeter and power-law representation of the high mass end of the Miller-Scalo IMF. (from Leitherer 1998)	21
1.16	The number of O stars and the mechanical luminosity (from SNe and stellar winds) for different IMFs and star-formation scenarios. The left panels correspond to continuous starburst with $\text{SFR}=1 M_{\odot} \text{ yr}^{-1}$, whereas the right pannel is for an instantaneous starburst wich converts $10^6 M_{\odot}$ of gas into stars. Solid line: Miller-Scalo IMF with $M_{\text{up}}=100 M_{\odot}$; short-dashed line: Miller-Scalo IMF with $M_{\text{up}}=30 M_{\odot}$; long-dashed line: Salpeter IMF with $M_{\text{up}}=100 M_{\odot}$ (Leitherer et al. 1999).	23
2.1	A histogram of the separation between the sources in the cross-correlated samples. The cross-correlation radius used was $300''$	32
2.2	The distribution of the $\log(f_X/f_{60\mu})$ for broad and narrow line objects (from Green, Anderson & Ward 1992).	33
2.3	The distribution of activity classes, and X-ray luminosities of the objects in the IRASFSC-RASSBSC sample.	34
2.4	The distribution of X-ray luminosities and velocities of objects of different activity classes in the IRASFSC-RASSBSC sample.	35
2.5	The distribution of activity classes, and X-ray luminosities of the objects in the IRASFSC-WGAcad sample.	36
2.6	The distribution of X-ray luminosities and velocities of objects of different activity classes in the IRASFSC-WGAcad sample.	37
2.7	The distribution of activity classes, and X-ray luminosities of the objects in the Markarian-RASSBSC sample.	53
2.8	The distribution of X-ray luminosities and velocities of objects of different activity classes in the Markarian-RASSBSC sample.	54

2.9	The distribution of activity classes, and X-ray luminosities of the objects in the Markarian-WGAcad sample.	55
2.10	The distribution of X-ray luminosities and velocities of objects of different activity classes in the Markarian-WGAcad sample.	56
2.11	The distribution of activity classes, and X-ray luminosities of the objects in the Kiso-RASSBSC sample.	65
2.12	The distribution of X-ray luminosities and velocities of objects of different activity classes in the Kiso-RASSBSC sample.	66
2.13	The distribution of activity classes, and X-ray luminosities of the objects in the Kiso-WGAcad sample.	67
2.14	The distribution of X-ray luminosities and velocities of objects of different activity classes in the Kiso-WGAcad sample.	68
2.15	The $[O_{III}] / H_{\beta}$ vs. $[N_{II}] / H_{\alpha}$ and $[O_{III}] / H_{\beta}$ vs. $[O_I] / H_{\alpha}$ diagnostic diagrams for the observed objects (red dots). The objects from the sample of Ho <i>et al.</i> have been plotted as well (dots: H II galaxies, stars: transition objects, circles: LINERS, right arrows Sy2s, up arrows Sy1s).	77
2.16	The $[O_{III}] / H_{\beta}$ vs. $[S_{II}] / H_{\alpha}$ diagnostic diagram for the observed objects (red dots). The other symbols are as in figure 2.15	78
2.17	The optical spectra of the observed objects (North)	79
2.17	The optical spectra of the observed objects (North) <i>continued</i>	80
2.17	The optical spectra of the observed objects (North) <i>continued</i>	81
2.17	The optical spectra of the observed objects (North) <i>continued</i>	82
2.17	The optical spectra of the observed objects (North) <i>continued</i>	84
2.17	The optical spectra of the observed objects (North) <i>continued</i>	85
2.17	The optical spectra of the observed objects (North) <i>continued</i>	86
2.17	The optical spectra of the observed objects (South) <i>continued</i>	87
2.17	The optical spectra of the observed objects (South) <i>continued</i>	88
2.17	The optical spectra of the observed objects (South) <i>continued</i>	89
2.17	The optical spectra of the observed objects (South) <i>continued</i>	90

2.17	The optical spectra of the observed objects (South) <i>continued</i>	95
2.18	The fraction of the observed and the estimated X-ray emission for star-forming, composite and LINER objects in our sample.	103
2.19	A comparison between the sample of star-forming galaxies presented here and the samples of Ho, Filippenko & Sargent (1997 <i>a</i>) (top) and Moran, Halpern & Helfand (1996)(bottom). In the top figure asterisks are the objects from Ho, Filippenko & Sargent (1997 <i>a</i>) and red circles are the starbursts from this sample. In the bottom figure open and filled circles are Sy1-1.5 and Sy1.8-1.9, asterisks are NLS1, diamonds are Sy2, crossed circles are composite objects and star symbols are normal/star-forming galaxies from the sample of Moran et al. (1996). Filled stars and open triangles are star-forming galaxies from this survey and the survey of Ho, Filippenko & Sargent (1997 <i>a</i>) respectively.	105
3.1	Overlay of contours from the PSPC observations of NGC520 and NGC521 on DSS images. In this and the following figures North is up and East is left. The bar in the bottom left corner is 1.5' long. The red circle corresponds to the nuclear region whereas the orange and the green ellipses are the D25 ellipse and the region used to measure the integrated emission respectively.	111
3.2	Overlay of contours from the PSPC observations of NGC598 and NGC660 on DSS images	112
3.3	Overlay of contours from the PSPC observations of NGC891 and NGC1569 on DSS images	113
3.4	Overlay of contours from the PSPC observations of NGC2146 and NGC2276 on DSS images.	114
3.5	Overlay of contours from the PSPC observations of NGC2342 and NGC2403 on DSS images.	115
3.6	Overlay of contours from the PSPC observations of NGC2537 and NGC2750 on DSS images	116
3.7	Overlay of contours from the PSPC observations of NGC2903 and NGC3034 on DSS images	117
3.8	Overlay of contours from the PSPC observations of NGC3077 and NGC3184 on DSS images	118
3.9	Overlay of contours from the PSPC observations of NGC3198 and NGC3310 on DSS images	119
3.10	Overlay of contours from the PSPC observations of NGC3319 and NGC3359 on DSS images	120

3.11	Overlay of contours from the PSPC observations of NGC3395 and NGC3665 on DSS images	121
3.12	Overlay of contours from the PSPC observations of NGC3690 and NGC4236 on DSS images	122
3.13	Overlay of contours from the PSPC observations of NGC4245 and NGC4303 on DSS images	123
3.14	Overlay of contours from the PSPC observations of NGC4459 and NGC4470 on DSS images	124
3.15	Overlay of contours from the PSPC observations of NGC4485/90 and NGC4526 on DSS images	125
3.16	Overlay of contours from the PSPC observations of NGC4559 and NGC4631 on DSS images	126
3.17	Overlay of contours from the PSPC observations of NGC4647 and NGC4654 on DSS images	127
3.18	Overlay of contours from the PSPC observations of NGC4656 and NGC5204 on DSS images	128
3.19	Overlay of contours from the PSPC observations of NGC5775 and NGC5866 on DSS images	129
3.20	Overlay of contours from the PSPC observations of NGC5905 and NGC5907 on DSS images	130
3.21	Overlay of contours from the PSPC observations of NGC6236 and NGC6946 on DSS images	131
3.22	Overlay of contours from the PSPC observations of NGC7448 on DSS images . .	140
3.23	Scatter plots of LB-LX,NUCL, LB-LX,INT, LB,BULGE-LX,INT and LB,BULGE-LX,NUCL	142
3.24	Scatter plots of $fH\alpha,INT-fx,INT$, $LH\alpha,INT-LX,INT$, $FH\alpha,NUCL-FX,NUCL$ and $LH\alpha,NUCL-LX,NUCL$	143
3.25	Scatter plots of $LX,NUCL/LH\alpha,NUCL$ and $LX,NUCL/LB,BULGE$, against $\log(D25)$.	144
3.26	Scatter plots of $FFIR,INT-FX,INT$, $LFIR,INT-LX,INT$, $FFIR,INT-FX,NUCL$ and $LFIR,INT-LX,NUCL$	146
3.27	Scatter plots of $ff60,INT-fx,INT$, $LF60,INT-LX,INT$, $FF60,INT-FX,NUCL$ and $LF60,INT-LX,NUCL$	147

3.28	Scatter plots of the FIR luminosity against the F_{60}/F_{100} colour for this sample (left) and plots of the F_{60}/F_{100} colour against the L_B/L_{FIR} ratio from Veilleux, Kim & Sanders (1999) (right). The H II galaxies are denoted by stars. Large symbols are from the 1Jy sample, whereas small symbols are from the Bright galaxy sample of Veilleux, Kim, Sanders, Mazzarella & Soifer (1995).	148
3.29	The evolution with time of the ratio of early type stars over late type stars for different star-formation scenarios. In the left diagram an instantaneous burst which converts $10^6 M_\odot$ into stars is assumed whereas the right diagram assumes continuous star-formation with a rate of $1 M_\odot yr^{-1}$. The dark blue line corresponds to a Salpeter IMF ($\alpha = 2.35$) with an upper mass cutoff at $100 M_\odot$, and the light blue line is for the same IMF but with an upper mass cutoff of $30 M_\odot$. The green and the red lines are for a Miller-Scalo IMF ($\alpha = 2.35$) with upper mass cutoffs of $100 M_\odot$ and $30 M_\odot$ respectively.	149
3.30	Scatter plots of the absorption corrected X-ray luminosity against the EW of the nuclear H α emission line (bottom panel) and the B-V and U-B colours of the galaxy (top panel).	150
3.31	Scatter plots of FRAD,INT-FX,INT, LRAD,INT-LX,INT, FRAD,INT-FX,NUCL and LRAD,INT-LX,NUCL.	151
3.32	The evolution of the cosmic star-formation rate with redshift (from Glazebrook, Blake, Economou, Lilly & Colless 1999). The blue points are from UV measurements (open triangle Treyer, Ellis, Milliard, Donas & Bridges (1998), open circles Lilly, Le Fevre, Hammer & Crampton (1996), open stars Connolly, Szalay, Dickinson, Subbarao & Brunner (1997), open squares Madau, Pozzetti & Dickinson (1998)). The red and green points are from Balmer lines and IR/sub-mm measurements (filled triangle Gallego, Zamorano, Aragon-Salamanca & Rego (1995), filled diamond Tresse & Maddox (1998), filled circle Glazebrook et al. (1999), open crosses Flores, Hammer, Thuan, Ceacute#sarsky, Desert, Omont, Lilly, Eales, Crampton & Le Fegrave#vre (1999), filled square Pettini, Kellogg, Steidel, Dickinson, Adelberger & Giavalisco (1998) and filled star Hughes, Serjeant, Dunlop, Rowan-Robinson, Blain, Mann, Ivison, Peacock, Efstathiou, Gear, Oliver, Lawrence, Longair, Goldschmidt & Jenness (1998)).	157
3.33	X-ray emissivity and intensity of the X-ray emission of star-forming galaxies calculated using the X-ray-H α correlation. Red points are from the optical/IR determination of the SFR history, and blue points are from the HDF.	158
3.34	X-ray emissivity and intensity of the X-ray emission of star-forming galaxies calculated using the X-ray-FIR correlation. Red points are from the optical/IR determination of the SFR history, and blue points are from the HDF.	159
4.1	The HRI radial profile of NGC3310 (circles) overlaid on the radial profile of AR Lac (stars).	166

4.2	X-ray contours from the HRI observation of NGC3310 overlaid on a POSS image. The contours are in levels of 2.2, 2.0, 1.7, 1.33, 0.88, 0.44, 0.35, 0.26, 0.17 counts arcsec ⁻²	167
4.3	The top panel shows <i>ROSAT</i> and <i>ASCA</i> spectra of NGC3310 with the best fit double Raymond Smith model. The bottom panel shows the ratio of the data points to the model. The SIS data are marked with dots while the PSPC data are marked with triangles.	170
4.4	X-ray contours from the HRI observation of Arp 299 overlaid on a POSS image. The contours are in levels of 0.57, 0.44, 0.4, 0.35, 0.31, 0.26, 0.22, 0.18, 0.13, 0.11 counts arcsec ⁻²	177
4.5	NICMOS and WFPC2 observations of IC694. North is up and East to the left. The size of all the images except the inset is 19.5'' × 19.5''. From Alonso-Herrero, Rieke & Rieke (2000).	178
4.6	NICMOS and WFPC2 observations of NGC3690. Orientation and size same as fig. 4.5. From Alonso-Herrero et al. (2000).	179
4.7	The top panel shows <i>ROSAT</i> and <i>ASCA</i> spectra of Arp 299 with the best fit double Raymond Smith model. The bottom panel shows the ratio of the data points to the model. The SIS data are marked with dots, while the PSPC data are marked with triangles.	181
4.8	Contours from the HRI observation overlaid on a POSS image of the galaxy. The contours correspond to levels of 0.09, 0.13, 0.18, 0.22, 0.44, 1.11, 2.22, 6.67, 8.0 cnts arcsec ⁻² . The epoch of the coordinates is J2000.0, and the positional error of the X-ray coordinates with respect to the optical is ~ 6''. The position of the X-ray centroid is 08 ^h 19 ^m 29.9 ^s + 70°42'18.0''J2000.0	188
4.9	The HRI radial profile of the source in Holmberg II compared with the radial profile of AR-Lac (stars).	189
4.10	The long-term light curve from all the <i>ROSAT</i> observations of Holmberg II. the first point corresponds to the RASS detection of the galaxy while the last point to the HRI observation.	190
4.11	The light curves for each observation of Holmberg II. The first three panels correspond to the three PSPC observations in chronological order and the last panel corresponds to the HRI observation.	192
4.12	The best fit power-law spectrum for Holmberg II. The top panel shows the data with the model and the bottom panel shows the $\Delta\chi^2$	194

5.1	Chandra ACIS-I observations of M82. Top left: soft band (0.2-2.5keV) image; top right: hard band (2.5-10.0keV) image; bottom left: diffuse emission in the soft band; bottom right: diffuse emission in the hard band. The bar in the top right image is 4.2' long whereas in the top right image is 2.1' long. The scale of the bottom images is the also 2.1'×2.1'	204
5.2	A simulated 20Ks observation of Arp299 with XMM (EPIC-MOS). The assumed model is the best fit double thermal model from the <i>ASCA</i> + <i>ROSAT</i> fits. . . .	204

List of Tables

1.1	The populations of X-ray sources in the Galaxy (from Watson 1990)	12
2.1	Comparison of the Markarian and the KISO samples	30
2.2	Results from the cross-correlations	31
2.3	Results of the IRASFSC - RASSBSC cross-correlation	38
2.3	Results of the IRASFSC - RASSBSC cross-correlation <i>continued</i>	39
2.3	Results of the IRASFSC - RASSBSC cross-correlation <i>continued</i>	40
2.4	Results of the IRASFSC - WGAcat cross-correlation	41
2.4	Results of the IRASFSC - WGAcat cross-correlation <i>continued</i>	42
2.4	Results of the IRASFSC - WGAcat cross-correlation <i>continued</i>	43
2.4	Results of the IRASFSC - WGAcat cross-correlation <i>continued</i>	44
2.4	Results of the IRASFSC - WGAcat cross-correlation <i>continued</i>	45
2.4	Results of the IRASFSC - WGAcat cross-correlation <i>continued</i>	46
2.4	Results of the IRASFSC - WGAcat cross-correlation <i>continued</i>	47
2.4	Results of the IRASFSC - WGAcat cross-correlation <i>continued</i>	48
2.4	Results of the IRASFSC - WGAcat cross-correlation <i>continued</i>	49
2.4	Results of the IRASFSC - WGAcat cross-correlation <i>continued</i>	50
2.4	Results of the IRASFSC - WGAcat cross-correlation <i>continued</i>	51
2.5	Results of the MARKARIAN - RASSBSC cross-correlation	57

2.5	Results of the MARKARIAN - RASSBSC cross-correlation <i>continued</i>	58
2.5	Results of the MARKARIAN - RASSBSC cross-correlation <i>continued</i>	59
2.5	Results of the MARKARIAN - RASSBSC cross-correlation <i>continued</i>	60
2.6	Results of the MARKARIAN - WGAcat cross-correlation	61
2.6	Results of the MARKARIAN - WGAcat cross-correlation <i>continued</i>	62
2.6	Results of the MARKARIAN - WGAcat cross-correlation <i>continued</i>	63
2.7	Results of the KISO - RASSBSC cross-correlation	69
2.7	Results of the KISO - RASSBSC cross-correlation <i>continued</i>	70
2.8	Results of the KISO - WGAcat cross-correlation	72
2.8	Results of the KISO - WGAcat cross-correlation <i>continued</i>	73
2.8	Results of the KISO - WGAcat cross-correlation <i>continued</i>	74
2.9	Classification criteria	76
2.10	Spectral properties of the observed objects which show optical emission lines	91
2.10	Spectral properties of the observed objects <i>continued</i>	92
2.10	Spectral properties of the observed objects <i>continued</i>	93
2.10	Spectral properties of the observed objects <i>continued</i>	94
2.11	Spectral classifications of the observed objects	96
2.11	Spectral classifications of the observed objects <i>continued</i>	97
2.12	Properties of the starforming galaxies with IRAS detections	99
2.12	Properties of the starforming galaxies <i>continued</i>	100
2.12	Properties of the starforming galaxies <i>continued</i>	101
3.1	General properties of the galaxies	109
3.2	Multiwavelength properties of the galaxies (I. fluxes)	133
3.3	Conversion factors to X-ray fluxes	134

3.4	Measured X-ray fluxes	135
3.5	Multiwavelength properties of the galaxies (II. luminosities)	136
3.6	The results of the correlations (bounds + detections)	140
3.7	The results of the correlations (only detections)	141
4.1	Summary of the observations of NGC3310	164
4.2	Sources in the <i>HRI</i> field of NGC3310	166
4.3	Spectral fitting results for NGC 3310	169
4.4	Summary of the observations of NGC3690	176
4.5	Sources in the <i>HRI</i> field of NGC3690	180
4.6	Spectral fitting results for NGC3690.	182
4.7	Summary of the observations of UGC 4305.	187
4.8	The spectral fitting results for Holmberg II.	193

Chapter 1

Starburst galaxies: An introduction

1.1 Activity in galaxies

In order to discuss the characteristics of starburst activity, we should first briefly review the other types of activity. Active galaxies can be separated in four basic activity classes based on their optical properties. Objects which exhibit broad permitted lines in their spectra are classified as Seyfert 1 type objects. On the other hand objects which exhibit narrow permitted and high excitation forbidden lines are classified as Seyfert 2 objects. Objects belonging in those two classes generally have bolometric luminosities in the range of $10^{11} - 10^{12} L_{\odot}$ (although the brightest quasars can reach as high luminosities as $10^{14} L_{\odot}$). In lower luminosity objects there are two major classes: Low Ionisation Emission Line Objects (LINERs) and star-forming galaxies. The former have narrow optical lines and some of the higher excitation lines encountered in Sy1 or Sy2 type objects, but usually these are much weaker in luminosity and in their ratio to other lines like $[OIII]$. The optical spectra of star-forming galaxies are typical of H II regions: narrow low excitation lines. Typical spectra from each class are presented in figure 1.1, whereas figure 1.2 shows some diagnostic line ratio diagrams used to classify the type of activity in galaxies. These diagrams have been developed by Baldwin, Phillips & Terlevich (1981) and Veilleux & Osterbrock (1987) and they are based on the different emission line strength ratios which are produced by different ionising continua, and hence probe the central engine of active galaxies.

The generally accepted scenario is that Seyfert type objects are powered by accretion onto a supermassive black hole ($M \sim 10^{8-9} M_{\odot}$) (eg Rees 1984), although there are suggestions that

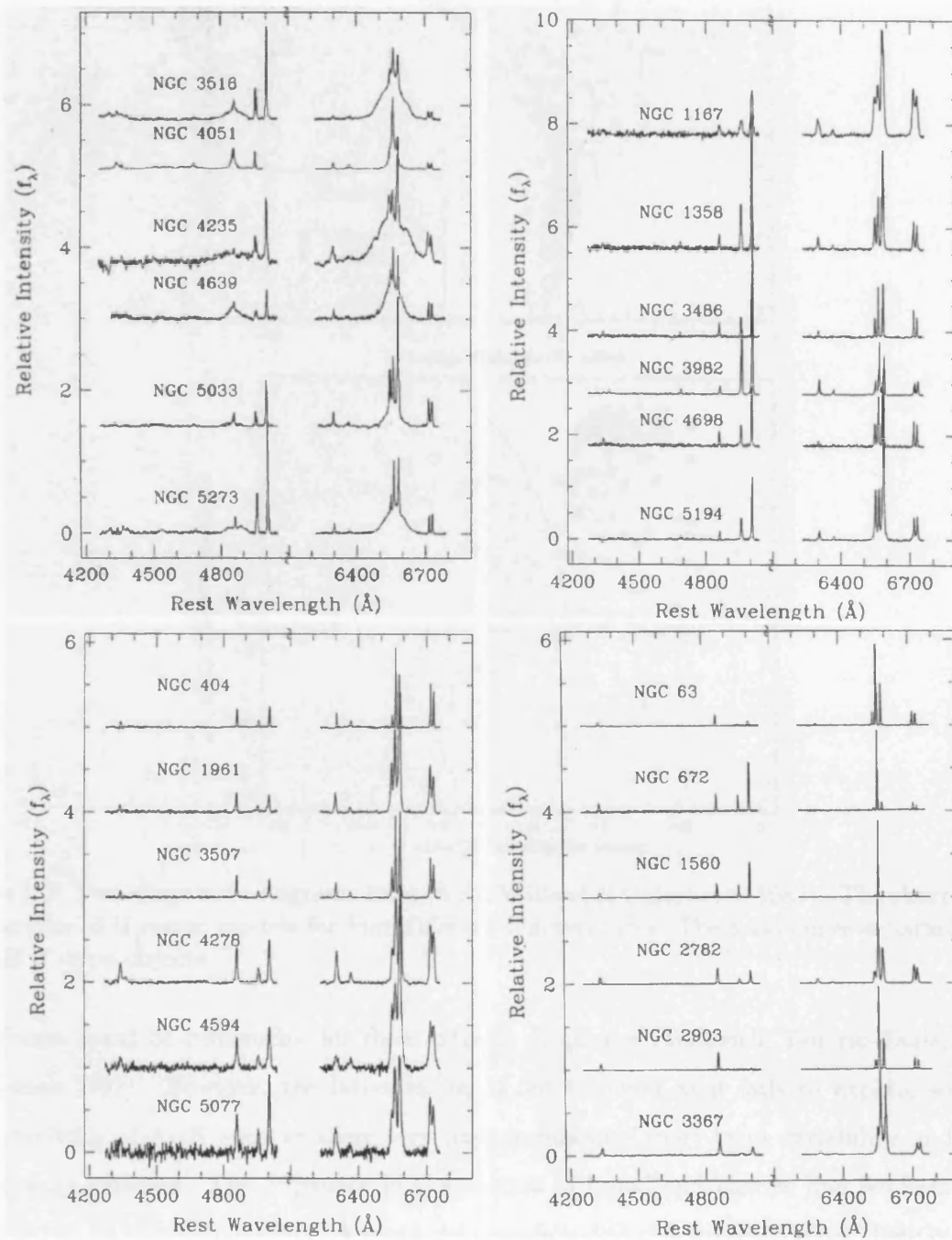


Figure 1.1: Typical spectra of Seyfert 1 (top left), Seyfert 2 (top right), LINER (bottom left) and starburst nuclei (bottom right) (from Ho, Filippenko & Sargent 1997a).

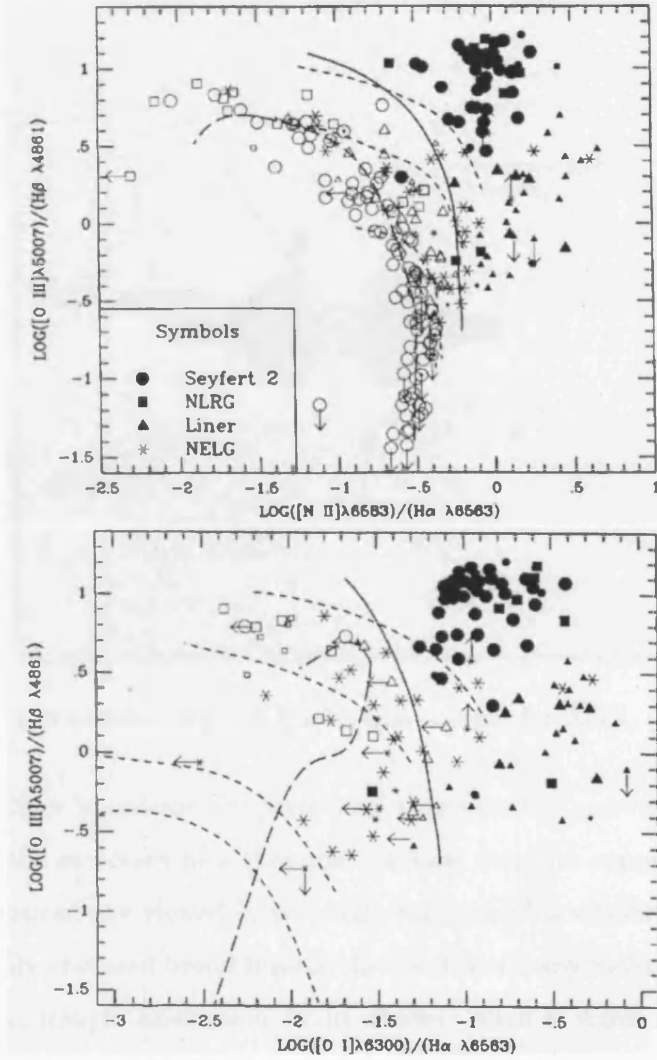


Figure 1.2: Two diagnostic diagrams from (from Veilleux & Osterbrock 1987). The short dashed lines are for H II region models for four different temperatures. The solid curve separates AGN from H II -type objects.

a starburst could be responsible for their extreme properties (Terlevich, Tenorio-Tagle, Franco & Melnick 1992). However, the latter model is not favoured as it fails to explain some key characteristics of AGN such as their very high luminosity, short term variability and strong high energy emission. The difference in the spectra of broad and narrow line Seyferts can be explained as an orientation effect. Around the accretion disk it is suggested that there is a dusty torus. If we view the central region through the opening angle of the torus then we directly see the accretion disk and in this case we observe the broad lines. In the case where the line of sight intersects the torus most of the emission from the central region is blocked and therefore the objects appear as Sy2 (fig. 1.3 Antonucci & Miller 1985, Antonucci 1993). The region which

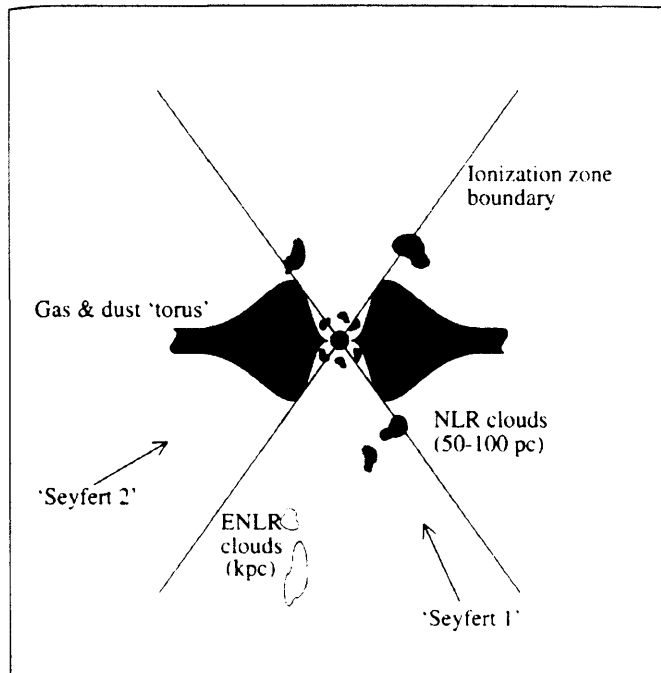


Figure 1.3: A sketch demonstrating the Unification scheme for AGN, (from Peterson 1997).

emits the forbidden lines is outside the torus and therefore the narrow forbidden lines which are not produced in the accretion disk (because the high densities suppress the forbidden lines by collisional deexcitation) are viewed in all cases. This model is supported by the discovery of polarised and/or highly obscured broad lines in the spectra of many Sy2-type objects (Antonucci & Miller 1985, Young, Hough, Efstathiou, Wills, Bailey, Ward & Axon 1996, Veilleux, Sanders & Kim 1999).

The nature of LINERS (Heckman 1980) is more controversial. Although in general it is suggested that they are powered by accretion onto a massive black hole (Peterson 1997) other models demonstrate that their emission can arise via bursts of star-formation (Filippenko & Terlevich 1992). The recent spectroscopic survey of Ho, Filippenko & Sargent (1997a) showed that the dichotomy observed in Seyfert galaxies is also present in LINERS: they found that a fraction of LINERS exhibit broad wings in their optical permitted lines, whereas others do not. A near-IR spectroscopic survey of LINER type galaxies demonstrated that their spectra are consistent with an evolved burst of star-formation (Alonso-Herrero et al. 2000). Similarly radio and X-ray observations do not give any strong evidence for the existence of a massive black hole.

Finally star-forming galaxies, which will be the focus of this work, are powered as the name

implies by intense bursts of star-formation. These may have been triggered by the formation of galactic bars which drive gas from the disk towards the nuclear region of the galaxy. Shocks which are formed, are responsible for the dissipation of the angular momentum of the gas (Athanasoula 1992). As Barnes & Hernquist (1992) showed, interactions can create large concentrations of gas in a very small region which result in enhanced star-formation. At this point it is noted that there is an empirical relation between the density of the gas and the rate of star-formation known as the Schmidt law. According to this law the star-formation rate $\text{SFR} \propto \rho^\alpha$ with $1 < \alpha < 2$ (e.g. Kennicutt 1998*a*). It should be noted that star-formation activity is present in almost all the galaxies (see e.g. Kennicutt 1998*b*). However, Weedman, Feldman, Balzano, Ramsey, Sramek & Wu (1981) first introduced the term starburst galaxy for galaxies in which the activity is dominated by the presence of young stars. The border-line between star-forming and starburst galaxies is not very clear. However, many workers define as starburst galaxies as those with H_α luminosity above $10^{41} \text{erg s}^{-1}$.

1.2 General properties of star-forming galaxies

Star-forming galaxies span a wide range of morphologies and luminosities. Although the majority of them are spirals there are a large number of irregulars which host intense bursts of star-formation (Ho, Filippenko & Sargent 1997*a*). Typical examples of the later case are M82 and the Magellanic clouds. Also there are many dwarf galaxies the emission from which is powered by a burst of star-formation (Davies, Sugai & Ward 1998). Because of their blue colours they are usually called Blue Dwarf starburst galaxies. In general the luminosities of star-forming galaxies lie between those of normal galaxies and AGN. In the X-ray band they range between ($10^{38} - 10^{42} \text{erg s}^{-1}$).

Their Spectral Energy Distributions are very different from those of AGN. Figure 1.4 shows the mean SED of starburst galaxies with different amounts of obscuration (from Schmitt et al. 1997). For comparison the SEDs of elliptical, Spiral, Seyfert 2 and LINERs are also presented. What becomes clear from this figure is that star-forming galaxies do not have a pronounced blue bump compared to other classes of active galaxy. On the other hand objects with high obscuration have a relatively stronger FIR bump at $\sim 60 - 100 \mu$.

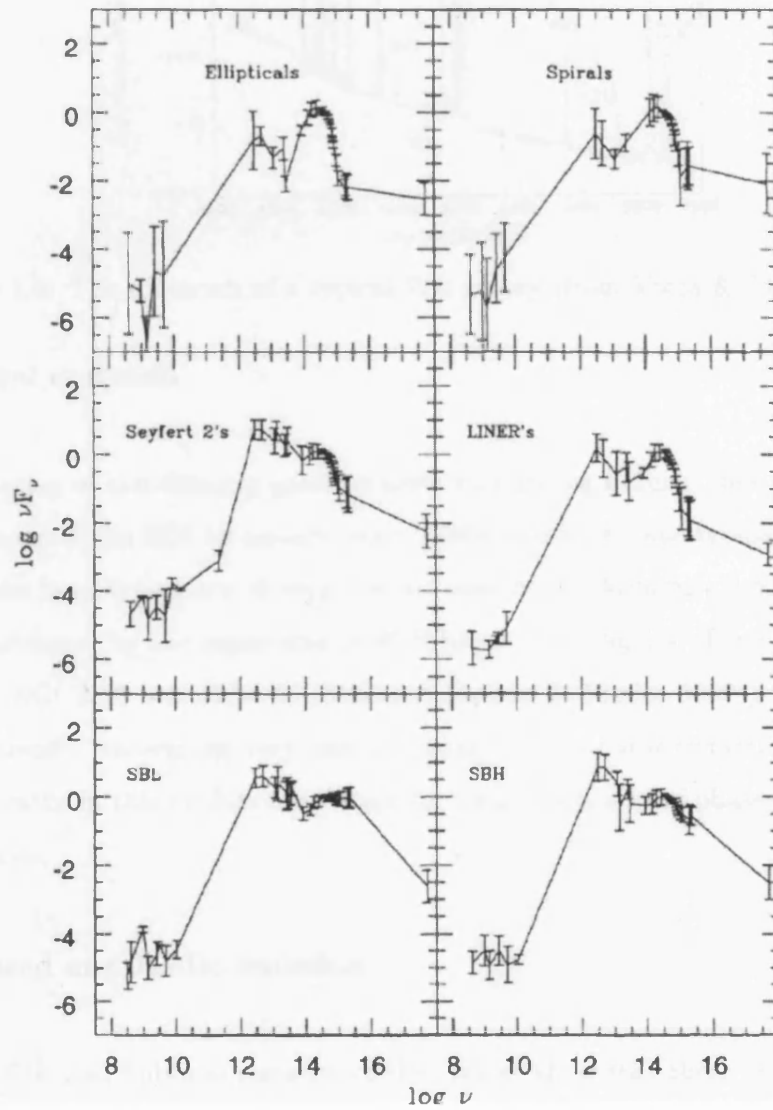


Figure 1.4: The mean SEDs of active (Sy2, LINER, starburst) and non-active (elliptical, spiral) galaxies. SBH and SBL refer to star-forming galaxies with high and low obscuration respectively (from Schmitt et al. 1997).

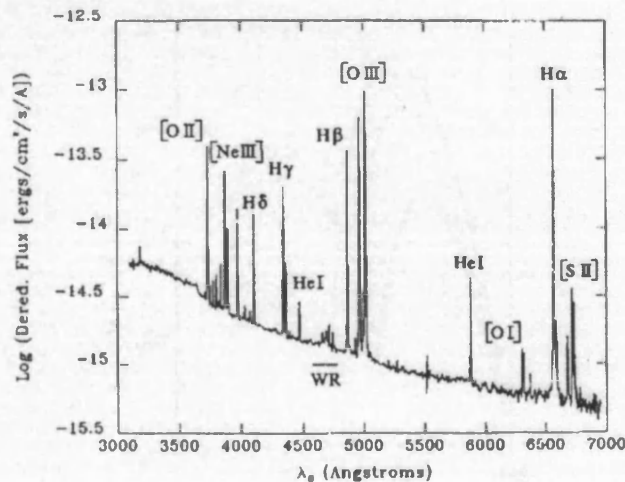


Figure 1.5: The spectrum of a typical WR galaxy (from Vacca & Conti 1992).

1.2.1 Optical emission

The optical spectra of star-forming galaxies show very strong Balmer lines which mainly arise by photoionisation of the ISM by massive stars. They also have some typical stellar absorption lines arising from later type stars. A very distinct class of star-forming galaxies are those whose spectra are dominated by the signatures of Wolf-Rayet stars (fig 1.5). Typical examples of this class are Tol3, NGC3125 and IIZw 40 (Schaerer, Contini & Pindao 1999). These Wolf-Rayet galaxies are currently undergoing very intense young bursts of star-formation. As Wolf-Rayet stars do not remain in this evolutionary stage for long this is a brief phase in the evolution of starburst galaxies.

1.2.2 Infrared and Radio emission

Models of the FIR and Sub-mm emission of the Galaxy show that there are three major components which produce the total continuum emission (Cox et al. 1986, Cox & Mezger 1989):

1. Cold ($T \sim 15 - 25\text{K}$) and cooler ($T < 14\text{K}$) dust which is heated by the general interstellar radiation field. This produces $\sim 37\%$ of the total IR emission of the Galaxy.
2. Warm dust ($T \sim 30 - 40\text{K}$) which is heated by early type stars (mainly O and B in ratio 2:1) accounts for $\sim 50\%$ of the Galactic IR emission.

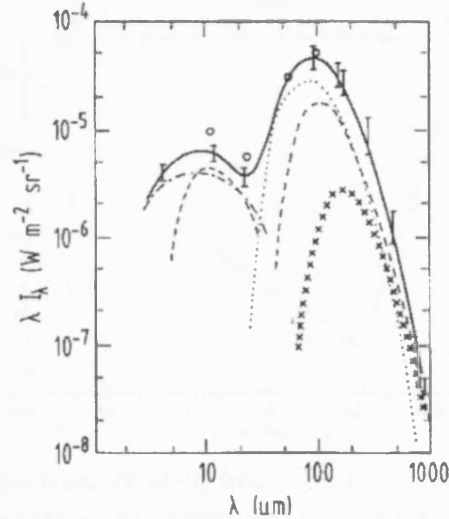


Figure 1.6: The contribution of the different components in the IR/sub-mm emission of the Galaxy. Dashed curve: cold dust; crosses: very cold dust; dotted curve: warm dust. (from Cox et al. 1986).

3. Hot dust ($T \sim 250 - 500\text{K}$) which is heated by the general interstellar radiation field (IRF) and by M giants with high mass loss, produces $\sim 13\%$ of the galactic IR emission.

Figure 1.6 shows the contribution of these different components to the IR continuum radiation of the Milky Way.

The relative contribution of these components will vary from galaxy to galaxy as shown by Rowan-Robinson & Crawford (1989). It has been suggested that simply a warm component heated by early type stars is sufficient to account for the total IR emission in star-forming galaxies (Devereux & Young 1990). However, the situation is still unclear as this component cannot explain the IR emission in elliptical galaxies which are not hosts of active star-formation (Devereux & Hameed 1997). Moreover, a recent study by Buat & Xu (1996) suggested that most of the dust heating is due to stars with masses from $3-7 M_{\odot}$ which produce the bulk of the non-ionising continuum.

The radio emission from star-forming galaxies can either be of thermal or non thermal origin. The thermal radiation is free-free emission in H II regions, whereas the non-thermal emission is synchrotron radiation by cosmic electrons accelerated by supernovae (Condon 1992). Figure 1.7 shows the radio spectrum of the prototypical star-forming galaxy M82 along with the con-

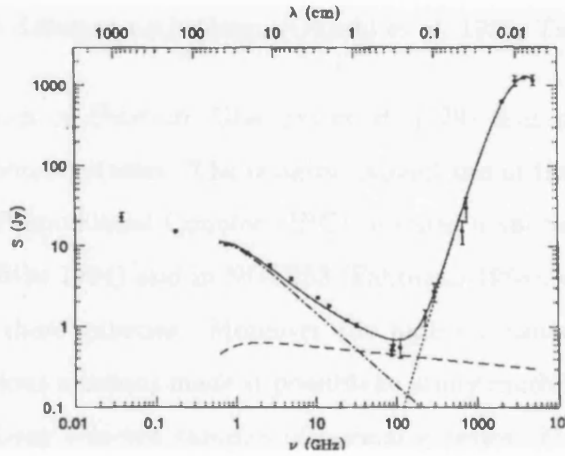


Figure 1.7: The radio/FIR spectrum of M82; from Condon (1992). The dot-dashed line shows the synchrotron component, whereas the dashed and the dotted lines show the free-free and dust components.

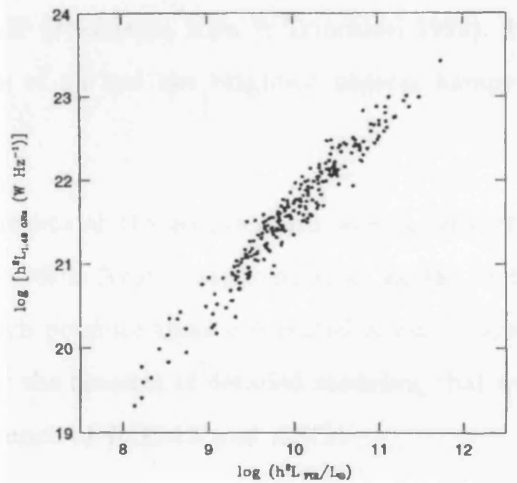


Figure 1.8: The radio-FIR correlation for normal galaxies (from Condon 1992).

tribution of the different components. In general most of the emission at frequencies lower than 10 GHz is of non thermal origin. A very tight correlation between the radio and FIR emission (fig 1.8) in normal galaxies suggests that the radio emission is closely related to star-formation (Condon 1992).

1.3 The X-ray emission

One of the first secure detection of a starburst galaxy in the X-ray band was that of M82 with Ariel 5 in the late 1970's (Ward et al. 1978). The two prototypical starburst galaxies, M82 and

NGC 253, have also been detected with *Ginga* (Ohashi et al. 1990, Tsuru et al. 1990).

However, it was the launch of *Einstein* (Giacconi et al. 1979) that made it possible to carry out detailed studies of normal galaxies. The imaging capabilities of the High Resolution Imager (HRI) and the Imaging Proportional Counter (IPC) revealed a spectacular superwind in M82 (Watson, Stanger & Griffiths 1984) and in NGC253 (Fabbiano 1988), extending for several Kpc along the minor axis of these galaxies. Moreover the higher sensitivity of these instruments compared to that of previous missions made it possible to study much fainter objects and create for the first time large X-ray selected samples of normal galaxies. Multiwavelength studies of these samples demonstrated that the X-ray emission of normal galaxies is very closely linked to their emission in other bands eg. optical, FIR, radio (Fabbiano, Gioia & Trinchieri 1988). The typical X-ray spectra of these objects as measured with the IPC were found to be thermal with temperatures of $\sim 3 - 5\text{keV}$ (Fabbiano, Kim & Trinchieri 1992). However, the relatively poor signal/noise of the spectra of all but the brightest objects hampered any attempts to model them in detail.

One of the major achievements of the *Einstein* era was the detection of individual sources in nearby galaxies (Fabbiano 1989). This made it possible for the first time to study the different populations of sources which produce their integrated X-ray emission. However, its sensitivity and energy range restricted the amount of detailed modeling that was possible. The next major advances came with the launch of *ROSAT* and *ASCA* .

ROSAT

ROSAT (Trumper 1984) carried two types of imaging detectors: the Position Sensitive Proportional Counter (PSPC) (Pfeffermann et al. 1987) which offered low resolution but high sensitivity spectroscopic and imaging data, and the High Resolution Imager (David et al. 1997) which had only imaging capabilities of similar spatial resolution to the HRI on-board *Einstein* but with much higher effective area. Both instruments were sensitive in the soft (0.1-2.5keV) X-ray band. Many star-forming galaxies have been observed with *ROSAT* , allowing detailed studies of their X-ray morphologies, the properties of the resolved sources and diffuse emission (e.g. Read, Ponman & Strickland 1997, Dahlem, Weaver & Heckman 1998). The higher sensitivity of *ROSAT* also made it possible to detect individual sources in a large number of other galaxies and to study their properties

as a class. Read et al. (1997) studied the spectral properties of different classes of sources resolved in spiral galaxies, whereas Roberts & Warwick (2000) derived their luminosity function. However, the limited energy range and spectral resolution of *ROSAT* hampered any detailed studies of the physical mechanisms which produce the X-ray emission. This situation was much improved with the launch of *ASCA*.

ASCA

ASCA (Tanaka, Inoue & Holt 1994) was the first X-ray satellite to carry CCDs. Its scientific payload consists of two CCD cameras (Solid state Imaging Spectrometer; SIS) (Gendreau 1995) and two proportional counters (Gas Imaging Spectrometer; GIS) (Ohashi, Ebisawa, Fukazawa, Hiyoshi et al. 1996), both sensitive over the 0.5-10.0keV energy band. Although the spatial resolution of *ASCA* is poorer than that of *ROSAT* its broader energy band and higher spectral resolution made it possible to study in detail the properties of the X-ray spectra of star-forming galaxies, and thus gain insights to the mechanisms which produce their soft and the hard X-ray emission. The typical broad band X-ray spectra of starburst galaxies can be modelled by a thermal plasma component with a temperature of $\sim 0.8\text{keV}$, and a higher temperature thermal plasma component ($\sim 10.0\text{keV}$) or a power-law with photon spectral index $\Gamma \sim 1.7 - 2.0$ (Ptak, Serlemitsos, Yaqoob & Mushotzky 1999). The better quality spectra of the brightest starburst galaxies require another soft thermal component with a temperature of $\sim 0.2\text{keV}$. In general the fits of the spectra suggest that the physical processes which produce the X-ray emission are complex, and cannot be described well by a simple optically thin plasma or a power-law spectrum (Dahlem, Parmar, Oosterbroek, Orr, Weaver & Heckman 2000).

Beppo-SAX

Beppo-SAX (Boella, Butler, Perola, Piro, Scarsi & Bleeker 1997) carries two sets of proportional counters (Low Energy Concentrator Spectrometer (LECS; Parmar et al. 1997) and Medium Energy Spectrometer (MECS; Boella, Chiappetti, Conti, Cusumano, del Sordo, La Rosa, Maccarone, Mineo, Molendi, Re, Sacco & Tripiciano 1997)) covering the 0.1-4.5keV and 1.5-10.0keV band respectively, and a high energy Phoswich Detector System (PDS; Frontera et al. 1997) which covers the 13-300keV band. Beppo-SAX has almost the same specifications as *ASCA* in the 0.1-10.0keV band but slightly better spatial resolution and higher effective area in the region of 6keV. Observations of M82 and NGC253 with

Table 1.1: The populations of X-ray sources in the Galaxy (from Watson 1990)

Type	No. in Galaxy	$\log \langle L_x \rangle$ erg s ⁻¹	$\log \langle L_{x, \text{tot}} \rangle$ erg s ⁻¹
HMXRB	30	37	38.5
LMXRB			
bulge	10	38	39
glob. clust	10	37	38
other	50	37	38.7
CVs	10 ⁵ – 10 ⁶	31.5	36.5-37.5
Stars			
O stars	5000	33	38.7
MS stars (B-K)	5 ⁹	28	37.7
MS stars (M)	10 ¹⁰	28	38
RS CVn	10 ⁶	31	37

Beppo-SAX detected an Fe-K line at 6.7keV which suggests that a fraction of the hard X-ray emission is of thermal origin (Cappi et al. 1999).

1.3.1 Discrete sources

As mentioned previously imaging observations of nearby galaxies show that a significant fraction of their X-ray emission arises from a population of point sources. Based on results for our own Galaxy these sources can be Supernova remnants and/or X-ray binaries of different types. Watson (1990) presented a comprehensive review of the populations of X-ray emitting sources in the Milky Way based on the *Einstein* results. His results are summarised in Table 1.1 and are indicative of the relative contribution of each source population. It is clear that the bulk of the X-ray emission of the Galaxy is produced by X-ray binaries, whereas there is a weaker component of supernova remnants and diffuse emission. High Mass X-ray binaries (HMXRBs) have almost the same contribution as the fainter Low Mass X-ray binaries because the latter outnumber the former. Other populations such as Cataclysmic variables (CVs) and normal stars have low X-ray luminosities but their numbers are very large and therefore their contribution is not negligible. However, in starburst galaxies the relative number of X-ray binaries is larger and therefore normal stars do not contribute significantly to the overall X-ray emission.

Although observations of other normal galaxies suggest that there is a large number of discrete sources, their populations may have different properties because of the different star-formation parameters. This becomes clear from a comparative study of the populations of X-ray binaries and SNRs in the Galaxy and the SMC by Yokogawa et al. (2000). They find that after rescaling for the size of SMC, it has a larger number of HMXRBs and SNRs than the Galaxy, but a deficiency of LMXRBs. In the next section the properties of the most important populations of X-ray sources will be discussed.

1.3.2 X-ray binaries

X-ray binaries can be separated into two major classes according to the mass of the donor star: High Mass X-ray binaries (HMXRBs) if its mass is $\geq 8 - 10 M_{\odot}$, and Low Mass X-ray binaries (LMXRBs) if its mass is $\sim 1 M_{\odot}$. Their spectral and variability properties are very different in all wavebands. Even the properties of objects belonging to the same class are very diverse since they depend on the evolutionary state of the system, the nature of the accreting object (neutron star or black hole), the type of the donor star and on other parameters of the system such as their separation, magnetic fields, inclination etc.

Recently there have been suggestions that discrete X-ray sources with extremely high X-ray luminosities (up to $\sim 10^{40} \text{erg s}^{-1}$) are found in star-forming galaxies (Komossa & Schulz 1998, Zezas, Georgantopoulos & Ward 1999, Lira 1999, Roberts & Warwick 2000). If these sources are X-ray binaries this means that they either accrete at super-Eddington rates or the mass of the compact object is of the order of a few hundred solar masses. One example of a such source is discussed in Chapter 4.

High Mass X-ray binaries

In this class the compact object accretes material from an early type (OB type) massive star. The mass transfer is either via Roche lobe overflow or direct accretion of a stellar wind in the closer systems. They have typical luminosities of $\sim 10^{35-38} \text{erg s}^{-1}$. Fig 1.9 shows a histogram of the luminosities of Galactic HMXRBs in comparison with the luminosities of binaries in the SMC. It is clear that objects from the SMC have systematically higher X-ray luminosities. There is evidence from observations in other galaxies (fig. 1.10) that

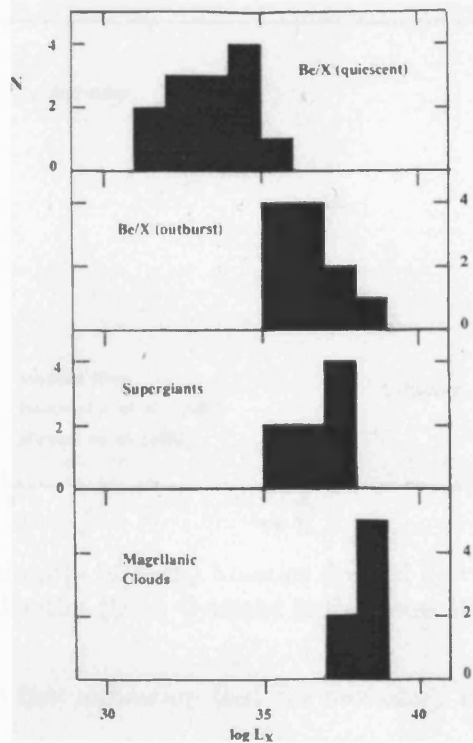


Figure 1.9: The distribution of the X-ray luminosities of various classes of X-ray binaries in the Galaxy. For comparison the distribution of X-ray luminosity of binaries in the Magellanic clouds is also presented. (from van Paradijs & McClintock 1995).

systems with lower metal abundances tend to have higher X-ray luminosities. This could be an effect of opacity, as for stars with lower metallicities the bulk of the continuum is able to escape. Also, high metallicities do not favour the formation of larger numbers of high mass stars as the radiation pressure from the heated dust grains (which are more numerous at high metallicity objects) inhibits further accretion during the star-formation process (Leitherer 1998).

The spectra of HMXRBs are typically hard, although they change dramatically during different states (see for example fig 1.11 showing the spectrum of Vela-X1 during pre eclipse, eclipse and post eclipse). The photon index of the underlying continuum of Vela-X1 during eclipse is ~ 1.3 . From this figure it is also clear that the spectra of HMXRBs are very rich in emission lines arising in the photoionised stellar wind which is irradiated by the hard X-rays from the neutron star (Nagase et al. 1994).

Low Mass X-ray binaries

Objects belonging to this class are mainly found in the bulge of the Galaxy or in globular

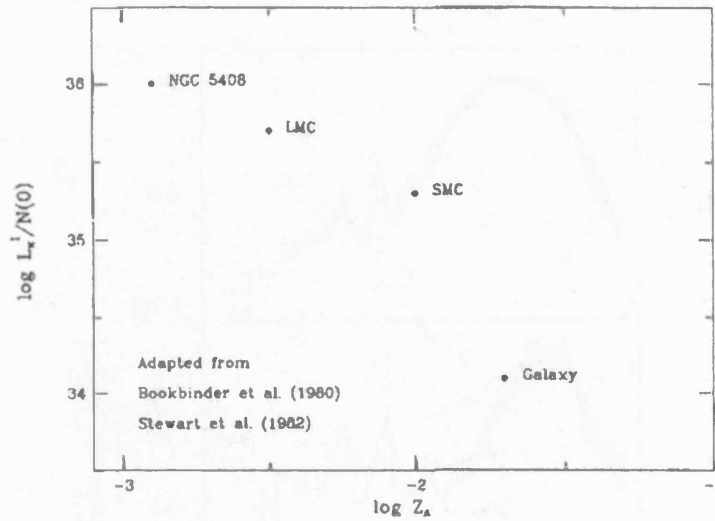


Figure 1.10: The X-ray luminosity of X-ray binaries divided by the number of O type stars, in systems with different metallicities (from Griffiths & Padovani 1990).

clusters. This was the first indication that the secondary star is of late type population-II. The mass transfer in these systems is via Roche lobe overflow. Their X-ray spectra are a superposition of an absorbed blackbody and a power-law component. Contrary to HMXRBs the spectra of LMXRBs do not exhibit strong lines apart from the FeK line at 6.4keV observed in a few cases (e.g. White et al. 1986, Kaastra 1997).

1.3.3 Supernova remnants

There are two major categories of SNRs in terms of their X-ray spectral properties. The first type includes SNRs with thermal spectra. In this case the X-ray emission arises by shock heated thermal gas, and they usually have shell-like morphology. The X-ray emission is mainly produced during the free and adiabatic expansion phase of the SNR (Charles 1995). The X-ray spectra of thermal SNRs are dominated by emission lines as is shown in fig 1.12 showing the X-ray spectrum of the Tycho SNR. As the gas is shock heated the effect of non-equilibrium ionisation may become very important. Indeed several studies of SNRs with *Einstein* and *ASCA* showed that their spectra are far from ionisation equilibrium (Hughes & Singh 1994, Masai 1994). The second major class are the non-thermal SNRs in which the X-ray emission arises in a synchrotron nebula. A typical example of this class is the Crab nebula. Their spectra are featureless and can be modelled with a power-law (Kaastra 1997).

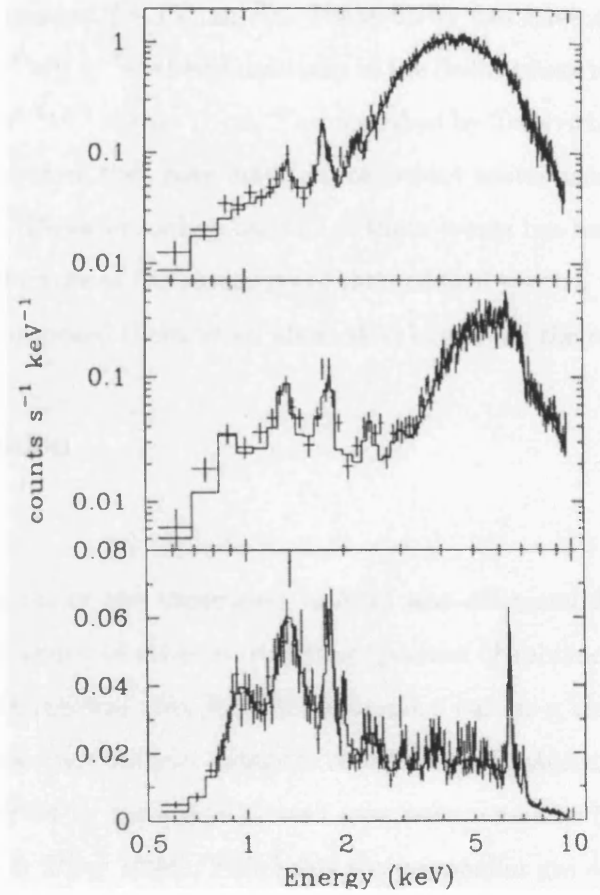


Figure 1.11: ASCA spectrum of Vela-X1 at post-eclipse (top), pre-eclipse (middle) and eclipse (bottom), from Nagase et al. (1994).

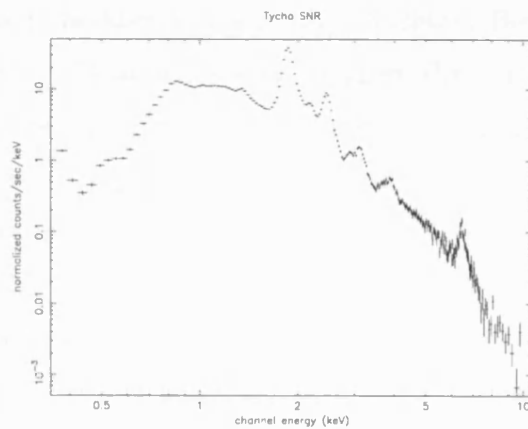


Figure 1.12: The ASCA SIS0 spectrum of Tycho SNR showing a wealth of emission lines.

A special case of SNRs are the so-called radio Supernovae. These are supernovae which detonate in a high density environment ($> 10^5 \text{ cm}^{-3}$). These SNRs can have exceptionally high X-ray luminosities reaching $10^{41} \text{ erg s}^{-1}$ as their luminosity in the Sedov phase is almost a linear function of density $L \sim 5 \times 10^{33} \eta^{6/5} t^{3/5} \text{ erg sec}^{-1} \text{ cm}^{-2}$ as described by Terlevich et al. (1992) and Fabian & Terlevich (1996). Therefore they may make an important contribution to the X-ray emission of star-forming galaxies. However, only a handful of these events has been observed in the X-ray band (Kaastra 1997). Because of the similarity of their optical spectra with the spectra of AGN Terlevich et al. (1992) proposed them as an alternative origin for the central engine of AGN.

1.3.4 Diffuse emission

Superwinds

The first observation of the superwind in M82 was discussed by Watson et al. (1984). Subsequent observations of other starbursting galaxies (Fabbiano 1988, Read et al. 1997, Dahlem et al. 1998) showed that the diffuse emission can be a very important component of the X-ray emission of starburst galaxies. A superwind is caused by the cumulative effect of stellar winds driven by massive stars and supernova remnants (Chevalier & Clegg 1985, Heckman, Armus & Miley 1990). This heats the interstellar gas and provides the required mechanical energy to form the wind. Figure 1.13 shows an optical image of M82 where the outflow is marked together with the position of supernovae detected in the radio band. It is clear that the SN are situated in the heart of the superwind, suggesting that they may provide the mechanical energy needed to drive it. This scenario is supported by detailed theoretical modelling (Chevalier & Clegg 1985, Suchkov, Berman, Heckman & Balsara 1996, Strickland 1998). These models also suggest that superwinds mainly contribute to the soft X-ray component of the emission from star-forming galaxies; although there may also be a very hot component with temperatures up to $\sim 10 \text{ keV}$, its contribution to the hard X-ray emission of the galaxy is minimal (Suchkov et al. 1996, Strickland & Stevens 2000). The morphology predicted by these models is remarkably similar to the observed morphologies, although it is not possible to constrain all the parameters of the models based on current observations, because of their poor spectral and spatial resolution. The X-ray luminosity of a superwind is directly proportional to the star-formation activity and also depends on the density of the ambient medium and the age

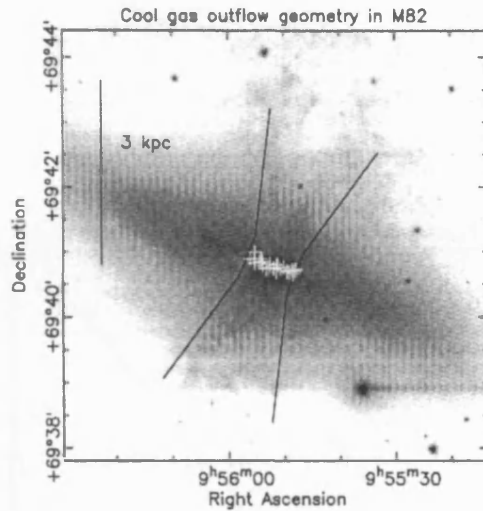


Figure 1.13: A DSS image of M82 showing the superwind geometry and the positions of the SNRs detected in radio observations (from Strickland & Stevens 2000)

of the starburst. Figure 1.14 shows the evolution of the X-ray luminosity of a superwind formed following an instantaneous burst of star-formation converting $10^8 M_{\odot}$ of gas to stars. The strength of the galactic gravitational potential plays an important role in the formation and evolution of a superwind, as in systems with weaker potential the escape velocity of the gas is lower and therefore less energy is needed to expell it from the galaxy. This is particularly important for the formation of superwinds in star-forming galaxies (Heckman et al. 1995, Della Ceca et al. 1997)

Diffuse hot gas

Early scanning studies of the galactic plane showed that there is a ridge of strong X-ray emission on the galactic plane (for an review see Watson 1990, Kaastra 1997). Recent observations with ASCA showed that the emission is thermal arising from a multicomponent plasma in non-ionisation equilibrium (Kaneda et al. 1997). However, the origin of this emission is still unclear. The main problem is that if it arises from hot gas it must be so hot that it cannot be confined to the galactic plane. For this reason a model involving the Galactic magnetic field has been proposed (Kaneda et al. 1997). Another possibility is that it arises from a population of faint discrete sources (Koyama, Makishima, Tanaka & Tsunemi 1986), but higher spatial resolution observations with *Chandra* will be needed to resolve this issue. Finally Yamasaki et al. (1997) suggested that it may be of non-thermal origin. However, this picture is not supported for the low latitude emission based

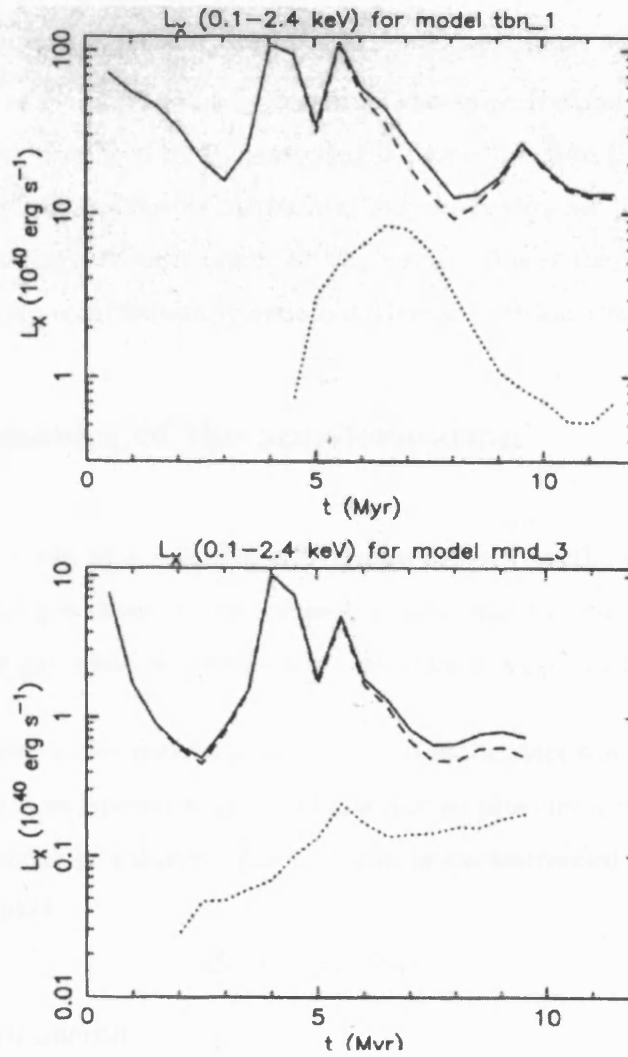


Figure 1.14: The evolution of the X-ray luminosity of the diffuse emission of a starburst which converts $10^8 M_\odot$ of gas to stars. The dashed line represents the emission from gas in the disk, and the dotted line is the emission from the halo. The total emission is shown by the solid line. The model in the top panel assumes a thick disk, whereas the one in the bottom panel assumes a thin disk (from Strickland & Stevens 2000)

on spectroscopic data which clearly point towards a thermal origin.

Inverse Compton scattering

Schaaf et al. (1989) first suggested that Inverse Compton scattering of infrared photons by relativistic electrons may produce the extended hard X-ray emission of M82. A similar scenario has been proposed by Goldshmidt & Rephaeli (1995) for the origin of the hard X-ray emission of NGC253, and by Moran, Lehnert & Helfand (1999) for NGC 3256. As the luminosity produced by IC scattering is proportional to the energy density of the radiation field, IC is a plausible mechanism only in cases when this field is very strong. For the ULIRGs (objects with $L_{\text{IR}} > 10^{11} L_{\odot}$) where this is the case, IC scattering may make an important contribution (Condon, Anderson & Helou 1991).

1.4 The parameters of the star-formation

The star-formation activity of a galaxy can be parameterized by the number of stars formed per unit space and time per mass interval (mass function), and the star-formation rate which is defined as the mass of gas which is transformed into stars in a certain amount of time.

An important parameter is the distribution of the mass of the stars when they form. The Initial Mass Function (IMF) is independent of age effects and so provides a uniform way to compare the mass function in different galaxies. The IMF can be parameterised by a power-law with an index α (Kennicutt 1998*b*):

$$dN(m)/dm = \alpha m^{-\gamma} \quad (1.1)$$

or for logarithmic mass intervals

$$dN(\log m)/d(\log m) = A m^{-\Gamma} \quad (1.2)$$

The relationship between Γ and γ is of course $\Gamma = \gamma - 1$. The IMF is defined between an upper and a lower mass limit ($M_{\text{up}}, M_{\text{low}}$). The index of the solar neighborhood IMF was initially measured by (Salpeter 1955) who found a slope of $\Gamma = 1.35$. This has been later revised by Miller & Scalo (1979) and Scalo (1986) who measured a slope of $\Gamma = 2.3$ for the high mass stars ($M > 10 M_{\odot}$). The Miller-Scalo IMF is presented in figure 1.15. From this plot it is clear that there is a turnover at lower masses, although the large error bars hamper the extraction

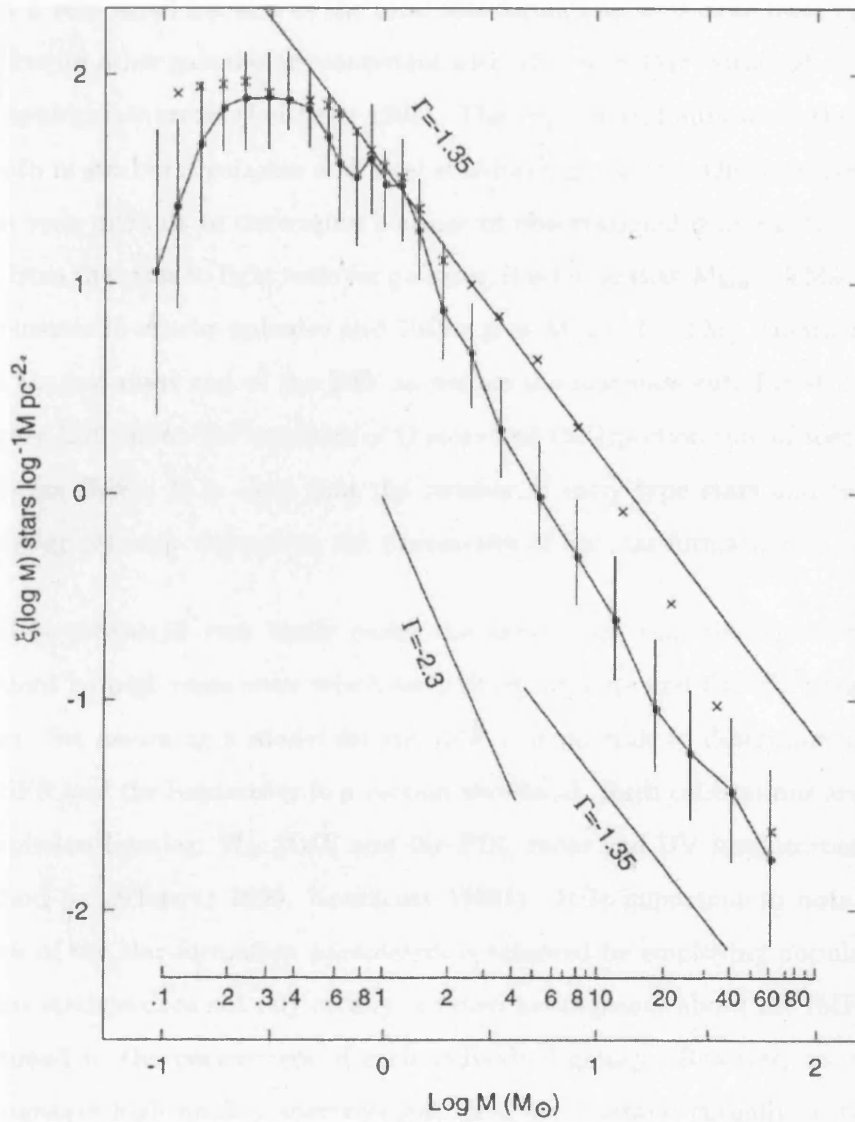


Figure 1.15: The IMF of Miller & Scalzo (1979) (crosses) and its revision by Scalzo (1986) (points). The two lines represent the Salpeter and power-law representation of the high mass end of the Miller-Scalzo IMF. (from Leitherer 1998)

of any conclusions regarding its shape at low masses. Determination of the parameters of the IMF depend on the stellar evolutionary tracks used to model the present day mass function (D'Antona 1998). Moreover, in other galaxies the determination of the IMF is a very difficult task as only the most luminous stars (typically $M > 10 M_{\odot}$) can be observed, and these stars represent only a very small fraction of the total star-formation, as is clear from figure 1.15. The measured indices for other galaxies are consistent with a Salpeter IMF, although it is very difficult to determine appropriate errors (Leitherer 1998). The upper mass limits are in the range between 50-100 M_{\odot} both in starburst galaxies and local star-forming regions. On the other hand the low mass cutoff is very difficult to determine because of observational constraints. Using indirect methods e.g. from the mass to light ratio for galaxies, it is found that $M_{\text{low}} \sim 5 M_{\odot}$. Measurements in superstar clusters in nearby galaxies and 30Dor give $M_{\text{low}} \sim 1 - 3 M_{\odot}$ (Leitherer 1998). The true shape of the low mass end of the IMF as well as the low mass cutoff is still an unresolved question. Figure 1.16 shows the numbers of O stars and the injection rate of mechanical energy for three different IMFs. It is clear that the number of early type stars and injection rate of mechanical energy strongly depend on the parameters of the star-formation.

The SFR can be estimated very easily under the assumption that the emission in an energy band is produced by high mass stars which have short lifetimes and therefore trace the current star-formation. So, assuming a model for the IMF it is possible to determine a scaling factor between the SFR and the luminosity in a certain waveband. Such calibrations are published for the optical emission lines eg. H_{α} , [OII] and the FIR, radio and UV luminosities (for a review of these method see Schaerer 1999, Kennicutt 1998b). It is important to note that the best determinations of the star-formation parameters is achieved by employing population synthesis modeling. This method does not rely on any *a priori* assumptions about the IMF and therefore can be fine tuned to the parameters of each individual galaxy. However, in order to derive all these parameters high quality spectroscopic data are essential (usually in the optical and NIR/Mid-IR bands) which are usually only available for the brightest galaxies.

1.5 Star-forming galaxies at High Redshift

Galaxies which experience intense bursts of star-formation may have important implications in cosmology. Firstly they may be directly related to the AGN phenomenon. There is a large num-

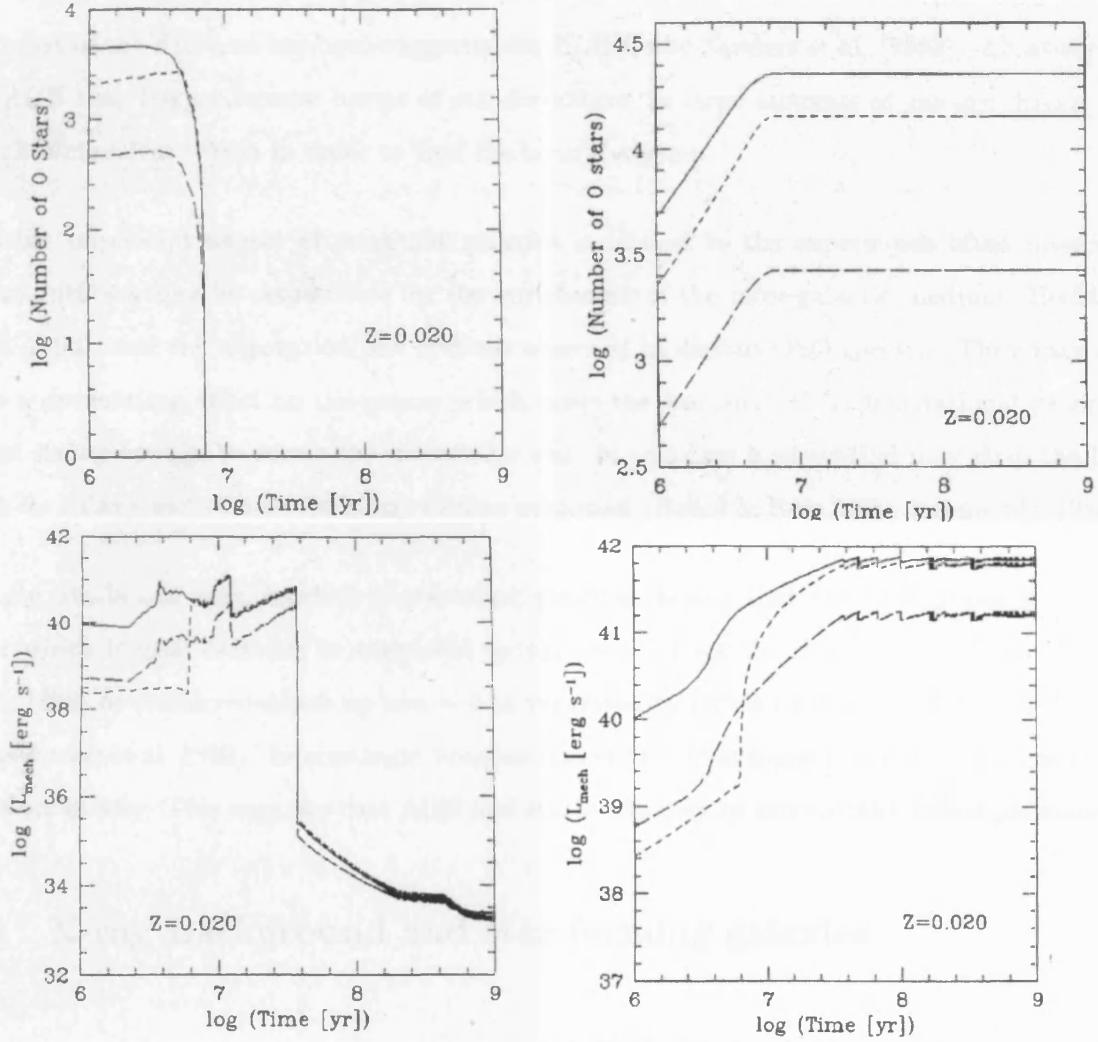


Figure 1.16: The number of O stars and the mechanical luminosity (from SNe and stellar winds) for different IMFs and star-formation scenarios. The left panels correspond to continuous starburst with $\text{SFR}=1 M_{\odot} \text{ yr}^{-1}$, whereas the right panel is for an instantaneous starburst which converts $10^6 M_{\odot}$ of gas into stars. Solid line: Miller-Scalo IMF with $M_{\text{up}}=100 M_{\odot}$; short-dashed line: Miller-Scalo IMF with $M_{\text{up}}=30 M_{\odot}$; long-dashed line: Salpeter IMF with $M_{\text{up}}=100 M_{\odot}$ (Leitherer et al. 1999).

ber of active galaxies which have composite spectra with both AGN and starburst components e.g Veron, Goncalves & Veron-Cetty (1997), Moran et al. (1996) and Ho, Filippenko & Sargent (1997*a*). This may be an indication of an evolutionary link between AGN and star-formation, in the sense that star-formation is responsible for the creation of the supermassive black hole at the heart of the AGN, as has been suggested for ULIRGs by Sanders et al. (1988). Alternatively the AGN may trigger intense bursts of star-formation, as large amounts of gas are driven into the circumnuclear region in order to feed the central engine.

Another important aspect of starburst galaxies is related to the superwinds often observed. These outflows may be responsible for the enrichment of the inter-galactic medium (Heckman et al. 1990), and the absorption line systems observed in distant QSO spectra. They may also have a devastating effect on the galaxy which hosts the starburst, if its gravitational potential is not strong enough to retain the interstellar gas. In this case a superwind may strip the ISM from its galaxy and thereby halt any further evolution (Babul & Rees 1992, Kormendy 1985).

Finally, studies of high redshift star-forming galaxies showed that the SFR peaks at $z \simeq 1.5$ after which it may decrease as suggested by the results from the Hubble Deep Field (Madau et al. 1998) or remain constant up to $z \sim 4$ as suggested by recent results from ISO and SCUBA (Glazebrook et al. 1999). Interestingly Franceschini et al. (1999) found a similar evolution for the AGN emissivity. This suggests that AGN and starbursts may be intrinsically linked phenomena.

1.6 X-ray Background and star-forming galaxies

The nature of the extragalactic X-ray background (XRB) has been one of the longest standing problems in X-ray astronomy since its discovery in 1962 (Giacconi, Gursky, Paolini & Rossi 1962). Deep surveys with *ROSAT* (Boyle et al. 1993, McHardy et al. 1998, Hasinger et al. 1998) have shown that much of it arises from a population of discrete sources. A large fraction of these sources are identified with QSOs (Boyle et al. 1993, Lehmann et al. 2000). However, the X-ray spectra of QSOs are much steeper with $\Gamma \sim 1.7$ (Schartel et al. 1996, Reeves et al. 1997) than the measured spectrum of the XRB which is $\Gamma \sim 1.4$ (Chen, Fabian & Gendreau 1997). This so-called spectral paradox requires that there is another population of sources with flatter spectra than that of QSOs, and which makes a significant contribution to the XRB. The similarity

between the residual spectrum of the XRB (after subtracting the contribution of QSOs) and the spectrum of redshifted HMXRBs led Griffiths & Padovani (1990) to suggest that star-forming galaxies may make an important contribution to the XRB. A similar suggestion was made earlier by Bookbinder et al. (1980), who estimated the contribution of star-forming galaxies to the XRB by assuming that their X-ray emission arises from a superwind and a HMXRBs component.

Initially the discovery of a population of sources with narrow-line optical spectra as counterparts of faint X-ray sources found in deep and medium sensitivity X-ray surveys (Fruscione & Griffiths 1991, Boyle et al. 1997, Griffiths et al. 1996) was taken as evidence that star-forming galaxies contribute to the XRB. However, more careful spectroscopy has shown that many of these sources are in fact AGN eg. Moran et al. (1996). This result is reinforced by the conclusions based on an extremely deep survey of the Lockman Hole region carried out with the HRI on-board *ROSAT*. Optical and IR follow up spectroscopy of the sources into which the XRB is resolved showed the majority of them to be AGN (Lehmann et al. 2000).

Recently, a model involving populations of AGN observed through different column densities has been used to successfully reproduce the hard (above 2keV) XRB (Comastri, Setti, Zamorani & Hasinger 1995). The use of such a model can be related to the discovery of a population of hard X-ray sources which emerges above 2keV (Ueda et al. 1998). A link between this model and the starburst scenario has been proposed by Fabian, Barcons, Almaini & Iwasawa (1998). According to this, the hard X-ray background is produced by AGN which in the soft X-ray band are obscured by circumnuclear starbursts which themselves produce the soft X-rays.

Theoretical modeling based on the luminosity function of IRAS selected normal galaxies showed that star-forming galaxies can produce between $\sim 10\% - 30\%$ of the soft XRB (Green et al. 1992, David, Jones & Forman 1992, Griffiths & Padovani 1990). On the other hand modeling based on the X-ray luminosity function of local starbursts gives a contribution of only 4%, if no evolution is assumed (Georgantopoulos, Basilakos & Plionis 1999). This discrepancy may arise because of the different methods used to estimate the fraction of the XRB which is produced by star-forming galaxies, or because Georgantopoulos et al. (1999) assumed no evolution.

1.7 Motivation for this work

This work is motivated by the need to better understand and quantify the possible contribution of star-forming galaxies to the extragalactic XRB. Having noted a large number of previous misclassifications of X-ray emitting starburst galaxies, which subsequently turned out to be AGN, we embarked on our own survey to discover ‘bona-fide’ examples of X-ray luminous star-forming galaxies and so finally settle the question of whether they do in fact exist. Here this problem is attacked from a different perspective. Instead of trying to classify the objects found in Deep Surveys, we attempt to find *local* examples of X-ray luminous star-forming galaxies. For this reason well defined X-ray selected samples of galaxies are used. The definition of these samples, the classification of the objects and a discussion of the properties of the X-ray starbursts found are presented in Chapter 2.

Chapter 3, presents a study of the largest sample of *bona-fide* star-forming galaxies studied so far in the X-ray band. We give a concise interpretation of the X-ray emission of starburst galaxies based on the correlations between X-ray emission and emission in other wavebands. Finally these results are used in order to constrain the contribution of star-forming galaxies to the extragalactic soft X-ray background.

Finally in Chapter 4, three examples of X-ray luminous star-forming galaxies are studied in detail. Their X-ray spectral and spatial properties are discussed in the context of the currently favoured models.

Chapter 2

A search for X-ray luminous star-forming galaxies

This chapter describes an optical spectroscopic survey conducted in order to search for X-ray luminous star-forming galaxies. X-ray luminous star-forming galaxies are an interesting class of galaxies for two reasons: firstly it has been suggested that they may make a significant contribution to the extragalactic soft X-ray (0.1-2.5keV) background. Secondly they need to be understood in their own right as they exhibit X-ray luminosities 100 times or more higher than the typical X-ray luminosities of normal galaxies. The initial attempts to identify large numbers of these objects have failed, due mostly to mis-classifications . Therefore the question remains: Do these objects exist at all, and if so how rare are they ? This work attempts to identify X-ray luminous star-burst galaxies in large appropriately selected samples of galaxies from X-ray catalogues. The search, the results, and a discussion of the properties of those objects are presented in this chapter.

2.1 Selection of the sample

In order to search for X-ray luminous star-forming galaxies we obviously need an X-ray selected sample. The best catalogues are those produced from data obtained with the *ROSAT* satellite. There are two reasons for this:

a) The X-ray emission of star-forming galaxies peaks in the soft (0.1-2.5keV) band, whereas at higher energies it drops off following a power-law with an energy index of ~ -0.7 (Ptak

et al. 1999).

b) *ROSAT* carried the most sensitive X-ray detectors launched so far. This when combined with the high effective area of its X-ray telescope, made it the most powerful instrument to detect faint soft X-ray sources, in the pre Chandra and XMM era.

From the data obtained during the course of the *ROSAT* mission (1991-1998) several catalogues of X-ray sources have been constructed. From these we selected the *ROSAT* All Sky Survey Bright Source Catalogue (RASSBSC) and the WGAcat catalogues. These catalogues are briefly described below:

The RASSBSC

ROSAT scanned the sky several times in stripes perpendicular to the direction of the sun. Then all the observations were coadded and several detection algorithms used in order to detect X-ray sources. A total of 145,060 sources were found. From these sources those which fulfill the following criteria formed the RASSBSC: count rate higher than $0.05 \text{ counts s}^{-1}$, number of source photons greater than 15 and detection likelihood greater than 15 (Voges et al. 1999). This catalogue has 18,811 entries. As some regions of the sky eg. the ecliptic poles are observed more times than others eg. the ecliptic equator, the effective exposure is not constant over the sky. Moreover, the hydrogen column density, which dominates the absorption in this band, varies significantly over the sky with a maximum along the galactic plane and a minimum of $\sim 5 \times 10^{19} \text{ cm}^{-2}$ at the Lockman hole. For these two reasons the RASSBSC contains neither a uniform nor a complete sample of X-ray selected sources. Nevertheless it is the only sensitive all sky soft X-ray survey carried out so far, and for the foreseeable future.

The WGAcat

The second X-ray catalogue used, WGAcat, is based on a different philosophy. It consists of the sources detected within the pointed observations with *ROSAT* PSPC, which became public prior to March 1994. The source search was performed by applying a sliding cell algorithm on the PSPC data. It contains a total of 98,326 detections. For the cross-correlations a subsample which contains only the detections with quality flag 5 or more ie. detections which have been inspected by eye and do not show any obvious problems has been used. This sample consists of 71,260 detections associated with 68,763 individual

sources. The multiple detections appear because of multiple observations of the same field. Due to the way WGAcat is defined, it is not a uniform sample, as it consists of serendipitous sources found in pointed observations. However, as it is constructed from PSPC pointed observations which are much deeper than the snapshots used for the RASSBSC, it contains a larger number of sources than the former, and extends to lower flux levels.

The spectral energy distribution of star-forming galaxies peaks in the FIR band (see Schmitt et al. 1997) as the UV/optical photons emitted by stars are absorbed by the galactic dust and reradiated at longer wavelengths. On the other hand young star-burst galaxies with a low dust content are relatively strong emitters in the blue and near UV part of the spectrum, as young early type stars have very strong UV continuum emission. Therefore the best source lists to search for star-forming galaxies are FIR and UV-excess selected samples. The RASSBSC and the WGAcat have been cross-correlated with the Markarian, Kiso-Schmidt and IRAS Faint Source Catalogue (IRASFSC) lists. More details on those three samples are given below.

The Markarian catalogue

The Markarian catalogue (Markarian 1967, Markarian, Lipovetskii & Stepanian 1981) contains 1500 objects with relatively strong blue and UV continuum. They were discovered in an objective prism survey using the 1.0-1.3m Schmidt telescope of the Byurakan Astrophysical Observatory covering 15,200 square degrees with $\delta > -15$ deg and avoiding the galactic plane. The survey is complete down to a $m_{pg} = 15.2$ mag. Objects brighter than 13th mag have been omitted. The objects have been identified from the photographic plates based on the strength of their blue/optical continuum. Follow up optical spectroscopy of a large fraction of this sample has shown that the majority of the objects are AGN, although there are also a significant number of H II -type galaxies eg. Mazzarella & Balzano (1986), Mazzarella & Boroson (1993).

The Kiso-Schmidt survey

The Kiso-Schmidt survey (eg Takase & Miyauchi-Isobe 1984, Takase & Miyauchi-Isobe 1993), has a similar aim as the Markarian survey; that is to select UV-excess objects, but it goes much deeper and is performed in a different way. The objects have been selected on the basis of their U,G and R colours: objects with strong U and G emission compared

Table 2.1: Comparison of the Markarian and the KISO samples

Table	Covered area sq. deg.	Objects	Obj. density deg ⁻²	Lim. magnitude m _{pg}
KISO	2,100	4,112	2.0	16.5-18.5
Markarian	17,000	1,500	0.1	17.5

Information from Takase & Miyauchi-Isobe (1988)

to their G and R emission respectively are classified as KISO galaxies. The U and R filters are almost identical to the Johnson filters, whereas the G filter peaks at $\sim 4800\text{\AA}$. The KISO catalogue contains a total of 8,162 objects down to a limiting photographic magnitude of 16.5-18.5mag depending on the conditions (Miyauchi-Isobe & Takase 1988). The amount of UV excess is measured from the relative brightness of the U to the G and/or R image. Objects with $U-G < -0.5$ are designated as having high UV excess (H), whereas objects with $-0.5 < U-G < 0.5$ and $U-G < 0.5$ are designated as medium (M) and low (L) UV-excess (Noguchi, Maehara & Kondo 1980, Takase, Noguchi & Maehara 1983). Table 2.1 presents a comparison between the Markarian and the Kiso surveys taken from Takase & Miyauchi-Isobe (1988).

The IRAS Faint Source Catalogue

The IRASFSC (Moshir 1991), resulted from the second processing of the data obtained during the All Sky survey carried out by the IRAS satellite. It is restricted to $|b_{II}| \geq 10$ deg at 12 and 25 μ and $|b_{II}| \geq 20$ deg at 60 μ in order to avoid source confusion. Also it does not contain any sources detected only in the 100 μ band as these most probably are related to infrared cirrus. It contains a total of 173,044 sources (of which 148,981 are associated with individual objects) and it is 2.5-3 times more sensitive than the Point Source Catalogue. Its major advantages over the Point Source Catalogue are that it goes to fainter flux limits, and therefore contains a much larger number of sources. Also the flux determinations are more accurate, although there may be a number of false detections at the lowest flux levels (the reliability exceeds 90% at 12 μ and 25 μ and 80% at 100 μ). However, as in the case of the RASSBSC, because of the non uniform coverage of the sky this sample is not uniform.

In order to define the search radius the catalogues have been crosscorrelated using a radius of 300". Then the number of coincidences has been plotted against the offset (see fig 2.1). The

Table 2.2: Results from the cross-correlations

Sample 1	Sample 2	Result	Chance-coincidences.
Markarian	RASSBSC	109	0 ± 0
Markarian	WGAcat	188	1 ± 1
IRAS FSC	RASSBSC	1776	19 ± 3
IRAS FSC	WGAcat	1514	66 ± 5
Kiso	RASSBSC	58	2 ± 1
Kiso	WGAcat	76	5 ± 1

radius has been selected in order to ensure that most of the coincidences are included in the sample and to minimise the number of chance coincidences. The final search radius is set to $30''$ for all the catalogues.

The chance coincidence probability has been assessed by shifting the coordinates of one catalogue by a few degrees in a random direction and cross-correlating the catalogues again. This test was done five times with different shifts to improve the statistics of the chance coincidences. The results from the cross-correlations together with the number of chance coincidences are presented in Table 2.2. It is noted that these numbers include a large number of multiple identifications of the same objects (specially in the case of the WGAcat catalogues).

From the cross-correlated lists all the Galactic objects (known stars, Supernova remnants, X-ray binaries etc) have been excluded. A total of 89 and 75 X-ray emitting galaxies are found in the Markarian and Kiso lists respectively, when cross-correlated with WGAcat. From the cross-correlations with the RASSBSC we find 108 and 77 coincidences respectively. In order to exclude the AGNs from the IRAS FSC samples, a further selection criterion has been applied. This criterion uses the $f_X/f_{60\mu}$ ratio to distinguish between broad-line objects (Seyfert 1s and QSOs) and NLEGs (Seyfert 2s, LINERs and starbursts) as is clear from fig. 2.2 (Green et al. 1992). All the objects with $\log(f_X/f_{60\mu}) > -1.6$ have been excluded. In this study the X-ray flux is in the 0.1-2.5 keV band, which corresponds to a ratio of 1.5 in figure 2.2 where the flux is measured in the 0.5-4.5keV band, assuming a thermal plasma model of 0.7keV. After the application of this selection criterion, the size of this catalogue was reduced to a total of 311 and 105 entries for the WGAcat and the RASSBSC samples respectively. These numbers do not contain any multiple coincidences of the same objects.

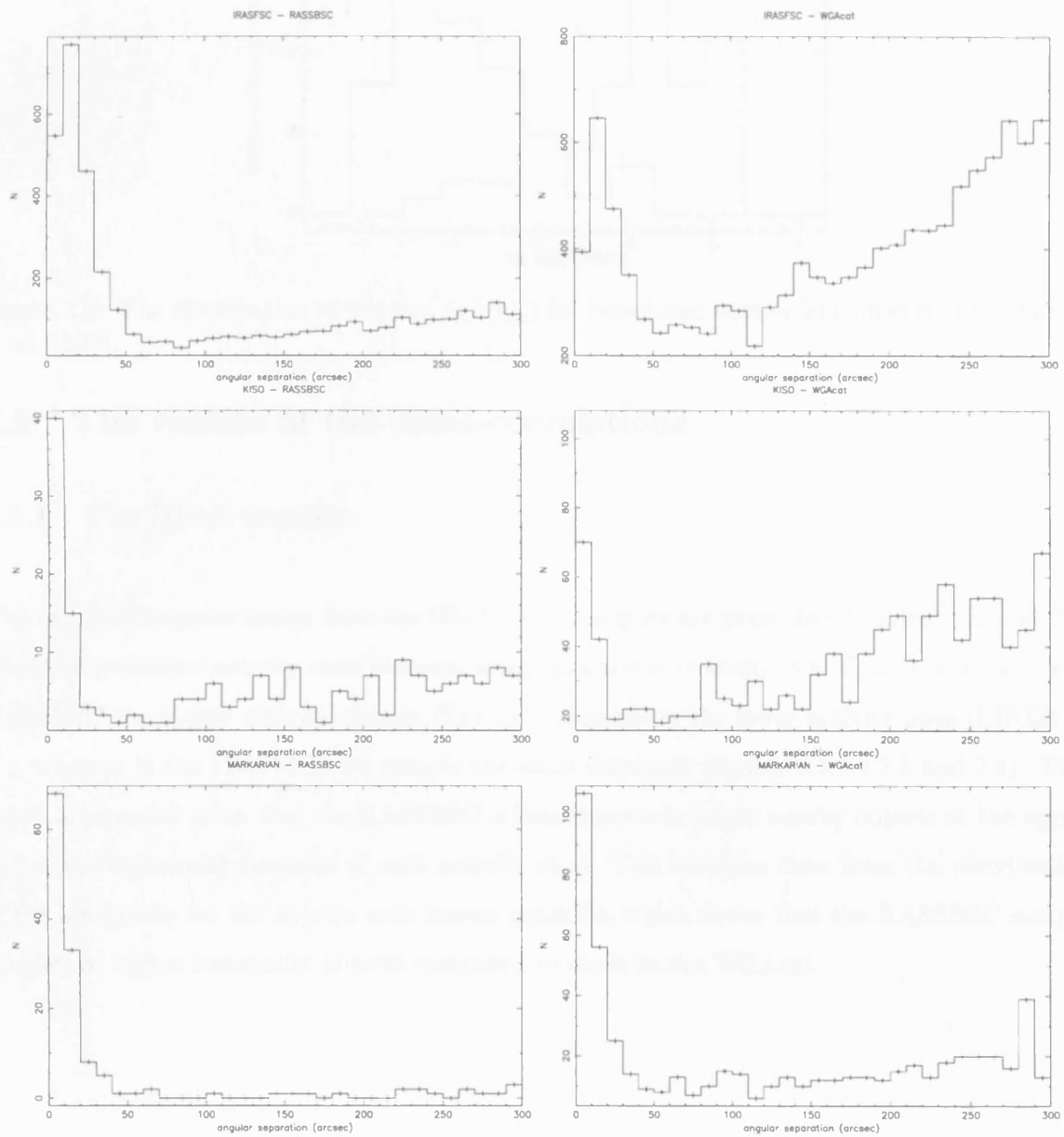


Figure 2.1: A histogram of the separation between the sources in the cross-correlated samples. The cross-correlation radius used was $300''$.

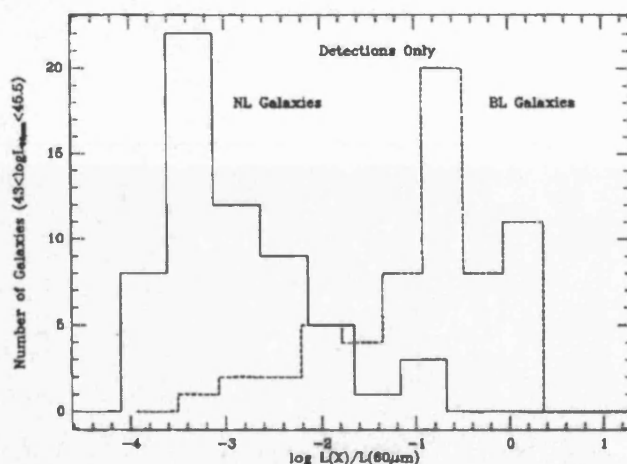


Figure 2.2: The distribution of the $\log(f_X/f_{60\mu})$ for broad and narrow line objects (from Green et al. 1992).

2.2 The results of the cross-correlations

2.2.1 The IRAS samples

The two final samples drawn from the IRASFSC catalogues are presented in Tables 2.3 and 2.4. Based on published activity classifications using optical spectroscopy, it is clear that in the FSC-RASSBSC the higher activity objects (Sy1-Sy2) outnumber the lower activity ones (LINER-H II), whereas in the FSC-WGAcad sample the latter dominate (figures 2.3,2.4,2.5 and 2.6). This result is expected given that the RASSBSC is biased towards bright nearby objects at the upper end of the luminosity function of each activity class. This becomes clear from the distribution of the luminosity for the objects with known redshifts, which shows that the RASSBSC sample consists of higher luminosity objects compared to those in the WGAcad.

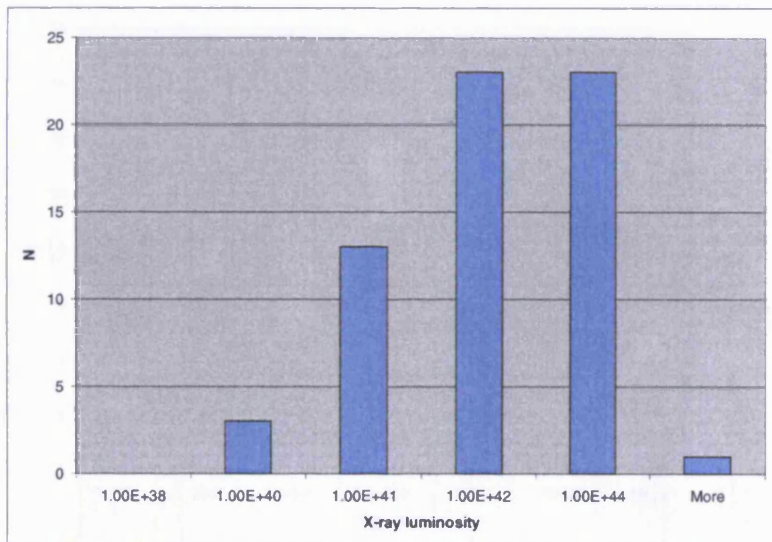
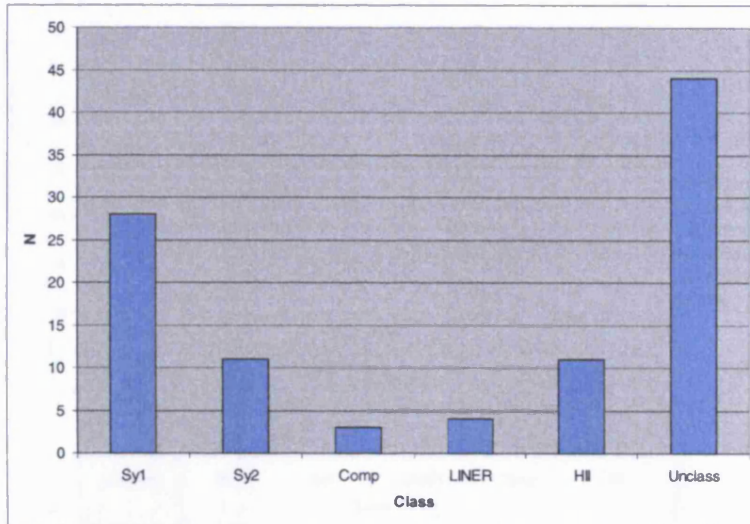


Figure 2.3: The distribution of activity classes, and X-ray luminosities of the objects in the IRASFSC-RASSBSC sample.

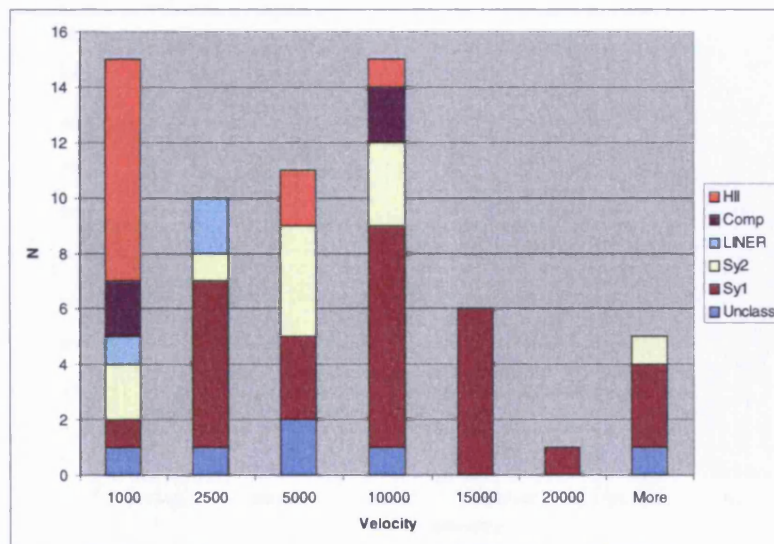
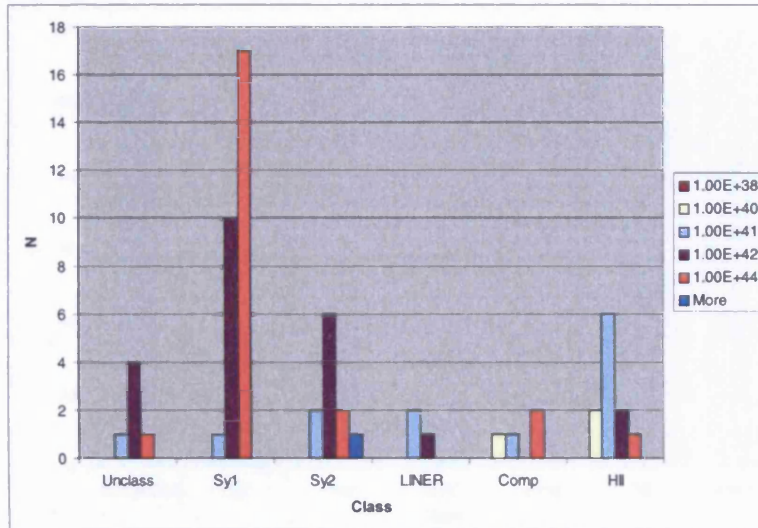


Figure 2.4: The distribution of X-ray luminosities and velocities of objects of different activity classes in the IRASFSC-RASSBSC sample.

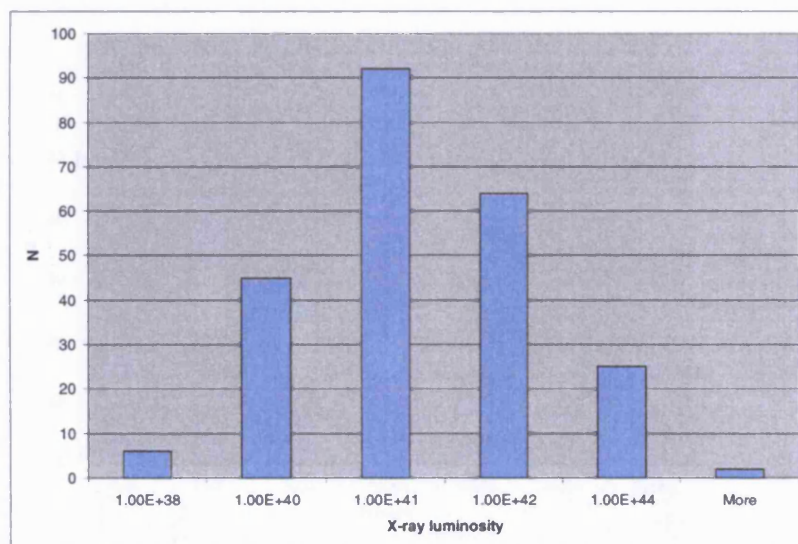
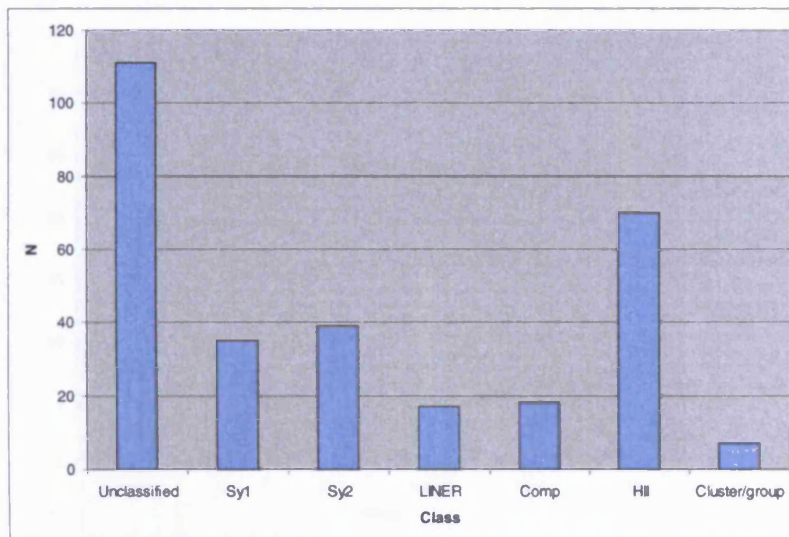


Figure 2.5: The distribution of activity classes, and X-ray luminosities of the objects in the IRASFSC-WGAcad sample.

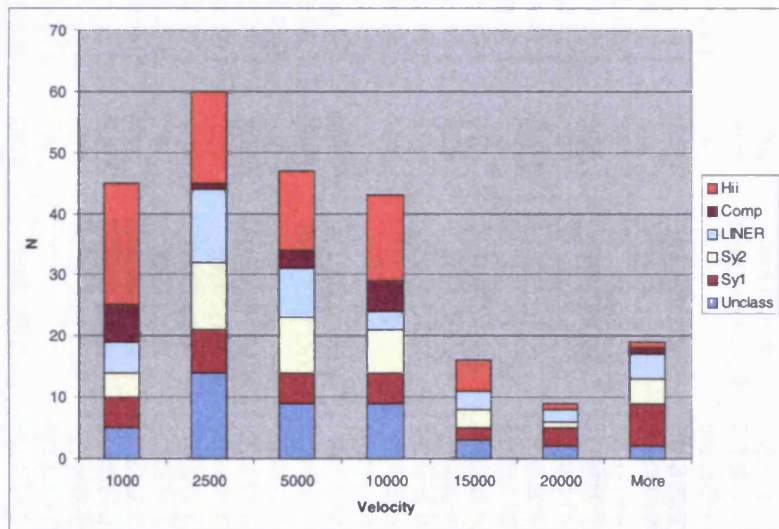
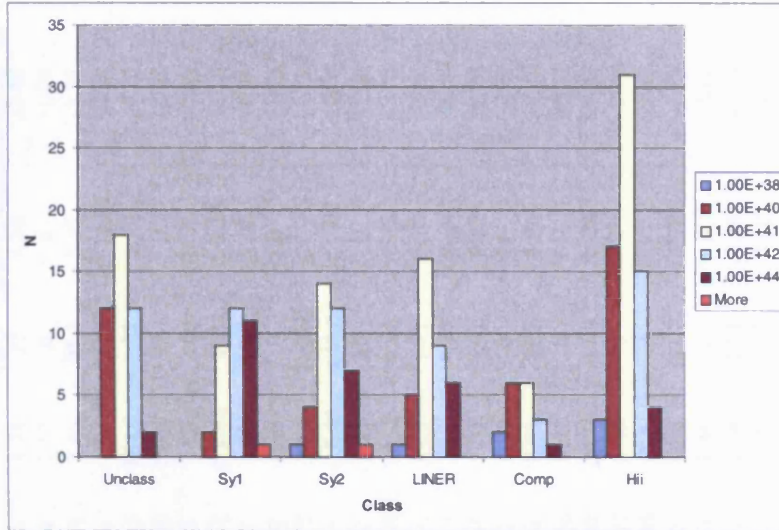


Figure 2.6: The distribution of X-ray luminosities and velocities of objects of different activity classes in the IRASFSC-WGAcad sample.

Table 2.3: Results of the IRASFSC - RASSBSC cross-correlation

IRAS name	RASSBSC name	Other name	Velocity km s ⁻¹	RA J2000 (h m s)	Dec J2000 (° ' ")	F _X	F _{60μ} Jy	L _X	L _{60μ}	log(F _X /F _{60μ})	Cirrus	Classification	Ref
(1)	(2)	(3)	(4)	(5)	(6)	(7)	(8)	(9)	(10)	(11)	(12)	(13)	(14)
F00006+2141	J000308.6+215728	MRK 0334	6582	0 3 9	21 57 45	8.68	4.34	18	4.50	-2.40		H II	12
F00108+7645	J001337.6+770210		0	0 13 40	77 2 18	9.04	1.12	0	0	-1.79			
F00317-2142	J003413.7-212619	ESO 540- G 00	8035	0 34 12	-21 26 17	29.71	3.85	91.8	5.95	-1.81		Comp	10
F00391+4004	J004154.0+402118	MRK 0957	21345	0 41 53	40 21 19	7.85	< 2.09	171.0	< 22.83	-2.12	Y	Sy1	4
F00450-2533	J004733.3-251722	NGC 0253	241	0 47 32	-25 17 15	26.83	784.2	0.07	1.09	-4.16	Y	H II	
F00445-1208	J004703.1-115217	NGC 0246	0	0 47 2	-11 51 59	52.26	15.87	0	0	-2.18			
F01091-3820	J011127.9-380507	NGC 0424	3496	1 11 26	-38 5 4	4.55	1.80	2.66	0.52	-2.29		Sy2	13
F01194-0118	J012159.9-010223	MRK 1503	16302	1 21 59	-1 2 22	13.57	< 1.45	173	< 9.25	-1.73	Y	Sy1	9
F01319-1604	J013425.0-154910	MCG -03-05-007	5974	1 34 25	-15 49 3	5.97	1.93	10.2	1.65	-2.21		Comp	9
F01416-1611	J014404.7-155632		0	1 44 6	-15 56 27	4.66	0.48	0	0	-1.71	Y		
F01572+0009	J015950.6+002337	KUG 0157+001	48903	1 59 49	0 23 44	18.73	2.22	2140.0	127.24	-1.77		Sy2	4
F02021-1213	J020436.8-115941	KUG 0202-122	21600	2 4 35	-11 59 49	6.64	< 0.81	148.0	< 9.03	-1.78			1
F02327+3428	J023547.9+344107		0	2 35 46	34 41 15	8.73	1.27	0	0	-1.86			
F02401-0013	J024240.9-000046	M77	1137	2 42 40	-0 0 45	160.65	176.2	9.94	5.45	-2.74		Sy1	5
F02441-3029	J024620.0-301639	NGC 1097	1275	2 46 17	-30 16 29	16.81	44.5	1.31	1.73	-3.12		Sy1	3
F03176-6640	J031819.4-662912	NGC 1313	475	3 18 16	-66 29 29	20.41	14.6	0.22	0.08	-2.55	Y	H II	8
F03207-3723	J032241.8-371239	NGC 1316	1760	3 22 40	-37 12 30	13.56	2.98	2.01	0.22	-2.04		LINER	9
F03300+3707	J033316.2+371815		0	3 33 16	37 18 1	6.21	0.63	0	0	-1.71	Y		
F04124-0803	J041451.8-075521		11373	4 14 51	-7 55 38	4.64	0.63	28.7	1.96	-1.83		Sy1	2
F04110+2804	J041411.9+281230		0	4 14 10	28 12 10	13.53	5.87	0	0	-2.34	Y		
F04188-5503	J042000.5-545617	NGC 1566	1496	4 19 59	-54 56 6	38.22	14.71	4.09	0.79	-2.28		Sy1	15
F04271+1807	J043004.5+181342		0	4 30 3	18 13 53	10.00	3.48	0	0	-2.24		star	
F04328+2248	J043553.6+225410		0	4 35 52	22 54 24	10.06	7.4	0	0	-2.57	Y		
F04358-1053	J043813.8-104740	PGC 015703	10737	4 38 13	-10 47 45	5.93	0.64	32.7	1.75	-1.73	Y	Sy1	4
F04390+2517	J044205.6+252305		0	4 42 6	25 23 10	5.50	1.46	0	0	-2.12	Y		
F04575-7537	J045602.3-753211	ESO 033- G 002	5426	4 55 58	-75 32 33	5.47	0.68	7.71	0.48	-1.79	Y	Sy2	4
F05059-3734	J050743.0-373030	NGC 1808	1000	5 7 41	-37 30 48	5.45	87.81	0.26	2.10	-3.91	Y	H II	11
F05054+1718	J050820.9+172134	CGCG 468-002	5454	5 8 21	17 22 4	5.42	10.21	7.71	7.27	-2.97			10
F05177-3242	J051936.1-323910	ESO 362- G 018	3790	5 19 36	-32 39 27	5.76	1.40	3.96	0.48	-2.08		Sy1	4
F05222-0844	J052437.4-084200		0	5 24 36	-8 42 2	11.43	2.89	0	0	-2.10	Y		
F05259-6607	J052559.2-660450	LMC ?	0	5 26 2	-66 5 9	105.75	13.31	0	0	-1.80	Y		9
F05261-2047	J052814.7-204546		0	5 28 15	-20 45 32	6.07	0.71	0	0	-1.77			
F05263-0824	J052842.2-082249		0	5 28 41	-8 22 37	4.82	0.52	0	0	-1.73	Y		
F05263+1149	J052908.4+115207		0	5 29 7	11 52 11	6.12	30.51	0	0	-3.40	Y		
F05294+0600	J053207.7+060217		0	5 32 8	6 2 33	4.59	10.6	0	0	-3.06			
F05494+6058	J055401.7+605834		27306	5 54 3	60 58 41	5.16	< 1.68	184.0	< 30.00	-2.21	Y	Sy1	4

Table 2.3: Results of the IRASFSC - RASSBSC cross-correlation *continued*

IRAS name (1)	RASSBSC name (2)	Other name (3)	Velocity (4)	RA (5)	Dec (6)	F_X (7)	$F_{60\mu}$ (8)	L_X (9)	$L_{60\mu}$ (10)	$F_X/F_{60\mu}$ (11)	Cirrus (12)	Classification (13)	Ref (14)
F05514+0139	J055402.6+014024		0	5 54 1	1 40 22	23.69	9.25	0	0	-2.29	Y		
F06098+7103	J061533.6+710207	MRK 0003	4050	6 15 36	71 2 15	5.03	3.77	3.95	1.48	-2.57		Sy2	4
F06228-5240	J062357.2-524139		0	6 23 56	-52 41 46	42.43	5.37	0	0	-1.80			
F06387+5531	J064255.9+552835		0	6 42 53	55 28 27	7.04	0.79	0	0	-1.75			
F06457+7429	J065209.8+742537	MRK 0006	5537	6 52 12	74 25 36	5.60	1.18	8.22	0.87	-2.02	Y	Sy1	4
F07422+2808	J074519.3+280123		0	7 45 17	28 1 37	5.34	4.90	0	0	-2.66			
F07555-5250	J075647.9-525901		0	7 56 47	-52 59 3	5.94	0.64	0	0	-1.72	Y		
F07568-4906	J075816.7-491439		0	7 58 15	-49 14 48	6.27	5.12	0	0	-2.61			
F07572+2645	J080020.5+263649	IC 0486	8057	8 0 18	26 36 52	5.69	0.93	17.7	1.45	-1.91		Sy1	2
F09497-0122	J095219.1-013639	MRK 1239	5974	9 52 18	-1 36 48	4.84	1.33	8.27	1.14	-2.14	Y	Sy1	4
F09517+6954	J095550.4+694052	M82	213	9 55 52	69 40 40	80.7	0.71	0.17	1.18	-3.8		H II	5
F10126+7338	J101655.5+732359	NGC 3147	2820	10 16 54	73 23 53	18.40	7.26	7	1.38	-2.29		Sy2	4
F10207+2007	J102331.5+195143	NGC 3227	1157	10 23 30	19 51 49	8.87	7.82	0.57	0.25	-2.64		Sy1	3
F10257-4339	J102753.4-435427	NGC 3256	2738	10 27 52	-43 54 24	5.47	88.3	1.96	15.84	-3.91		H II	5
F10295-1831	J103156.6-184628		12081	10 31 57	-18 46 38	11.69	2.54	81.6	8.89	-2.04		Sy1	5
F10354-2651	J103749.5-270715	ESO 501- G 059	2437	10 37 49	-27 7 20	4.61	< 0.80	1.31	< 0.11	-1.94			
F10356+5345	J103846.7+533002	NGC 3310	993	10 38 45	53 30 7	11.14	30.53	0.53	0.72	-3.14	Y	H II	3
F10578-7645	J105904.3-770141		0	10 59 5	-77 1 31	8.70	1.24	0	0	-1.85	Y		
F11011-7717	J110225.0-773331		0	11 2 24	-77 33 37	5.28	< 2.92	0	< 0	-2.44	Y	star	
F11034+7250	J110643.5+723407	NGC 3516	2649	11 6 48	72 34 0	12.63	1.76	4.24	0.29	-1.84		Sy1	5
F11048-7705	J110616.5-772201		0	11 6 14	-77 21 43	6.02	9.21	0	0	-2.88	Y		
F11083-2813	J111047.1-283001	ESO 438- G 009	7350	11 10 47	-28 30 7	22.37	< 3.14	57.8	< 4.06	-1.85		Sy1	5
F11196-2430	J112205.4-244632		0	11 22 4	-24 46 34	59.08	7.89	0	0	-1.82		star	
F11210-0823	J112332.4-083932	NGC 3660	3678	11 23 32	-8 39 35	5.46	1.87	3.53	0.61	-2.23	Y	Sy2	5
F11257+5850	J112831.5+583343	NGC 3690	3121	11 28 32	58 33 40	9.85	103.7	4.59	24.16	-3.72		H II	3
F11376+2458	J114014.0+244150	NGC 3798	3509	11 40 13	24 41 51	5.89	1.00	3.47	0.30	-1.93	Y		
F11472-7834	J114927.3-785059		0	11 49 30	-78 51 3	9.05	1.46	0	0	-1.91	Y		
F11500-0455	J115238.2-051229	MCG -01-30-041	5749	11 52 39	-5 12 38	9.75	< 1.31	15.4	< 1.03	-1.83	Y	Sy1	3
F11575-7754	J120005.7-781139		0	12 0 5	-78 11 41	11.23	14.27	0	0	-2.80		star	
F12351+1205	J123743.6+114909	NGC 4579	1519	12 37 42	11 49 12	34.02	4.74	3.76	0.26	-1.84		Sy1	3
F12374-1120	J123959.8-113725	NGC 4594	1091	12 40 0	-11 37 26	9.765	3.11	0.56	0.09	-2.20		LINER	5
F12442+4550	J124633.3+453421		0	12 46 32	45 34 33	6.87	< 0.77	0	< 0	-1.75	Y		
F13025-4912	J130528.0-492758	NGC 4945	560	13 5 27	-49 28 8	7.61	359.3	0.11	2.70	-4.37	Y	Sy2	5
F13086+3719	J131056.3+370337	NGC 5005	946	13 10 55	37 3 32	5.61	19.65	0.24	0.42	-3.24		LINER	3
F13111+3651	J131327.2+363542	NGC 5033	875	13 13 26	36 35 40	30.42	13.8	1.11	0.25	-2.36		Sy1	3
F13135+4217	J131549.3+420154	NGC 5055	504	13 15 49	42 1 38	5.44	30.15	0.07	0.18	-3.44		Comp	3
F13204+0825	J132254.2+081011	MRK 1347	14916	13 22 54	8 9 53	7.45	0.92	79.3	4.88	-1.79		Sy1	5

Table 2.3: Results of the IRASFSC - RASSBSC cross-correlation *continued*

IRAS name (1)	RASSBSC name (2)	Other name (3)	Velocity (4)	RA (5)	Dec (6)	F_X (7)	$F_{60\mu}$ (8)	L_X (9)	$L_{60\mu}$ (10)	$F_X/F_{60\mu}$ (11)	Cirrus (12)	Classification (13)	Ref (14)
F13225-4245	J132527.3-430105	Cen A	547	13 25 26	-43 1 11	36.99	162.2	0.53	1.16	-3.341			
F13277+5840	J132938.2+582507	NGC 5204	201	13 29 35	58 25 5	6.75	< 2.32	0.01	< 0.00	-2.236		H II	3
F13277+4727	J132953.8+471143	M51	463	13 29 53	47 11 42	11.77	32.68	0.12	0.17	-3.142		Sy2	
F13341-2936	J133657.0-295207	M83	516	13 36 58	-29 51 46	23.50	110.3	0.30	0.70	-3.37	Y	H II	
F13432+4157	J134518.5+414242	NGC 5290	2580	13 45 18	41 42 44	8.347	1.55	2.66	0.25	-1.968			
F14002-4108	J140320.0-412246	NGC 5408	509	14 3 18	-41 22 53	10.48	< 2.82	0.13	< 0.01	-2.13		H II	8
F14050-4109	J140809.8-412352		0	14 8 9	-41 23 56	8.03	0.88	0	0	-1.74	Y		
F14106-0258	J141315.2-031223	NGC 5506	1853	14 13 13	-3 12 23	9.57	8.41	1.57	0.69	-2.643	Y	Sy2	15
F14349+5900	J143622.2+584750	MRK 0817	9430	14 36 21	58 47 36	9.20	2.12	39.1	4.51	-2.061	Y	Sy1	6
F15361-0313	J153845.4-032309		7137	15 38 44	-3 22 48	6.38	4.06	15.6	4.95	-2.503		Sy1	15
F15420-3408	J154513.6-341733		0	15 45 12	-34 17 29	12.31	7.11	0	0	-2.461	Y		
F15456-1336	J154824.9-134532	NGC 5995	7553	15 48 24	-13 45 25	20.50	3.65	56.0	4.98	-1.949		Sy1	7
F15473-0346	J154957.0-035526		0	15 49 57	-3 55 16	8.40	5.33	0	0	-2.502	Y	star	
F16038-2735	J160658.5-274321		0	16 6 57	-27 43 7	7.02	5.68	0	0	-2.607			
F16126-2235	J161534.0-224218	Star VVSCO	0	16 15 34	-22 42 43	5.40	0.81	0	0	-1.876		star	
F16343-1028	J163709.4-103406		0	16 37 8	-10 34 3	31.26	6.25	0	0	-2			
F16424-2457	J164527.9-250319		0	16 45 28	-25 3 17	5.63	0.82	0	0	-1.86			
F16443-1509	J164713.0-151430		0	16 47 13	-15 14 51	7.52	1.17	0	0	-1.891			
F16433-6856	J164840.4-690138		0	16 48 39	-69 1 37	11.62	5.47	0	0	-2.372	Y		
F16504+0228	J165257.9+022353	NGC 6240	7339	16 52 58	2 24 2	7.71	22.68	19.9	29.22	-3.168		Sy2	11
F17123+1426	J171439.3+142320		0	17 14 37	14 23 25	26.39	80.59	0	0	-3.184			
F18325-5926	J183657.1-592412	Fairall 49	6065	18 36 57	-59 24 8	14.64	3.23	25.8	2.84	-2.042		Sy2	
F18489-3703	J185218.3-370020		0	18 52 17	-37 0 10	10.69	< 1.41	0	< 0	-1.819			
F18582-3657	J190138.8-365253		0	19 1 40	-36 52 42	11.37	469.0	0	0	-4.314	Y		
F19232+5008	J192433.0+501415		0	19 24 32	50 14 33	5.68	17.39	0	0	-3.185	Y		
F20060-2622	J200905.0-261328		0	20 9 4	-26 13 22	6.58	0.71	0	0	-1.733			
F20432+5851	J204427.0+590202		0	20 44 25	59 2 10	11.66	2.04	0	0	-1.942			
F22330-2618	J223546.0-260308	NGC 7314	1422	22 35 45	-26 2 59	21.23	3.74	2.05	0.18	-1.944		Sy1	5
F22347+3409	J223705.9+342519	NGC 7331	816	22 37 4	34 24 56	4.71	23.15	0.15	0.37	-3.39		Comp	3
F23007+0836	J230315.7+085226	NGC 7469	4892	23 3 15	8 52 25	169.38	25.87	194.0	14.81	-1.883	Y	Sy1	12
F23015+2221	J230402.8+223725	MRK 0315	11661	23 4 0	22 37 17	11.83	< 1.46	77.0	< 4.76	-1.791	Y	Sy1	8
F23279-0244	J233033.0-022754	MCG -01-59-027	10029	23 30 32	-2 27 35	6.67	< 0.71	32.1	< 1.73	-1.731		Sy1	5
F23411+0228	J234339.0+024445		27354	23 43 38	2 45 1	5.22	< 2.28	187.0	< 40.81	-2.339		Sy1	5
F23412-1533	J234351.0-151655		0	23 43 49	-15 17 3	10.84	68.15	0	0	-3.497	Y		

Notes: (1) Name from WGAcat, (2) Name from IRASFSC, (3) Other names, (4) Recession velocity, (5) RA (J2000) (6) Dec (2000) (7) X-ray flux in the 0.1-2.5keV band from RASSBSC in units of $10^{-13}\text{erg cm}^{-2}\text{ s}^{-1}$ (see text for the conversion), (8) 60μ flux from IRASFSC in Jy, (9) X-ray luminosity in units of 10^{41}erg s^{-1} , (10) 60μ luminosity in units of 10^{44}erg s^{-1} , (11) $\log(F_X/F_{60\mu})$ ratio, (12) Possible association with IR cirrus (from Strauss, Huchra, Davis, Yahil, Fisher & Tonry 1992), (13) activity classification, (14) reference for classification.

(1) This work, (2) de Grijp, Keel, Miley, Goudfrooij & Lub (1992), (3) Ho, Filippenko & Sargent (1997a), (4) Mazzarella & Balzano (1986), (5) Moran et al. (1996), (6) Osterbrock & Martel (1993), (7) Rush, Malkan & Spinoglio (1993), (8) Schaerer et al. (1999), (9) Strauss et al. (1992), (10) Coziol, Torres, Quast, Contini & Davoust (1998), (11) Kewley, Heisler, Dopita, Sutherland, Norris, Reynolds & Lumsden (2000), (12) Kim, Sanders, Veilleux, Mazzarella & Soifer (1995), (13) Vaceli, Viegas, Gruenwald & de Souza (1997), (14) Augarde, Chalabaev, Comte, Kunth & Maehara (1994), (15) Maiolino & Rieke (1995), (16) Veron-Cetty & Veron (1986), (17) Turner, Ho & Beck (1987)

Table 2.4: Results of the IRASFSC - WGAcat cross-correlation

IRAS name	WGA name	Other name	Velocity km s ⁻¹ (h m s)	RA J2000 (^o ' ")	Dec J2000	F _X	L _X	F _{60μ} Jy	L _{60μ}	F _X /F _{60μ}	Cirrus	Classification	Ref
(1)	(2)	(3)	(4)	(5)	(6)	(7)	(8)	(9)	(10)	(11)	(12)	(13)	(14)
F 23589+3109	J0001.5+3126	NGC 7806	4768	0 1 28	31 26 28	0.014	0.16	0.22	12.13	-2.89			
F 00124-3929	J0014.9-3912	NGC 55	129	0 14 57	-39 12 26	0.01	8.0E-05	32.00	1.28	-5.23		H II	15
F 00183+2135	J0020.9+2152	IC 1543	5622	0 20 55	21 51 59	0.045	0.67	0.55	41.75	-2.79			
F 00248-7220	J0026.9-7203		120000	0 27 2	-72 4 7	0.019	132.70	0.16	5473.91	-2.62			
F 00276+2555	J0030.2+2611		60000	0 30 17	26 11 46	0.066	113.32	0.32	2725.76	-2.38		Comp	20
F 00287+0811	J0031.3+0828	PGC1914	4360	0 31 18	8 28 24	0.024	0.21	3.60	163.76	-3.88			
F 00317-2142	J0034.2-2126	PGC2047	8035	0 34 12	-21 26 17	2.322	71.73	3.85	594.94	-1.92		H II	1
F 00342+2342	J0036.8+2359	Arp 282	4831	0 36 52	23 59 24	0.037	0.41	1.12	62.42	-3.18	Y	LINER	6
F 00375-2407	J0040.0-2350		18457	0 40 1	-23 50 40	0.023	3.79	0.28	230.88	-2.79		H II	1
F 00391+4004	J0041.8+4021	MARK 957	21345	0 41 53	40 21 19	0.972	211.89	2.10	2283.5	-2.03		Sy1	10
F 00400+4059	J0042.7+4116		0	0 42 44	41 16 12	7.299	0.00	10.80	0.00	-1.87	Y	in M31	26
F 00446-2053	J0047.0-2036		0	0 47 2	-20 37 11	0.101	0.00	0.44	0.00	-2.34			
F 00460+3141	J0048.7+3157	MARK 348	4200	0 48 47	31 57 24	0.08	0.67	1.29	54.44	-2.91		Sy1	10
F 00470+3200	J0049.8+3216	NGC 266	4661	0 49 46	32 16 36	0.086	0.89	0.81	42.31	-2.68		LINER	5
F 00528-3757	J0055.1-3742		0	0 55 9	-37 41 51	0.195	0.00	1.85	0.00	-2.68		gal H II	16
F 00567+2647	J0059.3+2703		0	0 59 24	27 3 42	0.04	0.00	0.66	0.00	-2.92	Y		
F 01071+3205	J0109.9+3222	PGC4153	5179	1 9 57	32 21 49	0.075	0.96	0.51	32.92	-2.54		group/clust	26
F 01091-3820	J0111.4-3804	NGC 424	3496	1 11 26	-38 5 4	0.389	2.27	1.80	52.51	-2.36		Sy2	6
F 01219+0331	J0124.5+0347	NGC 520	2215	1 24 34	3 47 28	0.063	0.15	30.90	362.32	-4.39		H II	5
F 01220+0128	J0124.5+0144	NGC 521	5040	1 24 33	1 43 51	0.068	0.83	0.65	39.63	-2.68		H II	5
F 01307+3017	J0133.5+3032		0	1 33 36	30 32 22	0.529	0.00	9.30	0.00	-2.94	Y	in NGC598	16
F 01312+3023	J0134.0+3038		0	1 34 1	30 38 35	0.007	0.00	< 7.83	0.00	> -4.74	Y	in NGC598	16
F 01317+3031	J0134.5+3047			1 34 33	30 47 0	0.057	0.00	30.50	0.00	-4.43	Y		
F 01319-1604	J0134.4-1549		5974	1 34 25	-15 49 3	1.305	22.28	1.93	165.12	-1.87		H II	1
F 01344+4740	J0137.4+4755		0	1 37 29	47 55 42	0.104	0.00	0.38	0.00	-2.27			
F 01403+1323	J0143.0+1338	NGC 660	850	1 43 1	13 38 45	0.085	0.029	65.50	113.28	-4.59		Comp	5
F 01413+0205	J0143.9+0220	MRK 573	5100	1 43 55	2 20 55	0.37	4.60	1.09	67.70	-2.17		Sy2	10
F 01572+0009	J0159.8+0023	MARK 1014	48903	1 59 49	0 23 44	1.359	1555.01	2.22	12723.8	-1.91		Sy2	10
F 01590-3158	J0201.2-3143	PGC7668	5574	2 1 13	-31 43 43	0.253	3.76	1.94	144.34	-2.58		Sy2	11
F 02072-1025	J0209.7-1011	NGC 839	3934	2 9 42	-10 11 3	0.038	0.29	10.60	390.60	-4.14		H II	3
F 02069-1022	J0209.4-1008	NGC 837	3864	2 9 23	-10 8 13	0.09	0.64	5.31	189.63	-3.47		LINER	3
F 02071-1023	J0209.6-1008	NGC 838	3860	2 9 38	-10 8 45	0.136	0.97	9.23	328.92	-3.53		H II	3

Table 2.4: Results of the IRASFSC - WGAcat cross-correlation *continued*

IRAS name (1)	WGA name (2)	Other name (3)	Velocity (4)	RA (5)	Dec (6)	F_X (7)	L_X (8)	$F_{60\mu}$ (9)	$L_{60\mu}$ (10)	$F_X/F_{60\mu}$ (11)	Cirrus 12)	Classification (13)	Ref (14)
F 02078-1033	J0210.2-1019	NGC 848	4001	2 10 15	-10 19 23	0.02	0.15	1.44	55.07	-3.55		Comp	8
F 02194+4207	J0222.5+4221	PGC9031	528	2 22 32	42 21 18	0.036	0.005	35.20	23.46	-4.69		H II	5
F 02259-1015	J0228.3-1001		0	2 28 24	-10 1 45	0.036	0.00	0.65	0.00	-2.95			
F 02267-1103	J0229.2-1049	PGC9457	4700	2 29 10	-10 49 36	0.264	2.79	0.35	18.36	-1.82			
F 02304+0012	J0232.9+0025	PGC9711	6714	2 33 0	0 25 15	0.058	1.26	2.49	268.30	-3.33		Sy2	6
F 02379-0838	J0240.4-0826	PGC10122	1373	2 40 25	-8 25 47	0.019	0.017	1.57	7.08	-3.61	Y	H II	24
F 02401-0013	J0242.6-0000	NGC 1068	1137	2 42 40	0 0 45	13.05	8.07	176.00	544.93	-2.83		Sy2	5
F 02441-3029	J0246.3-3016	NGC 1097	1275	2 46 17	-30 16 29	1.719	1.34	44.50	173.21	-3.11		Sy1	5
F 03145-5458	J0315.8-5447		0	3 15 53	-54 47 44	0.055	0.00	0.21	0.00	-2.28			
F 03154-4117	J0317.3-4106	NGC 1269	838	3 17 18	-41 6 28	0.193	0.065	1.77	2.97	-2.66			
F 03176-6640	J0318.2-6629			3 18 16	-66 29 29	0.909	0.00	14.60	0.00	-2.90	Y		
F 03161-3437	J0318.1-3426		78530	3 18 6	-34 26 43	0.071	208.99	0.21	3084.9	-2.17		Sy1	1
F 03201-5150	J0321.6-5139	ESO 032012-5	17100	3 21 39	-51 39 27	0.274	38.28	0.51	358.51	-1.97		Sy1	18
F 03208-3716	J0322.7-3706	NGC 1317	1941	3 22 43	-37 6 12	0.064	0.12	3.29	29.66	-3.41			
F 03207-3723	J0322.7-3712	NGC 1316	1760	3 22 40	-37 12 30	0.644	0.95	2.98	22.06	-2.36		LINER	11
F 03220-3638	J0323.9-3627	NGC 1326	1360	3 23 55	-36 27 51	0.159	0.14	8.06	35.67	-3.40			
F 03234-4925	J0325.0-4915	PGC12774	11664	3 25 2	-49 15 21	0.08	5.18	0.39	125.50	-2.38			
F 03229-0619	J0325.4-0608	MARK 609	9600	3 25 26	-6 8 32	1.701	75.01	< 2.95	<651.1	> -1.94		Sy1	10
F 03240-2130	J0326.2-2119	NGC 1332	1524	3 26 17	-21 20 3	0.32	0.36	0.51	2.81	-1.90			
F 03260+3111	J0329.1+3122	STVS7	0	3 29 8	31 22 2	0.401	0.00	503.00	0.00	-4.80	Y		16
F 03275+3020	J0330.5+3030		0	3 30 34	30 30 27	0.259	0.00	< 2.30	0.00	> -2.65	Y		
F 03290-5326	J0330.4-5316	PGC13020	13500	3 30 26	-53 16 16	0.033	2.92	1.42	617.8	-3.33			
F 03316-3618	J0333.6-3608	NGC 1365	1800	3 33 35	-36 8 23	0.795	1.23	76.10	590.1	-3.68		Sy1	5
F 03322-3904	J0334.1-3854		0	3 34 5	-38 54 41	0.058	0.00	0.21	0.00	-2.26			
F 03345-3508	J0336.4-3458			3 36 26	-34 58 36	0.159	0.00	1.08	0.00	-2.53			
F 03348-3609	J0336.7-3559	NGC 1386	868	3 36 45	-35 59 58	0.461	0.17	5.40	9.73	-2.77		Sy2	5
F 03350-3540	J0336.9-3530	NGC 1387	1302	3 36 57	-35 30 20	0.718	0.58	2.16	8.75	-2.18		ET	26
F 03363-2515	J0338.4-2505		0	3 38 27	-25 5 53	0.032	0.00	0.80	0.00	-3.10			

Table 2.4: Results of the IRASFSC - WGAcat cross-correlation *continued*

IRAS name (1)	WGA name (2)	Other name (3)	Velocity (4)	RA (5)	Dec (6)	F_X (7)	L_X (8)	$F_{60\mu}$ (9)	$L_{60\mu}$ (10)	$F_X/F_{60\mu}$ (11)	Cirrus (12)	Classification (13)	Ref (14)
F 03372-1850	J0339.5-1841	NGC 1400	558	3 39 30	-18 41 18	0.082	0.012	0.72	0.53	-2.64		Comp	6
F 03372-1841	J0339.5-1831	PGC13467	5614	3 39 30	-18 31 37	0.031	0.46	2.58	194.83	-3.62		Comp	1
F 03380-5514	J0339.3-5505		9500	3 39 19	-55 4 52	0.061	2.63	0.39	84.72	-2.51	Y	H II	1
F 03428-4448	J0344.5-4438	NGC 1448	1164	3 44 31	-44 38 41	0.083	0.054	8.58	27.81	-3.71			
F 03540-4230	J0355.7-4222	NGC 1487	848	3 55 44	-42 22 6	0.083	0.029	3.25	5.59	-3.29		H II	3
F 04113+2758	J0414.4+2806		0	4 14 26	28 5 45	0.1	0.00	13.20	0.00	-3.82	Y		
F 04188-5503	J0420.0-5456	NGC 1566	1496	4 19 59	-54 56 6	1.539	1.65	14.70	78.76	-2.68		Sy1	8
F 04187-3904	J0420.5-3857		12000	4 20 30	-38 57 32	0.053	3.64	0.53	181.17	-2.70			
F 04185+2022	J0421.5+2029		0	4 21 30	20 29 55	0.123	0.00	3.17	0.00	-3.11			
F 04275-5357	J0428.7-5351	0427-5357	13000	4 28 43	-53 51 0	0.09	7.24	0.16	64.65	-1.95		group/clust	26
F 04287+6444	J0433.4+6451		0	4 33 28	64 50 56	0.028	0.00	3.40	0.00	-3.79	Y		
F 04315-0840	J0434.0-0834	NGC 1614	4778	4 33 59	-8 34 45	0.129	1.41	32.30	1764.6	-4.10	Y	H II	6
F 04370+2559	J0440.1+2605		0	4 40 9	26 5 29	0.017	0.00	< 2.46	0.00	> -3.85		group/clust	26
F 04449-5920	J0445.7-5914	NGC 1672	1350	4 45 42	-59 14 48	0.236	0.21	33.00	143.70	-3.84		H II	6
F 04504-4229	J0452.0-4224	ESO 045028-4	0	4 52 1	-42 24 8	0.027	0.00	0.23	0.00	-2.63			
F 04502-0317	J0452.7-0312		4800	4 52 45	-3 12 55	0.047	0.52	0.83	45.97	-2.95		Sy2	6
F 04500-0311	J0452.5-0306	PGC16219	4456	4 52 31	-3 6 16	0.112	1.06	0.78	36.85	-2.54		ET	26
F 04575-7537	J0456.0-7532	ESO 033-G02	5426	4 55 58	-75 32 33	0.434	6.11	0.68	47.73	-1.89	Y	Sy2	11
F 04591-0419	J0501.6-0415	NGC 1741	4139	5 1 37	-4 15 31	0.068	0.56	3.92	160.53	-3.46	Y	H II	1
F 05005-3045	J0502.4-3041		0	5 2 25	-30 41 13	0.105	0.00	0.15	0.00	-1.85			
F 05028-6754	J0502.7-6750		7339	5 2 42	-67 50 42	0.087	2.24	< 1.54	<197.91	> -2.95	Y	group/clust	26
F 05035-3802	J0505.1-3758	NGC 1792	1211	5 5 13	-37 58 46	0.302	0.21	25.80	90.41	-3.63			
F 05040-2837	J0506.0-2834		0	5 6 2	-28 33 49	0.013	0.00	0.19	0.00	-2.85			
F 05059-3734	J0507.7-3730	NGC 1808	1000	5 7 41	-37 30 48	0.56	0.27	87.80	210.07	-3.89		H II	6
F 05147+0657	J0517.3+0700		0	5 17 24	7 0 22	0.193	0.00	< 0.66	0.00	> -2.23	Y		
F 05197-6118	J0520.3-6115	PGC17131	4911	5 20 20	-61 15 35	0.185	2.14	0.32	18.28	-1.93		group/clust	26
F 05189-2524	J0521.0-2521		12600	5 21 0	-25 21 45	0.225	17.09	13.70	5191.8	-3.48		Sy2	7
F 05206+0052	J0523.2+0054	HD287803	0	5 23 11	0 54 47	0.048	0.00	1.23	0.00	-3.11		star	
F 05340-5804	J0534.8-5803		0	5 34 50	-58 3 3	0.012	0.00	0.92	0.00	-3.59			
F 05328-0113	J0535.3-0111		0	5 35 22	-1 11 26	0.063	0.00	< 6.63	0.00	> -3.72			
F 05375-0739	J0539.9-0737		0	5 39 58	-7 37 32	0.248	0.00	< 3.27	0.00	> -2.82			
F 05393-0838	J0541.7-0836		0	5 41 42	-8 37 7	0.131	0.00	< 7.93	0.00	> -3.48			
F 05404-0839	J0542.8-0838		0	5 42 48	-8 38 34	0.113	0.00	< 6.93	0.00	> -3.49	Y		

Table 2.4: Results of the IRASFSC - WGAcat cross-correlation *continued*

IRAS name (1)	WGA name (2)	Other name (3)	Velocity (4)	RA (5)	Dec (6)	F_X (7)	L_X (8)	$F_{60\mu}$ (9)	$L_{60\mu}$ (10)	$F_X/F_{60\mu}$ (11)	Cirrus (12)	Classification (13)	Ref (14)
F 05365+6921	J0542.0+6922	NGC 1961	3934	5 42 3	69 22 33	0.101	0.75	6.38	236.29	-3.50		LINER	5
F 05499-3157	J0551.8-3156		0	5 51 49	-31 56 29	0.051	0.00	0.21	0.00	-2.32			
F 05550-1349	J0557.3-1349		0	5 57 20	-13 49 21	0.057	0.00	0.36	0.00	-2.50	Y		
F 06035-7102	J0602.8-7102		24000	6 2 54	-71 3 8	0.06	16.64	5.13	7064.6	-3.63			
F 06098+7103	J0615.5+7102	MARK 3	4050	6 15 36	71 2 15	0.566	4.44	3.77	147.93	-2.52		Sy2	10
F 06107+7822	J0618.6+7821	NGC 2146	893	6 18 39	78 21 24	0.383	0.15	131.00	249.91	-4.23		H II	5
F 06141+8220	J0624.9+8219	PGC18991	4310	6 24 57	82 19 6	0.045	0.40	4.19	186.33	-3.67	Y	H II	3
F 07062+2041	J0709.2+2036	NGC 2341	5159	7 9 11	20 36 12	0.065	0.83	< 8.46	<538.34	> -3.81		H II	1
F 07063+2043	J0709.3+2038	NGC 2342	5376	7 9 18	20 38 11	0.083	1.15	< 8.85	<612.03	> -3.73		H II	5
F 07107+3521	J0714.0+3516	PGC20450	4705	7 14 1	35 16 47	0.079	0.84	2.06	108.83	-3.12		Sy2	23
F 07106+4547	J0714.2+4541	MARK 376	16782	7 14 14	45 41 55	0.094	12.61	0.81	544.93	-2.64		Sy1	10
F 07336+3521	J0736.9+3514	NGC 2415	3784	7 36 56	35 14 31	0.121	0.83	8.57	293.46	-3.55			
F 07322+6541	J0737.1+6534	BD+65582	0	7 37 5	65 34 50	0.016	0.00	< 19.50	0.00	> -4.79			
F 07379+6517	J0742.6+6510	MARK 78	11400	7 42 39	65 10 39	0.054	3.36	1.11	345.10	-3.01		Sy2	10
F 07410+2922	J0744.1+2914	UGC 3995A	4500	7 44 8	29 14 52	0.079	0.77	0.56	27.03	-2.55			
F 08104+4553	J0813.9+4544	PGC23071	563	8 13 59	45 44 17	0.144	0.022	0.33	0.25	-2.06			
F 08326+1903	J0835.4+1853		0	8 35 28	18 53 20	0.153	0.00	0.24	0.00	-1.89			
F 08346+2602	J0837.6+2551		0	8 37 36	25 51 55	0.05	0.00	0.24	0.00	-2.39			
F 08339+6517	J0838.4+6507	0833+6517	5730	8 38 22	65 7 13	0.097	1.53	5.90	463.42	-3.48	Y		
F 08400+5023	J0843.6+5012	NGC 2639	3336	8 43 38	50 12 18	0.146	0.78	1.99	52.93	-2.83		Sy1	5
F 08447+3815	J0847.9+3804	I 2400	7979	8 47 58	38 4 17	0.084	2.55	0.62	94.69	-2.57			
F 08452+1753	J0848.0+1742	PGC24721	4734	8 48 3	17 42 8	0.094	1.00	1.80	96.56	-2.98			
F 09077+6014	J0911.6+6002	NGC 2768	1335	9 11 39	60 2 10	0.091	0.08	0.37	1.58	-2.31		LINER	5
F 09131+5343	J0916.7+5330		0	9 16 42	53 31 2	0.024	0.00	0.52	0.00	-3.04			
F 09174+0646	J0920.1+0633		0	9 20 7	6 33 35	0.075	0.00	0.29	0.00	-2.29			
F 09186+5111	J0922.0+5058	NGC 2841	638	9 22 3	50 58 20	0.152	0.030	3.03	2.95	-3.00		LINER	5
F 09300-1112	J0932.4-1126		0	9 32 25	-11 25 42	0.146	0.00	0.18	0.00	-1.78			
F 09293+2143	J0932.1+2129	NGC 2903	556	9 32 9	21 30 4	0.088	0.013	35.80	26.50	-4.31	Y	H II	5
F 09275+8121	J0934.5+8108	0928+8122	0	9 34 29	81 8 39	0.141	0.00	0.18	0.00	-1.80			

Table 2.4: Results of the IRASFSC - WGAcat cross-correlation *continued*

IRAS name (1)	WGA name (2)	Other name (3)	Velocity (4)	RA (5)	Dec (6)	F_X (7)	L_X (8)	$F_{60\mu}$ (9)	$L_{60\mu}$ (10)	$F_X/F_{60\mu}$ (11)	Cirrus (12)	Classification (13)	Ref (14)
F 09433-1408	J0945.7-1422	PGC27991	2420	9 45 47	-14 21 58	0.134	0.38	11.30	158.31	-3.63		H II	6
F 09497-0122	J0952.3-0136	MARK 1239	5974	9 52 18	-1 36 48	0.527	8.99	1.34	113.98	-2.10		Sy1	10
F 09518+6913	J0955.9+6858		0	9 55 56	68 59 6	0.019	0.00	2.58	0.00	-3.83		gal H II	16
F 09514+6918	J0955.5+6903	NGC 3031	-34	9 55 32	69 3 55	5.967	0.003	6.81	0.02	-1.76		Sy1	5
F 09517+6954	J0955.8+6940	M82	213	9 55 52	69 40 40	9.72	0.21	1090.00	118.20	-3.75		H II	5
F 09554+3236	J0958.3+3222	NGC 3067	1476	9 58 19	32 22 18	0.047	0.049	8.50	44.28	-3.96			
F 09585+5555	J1001.9+5540	NGC 3079	1125	10 1 57	55 40 50	0.207	0.13	44.50	134.73	-4.03		Sy2	5
F 09593+6858	J1003.2+6843	NGC 3077	14	10 3 19	68 43 59	0.043	4.0E-06	13.70	0.01	-4.20		H II	5
F 10027-0728	J1005.2-0742	PGC29265	663	10 5 15	-7 43 16	0.095	0.020	< 0.21	<0.23	> -2.05			
F 10039+5634	J1007.3+5620		0	10 7 18	56 20 7	0.237	0.00	0.27	0.00	-1.76			
F 10148+2156	J1017.6+2141	NGC 3185	1293	10 17 38	21 41 15	0.033	0.027	1.43	5.71	-3.33		Sy2	5
F 10153+2205	J1018.0+2149	NGC3190	1293	10 18 3	21 50 8	0.051	0.041	3.19	12.75	-3.50		LINER	5
F 10207+2007	J1023.5+1951	NGC 3227	1157	10 23 30	19 51 49	4.473	2.87	7.83	25.06	-1.94		Sy1	5
F 10257-4339	J1027.8-4354	NGC 3256	2738	10 27 52	-43 54 24	0.605	2.17	88.30	1583.6	-3.86		H II	8
F 10250+6843	J1028.7+6828		0	10 28 44	68 28 23	0.083	0.00	1.05	0.00	-2.80	Y	gal H II	1
F 10293+5439	J1032.5+5423	ARP 233	1461	10 32 30	54 24 7	0.036	0.037	4.68	23.88	-3.81		H II	10
F 10331+4141	J1036.0+4125		0	10 36 4	41 25 46	0.314	0.00	0.35	0.00	-1.75			
F 10356+5345	J1038.7+5330	NGC 3310	993	10 38 45	53 30 7	0.61	0.29	30.50	72.02	-3.40		H II	5
F 10413+1157	J1043.9+1142	NGC 3351	778	10 43 57	11 42 10	0.2	0.058	17.10	24.78	-3.63		H II	5
F 10422+5613	J1045.3+5557	NGC 3353	944	10 45 21	55 57 41	0.077	0.033	4.95	10.55	-3.51		H II	15
F 10433+6329	J1046.6+6313	NGC 3359	1013	10 46 36	63 13 24	0.064	0.031	4.06	9.97	-3.50		H II	5
F 10465+3302	J1049.4+3246	PGC32390	1633	10 49 22	32 46 23	0.081	0.10	0.34	2.15	-2.32			
F 10479-2808	J1050.2-2824		57000	10 50 18	-28 24 1	0.093	144.10	1.00	7788.0	-2.73		Sy1	6
F 10515+5715	J1054.5+5659	NGC 3445	2026	10 54 36	56 59 20	0.021	0.041	2.09	20.55	-3.70			
F 10516+5434	J1054.6+5418	NGC 3448	1350	10 54 38	54 18 25	0.189	0.17	5.87	25.57	-3.19		H II	5
F 11001+2520	J1102.8+2504		0	11 2 49	25 4 18	0.009	0.00	0.24	0.00	-3.13			
F 11000+2527	J1102.7+2511		17936	11 2 44	25 11 36	0.011	1.64	0.62	477.38	-3.47		LINER	1
F 11026+3830	J1105.3+3813		8464	11 5 22	38 13 55	0.038	1.30	1.37	233.94	-3.26			

Table 2.4: Results of the IRASFSC - WGAcat cross-correlation *continued*

IRAS name (1)	WGA name (2)	Other name (3)	Velocity (4)	RA (5)	Dec (6)	F_X (7)	L_X (8)	$F_{60\mu}$ (9)	$L_{60\mu}$ (10)	$F_X/F_{60\mu}$ (11)	Cirrus (12)	Classification (13)	Ref (14)
F 11048-7705	J1106.2-7721		0	11 6 14	-77 21 43	0.499	0.00	< 9.22	0.00	> -2.97	Y		
F 11065-7701	J1107.9-7717		0	11 7 57	-77 17 29	0.089	0.00	< 0.35	0.00	> -2.29	Y		
F 11068-7717	J1108.2-7733		0	11 8 14	-77 33 53	0.246	0.00	< 12.00	0.00	> -3.39	Y		
F 11091-7716	J1110.6-7732		0	11 10 37	-77 32 42	0.068	0.00	0.28	0.00	-2.31	Y		
F 11143-7556	J1116.0-7612	NGC 3620	1680	11 16 3	-76 12 53	0.087	0.12	42.80	288.98	-4.39			
F 11176+1351	J1120.2+1335	NGC 3628	843	11 20 16	13 35 18	0.412	0.14	49.60	84.26	-3.78		Sy1	5
F 11193+5921	J1122.2+5904	NGC 3642	1588	11 22 14	59 4 45	0.171	0.21	1.44	8.66	-2.62		LINER	5
F 11220+3902	J1124.7+3845	NGC 3665	2080	11 24 42	38 45 49	0.112	0.23	1.92	19.84	-2.93		H II	5
F 11257+5850	J1128.5+5833	ARP 299	3121	11 28 32	58 33 40	0.509	2.37	104.00	2416.5	-4.01		H II	5
F 11333+6231	J1136.1+6215	MCG+11-14-03	9353	11 36 5	62 14 52	0.05	2.09	1.47	307.84	-3.17			
F 11340+2157	J1136.5+2141		18779	11 36 36	21 40 56	0.027	4.59	0.33	279.92	-2.79			
F 11538+5524	J1156.4+5507	NGC 3982	900	11 56 26	55 7 35	0.065	0.025	6.57	12.73	-3.71		Sy1	5
F 12001+0215	J1202.7+0158	NGC 4045	1981	12 2 41	1 58 32	0.072	0.14	7.10	66.61	-3.69			
F 12006+4448	J1203.1+4431	NGC 4051	600	12 3 9	44 31 49	6.084	1.05	7.13	6.14	-1.77		Sy1	5
F 12056+6527	J1208.1+6510	NGC 4125	1356	12 8 6	65 10 23	0.268	0.24	0.60	2.62	-2.05		Comp	5
F 12112+1510	J1213.7+1453	NGC 4192	-142	12 13 48	14 53 51	0.06	1.0E-03	5.92	0.29	-3.69		Comp	5
F 12133+1325	J1215.9+1309	NGC 4216	131	12 15 53	13 8 53	0.089	0.001	0.96	0.04	-2.73		Comp	5
F 12131+1410	J1215.6+1354	NGC 4212	-81	12 15 38	13 54 2	0.063	0.021	6.25	10.55	-3.70		H II	5
F 12173+0537	J1219.9+0520	NGC 4273	2378	12 19 56	5 20 34	0.127	0.34	9.33	126.26	-3.57		H II	5
F 12176+2933	J1220.1+2916	NGC 4278	600	12 20 6	29 16 52	0.615	0.11	0.56	0.48	-1.66		Sy1	5
F 12178+0539	J1220.3+0523	NGC 4281	2711	12 20 22	5 23 8	0.113	0.40	0.64	11.17	-2.45		Comp	5
F 12193+0445	J1221.9+0428	NGC 4303	1566	12 21 55	4 28 23	0.343	0.40	23.60	138.69	-3.54		H II	5
F 12200+3010	J1222.5+2953	NGC 4314	963	12 22 32	29 53 38	0.127	0.056	3.79	8.40	-3.17		LINER	5
F 12208+0744	J1223.4+0728	NGC 4334	4245	12 23 23	7 28 18	0.052	0.45	4.80	206.71	-3.66			
F 12239+3130	J1226.4+3113	NGC 4464	716	12 26 26	31 13 23	0.275	0.07	26.80	32.88	-3.69	Y	Comp	5
F 12259+1721	J1228.4+1704	NGC 4450	1800	12 28 28	17 5 13	0.761	1.18	1.34	10.41	-1.95		LINER	5
F 12281+4155	J1230.5+4138	NGC 4490	565	12 30 34	41 38 46	0.254	0.039	41.30	31.50	-3.91	Y	H II	5
F 12275+1354	J1230.0+1338	NGC 4477	1353	12 30 2	13 38 8	0.181	0.16	0.54	2.36	-2.17		Sy2	5
F 12299+6903	J1232.1+6847		0	12 32 7	68 47 12	0.148	0.00	0.18	0.00	-1.78			
F 12313+1526	J1233.8+1509	NGC 4523	262	12 33 49	15 9 55	0.091	0.003	0.38	0.06	-2.32			

Table 2.4: Results of the IRASFSC - WGAcat cross-correlation *continued*

IRAS name (1)	WGA name (2)	Other name (3)	Velocity (4)	RA (5)	Dec (6)	F_X (7)	L_X (8)	$F_{60\mu}$ (9)	$L_{60\mu}$ (10)	$F_X/F_{60\mu}$ (11)	Cirrus (12)	Classification (13)	Ref (14)
F 12315+0758	J1234.0+0742	NGC 4526	448	12 34 2	7 41 56	0.12	0.011	6.06	2.91	-3.40		H II	5
F 12323+1331	J1234.8+1315		16800	12 34 50	13 15 4	0.061	8.18	0.41	274.94	-2.53			
F 12343+1326	J1236.8+1309	NGC 4569	-235	12 36 50	13 9 42	0.139	0.004	7.56	1.00	-3.44		Comp	5
F 12341+1332	J1236.7+1315	PGC42081	1121	12 36 42	13 15 31	0.028	0.017	0.49	1.47	-2.94			
F 12338+2615	J1236.3+2559	PGC42038	1227	12 36 20	25 59 15	0.146	0.11	6.65	23.95	-3.36		Sy1	5
F 12340+2628	J1236.5+2612	Mrk 649	7128	12 36 30	26 11 59	0.028	0.67	0.34	41.40	-2.79			
F 12374-1120	J1239.9-1137	NGC 4594	1091	12 40 0	-11 37 26	0.697	0.40	3.11	8.86	-2.35		Sy1	5
F 12396+3249	J1242.0+3232	NGC 4631	606	12 42 6	32 32 32	0.034	0.006	57.00	50.04	-4.92		H II	5
F 12403+1331	J1242.8+1315	NGC 4639	300	12 42 50	13 15 27	0.254	0.011	1.41	0.30	-2.44		Sy1	5
F 12416+3228	J1244.1+3212	NGC4656	614	12 44 5	32 12 23	0.019	0.003	1.69	1.52	-3.65		H II	5
F 12425-0011	J1245.1-0027		0	12 45 6	0 27 40	0.096	0.00	28.20	0.00	-4.17			
F 12437+3100	J1246.1+3043	NGC 4676	6607	12 46 9	30 43 51	0.017	0.36	2.67	279.24	-3.89			
F 12505-4121	J1253.3-4138	ESO 323-G32	4800	12 53 20	-41 38 14	0.034	0.38	0.99	54.61	-3.16		Sy2	6
F 12585-3208	J1301.3-3224	PGC44892	9397	13 1 19	-32 24 16	0.012	0.49	0.59	125.06	-3.41			
F 12593-3230	J1302.1-3246	PGC44965	9000	13 2 4	-32 46 36	0.071	2.74	1.30	252.49	-2.96			
F 13022-4914	J1305.1-4930		549	13 5 10	-49 30 58	0.016	0.002	10.00	7.23	-4.48		gal H II	16
F 13026-4910	J1305.6-4925	NGC 4945	560	13 5 36	-49 26 14	0.067	0.010	< 207.00	<155.30	> -5.19		Sy2	11
F 13025-4912	J1305.4-4928		560	13 5 27	-49 28 8	0.105	0.016	359.00	269.55	-5.23			
F 13086+3719	J1310.9+3703	NGC 5005	946	13 10 55	37 3 32	0.364	0.16	19.70	42.07	-3.43		LINER	5
F 13106-3236	J1313.4-3252		0	13 13 23	-32 52 39	0.029	0.00	< 0.55	0.00	> -2.98	Y		
F 13111+3651	J1313.4+3635	NGC 5033	875	13 13 26	36 35 40	2.169	0.80	13.80	25.28	-2.50		Sy1	5
F 13135+4217	J1315.8+4201	NGC 5055	504	13 15 49	42 1 38	0.214	0.026	30.20	18.32	-3.85		Comp	5
F 13144+4508	J1316.6+4452	1314+4508	27131	13 16 40	44 52 30	0.077	27.10	0.67	1186.3	-2.64		Sy2	6
F 13173+3031	J1319.6+3015	NGC 5089	2141	13 19 39	30 15 17	0.024	0.054	0.71	7.83	-3.16		Sy2	3
F 13191-3622	J1321.9-3637	NGC 5102	467	13 21 56	-36 37 44	0.022	0.002	0.80	0.42	-3.26		H II	12
F 13220+1421	J1324.4+1405	NGC 5132	6652	13 24 28	14 5 37	0.02	0.42	0.82	86.95	-3.32	Y	ET	26
F 13223+1400	J1324.8+1344	NGC 5136	6709	13 24 49	13 44 27	0.043	0.93	0.34	36.79	-2.60	Y	H II	1
F 13229-2934	J1325.7-2950		4112	13 25 42	-29 49 54	0.332	2.69	16.90	684.01	-3.41			
F 13271+1157	J1329.6+1141		0	13 29 36	11 41 37	0.039	0.00	0.22	0.00	-2.45	Y		
F 13277+5840	J1329.6+5824	NGC 5204	201	13 29 35	58 25 5	0.821	0.016	2.33	0.23	-2.15		H II	5

Table 2.4: Results of the IRASFSC - WGAcat cross-correlation *continued*

IRAS name (1)	WGA name (2)	Other name (3)	Velocity (4)	RA (5)	Dec (6)	F_X (7)	L_X (8)	$F_{60\mu}$ (9)	$L_{60\mu}$ (10)	$F_X/F_{60\mu}$ (11)	Cirrus (12)	Classification (13)	Ref (14)
F 13299+1121	J1332.4+1106	Mrk 789	9476	13 32 24	11 6 17	0.039	1.66	3.35	720.06	-3.64		H II	1
F 13331-3312	J1335.9-3327	NGC 5220	4180	13 35 58	-33 27 31	0.37	3.09	0.59	24.54	-1.90			
F 13340-2937	J1336.8-2953		0	13 36 52	-29 52 53	0.096	0.00	< 100.00	0.00	> -4.72			
F 13358+4823	J1337.8+4808		0	13 37 52	48 8 19	0.176	0.00	< 0.20	0.00	> -1.76			
F 13351+2740	J1337.4+2725	NGC 5251	11217	13 37 25	27 25 11	0.016	0.99	0.35	105.17	-3.03		H II	1
F 13354+3924	J1337.6+3909	1335+39	6023	13 37 38	39 9 22	0.137	2.37	0.97	83.78	-2.55		Comp	37
F 13356-3100	J1338.4-3115	ESO 133535-3	11633	13 38 26	-31 15 55	0.028	1.84	0.28	91.65	-2.70		H II	1
F 13362+4831	J1338.3+4816	NGC 5256	8353	13 38 17	48 16 27	0.23	7.66	7.34	1225.49	-3.20		H II	10
F 13370-3123	J1339.9-3138	NGC 5253	404	13 39 54	-31 38 21	0.073	0.006	30.50	11.91	-4.32		H II	15
F 13365-3116	J1339.3-3131		7239	13 39 21	-31 31 49	0.011	0.28	0.41	51.80	-3.27		Sy2	1
F 13386-3145	J1341.4-3159	ESO 133836-3	6839	13 41 28	-32 0 20	0.06	1.34	0.58	64.64	-2.68		H II	1
F 13408+4047	J1342.9+4032		0	13 42 59	40 32 28	0.211	0.00	0.23	0.00	-1.74	Y		
F 13414+5551	J1343.2+5536		22096	13 43 15	55 36 12	0.062	14.38	0.17	197.74	-2.14		H II	1
F 13428+5608	J1344.6+5553	MARK 273	11326	13 44 41	55 53 13	0.086	5.07	21.70	6407.9	-4.10		LINER	7
F 13451+1232	J1347.5+1217	PKS1345+12	36300	13 47 33	12 17 22	0.033	20.60	1.92	6039.8	-3.47		Sy2	7
F 13475+6026	J1349.2+6011	NGC 5322	1915	13 49 13	60 11 26	0.09	0.16	0.41	3.57	-2.35		LINER	5
F 13472-2953	J1350.0-3008		0	13 50 4	-30 8 9	0.073	0.00	0.42	0.00	-2.46		0	
F 13517+6400	J1353.2+6345			13 53 15	63 45 47	0.593	0.00	0.73	0.00	-1.79			
F 13512+4036	J1353.3+4021	NGC 5350	2321	13 53 20	40 21 53	0.045	0.12	2.22	28.61	-3.39		H II	10
F 13536+1836	J1356.0+1822	MARK 463	15300	13 56 1	18 22 17	0.111	12.40	2.18	1223.1	-2.99		Sy2	10
F 13546-3941	J1357.6-3956		0	13 57 39	-39 56 15	0.031	0.00	< 69.50	0.00	> -5.05		group/clust	
F 14007-4104	J1403.8-4118		0	14 3 47	-41 18 27	0.047	0.00	< 0.11	0.00	> -2.07			
F 14002-4108	J1403.3-4122	NGC 5408	509	14 3 18	-41 22 53	1.152	0.14	2.83	1.75	-2.09		H II	15
F 14047+2841	J1406.9+2827	OQ 208	22957	14 6 58	28 27 23	0.059	14.98	0.73	918.9	-2.79		Sy1	18
F 14106-0258	J1413.2-0312	NGC 5506	1853	14 13 13	-3 12 23	1.746	2.87	8.41	69.07	-2.38	Y	Sy2	8
F 14150+2705	J1417.3+2651	MARK 673	10946	14 17 20	26 51 27	0.039	2.21	2.60	746.10	-3.53		Sy2	10
F 14337+4857	J1435.4+4844		2160	14 35 28	48 44 33	0.021	0.047	0.46	5.18	-3.04			
F 14348-1447	J1437.6-1500		24300	14 37 36	-15 0 20	0.024	6.69	6.87	9704.7	-4.16		Sy1	
F 14592+1037	J1501.6+1025	MARK 1494	9216	15 1 37	10 25 19	0.142	5.78	0.19	38.69	-1.83		Sy1	10
F 15051+5557	J1506.4+5545	NGC 5866	672	15 6 29	55 45 48	0.095	0.020	4.88	5.27	-3.41		Comp	5

Table 2.4: Results of the IRASFSC - WGAcat cross-correlation *continued*

IRAS name (1)	WGA name (2)	Other name (3)	Velocity (4)	RA (5)	Dec (6)	F_X (7)	L_X (8)	$F_{60\mu}$ (9)	$L_{60\mu}$ (10)	$F_X/F_{60\mu}$ (11)	Cirrus (12)	Classification (13)	Ref (14)
F 15140+5542	J1515.3+5530	NGC 5905	3390	15 15 22	55 31 1	0.022	0.12	2.60	71.43	-3.77		H II	5
F 15153+5535	J1516.6+5524	NGC 5908	3306	15 16 43	55 24 31	0.039	0.21	3.99	104.30	-3.71		LINER	7
F 15246+4128	J1526.4+4117		2491	15 26 27	41 17 42	0.044	0.13	0.16	2.39	-2.27	Y		
F 15243+4150	J1526.1+4140	NGC 5930	2672	15 26 7	41 40 33	0.08	0.27	9.10	155.36	-3.76		H II	13
F 15327+2340	J1534.9+2330	Arp 220	5434	15 34 56	23 30 10	0.046	0.65	104.00	7332.4	-5.06		H II	7
F 15353+5443	J1536.6+5433	MARK 486	11700	15 36 39	54 33 25	0.047	3.07	< 0.12	<40.38	> -2.12	Y	Sy1	10
F 15361-0313	J1538.7-0322	1536-0313	7137	15 38 44	-3 22 48	0.088	2.14	4.06	494.97	-3.36		Sy1	11
F 15487-3738	J1552.0-3747		0	15 52 3	-37 47 40	0.442	0.00	< 0.49	0.00	> -1.74		star	
F 15511+4047	J1552.8+4038	NGC 6013	4585	15 52 52	40 38 48	0.309	3.11	0.34	17.29	-1.75		H II	1
F 15531-3759	J1556.4-3807		0	15 56 27	-38 7 50	0.048	0.00	< 0.40	0.00	> -2.62	Y		
F 16030+2040	J1605.2+2032	NGC 6052	4726	16 5 11	20 32 32	0.068	0.73	6.15	328.77	-3.65	Y	Sy2	23
F 16114-1858	J1614.3-1906		0	16 14 19	-19 6 17	0.029	0.00	< 2.45	0.00	> -3.63	Y		
F 16155+6831	J1615.5+6823	PGC57638	7255	16 15 35	68 23 54	0.023	0.58	1.16	145.94	-3.40			
F 16277+2433	J1629.8+2426	Mrk 883	11250	16 29 52	24 26 35	0.476	28.83	1.02	308.53	-2.03		Sy1	10
F 16254-6735	J1630.4-6742		12000	16 30 28	-67 42 18	0.031	2.12	0.78	269.91	-3.11			
F 16350+7817	J1632.6+7811	NGC 6217	1362	16 32 38	78 11 50	0.191	0.17	10.80	48.06	-3.45		H II	5
F 16314+4203	J1633.1+4157		40800	16 33 5	41 57 29	0.118	93.90	0.18	720.39	-1.89		Sy2	2
F 16419+8213	J1637.0+8207		12055	16 36 56	82 7 43	0.08	5.54	0.20	69.64	-2.10		H II	1
F 16400+3944	J1641.7+3938		8953	16 41 44	39 38 36	0.046	1.75	1.28	245.83	-3.15		H II	1
F 16443-1509	J1647.2-1514			16 47 13	-15 14 51	1.26	0.00	1.17	0.00	-1.67			
F 16465+5939	J1647.2+5934			16 47 16	59 34 8	0.172	0.00	0.17	0.00	-1.69	Y		
F 16505+5330	J1651.7+5325			16 51 42	53 25 40	0.435	0.00	0.41	0.00	-1.67	Y		
F 16504+0228	J1652.9+0223	NGC 6240	7339	16 52 58	2 24 2	0.53	13.66	22.70	2922.3	-3.33		Sy2	7
F 16542+5301	J1655.3+5256		0	16 55 20	52 56 28	0.034	0.00	0.68	0.00	-3.00	Y		
F 16559+6237	J1656.4+6232		0	16 56 26	62 32 28	0.025	0.00	< 0.17	0.00	> -2.52	Y		
F 17039+6039	J1704.6+6035		29382	17 4 37	60 35 10	0.021	8.77	0.40	823.01	-2.97		LINER	1
F 17326+3859	J1734.3+3857		29280	17 34 20	38 57 50	0.149	6091.30	0.33	67271.0	-2.04		Sy1	25
F 17499+7009	J1749.4+7008	NGC 6503	14	17 49 27	70 8 35	0.039	0.00	7.58	0.00	-3.99		Sy2	5
F 18325-5926	J1836.9-5924		6065	18 36 57	-59 24 8	1.737	30.57	3.23	283.97	-1.97		Sy2	8
F 18333-6528	J1838.3-6525		3900	18 38 19	-65 25 38	0.041	0.30	2.31	84.20	-3.46			

Table 2.4: Results of the IRASFSC - WGAcat cross-correlation *continued*

IRAS name (1)	WGA name (2)	Other name (3)	Velocity (4)	RA (5)	Dec (6)	F_X (7)	L_X (8)	$F_{60\mu}$ (9)	$L_{60\mu}$ (10)	$F_X/F_{60\mu}$ (11)	Cirrus (12)	Classification (13)	Ref (14)
F 18430-6312	J1847.7-6309	PGC62428	4500	18 47 43	-63 9 24	0.035	0.34	4.38	211.99	-3.80	Y		
F 19337-4626	J1937.4-4620			19 37 22	-46 20 8	0.046	0.00	< 0.16	0.00	> -2.25			
F 19559+7723	J1954.1+7731		0	19 54 7	77 31 51	0.029	0.00	0.22	0.00	-2.59			
F 20003-5551	J2004.3-5543		0	20 4 19	-55 43 29	0.579	0.00	2.52	0.00	-2.34			
F 20036-4830	J2007.2-4822	NGC 6861	2819	20 7 19	-48 22 14	0.646	2.46	0.84	16.01	-1.81	Y	ET	26
F 20333+6000	J2034.3+6010		0	20 34 22	60 10 43	0.006	0.00	< 9.54	0.00	> -4.89			
F 20338+5958	J2034.8+6009	NGC 6946	48	20 34 52	60 9 12	0.088	1.0E-04	53.90	0.30	-4.49		H II	5
F 20482-5715	J2052.0-5704	PKS2048-57	3300	20 52 3	-57 4 3	0.088	0.46	5.34	139.04	-3.48		Sy1	8
F 21219-1757	J2124.6-1744		33900	21 24 42	-17 44 40	0.149	81.65	1.07	2933.43	-2.56		Sy1	7
F 21370-4245	J2140.2-4232	NGC 7095/7	2539	21 40 12	-42 32 17	0.113	0.35	0.22	3.33	-1.98		ET	26
F 21475-1617	J2150.2-1603		0	21 50 14	-16 3 34	0.333	0.00	0.41	0.00	-1.79	Y		
F 21596-1909	J2202.3-1855	PGC67892	2636	22 2 21	-18 55 2	0.029	0.10	1.05	17.40	-3.25			
F 21591-3206	J2202.0-3152	NGC 7172	2400	22 2 1	-31 52 8	0.07	0.19	5.71	78.71	-3.61		Sy2	8
F 21592-3214	J2202.1-3159	NGC 7174/6	2654	22 2 6	-31 59 31	0.114	0.39	3.19	53.70	-3.14		group/clust	26
F 22115-3013	J2214.4-2958		4515	22 14 24	-29 58 52	0.023	0.22	4.15	202.29	-3.96		H II	1
F 22179-2455	J2220.7-2440	NGC 7252	4688	22 20 44	-24 40 35	0.062	0.65	3.98	208.99	-3.51		Comp	9
F 22212-0221	J2223.8-0206	3C 445.0 -	17100	22 23 48	-2 6 14	0.144	20.15	0.31	214.13	-2.03		Sy1	18
F 22232+2057	J2225.6+2112		0	22 25 39	21 12 47	0.025	0.00	< 0.15	0.00	> -2.46		star	
F 22330-2618	J2235.7-2602	NGC 7314	1800	22 35 45	-26 2 59	2.394	3.71	3.74	28.96	-1.89		Sy1	8
F 22541-3649	J2256.8-3633	PGC70081	1940	22 56 52	-36 33 8	0.015	0.028	0.53	4.81	-3.24			
F 22595+1541	J2302.0+1557	NGC 7465	1968	23 2 1	15 57 59	1.485	2.75	< 4.94	<45.76	> -2.22		Sy2	11
F 23007+0836	J2303.2+0852	NGC 7469	4892	23 3 15	8 52 25	15.3	175.19	25.90	1481.09	-1.93	Y	Sy1	7
F 23069-4341	J2309.7-4325	NGC 7496	1500	23 9 45	-43 25 43	0.109	0.12	8.46	45.53	-3.59		Sy2	21
F 23133-4251	J2316.1-4235	NGC 7552	1585	23 16 8	-42 35 9	0.555	0.67	72.00	432.90	-3.81		H II	3
F 23135+2517	J2316.0+2533	PGC70877	8197	23 16 1	25 33 32	0.099	3.18	9.76	1568.97	-3.69		Comp	25
F 23161-4230	J2318.9-4214	NGC 7590	1500	23 18 54	-42 14 16	0.149	0.16	6.91	37.21	-3.36		Sy2	21
F 23156-4238	J2318.3-4222	NGC 7582	1500	23 18 22	-42 22 19	0.355	0.38	49.10	264.29	-3.84		Sy2	8
F 23179+1657	J2320.5+1713	NGC 7625	1633	23 20 29	17 13 34	0.102	0.13	9.33	59.50	-3.66		H II	3
F 23196+0805	J2322.1+0822		11612	23 22 9	8 21 48	0.042	2.71	0.52	168.29	-2.79		H II	1
F 23225-5514	J2325.3-5458		0	23 25 22	-54 58 14	0.049	0.00	< 0.13	0.00	> -2.11			

Table 2.4: Results of the IRASFSC - WGAcat cross-correlation *continued*

IRAS name (1)	WGA name (2)	Other name (3)	Velocity (4)	RA (5)	Dec (6)	F_X (7)	L_X (8)	$F_{60\mu}$ (9)	$L_{60\mu}$ (10)	$F_X/F_{60\mu}$ (11)	Cirrus (12)	Classification (13)	Ref (14)
F 23254+0830	J2327.9+0846	NGC 7674	8713	23 27 56	8 46 45	0.14	5.10	5.59	1014.85	-3.30		Sy1	7
F 23309-0215	J2333.4-0159	PGC71737	5305	23 33 28	-1 59 2	0.049	0.66	2.05	137.75	-3.32		Comp	1
F 23338+4811	J2336.3+4827		0	23 36 18	48 27 40	0.169	0.00	0.45	0.00	-2.13			
F 23336+0152	J2336.2+0209	NGC 7714	2798	23 36 13	2 9 17	0.177	0.66	10.40	194.03	-3.47		H II	6
F 23363+4602	J2338.8+4619		0	23 38 48	46 19 32	0.036	0.00	< 0.14	0.00	> -2.28			
F 23485+1952	J2351.0+2009	NGC 7769	4204	23 51 4	20 9 5	0.048	0.41	4.34	183.45	-3.65	Y		
F 23488+1949	J2351.4+2006	NGC 7771	4345	23 51 24	20 6 39	0.091	0.82	19.00	857.66	-4.02	Y	H II	19
F 23488+2018	J2351.4+2035	Mrk 331	5541	23 51 25	20 35 8	0.076	1.11	18.60	1366.16	-4.09		H II	24
F 23487+1957	J2351.2+2013	1E2348+1956	13049	23 51 14	20 13 54	0.329	26.76	0.93	380.26	-2.15	Y	H II	22
F 23498+2829	J2352.4+2846	NGC 7775	6747	23 52 24	28 46 25	0.038	0.83	1.85	201.90	-3.39		H II	1
F 23567-3243	J2359.2-3226		0	23 59 15	-32 26 53	0.082	0.00	0.38	0.00	-2.36			

Notes: (1) Name from IRASFSC, (2) Name from WGAcat, (3) Other names, (4) Recession velocity, (5) RA (J2000) from WGAcat, (6) Dec (2000) from WGAcat, (7) X-ray flux in the 0.1-2.5keV band from WGAcat in units of $10^{-12} \text{erg cm}^{-2} \text{s}^{-1}$, (8) X-ray luminosity in units of $10^{41} \text{erg s}^{-1}$, (9) 60μ flux from IRASFSC in Jy, (10) 60μ luminosity in units of $10^{42} \text{erg s}^{-1}$, (11) $\log(F_X/F_{60\mu})$ ratio, (12) activity classification, (13) reference for classification.

The references for the classifications are: (1) This work, (2) Bade, Fink, Engels, Voges, Hagen, Wisotzki & Reimers (1995), (3) Coziol et al. (1998), (4) Fairall (1981), (5) Ho, Filippenko & Sargent (1997a), (6) Kewley et al. (2000), (7) Kim et al. (1995), (8) Kirhakos & Steiner (1990), (9) Liu & Kennicutt (1995), (10) Mazzarella & Balzano (1986), (11) Moran et al. (1996), (12) Osterbrock & Martel (1993), (13) Dahari (1985), (14) Rigopoulou, Lutz, Genzel et al. (1996), (15) Schaerer et al. (1999), (16) Strauss et al. (1992), (17) de Grijp et al. (1992), (18) Hewitt & Burbidge (1991), (19) Davies, Alonso-Herrero & Ward (1997), (20) Maiolino & Rieke (1995), (21) Vaceli et al. (1997), (22) Fruscione & Griffiths (1991), (23) Bothun, Schmitz, Halpern, Lonsdale & Impey (1989), (24) Goldader, Joseph, Doyon & Sanders (1997), (25) Hook, McMahon, Irwin & Hazard (1996), (26) NED

2.2.2 The Markarian samples

The results of the cross-correlation are presented in Tables 2.5 and 2.6 . From these catalogues any multiple identifications of the same object have been excluded. As expected, given the nature of the Markarian objects, both catalogues predominantly consist of Sy1 type objects, with the WGAcat sample containing more low activity objects than the BSC . Also the BSC sample is biased towards X-ray luminous objects as it contains very few objects with $L_X < 10^{40} \text{erg cm}^{-2} \text{s}^{-1}$ (figs. 2.7,2.8,2.9 and 2.10).

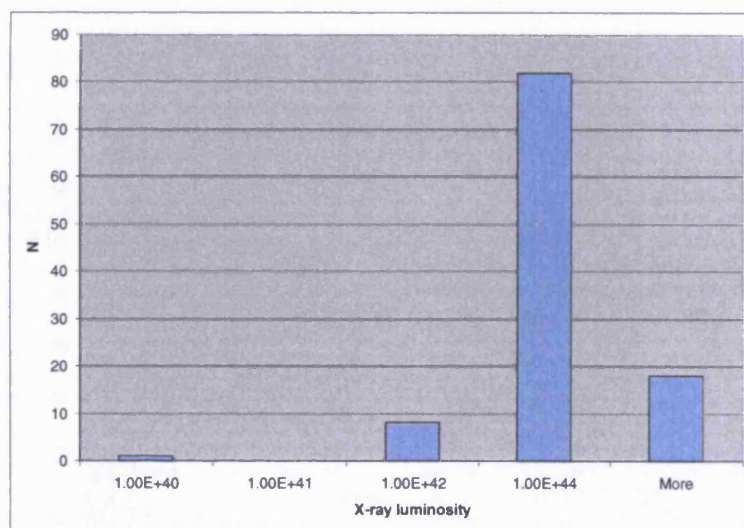
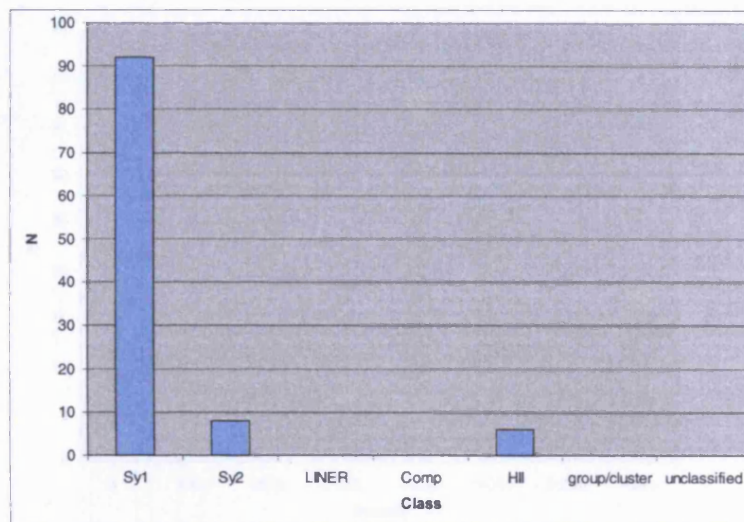


Figure 2.7: The distribution of activity classes, and X-ray luminosities of the objects in the Markarian-RASSBSC sample.

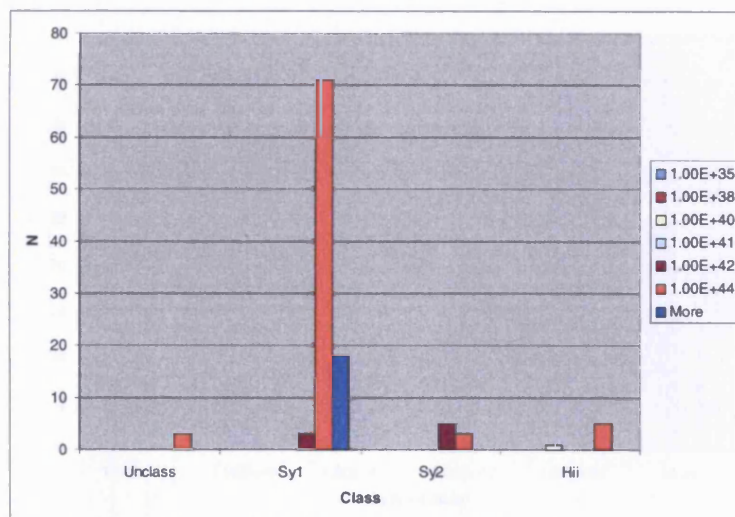
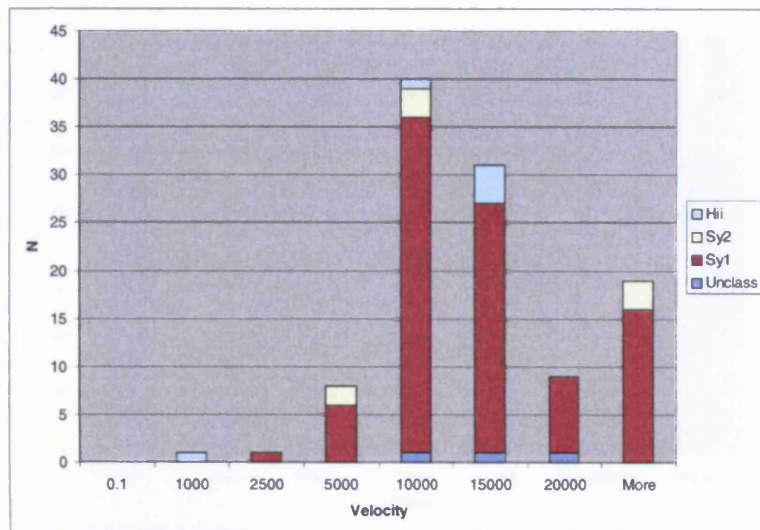


Figure 2.8: The distribution of X-ray luminosities and velocities of objects of different activity classes in the Markarian-RASSBSC sample.

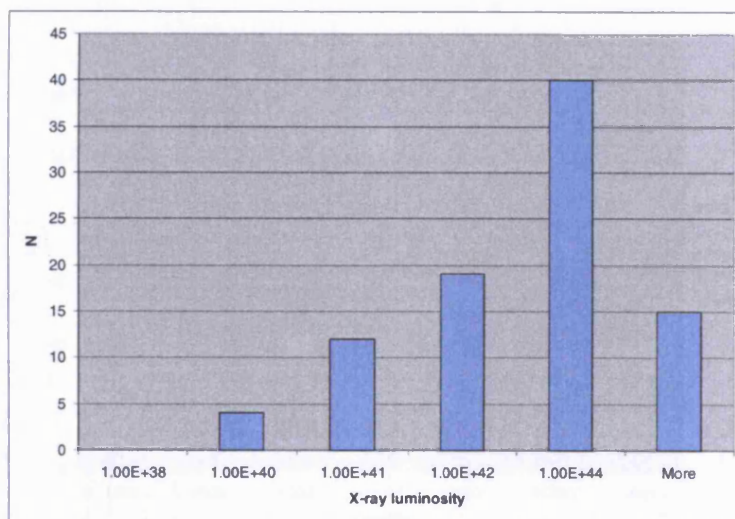
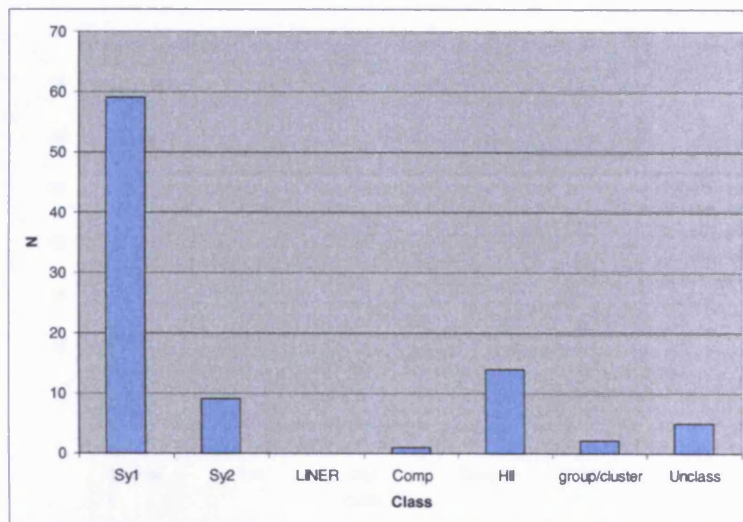


Figure 2.9: The distribution of activity classes, and X-ray luminosities of the objects in the Markarian-WGAcad sample.

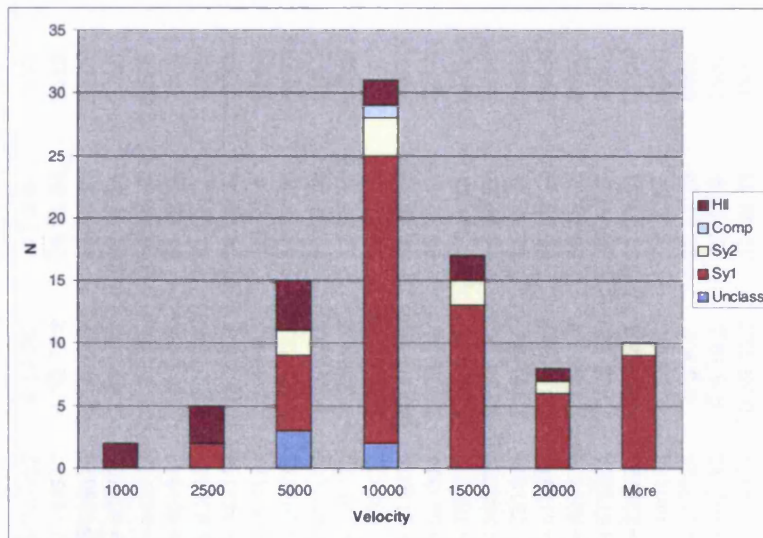
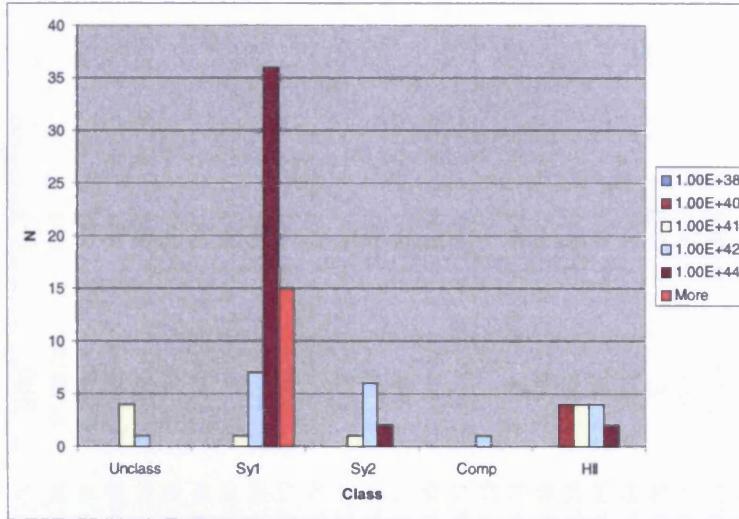


Figure 2.10: The distribution of X-ray luminosities and velocities of objects of different activity classes in the Markarian-WGacat sample.

Table 2.5: Results of the MARKARIAN - RASSBSC cross-correlation

Mrk Name	BSC Name	RA (2000) (h m s)	DEC (2000) ($^{\circ}$ ' ")	Velocity km s $^{-1}$	F _X	L _X	Vmag	Morph	Classification
(1)	(2)	(3)	(4)	(5)	(6)	(7)	(8)	(9)	
MKN 3	J061533.6+710207	6 15 36	71 2 4	4230	0.50	0.43	12.77	SB0	Sy2
MKN 6	J065209.8+742537	6 52 11.8	74 25 34	5910	0.56	0.94	13.28	SAB0/a	Sy1
MKN 9	J073657.0+584610	7 36 56.8	58 46 17	12000	1.17	8.04	14.41	S0p	Sy1
MKN 10	J074729.4+605601	7 47 29.1	60 55 58	8790	5.28	19.51	13.03	(R)SBbc	Sy1
MKN 40	J112536.7+542243	11 25 36.3	54 22 55	6240	0.91	1.70	15.12	S0	Sy1
MKN 42	J115342.4+461244	11 53 41.3	46 12 38	7200	1.73	4.29	15.45	SBb	Sy1
MKN 50	J122324.4+024040	12 23 24.3	2 40 42	6960	4.43	10.26	14.69	S0	Sy1
MKN 64	J130708.4+342414	13 7 8.3	34 24 21	55200	2.10	305.85	16.97		Sy1
MKN 69	J134607.5+293814	13 46 8.1	29 38 4	22860	2.35	58.80	15.93		Sy1
MKN 79	J074232.9+494830	7 42 32.3	49 48 40	6600	19.76	41.19	13.13	SBc	Sy1
MKN 106	J091954.9+552120	9 19 55.1	55 21 38	36600	1.93	123.67	16.22		Sy1
MKN 110	J092512.3+521716	9 25 12.8	52 17 16	10800	15.22	84.93	15.37		Sy1
MKN 141	J101912.1+635802	10 19 11.9	63 58 10	11700	4.55	29.80	14.9	E	Sy1
MKN 142	J102531.2+514039	10 25 31.3	51 40 24	13500	15.72	137.10	15.56	S0:	Sy1
MKN 171	J112831.5+583343	11 28 32.2	58 33 51	3100	0.99	0.42	11.85	Sc+Im DB	H II
MKN 180	J113626.6+700932	11 36 26.7	70 9 23	13740	40.79	368.42	14.31		Sy1
MKN 202	J121754.7+583936	12 17 54.7	58 39 26	6300	1.92	3.65	15.32		
MKN 205	J122144.4+751848	12 21 42.4	75 18 31	21000	7.78	164.11	15.24	p	Sy1
MKN 236	J130021.2+613919	13 0 19.8	61 39 18	15600	1.82	21.19	15.48	SB	Sy1
MKN 279	J135304.8+691832	13 53 1.7	69 18 28	9060	25.28	99.29	14.18	S0	Sy1
MKN 290	J153552.0+575404	15 35 52.8	57 54 8	9030	7.96	31.07	14.68	E	Sy1
MKN 315	J230402.8+223725	23 4 2.4	22 37 21	11850	1.18	7.95	14.54	E0p	Sy1
MKN 316	J231341.0+140113	23 13 40.2	14 1 17	12300	0.93	6.76	15.09	E	H II
MKN 334	J000308.6+215728	0 3 9.4	21 57 35	6900	0.87	1.98	14.15	[Scp]	Sy1
MKN 335	J000618.9+201215	0 6 19.3	20 12 9	7500	22.34	60.13	13.74	S0/a	Sy1
MKN 352	J005953.3+314934	0 59 52.7	31 49 36	4500	5.54	5.37	14.46	(R)SA0	Sy1
MKN 358	J012634.2+313659	1 26 33.6	31 36 46	13770	1.55	14.03	14.08	Sbc	Sy1
MKN 359	J012732.9+191043	1 27 32.2	19 10 39	5100	5.47	6.80	13.59	SB0/a	Sy1
MKN 372	J024920.8+191813	2 49 20.1	19 18 19	9300	2.10	8.7	14.54	S0	Sy1
MKN 374	J065938.5+541136	6 59 37.4	54 11 43	13200	6.98	58.16	14.61	"dbl,S"	Sy1
MKN 382	J075526.1+391111	7 55 24.9	39 11 9	10200	4.04	20.09	14.75	SBc	Sy1
MKN 421	J110427.1+381231	11 4 27	38 12 22	9240	239.13	976.83	13.37	E1	BL Lac
MKN 464	J135553.3+383427	13 55 53.1	38 34 14	15300	1.55	17.35	16.12		
MKN 474	J143452.3+483938	14 34 52.2	48 39 42	10800	2.23	12.43	15.25	SB0	Sy1
MKN 478	J144207.7+352632	14 42 7.4	35 26 8	23550	52.05	1381.08	14.57		Sy1

Table 2.5: Results of the MARKARIAN - RASSBSC cross-correlation *continued*

Mrk Name (1)	BSC Name (2)	RA (2000) (3)	DEC (2000) (4)	Velocity (5)	F _x (6)	L _x (7)	Vmag (8)	Morph (9)	Classification (10)
MKN 493	J155909.5+350144	15 59 9.8	35 1 45	9570	4.64	20.33	13.87	RSBb	Sy1
MKN 501	J165352.6+394538	16 53 52.1	39 45 18	10110	37.10	181.42	13.39	E2/S0	Sy1
MKN 504	J170107.8+292421	17 1 7.6	29 24 28	11190	1.14	6.83	15.78	SB	Sy1
MKN 506	J172239.8+305252	17 22 39.8	30 52 43	13050	13.73	111.91	14.03	(R)Sa	Sy1
MKN 509	J204409.9-104330	20 44 9.8	-10 43 22	10650	34.65	188.04	13.48	E/S0	Sy1
MKN 530	J231856.8+001436	23 18 56.4	0 14 37	8700	3.68	13.31	13.04	SABbp	Sy1
MKN 534	J232846.9+033042	23 28 46.7	3 30 41	5370	0.61	0.84	12.96	Sap	
MKN 543	J000226.6+032105	0 2 26.6	3 21 8	7800	2.04	5.93	13.97	S0p	Sy1
MKN 573	J014358.4+022057	1 43 57.5	2 20 57	5160	0.60	0.76	13.03	S0	Sy2
MKN 584	J020026.7+024012	2 0 26.3	2 40 18	23640	3.25	86.82	16.08	E/S0	Sy1
MKN 586	J020749.0+024250	2 7 49.7	2 42 45	46950	1.07	112.48	14.26		Sy1
MKN 590	J021433.7-004603	2 14 33.6	0 45 59	8250	24.20	78.81	12.96	S0/a	Sy1
MKN 595	J024135.2+071117	2 41 34.8	7 11 14	8250	1.32	4.30	14.42	E/S0	Sy1
MKN 609	J032525.2-060830	3 25 25.9	-6 8 27	10350	3.72	19.05	14.4	E/S0	Sy1
MKN 618	J043622.3-102226	4 36 21.9	-10 22 37	10710	5.21	28.60	13.56	SBap	Sy1
MKN 648	J120719.4+241204	12 7 19.8	24 11 51	15270	1.77	19.7			
MKN 662	J135405.7+232549	13 54 6.2	23 25 45	16590	1.05	13.88	15.37		Sy1
MKN 663	J135420.2+325547	13 54 20	32 55 46	7740	7.51	21.53		SBa	
MKN 684	J143104.8+281716	14 31 4.8	28 17 13	13590	5.20	45.93	14.68		H II
MKN 704	J091826.2+161825	9 18 26	16 18 19	8700	6.80	24.64	13.51	Sa	Sy1
MKN 705	J092603.6+124406	9 26 3.2	12 44 2	8460	11.21	38.40	14	(R)S0	Sy1
MKN 707	J093701.0+010548	9 37 1	1 5 42	14760	4.11	42.89	14.88	E/S0	Sy1
MKN 715	J100446.0+144651	10 4 47.5	14 46 45	25230	0.63	19.29	15.45	S0/a	Sy2
MKN 720	J101737.6+065820	10 17 37.8	6 58 16	13500	0.78	6.77	15.1		Sy1
MKN 728	J110101.4+110246	11 1 1.7	11 2 48	10290	1.80	9.10	15.53		Sy1
MKN 732	J111349.5+093518	11 13 49.5	9 35 12	8610	2.41	8.54		p	H II
MKN 734	J112147.3+114420	11 21 47	11 44 19	14760	3.76	39.17	14.81	S0/a:	Sy1
MKN 739	J113629.4+213552	11 36 29.1	21 35 47	9000	4.38	16.98	13.81	S0p	Sy1
MKN 766	J121827.0+294853	12 18 26.3	29 48 47	3840	42.39	29.91	12.64	(R)SB0a	Sy1
MKN 771	J123203.6+200930	12 32 3.5	20 9 28	18900	5.70	97.44	14.93		Sy1
MKN 783	J130258.8+162423	13 2 58.8	16 24 27	19950	2.59	49.41	15.55		Sy1
MKN 813	J142725.3+194954	14 27 25	19 49 54	39300	6.92	511.04	15.27		Sy1
MKN 817	J143622.2+584750	14 36 22.1	58 47 40	9630	0.92	4.08	13.62	E/S0	Sy1
MKN 841	J150401.5+102620	15 4 1.2	10 26 19	10950	7.29	41.83	14.48		NLS1
MKN 845	J150744.6+512709	15 7 44.9	51 27 14	14040	2.17	20.51	14.2	Sab	Sy1

Table 2.5: Results of the MARKARIAN - RASSBSC cross-correlation *continued*

Mrk Name (1)	BSC Name (2)	RA (2000) (3)	DEC (2000) (4)	Velocity	F _x (5)	L _x (6)	Vmag (7)	Morph (8)	Classification (9)
MKN 849	J151956.7+283434	15 19 56.7	28 34 38	24870	0.565	16.729			Sy1
MKN 863	J155625.4+090311	15 56 26	9 3 19	12750	1.04	8.092			H II
MKN 864	J155818.7+255118	15 58 18.7	25 51 25	21570	1.523	33.899			Sy2
MKN 867	J160209.4+261936	16 2 9	26 19 56	21720	0.874	19.721			
MKN 876	J161357.0+654313	16 13 57	65 43 8	39000	7.779	566.08	15.17	S0	Sy1
MKN 877	J162011.5+172413	16 20 11.3	17 24 27	33870	1.514	83.088	15.27		Sy1
MKN 885	J162948.3+672247	16 29 48.3	67 22 41	7860	1.746	5.161	14.56	Sa	Sy1
MKN 896	J204621.0-024849	20 46 20.7	-2 48 46	8040	3.94	12.186	14.61		Sy1
MKN 915	J223647.3-123228	22 36 46.2	-12 32 40	7380	1.107	2.885	13.43	Sa	Sy1
MKN 926	J230443.8-084106	23 4 43.3	-8 41 8	14340	15.48	152.304	13.82	S0/a	Sy1
MKN 937	J001010.2-044225	0 10 10	-4 42 37	9030	1.991	7.767		p	
MKN 957	J004154.0+402118	0 41 53.3	40 21 17	22200	0.786	18.523	15.14	E/S0	Sy2
MKN 993	J012531.4+320800	1 25 31.4	32 8 10	5070	0.75	0.922	13.39	Sa	Sy2
MKN 1014	J015950.6+002337	1 59 49.6	0 23 41	48990	1.873	215.066	15.73		Sy1
MKN 1018	J020615.9-001728	2 6 16	0 17 30	12750	3.208	24.948	13.82	S0	Sy1
MKN 1040	J022814.6+311838	2 28 12.3	31 18 46	5190	3.074	3.962	13.26	SAbc	Sy1
MKN 1044	J023005.5-085951	2 30 5.4	-8 59 52	4920	19.269	22.317	13.67	E/S0	Sy1
MKN 1048	J023438.0-084714	2 34 37.3	-8 47 7	12720	11.529	89.25	13.38	(R)Sap	Sy1
MKN 1126	J230048.1-125518	23 0 47.7	-12 55 6	3360	3.154	1.703	13.47	(R)S0	Sy1
MKN 1146	J004719.4+144215	0 47 19.3	14 42 12	12090	0.603	4.22	14.58	SBb	Sy1
MKN 1148	J005154.8+172552	0 51 54.8	17 25 57	19500	3.762	68.443	15.96		Sy1
MKN 1152	J011350.0-145041	1 13 50	-14 50 46	15630	8.51	99.474	14.58	S0/a	Sy1
MKN 1218	J083811.0+245336	8 38 10.9	24 53 43	9450	1.921	8.206	13.86	SBb	Sy1
MKN 1220	J085439.9+174111	8 54 39.3	17 41 22	19470	1.748	31.7			Sy1
MKN 1239	J095219.1-013639	9 52 19	-1 36 42	6180	0.484	0.885	14.16	E	Sy1
MKN 1243	J095955.4+130246	9 59 56	13 2 37	10950	1.967	11.287	14.33	Sa	Sy1
MKN 1253	J101932.9-032014	10 19 33	-3 20 12	14040	2.408	22.706	15.1	E/S0p	
MKN 1269	J105519.1+402739	10 55 19.5	40 27 19	36000	2.158	133.825	16.06	Sab	Sy1
MKN 1291	J112332.4-083932	11 23 32.1	-8 39 29	3450	0.546	0.311		SBbc	Sy2
MKN 1310	J120114.3-034040	12 1 14.4	-3 40 40	5670	7.48	11.505	15.46	S0/a	Sy1
MKN 1330	J123939.6-052035	12 39 39.2	-5 20 40	2550	30.888	9.61	11.56	(R)SBb	Sy1
MKN 1376	J141315.2-031223	14 13 14.7	-3 12 26	1770	0.957	0.143	12.54	SB0ap	Sy1
MKN 1383	J142906.7+011708	14 29 6.4	1 17 6	26490	9.126	306.398	14.55	E/S0	Sy1
MKN 1447	J113030.1+493520	11 30 29	49 34 58	28890	0.471	18.793			Sy1
MKN 1469	J121607.4+504926	12 16 6.9	50 49 29	9420	0.713	3.029	14.32	SBa	Sy1

Table 2.5: Results of the MARKARIAN - RASSBSC cross-correlation *continued*

Mrk Name (1)	BSC Name (2)	RA (2000) (3)	DEC (2000) (4)	Velocity (5)	F _x (6)	L _x (7)	Vmag (8)	Morph (9)	Classification (10)
MKN 1505	J031947.4+413052	3 19 48.5	41 30 50	5340	132.93	181.362	11.62	S0p	Sy1
MKN 1506	J043311.2+052112	4 33 9.4	5 21 16	9930	15.345	72.395	14.27		Sy1
MKN 1509	J141759.6+250817	14 17 59.2	25 8 11	5040	44.586	54.188	12.51	(R)SA0a	Sy1
MKN 1514	J230315.7+085226	23 3 15.5	8 52 28	4980	16.938	20.098	12.42	(R)SBa	Sy1

Notes: (1) Markarian name, (2) WGAcat name, (3) RA (2000), (4) Dec (2000), (5) Recession velocity from Mazzarella & Balzano (1986) (6) X-ray flux in the 0.1-2.5keV band in units of 10^{-13} erg cm⁻² s⁻¹, (7) X-ray luminosity in the 0.1-2.5keV band in units of 10^{42} erg s⁻¹, (8) Morphological classification, (9) V magnitude, (10) Spectroscopic classification from Mazzarella & Balzano (1986) and Mazzarella & Boroson (1993).

Table 2.6: Results of the MARKARIAN - WGAcat cross-correlation

Mrk Name	WGAcat Name	RA (2000)	DEC (2000)	Velocity	F _x	L _x	Morph	Vmag	Classification
(1)	(2)	h m s	(^o ' ")	km s ⁻¹	(6)	(7)	(8)	(9)	(10)
MKN 3	J0615.6+7102	6 15 36	71 2 4	4230	0.56	0.48	SB0	12.77	Sy2
MKN 10	J0747.4+6055	7 47 29.1	60 55 58	8790	7.95	29.38	(R)SBbc	13.03	Sy1
MKN 33	J1032.5+5423	10 32 31.4	54 23 55	1410	0.04	0.003	Im?	13.3	H II
MKN 35	J1045.3+5557	10 45 22.5	55 57 32	1020	0.08	0.004	Im	13.06	H II
MKN 40	J1125.6+5423	11 25 36.3	54 22 55	6240	3.03	5.65	S0	15.12	Sy1
MKN 42	J1153.6+4612	11 53 41.3	46 12 38	7200	1.49	3.71	SBb	15.45	Sy1
MKN 78	J0742.6+6510	7 42 40.8	65 10 38	11400	0.05	0.34	SB0	14.44	Sy2
MKN 78	J0742.6+6510	7 42 40.8	65 10 38	11400	0.12	0.68	SB0	14.44	
MKN 110	J0925.2+5217	9 25 12.8	52 17 16	10800	37.35	208.44		15.37	Sy1
MKN 116	J0934.0+5514	9 34 2.1	55 14 24	750	0.06	0.002	dbl	16.21	H II
MKN 171	J1128.5+5833	11 28 32.2	58 33 51	3100	0.51	0.22	Sc+Im DB	11.85	H II
MKN 180	J1136.4+7009	11 36 26.7	70 9 23	13740	12.96	117.06		14.31	Sy1
MKN 205	J1221.7+7518	12 21 42.4	75 18 31	21000	6.14	129.51	p	15.24	
MKN 266	J1338.3+4816	13 38 17.4	48 16 39	8250	0.23	0.74	dbl	13.25	Sy2
MKN 273	J1344.6+5553	13 44 41.5	55 53 18	11400	0.09	0.53	p	14.91	Sy2
MKN 279	J1353.0+6918	13 53 1.7	69 18 28	9060	30.51	119.82	S0	14.18	Sy1
MKN 290	J1535.8+5754	15 35 52.8	57 54 8	9030	4.10	16.01	E	14.68	Sy1
MKN 304	J2217.1+1414	22 17 11.5	14 14 27	20190	0.12	2.3.0	E/S0	14.5	Sy1
MKN 313	J2302.0+1557	23 2 0.6	15 57 55	2040	1.48	0.29	Ep	12.72	Sy1
MKN 331	J2351.4+2035	23 51 26.1	20 35 8	5460	0.07	0.11	Sa	13.82	H II
MKN 333	J0001.4+3126	0 1 26.4	31 26 2	4950	0.01	0.02	E0/S0	13.65	
MKN 335	J0006.3+2012	0 6 19.3	20 12 9	7500	21.70	58.37	S0/a	13.74	Sy1
MKN 341	J0036.8+2359	0 36 51.7	23 59 4	5010	0.04	0.044	E3	14.24	Sy1
MKN 348	J0048.7+3157	0 48 46.6	31 57 20	4200	0.08	0.07	SAa	13.4	Sy2
MKN 352	J0059.8+3149	0 59 52.7	31 49 36	4500	0.84	0.82	(R)SA0	14.46	Sy1
MKN 359	J0127.5+1910	1 27 32.2	19 10 39	5100	6.83	8.50	SB0/a	13.59	Sy1
MKN 372	J0249.3+1918	2 49 20.1	19 18 19	9300	2.58	10.69	S0	14.54	Sy1
MKN 376	J0714.2+4541	7 14 14.7	45 41 55	16800	0.09	1.26	S0/a	14.37	Sy1
MKN 421	J1104.4+3812	11 4 27	38 12 22	9240	176.4	720.58	E1	13.37	BL Lac
MKN 463	J1356.0+1822	13 56 2.7	18 22 0	15180	0.11	1.22	pec	13.81	Sy2
MKN 464	J1355.8+3834	13 55 53.1	38 34 14	15300	1.93	21.57		16.12	Sy1
MKN 471	J1422.9+3251	14 22 55.4	32 51 0	10200	0.18	0.91	SBa	13.86	Sy1
MKN 474	J1434.8+4839	14 34 52.2	48 39 42	10800	6.74	37.62	SB0	15.25	Sy1
MKN 478	J1442.1+3526	14 42 7.4	35 26 8	23550	15.57	413.15		14.57	Sy1

Table 2.6: Results of the MARKARIAN - WGAcat cross-correlation *continued*

Mrk Name	WGAcat Name	RA (2000) (^h ^r ^{''})	DEC (2000) (^o ['] ^{''})	Velocity km s ⁻¹	F _X ⁻¹³ erg cm ⁻² s ⁻¹	L _X ×10 ⁴² erg s ⁻¹	Morph	Vmag	Classification
(1)	(2)	(3)	(4)	(5)	(6)	(7)	(8)	(9)	(10)
MKN 486	J1536.6+5433	15 36 39	54 33 14	11910	0.05	0.32		14.78	Sy1
MKN 493	J1559.1+3501	15 59 9.8	35 1 45	9570	2.25	9.86	RSBb	13.87	Sy1
MKN 501	J1653.8+3945	16 53 52.1	39 45 18	10110	47.25	231.07	E2/S0	13.39	Sy1
MKN 506	J1722.6+3052	17 22 39.8	30 52 43	13050	3.28	26.69	(R)Sa	14.03	Sy1
MKN 509	J2044.1-1043	20 44 9.8	-10 43 22	10650	33.12	179.73	E/S0	13.48	Sy1
MKN 516	J2156.3+0722	21 56 22.1	7 22 0	8760	0.14	0.51	E/S0	14.53	Sy1
MKN 530	J2318.9+0014	23 18 56.4	0 14 37	8700	4.53	16.39	SABbp	13.04	Sy1
MKN 533	J2327.9+0846	23 27 57	8 46 48	8850	0.14	0.52	SBbc	13	Sy2
MKN 538	J2336.2+0209	23 36 14.6	2 9 18	2970	0.18	0.07	SBbp	12.67	H II
MKN 552	J0031.3+0828	0 31 18.9	8 28 32	4200	0.02	0.01	SB		
MKN 573	J0143.9+0220	1 43 57.5	2 20 57	5160	0.37	0.47	S0	13.03	Sy2
MKN 586	J0207.8+0242	2 7 49.7	2 42 45	46950	4.36	459.41		14.26	Sy1
MKN 590	J0214.5-0046	2 14 33.6	0 45 59	8250	37.35	121.63	S0/a	12.96	Sy1
MKN 609	J0325.4-0608	3 25 25.9	-6 8 27	10350	1.70	8.71	E/S0	14.4	Sy1
MKN 617	J0434.0-0834	4 33 59.8	-8 34 29	4590	0.13	0.13	SBbp	13.05	H II
MKN 649	J1236.5+2612	12 36 30.8	26 12 3	7170	0.03	0.07	Sab		
MKN 668	J1406.9+2827	14 7 0.6	28 27 20	23910	0.06	1.62		14.98	Sy1
MKN 673	J1417.3+2651	14 17 20.7	26 51 24	10860	0.04	0.22	S		H II
MKN 679	J1423.4+3252	14 23 26.4	32 52 18	573600	0.06	963.41			Sy1
MKN 705	J0926.0+1244	9 26 3.2	12 44 2	8460	7.51	25.73	(R)S0	14	Sy1
MKN 739	J1136.4+2135	11 36 29.1	21 35 47	9000	2.74	10.60	S0p	13.81	Sy1
MKN 744	J1139.7+3154	11 39 42.3	31 54 35	2910	3.31	1.34	Sabp	12.49	Sy1
MKN 764	J1215.9+1241	12 16 0	12 41 13	19590	0.82	15.10			H II
MKN 766	J1218.4+2948	12 18 26.3	29 48 47	3840	8.12	5.79	(R)SB0a	12.64	Sy1
MKN 771	J1232.0+2009	12 32 3.5	20 9 28	18900	7.87	134.44		14.93	Sy1
MKN 789	J1332.4+1106	13 32 23.9	11 6 18	9600	0.04	0.17		14.68	H II
MKN 841	J1504.0+1026	15 4 1.2	10 26 19	10950	14.58	83.64		14.48	NLS1
MKN 876	J1613.9+6543	16 13 57	65 43 8	39000	3.77	274.43	S0	15.17	Sy1
MKN 877	J1620.1+1724	16 20 11.3	17 24 27	33870	1.12	61.75		15.27	Sy1
MKN 883	J1629.8+2426	16 29 52.7	24 26 37	11580	0.48	3.05	S0p	14.34	Sy1
MKN 896	J2046.3-0248	20 46 20.7	-2 48 46	8040	2.51	7.77		14.61	Sy1
MKN 926	J2304.7-0841	23 4 43.3	-8 41 8	14340	7.43	73.14	S0/a	13.82	Sy1
MKN 957	J0041.8+4021	0 41 53.3	40 21 17	22200	0.17	3.97	E/S0	15.14	Sy2
MKN 1014	J0159.8+0023	1 59 49.6	0 23 41	48990	1.22	140.55		15.73	Sy1

Table 2.6: Results of the MARKARIAN - WGAcat cross-correlation *continued*

Mrk Name	WGAcat Name	RA (2000) (^{hr} ['] ["])	DEC (2000) (^o ['] ["])	Velocity km s ⁻¹	F _X - ¹³ erg cm ⁻² s ⁻¹	L _X ×10 ⁴² erg s ⁻¹	Morph	Vmag	Classification
(1)	(2)	(3)	(4)	(5)	(6)	(7)	(8)	(9)	(10)
MKN 1018	J0206.2-0017	2 6 16	0 17 30	12750	1.81	14.07	S0	13.82	Sy1
MKN 1021	J0209.4-1008	2 9 24.8	-10 8 8	4260	0.09	0.08	Sp	12.5	group/clust
MKN 1022	J0209.6-1008	2 9 38.3	-10 8 46	3870	0.13	0.10	I0p	12.93	group/clust
MKN 1026	J0210.2-1019	2 10 17.3	-10 19 11	3780	0.02	0.01	SB	13.3	H II
MKN 1044	J0230.0-0859	2 30 5.4	-8 59 52	4920	15.3	17.72	E/S0	13.67	Sy1
MKN 1048	J0234.6-0847	2 34 37.3	-8 47 7	12720	9.45	73.16	(R)Sap	13.38	Sy1
MKN 1088	J0454.6+0316	4 54 38.3	3 16 6	4500	0.08	0.08	SB0/a		
MKN 1089	J0501.6-0415	5 1 38.2	-4 15 25	3810	0.07	0.05	p	13.57	H II
MKN 1095	J0516.1-0008	5 16 11.3	0 8 58	9900	13.68	64.15	S0/a	12.87	Sy1
MKN 1152	J0113.8-1450	1 13 50	-14 50 46	15630	12.42	145.17	S0/a	14.58	Sy1
MKN 1218	J0838.1+2453	8 38 10.9	24 53 43	9450	3.50	14.96	SBb	13.86	Sy1
MKN 1220	J0854.6+1741	8 54 39.3	17 41 22	19470	2.00	36.24			Sy1
MKN 1239	J0952.3-0136	9 52 19	-1 36 42	6180	0.53	0.96	E	14.16	Sy1
MKN 1298	J1129.2-0424	11 29 16.6	-4 24 6	17790	0.10	1.48	S0	14.18	Sy1
MKN 1310	J1201.2-0340	12 1 14.4	-3 40 40	5670	1.42	2.19	S0/a	15.46	Sy1
MKN 1325	J1226.4+0901	12 26 27.8	9 1 17	7320	0.23	0.61	Sabp		Comp
MKN 1330	J1239.6-0520	12 39 39.2	-5 20 40	2550	10.34	3.28	(R)SBb	11.56	Sy1
MKN 1376	J1413.2-0312	14 13 14.7	-3 12 26	1770	1.74	0.26	SB0ap	12.54	Sy1
MKN 1485	J1353.3+4021	13 53 21.4	40 21 47	2400	0.04	0.01	SBbc	13.64	H II
MKN 1494	J1501.6+1025	15 1 38.7	10 25 13	9150	0.14	0.57			
MKN 1506	J0433.1+0521	4 33 9.4	5 21 16	9930	17.01	80.25		14.27	Sy1
MKN 1509	J1417.9+2508	14 17 59.2	25 8 11	5040	29.7	36.09	(R)SA0a	12.51	Sy1
MKN 1514	J2303.2+0852	23 3 15.5	8 52 28	4980	15.3	18.15	(R)SBa	12.42	Sy1

Notes: (1) Markarian name, (2) WGAcat name, (3) RA (2000), (4) Dec (2000), (5) Recession velocity from Mazzarella & Balzano (1986) (6) X-ray flux in the 0.1-2.5keV band in units of 10⁻¹³erg cm⁻² s⁻¹, (7) X-ray luminosity in the 0.1-2.5keV band in units of 10⁴²erg s⁻¹, (8) Morphological classification, (9) V magnitude, (10) Spectroscopic classification from Mazzarella & Balzano (1986) and Mazzarella & Boroson (1993).

2.2.3 The KISO samples

These samples (Tables 2.7, 2.7 for the KISO-BSC and the KISO-WGAcad) like the samples extracted using the Markarian catalogue, mainly consist of Sy1-type objects. Again the BSC sample is biased towards more luminous objects. However, this sample contains a larger number of starforming galaxies than the Markarian samples (fig.2.11, 2.12, 2.13, 2.14). This is mainly due to the much fainter flux limit of the KISO survey, because at fainter fluxes the numbers of starforming galaxies increase.

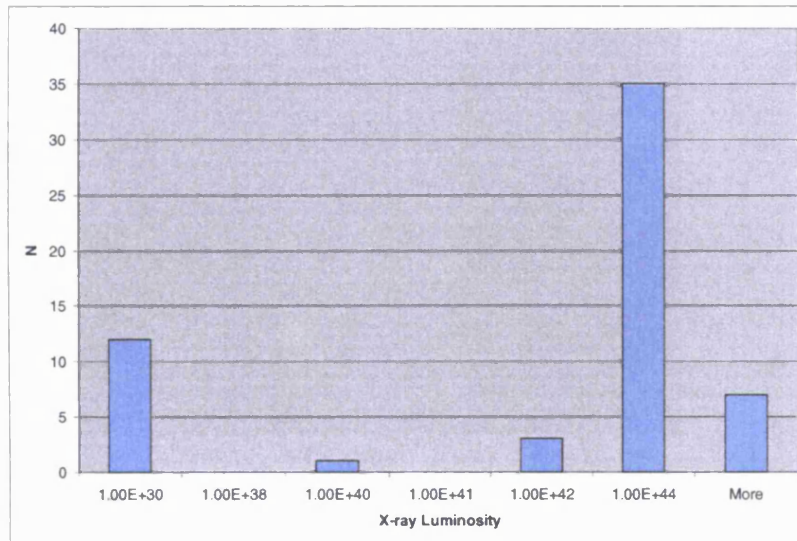
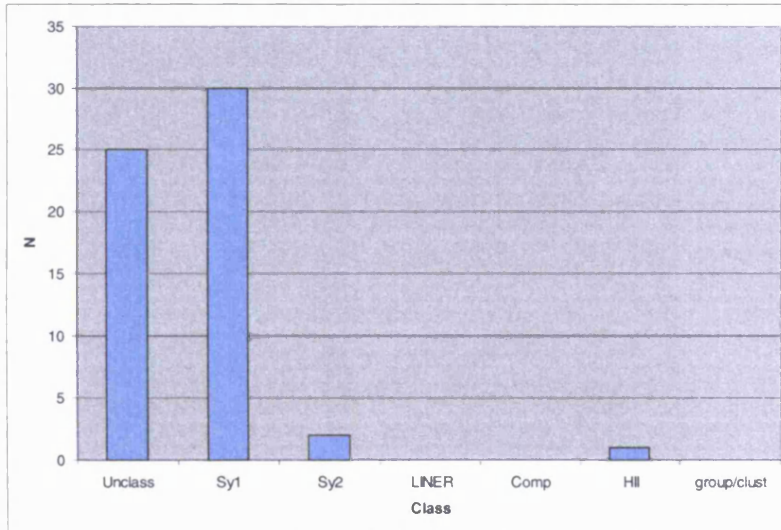


Figure 2.11: The distribution of activity classes, and X-ray luminosities of the objects in the Kiso-RASSBSC sample.

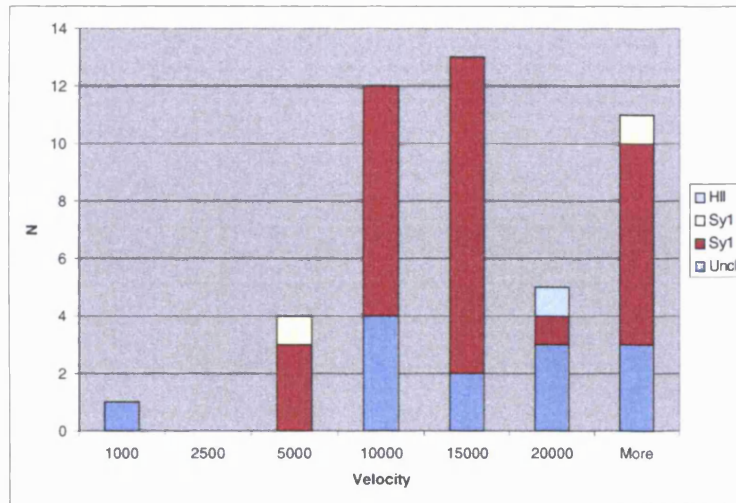
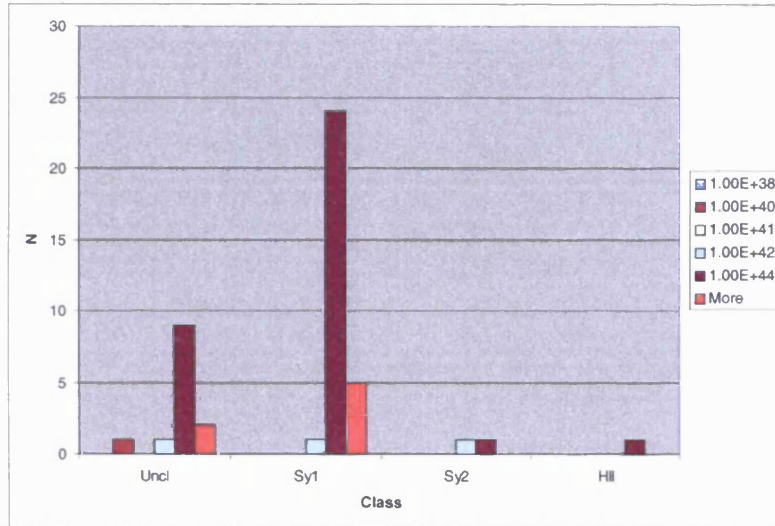


Figure 2.12: The distribution of X-ray luminosities and velocities of objects of different activity classes in the Kiso-RASSBSC sample.

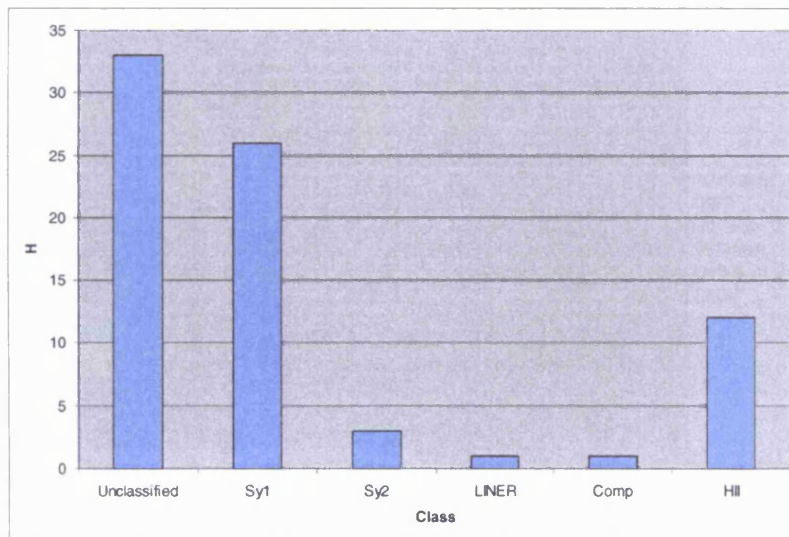
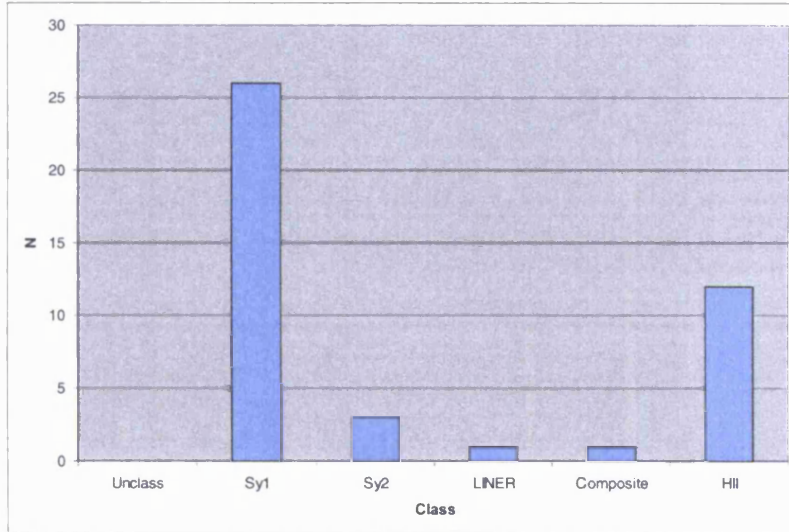


Figure 2.13: The distribution of activity classes, and X-ray luminosities of the objects in the Kiso-WGAcet sample.

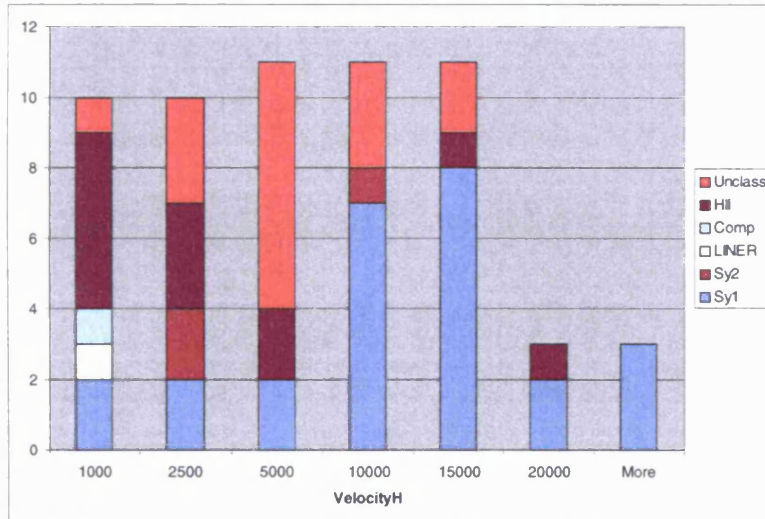
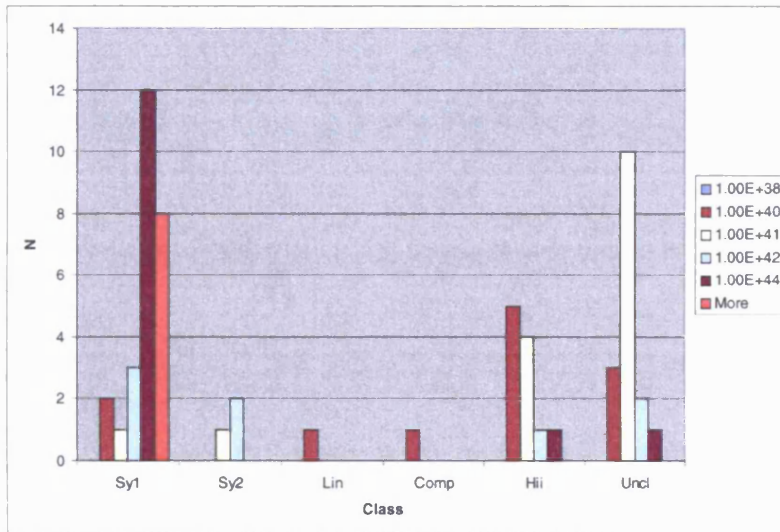


Figure 2.14: The distribution of X-ray luminosities and velocities of objects of different activity classes in the Kiso-WGAcad sample.

Table 2.7: Results of the KISO - RASSBSC cross-correlation

KISO Name	BSC Name	Mrk Name	Velocity (h m s)	RA (2000) ($^{\circ}$ $'$ $''$)	DEC (2000) km s $^{-1}$	F _x	L _x	Vmag	UV-Excess	Morph	Classification
(1)	(2)	(3)	(4)	(5)	(6)	(7)	(8)	(9)	(10)	(11)	(12)
0000+216	J000308.6+215728	Mrk 334	6582	00 03 09.6	21 57 36.2	0.87	1.80	14.4	M	Sp	Sy1
0003+199	J000618.9+201215	Mrk 0335	7730	00 06 19.4	20 12 11.0	22.34	63.86	14	M	C	Sy1
0116+317	J011922.8+320244		17373	01 19 22.1	32 02 37.8	0.52	7.54	15.7	L	Sp	
0122+318	J012531.4+320800	Mrk 0993	4658	01 25 31.3	32 08 10.5	0.75	0.78	14	L	Sk	Sy2
0123+313	J012634.2+313659	Mrk 0358	13563	01 26 33.5	31 36 58.8	1.545	13.62	15	M	Sp	Sy1
0128+328	J013124.2+330837		0	01 31 23.8	33 08 39.0	0.94	0	16.5	L	Sp	
0157+001	J015950.6+002337	Mrk 1014	48903	01 59 49.6	00 23 41.1	1.87	214.30	16	M	C	Sy1
0157+024	J020026.7+024012	Mrk 0584	23631	02 00 26.3	02 40 10.8	3.25	86.75	15.3	M	C	Sy1
0202-122	J020436.8-115941		21600	02 04 36.7	-11 59 41.5	0.66	14.82	16.5	M	C	
0205+024	J020749.0+024250	Mrk 0586	46590	02 07 49.8	02 42 45.3	1.07	110.76	16	M	C	Sy1
0212-009	J021433.7-004603	Mrk 0590	7910	02 14 33.4	-00 45 59.5	24.20	72.45	14	L	Sp	Sy1
0225+310	J022814.6+311838	Mrk 1040	4992	02 28 14.4	31 18 41.7	3.07	3.67	13.9	L	Sk	Sy1
0227-092	J023005.5-085951	Mrk 1044	4932	02 30 05.4	-08 59 53.8	19.27	22.43	15	M	Sp	Sy1
0232-090	J023438.0-084714	Mrk 1048	12942	02 34 37.8	-08 47 16.0	11.53	92.39	14.5	M	Sp	Sy1
0235+016	J023827.5+015426		0	02 38 27.4	01 54 27.6	2.85	0	14.6	L	Sk	
0240-002	J024240.9-000046		0	02 42 40.7	-00 00 47.1	16.06	0	9.7	L	Sk	
0322-063B	J032525.2-060830	Mrk 0609	10242	03 25 25.3	-06 08 38.9	3.72	18.65	14.5	M	C	Sy1
0645+744	J065209.8+742537	Mrk 0006	5536	06 52 12.4	74 25 37.4	0.56	0.82	14.8	L	Sk	Sy1
0732+588	J073657.0+584610	Mrk 0009	11961	07 36 56.9	58 46 13.0	1.17	8.00	14.5	M	C	Sy1
0743+610	J074729.4+605601	Mrk 0010	8770	07 47 29.2	60 56 00.5	5.28	19.42	14.5	M	Sk	Sy1
0752+393	J075526.1+391111	Mrk 0382	10146	07 55 25.3	39 11 09.7	4.04	19.88	15.5	H	Sp	Sy1
0811+462	J081517.8+460429		12291	08 15 17.0	46 04 30.5	1.25	9.00	15.2	M	Sp	Sy1
0921+525	J092512.3+521716	Mrk 0110	10587	09 25 12.9	52 17 10.5	15.22	81.62	16	H	Pi	Sy1
0929+540	J093308.2+534754		0	09 33 08.9	53 47 48.1	0.61	0	17	M	C	
0933+511	J093642.6+505249		0	09 36 43.0	50 52 49.6	0.49	0	15.5	M	Sp	
1025+576	J102915.4+572402		55800	10 29 14.8	57 23 56.0	2.30	342.03	17	M	C	
1031+398	J103438.7+393834		12732	10 34 38.4	39 38 27.7	23.92	185.54	15.6	M	C	
1052+407	J105519.1+402739	Mrk 1269	36000	10 55 19.5	40 27 16.1	2.16	133.82	17	H	C	Sy1
1101+384A	J110427.1+381231	Mrk 0421	9000	11 04 27.3	38 12 31.5	239.13	926.75	13.1	L	Pd	Sy1
1136+342	J113913.6+335552		9834	11 39 13.7	33 55 51.3	7.76	35.92	15.4	M	Sp	
1141+371	J114429.9+365314		12000	11 44 29.9	36 53 08.4	12.31	84.83	16.5	L	Sp	
1204+244	J120719.4+241204	Mrk 0648	15330	12 07 19.2	24 11 47.0	1.77	19.85	16	M	C	
1211+369	J121345.2+363754		228	12 13 44.0	36 37 55.2	1.27	0.003	13.5	M	Ic	
1215+300	J121827.0+294853	Mrk 0766	3876	12 18 26.4	29 48 46.5	42.39	30.47	13.7	L	Sk	Sy1

Table 2.7: Results of the KISO - RASSBSC cross-correlation *continued*

KISO Name (1)	BSC Name (2)	Mrk Name (3)	Velocity (4)	RA (2000) (5)	DEC (2000) (6)	F _x (7)	L _x (8)	Vmag (9)	UV-Excess (10)	Morph (11)	Classification (12)
1229+204	J123203.6+200930		0	12 32 03.6	20 09 29.7	5.70	0	15.1	H	C	
1235+269	J123741.4+264229		6442	12 37 41.1	26 42 27.3	45.85	91.05	15.7	M	Sp	
1240+359	J124306.5+353859		0	12 43 07.3	35 39 04.4	0.75	0	16.5	H	C	
1256+241	J125851.4+235532		0	12 58 51.5	23 55 25.2	3.87	0	17	M	Sp	
1259+280	J130158.9+274708		7102	13 02 00.0	27 46 57.8	1.12	2.70	15.4	L	?	
1304+346	J130708.4+342414	Mrk 0064	55755	13 07 08.6	34 24 20.9	2.10	312.03	17	H	C	Sy1
1343+298	J134607.5+293814	Mrk 0069	22800	13 46 08.0	29 38 10.0	2.35	58.49	16.5	M	C	Sy1
1351+236	J135405.7+232549		0	13 54 06.2	23 25 45.9	1.05	0	15.5	M	C	
1351+695	J135304.8+691832	Mrk 0279	8814	13 53 01.7	69 18 28.9	25.28	93.97	14.5	H	C	Sy1
1353+388	J135553.3+383427	Mrk 0464	15300	13 55 53.5	38 34 27.9	1.55	17.35	17	H	C	Sy1
1415+253	J141759.6+250817	Mrk 1509	5149	14 17 59.5	25 08 13.2	44.59	56.56	13.1	M	Sp	Sy1
1433+488	J143452.3+483938	Mrk 0474	10740	14 34 52.4	48 39 46.5	2.23	12.30	15.5	L	C	Sy1
1436+487	J143804.6+483325		0	14 38 07.0	48 33 31.5	0.54	0	17.5	L	Sp	
1506+516	J150744.6+512709	Mrk 0845	13815	15 07 44.8	51 27 10.1	2.17	19.86	15.6	M	Sp	Sy1
1556+259	J155818.7+255118	Mrk 0864	21570	15 58 18.6	25 51 25.5	1.52	33.90	16.5	H	C	Sy2
1600+264	J160209.4+261936	Mrk 0867	21624	16 02 08.9	26 19 46.0	0.87	19.55	15.3	M	Pd	Sy1
1611+374B	J161301.5+371656		20886	16 13 01.4	37 17 17.4	3.74	78.12	15.5	M	Sp	
1618+402	J162013.1+400858		0	16 20 12.6	40 09 05.8	3.20	0	16	M	Sp	
1618+410	J161951.7+405834		0	16 19 51.2	40 58 45.5	4.60	0	16	L	Sk	
1659+294	J170107.8+292421	Mrk 0504	10767	17 01 07.6	29 24 24.2	1.14	6.32	15.5	H	C	Sy1
2301+223	J230402.8+223725	Mrk 0315	11661	23 04 02.5	22 37 19.2	1.18	7.7	15	L	C	Sy1
2311+137	J231341.0+140113	Mrk 0316	12270	23 13 40.5	14 01 14.7	0.93	6.72	15.7	M	C	H II
2326+032	J232846.9+033042	Mrk 0534	5138	23 28 46.7	03 30 41.2	0.61	0.77	13.2	L	Sp	
2353+252A	J235547.6+253044		17100	23 55 48.1	25 30 31.9	2.36	33.03	16	H	Sp	

Notes: (1) Kiso name, (2) RASSBSC name, (3) Markarian name, (4) Recession velocity km s^{-1} , (5) RA (2000), (6) Dec (2000), (7) X-ray flux in the 0.1-2.5keV band in units of $10^{-13} \text{erg cm}^{-2} \text{s}^{-1}$, (8) X-ray luminosity in the 0.1-2.5keV band in units of $10^{42} \text{erg s}^{-1}$, (9) V magnitude, (10) Amount of UV excess; L: low, M: medium, H: high, (11) Morphological classification, (12) Spectroscopic classification from Augarde et al. (1994), Mazzarella & Balzano (1986) and Mazzarella & Boroson (1993).

2.3 Spectroscopic classifications

Firstly the literature has been investigated for spectroscopic activity classifications of the objects in these samples, based on optical spectroscopy. For X-ray luminous objects ($L_X > 10^{41}$ erg s $^{-1}$) with uncertain classifications or without published classification, new optical spectra have been obtained. Moreover, all the objects without published redshifts, for which it was obviously impossible to calculate luminosities, have been observed. From this sample we have excluded a few objects which have been identified as H II regions in our or nearby galaxies by Strauss et al. (1992) Unfortunately as a number of objects (mainly from the IRAS FSC) are very faint it has not been possible to obtain spectra of these with the 2m class telescopes we used for this survey.

2.3.1 Observations and Data reduction

The optical spectra for objects accessible from the northern hemisphere, have been obtained during three observing runs on the 2nd-5th of May 1998, 12th-14th of September 1998 and 15th-16th February 1999 at the 90'' University of Arizona telescope at Kitt Peak. The Boller and Chivens Spectrograph with the 800×1200 CCD and the 300l/mm grating has been used. This setting gives a dispersion of 3.7Å/pix, which corresponds to an effective resolution of $\sim 8.5\text{\AA}$ FWHM at 5500Å and a spectral coverage of 3700Å. The spectra were taken using a $2.5'' \times 4'$ long slit.

Southern objects have been observed with the Double Beam Spectrograph (DBS) at the 2.3m MSO telescope, during one observing run on the 5th and 6th of August 1999. The DBS gives the possibility to observe simultaneously the red and the blue part of the spectrum with the two CCDs attached to each arm. The 600l/mm grating has been used, giving a dispersion of 1.1Å/pix which corresponds to an effective spectral resolution of $\sim 2.5\text{\AA}$ FWHM and a wavelength coverage of 1900Å. The spectra are taken using a $3'' \times 4'$ long slit.

These data have been reduced following the standard procedures using the Image Reduction and Analysis Facility (IRAF). Firstly the CCD frames were trimmed in order to remove the unexposed region and the pedestal bias subtracted using a linear fit at the bias section. Any residual bias was subtracted using the average of several bias frames taken at the beginning of

Table 2.8: Results of the KISO - WGAcat cross-correlation

KISO Name	WGAcat Name	Mrk Name	Velocity h m s	RA (2000) ($^{\circ}$ $'$ $''$)	DEC (2000) km s $^{-1}$	F _X	L _X	Vmag	UV-Excess	Morph	Classification
(1)	(2)	(3)	(4)	(5)	(6)	(7)	(8)	(9)	(10)	(11)	(12)
0003+199	J0006.3+2012	Mrk 0335	7730	0 6 19.4	20 12 11	21.69	62.01	14	M	C	Sy1
0157+001	J0159.8+0023	Mrk 1014	48903	1 59 49.6	0 23 41.1	1.36	155.5	16	M	C	Sy1
0205+024	J0207.8+0242	Mrk 0586	46590	2 7 49.8	2 42 45.3	4.36	452.39	16	M	C	Sy1
0206-103	J0209.4-1008	Mrk 1021	4073	2 9 24.6	-10 8 9.4	0.09	0.07	13	L	Sp	
0207-103	J0209.6-1008	Mrk 1022	3859	2 9 38.3	-10 8 47.9	0.14	0.10	13	L	Sp	
0207-105	J0210.2-1019	Mrk 1026	3989	2 10 17.5	-10 19 18.5	0.02	0.01	13.5	L	Sk	
0212-009	J0214.5-0046	Mrk 0590	7910	2 14 33.4	0 45 59.5	37.35	111.81	14	L	Sp	Sy1
0227-092	J0230.0-0859	Mrk 1044	4932	2 30 5.4	-8 59 53.8	15.3	17.81	15	M	Sp	Sy1
0232-090	J0234.6-0847	Mrk 1048	12942	2 34 37.8	-8 47 16	9.45	75.73	14.5	M	Sp	Sy1
0235+016	J0238.4+0154		0	2 38 27.4	1 54 27.6	3.54	0	14.6	L	Sk	
0240-002	J0242.6-0000		0	2 42 40.7	0 0 47.1	12.96	0	9.7	L	Sk	
0301+002	J0304.2+0028		0	3 4 17.6	0 28 27.3	0.42	0	17	L	C	
0314-027	J0316.8-0233		0	3 16 48.9	-2 33 30.9	0.09	0	17	L	?	
0322-063B	J0325.4-0608	Mrk 0609	10242	3 25 25.3	-6 8 38.9	1.70	8.54	14.5	M	C	Sy1
0325+023B	J0328.0+0233		0	3 28 2.5	2 33 19.3	0.13	0	16.5	L	?	
0710+457	J0714.2+4541	Mrk 0376	16794	7 14 14.7	45 41 55.5	0.09	1.26	16	M	C	Sy1
0737+652	J0742.6+6510	Mrk 0078	11145	7 42 41.8	65 10 37.1	0.05	0.32	15	L	?	
0743+610	J0747.4+6055	Mrk 0010	8770	7 47 29.2	60 56 0.5	7.95	29.24	14.5	M	Sk	Sy1
0811+462	J0815.2+4604		12291	8 15 17	46 4 30.5	0.81	5.83	15.2	M	Sp	Sy1
0921+525	J0925.2+5217	Mrk 0110	10587	9 25 12.9	52 17 10.5	37.35	200.30	16	H	Pi	Sy1
0930+554	J0934.0+5514	Mrk 0116	745	9 34 2	55 14 27.8	0.06	0.002	15.5	H	C	H II
0955+326	J0958.3+3222		1476	9 58 21.2	32 22 8.8	0.05	0.005	12.7	M	Sp	H II
1031+398	J1034.6+3938		12732	10 34 38.4	39 38 27.7	16.29	126.34	15.6	M	C	Sy1
1036+419	J1039.1+4141		739	10 39 9.6	41 41 14.6	0.02	0.001	12	M	Sp	H II
1046+330	J1049.4+3246		1633	10 49 25.3	32 46 20.7	0.08	0.01	15	L	Ic	
1101+384A	J1104.4+3812	Mrk 0421	9000	11 4 27.3	38 12 31.5	181.8	704.56	13.1	L	Pd	Sy1
1136+325	J1138.6+3214		0	11 38 41.7	32 14 47.6	0.29	0	17	L	Sk	
1136+342	J1139.2+3355		9834	11 39 13.7	33 55 51.3	3.81	17.61	15.4	M	Sp	
1141+553B	J1144.1+5501		1436	11 44 13.3	55 1 59.5	0.02	0.002	14.2	M	Sp	
1153+554	J1156.4+5507		1109	11 56 28.5	55 7 35.9	0.06	0.004	11.6	M	Sk	Sy1
1208+394	J1211.5+3911		0	12 11 31.1	39 10 41.7	0.04	0	16.5	M	Sp	
1208+396A	J1210.5+3924		995	12 10 32.4	39 24 20.5	5.12	0.24	11.2	L	Sk	Sy1
1213+129	J1215.9+1241	Mrk 0764	19827	12 16 0	12 41 13.8	0.82	15.47	15	L	C	H II
1213+306	J1216.3+3021		0	12 16 21.7	30 21 3.9	0.04	0	16.5	L	Sp	
1215+300	J1218.4+2948	Mrk 0766	3876	12 18 26.4	29 48 46.5	27.81	19.99	13.7	L	Sk	Sy1

Table 2.8: Results of the KISO - WGAcat cross-correlation *continued*

KISO Name (1)	WGAcat Name (2)	Mrk Name (3)	Velocity (4)	RA (2000) (5)	DEC (2000) (6)	F _X (7)	L _X (8)	Vmag (9)	UV-Excess (10)	Morph (11)	Classification (12)
1220+301	J1222.5+2953		963	12 22 31.9	29 53 43	0.13	0.006	11.5	M	Sp	LINER
1221+276	J1224.2+2724		0	12 24 15.2	27 25 3.7	0.35	0	16.5	H	Sp	
1223+315	J1226.4+3113		716	12 26 27.1	31 13 23.8	0.27	0.007	10.9	L	Sk	Comp
1223+338	J1225.7+3332		319	12 25 49	33 32 41.5	0.02	0	11.7	M	Sk	Sy1
1228+419	J1230.5+4138		299	12 30 35.7	41 38 38.9	0.25	0.001	10.1	H	Pi	
1229+204	J1232.0+2009		0	12 32 3.6	20 9 29.7	7.87	0	15.1	H	C	
1231+280	J1233.5+2746		0	12 33 31.7	27 46 58.6	0.74	0	16.5	L	C	
1233+262	J1236.3+2559		1282	12 36 20.5	25 59 10.4	0.27	0.02	10.3	L	Sk	Sy1
1234+264	J1236.5+2612	Mrk 0649	7128	12 36 30.8	26 12 3.5	0.03	0.07	14.3	L	C	
1235+269	J1237.6+2642		6442	12 37 41.1	26 42 27.3	0.16	0.32	15.7	M	Sp	Sy1
1239+328B	J1242.0+3232		606	12 42 6.9	32 32 21.6	0.02	0	9.8	H	Ic	H II
1241+324	J1243.9+3210		646	12 43 57.1	32 10 10.1	0.01	0	10.6	H	Pi	H II
1247+257B	J1250.4+2530		1206	12 50 26.5	25 30 2.7	0.27	0.02	10.2	L	Sk	Sy2
1247+262A	J1249.5+2559		0	12 49 31.8	25 59 46.9	0.11	0	15.5	H	C	
1256+351	J1259.0+3451		847	12 59 1.9	34 51 32.5	0.10	0.004	12.8	H	Ig	H II
1317+305	J1319.6+3015		2141	13 19 39.1	30 15 21.9	0.02	0.005	14.4	M	Sp	
1335+276	J1337.4+2725		11136	13 37 24.8	27 25 8.8	0.02	0.10	14.7	L	Sk	
1351+406	J1353.3+4021	Mrk 1485	2321	13 53 21.5	40 21 49.6	0.04	0.01	12.4	L	Sp	H II
1351+695	J1353.0+6918	Mrk 0279	8814	13 53 1.7	69 18 28.9	30.51	113.40	14.5	H	C	Sy1
1353+186	J1356.0+1822	Mrk 0463	14904	13 56 2.7	18 22 0.9	0.11	1.18	14.8	L	C	Sy1
1353+388	J1355.8+3834	Mrk 0464	15300	13 55 53.5	38 34 27.9	1.93	21.57	17	H	C	Sy1
1413+366	J1415.6+3622		4731	14 15 38.2	36 22 30.6	0.04	0.04	15.4	M	C	
1415+253	J1417.9+2507	Mrk 1509	5149	14 17 59.5	25 8 13.2	55.80	70.78	13.1	M	Sp	Sy1
1415+270	J1417.3+2651	Mrk 0673	10953	14 17 20.8	26 51 27.6	0.04	0.22	15.1	L	Sk	H II
1420+330	J1422.9+3251	Mrk 0471	10269	14 22 55.1	32 51 2.6	0.18	0.92	14.5	L	Sk	Sy1
1421+330	J1423.4+3252	Mrk 0679	571200	14 23 25.9	32 52 19.9	0.06	955.36	17	H	C	Sy1
1425+238	J1428.1+2337		0	14 28 7.7	23 37 22.9	0.50	0	16	L	?	
1433+488	J1434.8+4839	Mrk 0474	10740	14 34 52.4	48 39 46.5	6.74	37.20	15.5	L	C	Sy1
1436+487	J1438.0+4833		0	14 38 7	48 33 31.5	0.60	0	17.5	L	Sp	
1603+206	J1605.2+2032	Mrk 0297	4716	16 5 13.1	20 32 31.5	0.07	0.07	14.1	M	Ic	
1615+350C	J1617.3+3454		0	16 17 19.9	34 54 5.2	0.16	0	14.7	M	C	
1615+351C	J1617.7+3500		0	16 17 40.4	35 0 14.5	0.07	0	14.9	M	C	
2259+156	J2302.0+1557	Mrk 0313	1968	23 2 0.8	15 57 52.9	1.48	0.27	13.3	M	?	Sy2
2317+169	J2320.5+1713		1633	23 20 29.9	17 13 32.4	0.10	0.01	12.8	L	Ic	H II

Table 2.8: Results of the KISO - WGAcat cross-correlation *continued*

KISO Name (1)	WGAcat Name (2)	Mrk Name (3)	Velocity (4)	RA (2000)	DEC (2000) (5)	F _x (6)	L _x (7)	Vmag (8)	UV-Excess (9)	Morph (10)	Classification
2323+085	J2325.8+0847		0	23 25 51.3	8 47 10.3	0.95	0	16	L	Sk	
2325+085	J2327.9+0846	Mrk 0533	8713	23 27 56.6	8 46 44.6	0.14	0.51	13.6	L	Sk	Sy2
2348+198A	J2351.0+2009	Mrk 9005	4211	23 51 3.9	20 9 2.2	0.05	0.04	12.9	M	Sp	H II
2348+198B	J2351.3+2005		4286	23 51 22.4	20 5 48.3	0.03	0.03	14.5	M	C	
2348+198C	J2351.4+2006	Mrk 9006	4277	23 51 24.9	20 6 42.3	0.09	0.08	13.1	L	Sk	H II
2348+203	J2351.4+2035	Mrk 0331	5541	23 51 26.3	20 35 9.3	0.08	0.11	14.9	L	C	
2358+311	J0001.4+3126	Mrk 0333	4948	0 1 26.8	31 26 2.2	0.01	0.02	14.3	L	?	

Notes: (1) Kiso name, (2) WGAcat name, (3) Markarian name, (4) Recession velocity km s^{-1} , (5) RA (2000), (6) Dec (2000), (7) X-ray flux in the 0.1-2.5keV band in units of $10^{-13} \text{erg cm}^{-2} \text{s}^{-1}$, (8) X-ray luminosity in the 0.1-2.5keV band in units of $10^{42} \text{erg s}^{-1}$, (9) V magnitude, (10) Amount of UV excess; L: low, M: medium, H: high, (11) Morphological classification, (12) Spectroscopic classification from Augarde et al. (1994), Mazzarella & Balzano (1986) and Mazzarella & Boroson (1993).

each night. Then the CCD frames were flat-fielded using the median of 10 dome flats taken on each night.

For the wavelength calibration, exposures of a Helium-Argon lamp were taken at the beginning and the end of each night. Firstly the dispersion solution was defined by fitting with a polynomial, the wavelengths of the identified lines of a lamp spectrum extracted from the middle lines of the CCD. Any flexure along the spatial axis was measured by fitting polynomials to calibration arc spectra extracted from different positions across the spatial direction of the CCD, usually in steps of 10 rows. Finally, this two-dimensional dispersion solution was applied to the object observations. Any deviations from this dispersion solution have been corrected by using strong sky lines.

The limits of the projected aperture used to extract the spectrum of each object have been defined to be at the 1/10th of the peak intensity, in order to maximise the signal to noise ratio. Background subtraction has been performed using two sky regions close to the object, one above and one below, and interpolating over the region covered by the object.

Finally the spectra were flux calibrated using standard stars from the lists of Massey, Strobel, Barnes & Anderson (1988) and Oke (1990). The stars were selected to lie nearby to the objects and at similar air-mass. The spectrophotometrically calibrated model spectrum of the standard has been divided by the observed spectrum, to construct a sensitivity curve in order to correct for atmospheric features and perform the flux calibration. Finally each object spectrum has been multiplied by the appropriate sensitivity curve in order to create a flux calibrated spectrum. The spectra are presented in figure 2.17

2.3.2 Spectroscopic classifications

As mentioned in the introduction, active galaxies can be classified in two major categories. The first includes objects which exhibit broad permitted lines in their spectra (broad line galaxies), whereas the second class consists of objects for which the width of the permitted lines is similar or smaller than that of the forbidden lines (narrow line galaxies). In order to classify the galaxies in these two categories, we consider the velocity widths of H_α , H_β and $[OIII]$, $[NII]$. More specifically the full width at half maximum (FWHM) of H_α and H_β is compared with

Table 2.9: Classification criteria

Class	$[\text{O III}]/\text{H}\beta$	$[\text{O I}]/\text{H}\alpha$	$[\text{N II}]/\text{H}\alpha$	$[\text{S II}]/\text{H}\alpha$
H II	Any	< 0.08	< 0.6	< 0.4
Seyfert	$\gtrsim 3$	$\gtrsim 0.08$	$\gtrsim 0.6$	$\gtrsim 0.4$
LINERs	$\gtrsim 3$	$\gtrsim 0.17$	$\gtrsim 0.6$	$\gtrsim 0.4$
Transition	< 3	$0.08 \lesssim [\text{O I}]/\text{H}\alpha < 0.17$	$\gtrsim 0.6$	$\gtrsim 0.4$

the FWHM of $[\text{N II}] \lambda 6584$ and $[\text{O III}] \lambda 5007$, respectively. The compared lines are very close in wavelength and so the effect of extinction can be neglected.

Furthermore, the objects have been classified as Seyfert type, LINER or H II type galaxies, according to the criteria of Veilleux & Osterbrock (1987) (Table 2.9). These criteria are based on the comparison of the ratios of the brightest emission lines observed in the optical spectrum of active galaxies: eg. $\text{H}\alpha$, $[\text{N II}]$, $[\text{S II}]$, $\text{H}\beta$, $[\text{O III}]$, $[\text{O I}]$. Different classes of galaxies occupy different regions in the line ratio diagrams (figures 2.15, 2.16), although some overlap between H II - Seyfert-2 and LINER occurs. A major advantage of this method is that the lines used to calculate the ratios are close in wavelength and therefore the effect of reddening is negligible.

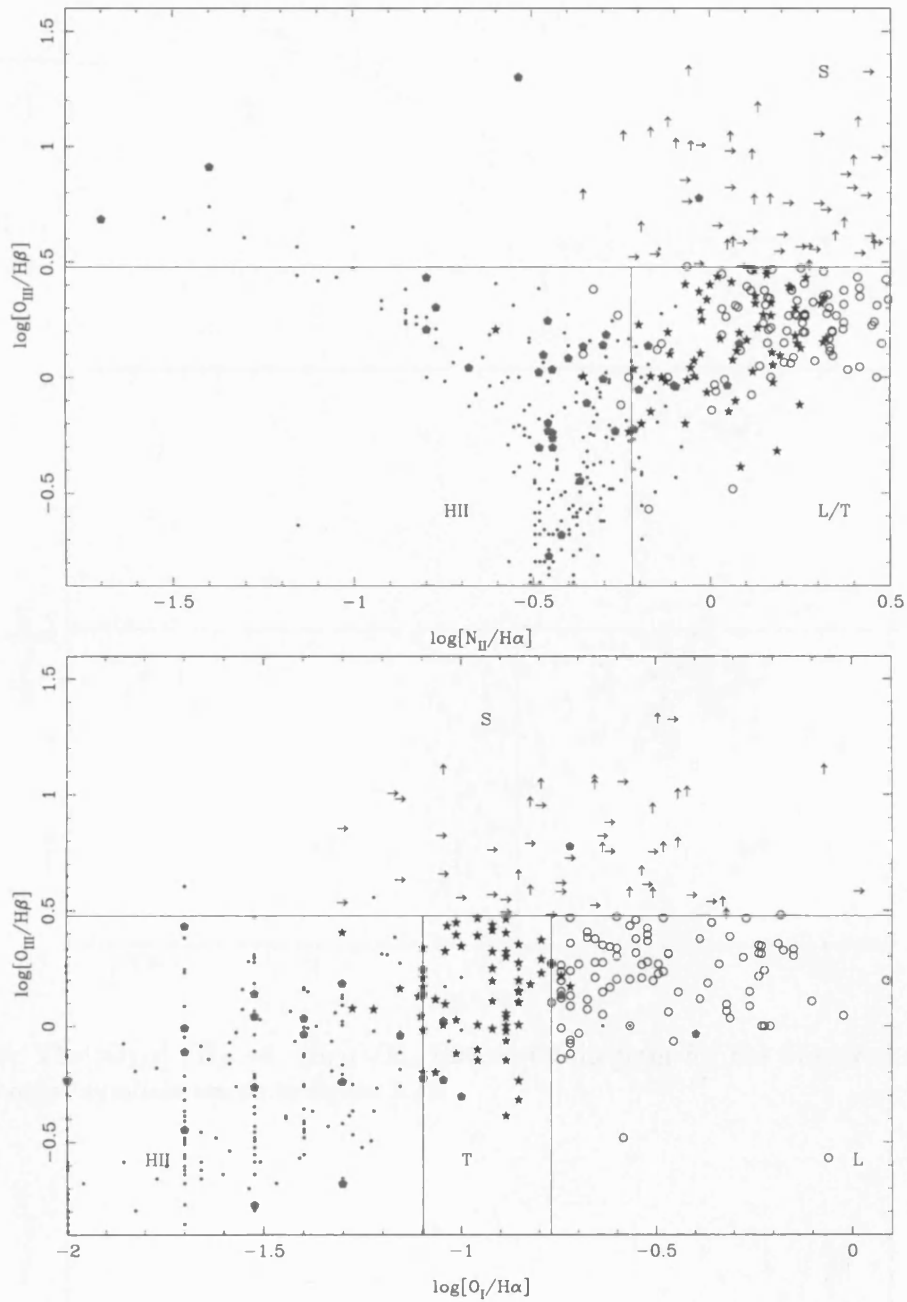


Figure 2.15: The $[\text{O}_{III}]/\text{H}\beta$ vs. $[\text{N}_{II}]/\text{H}\alpha$ and $[\text{O}_{III}]/\text{H}\beta$ vs. $[\text{O}_I]/\text{H}\alpha$ diagnostic diagrams for the observed objects (red dots). The objects from the sample of Ho *et al.* have been plotted as well (dots: H II galaxies, stars: transition objects, circles: LINERS, right arrows Sy2s, up arrows Sy1s).

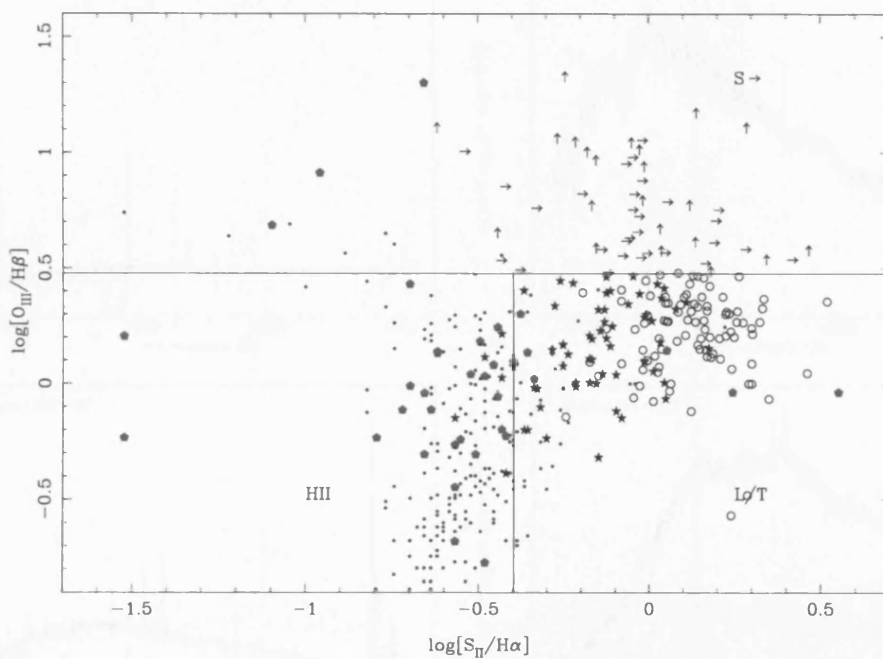


Figure 2.16: The $[O_{III}]/H\beta$ vs. $[S_{II}]/H\alpha$ diagnostic diagram for the observed objects (red dots). The other symbols are as in figure 2.15

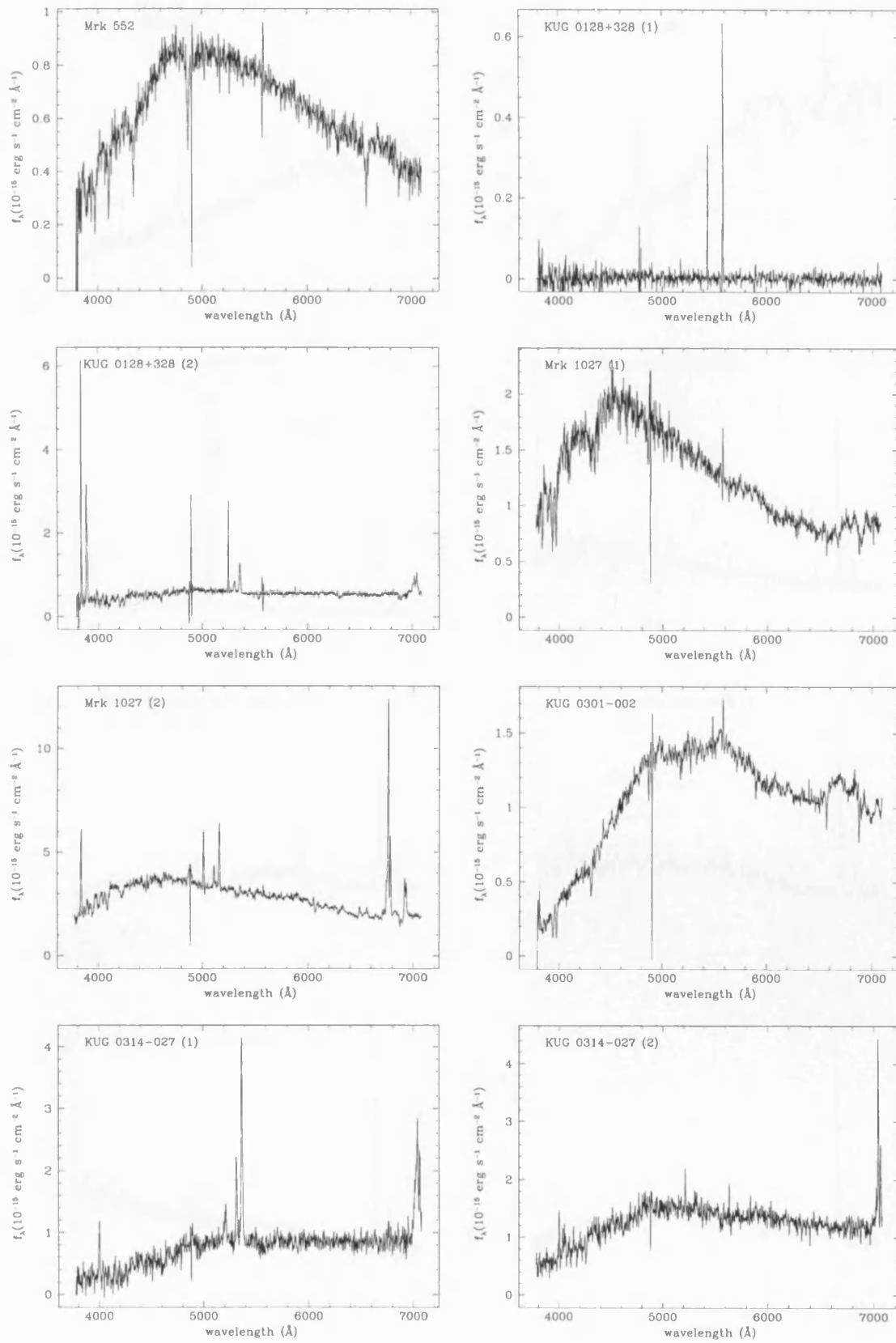


Figure 2.17: The optical spectra of the observed objects (North)

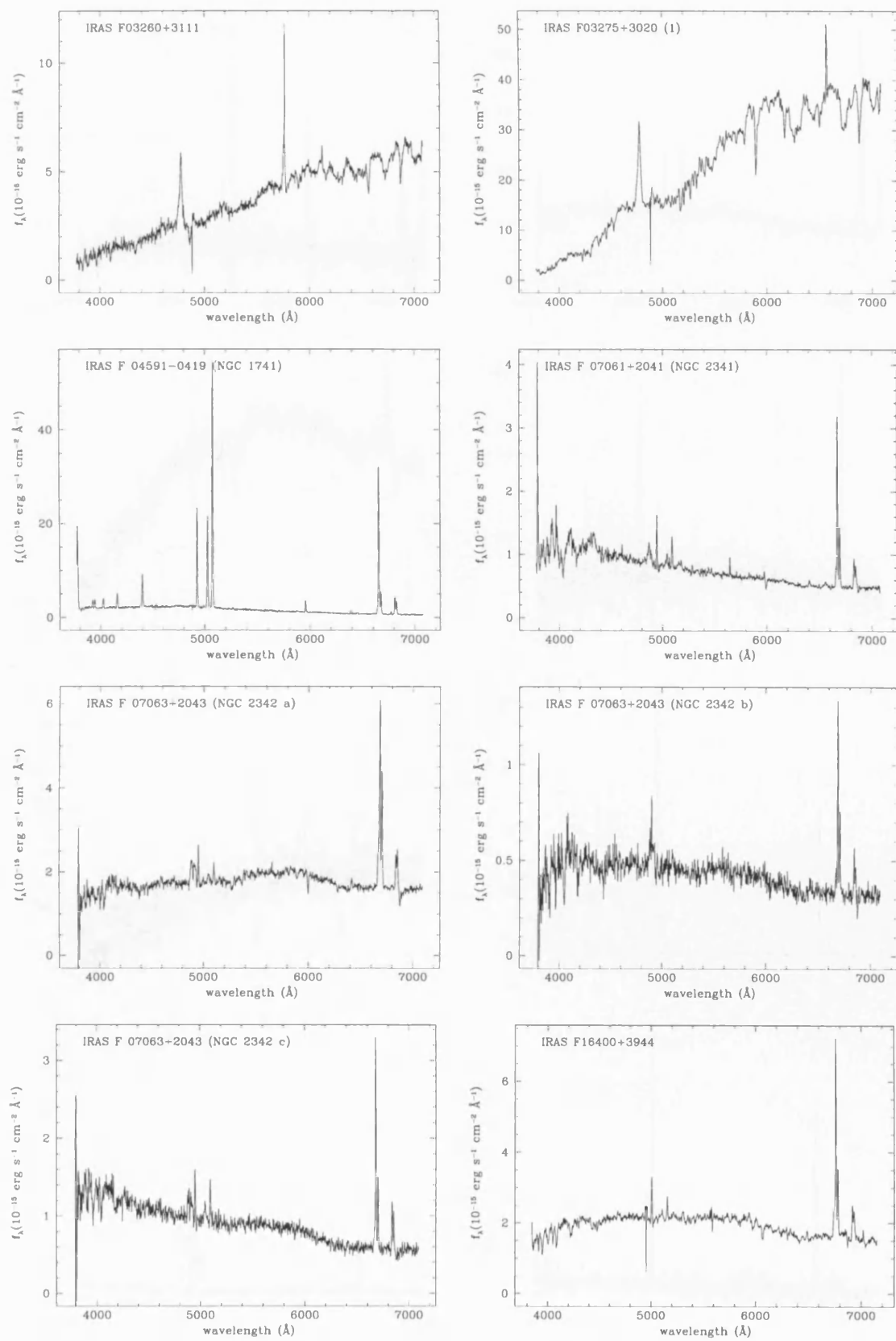


Figure 2.17: The optical spectra of the observed objects (North)*continued*

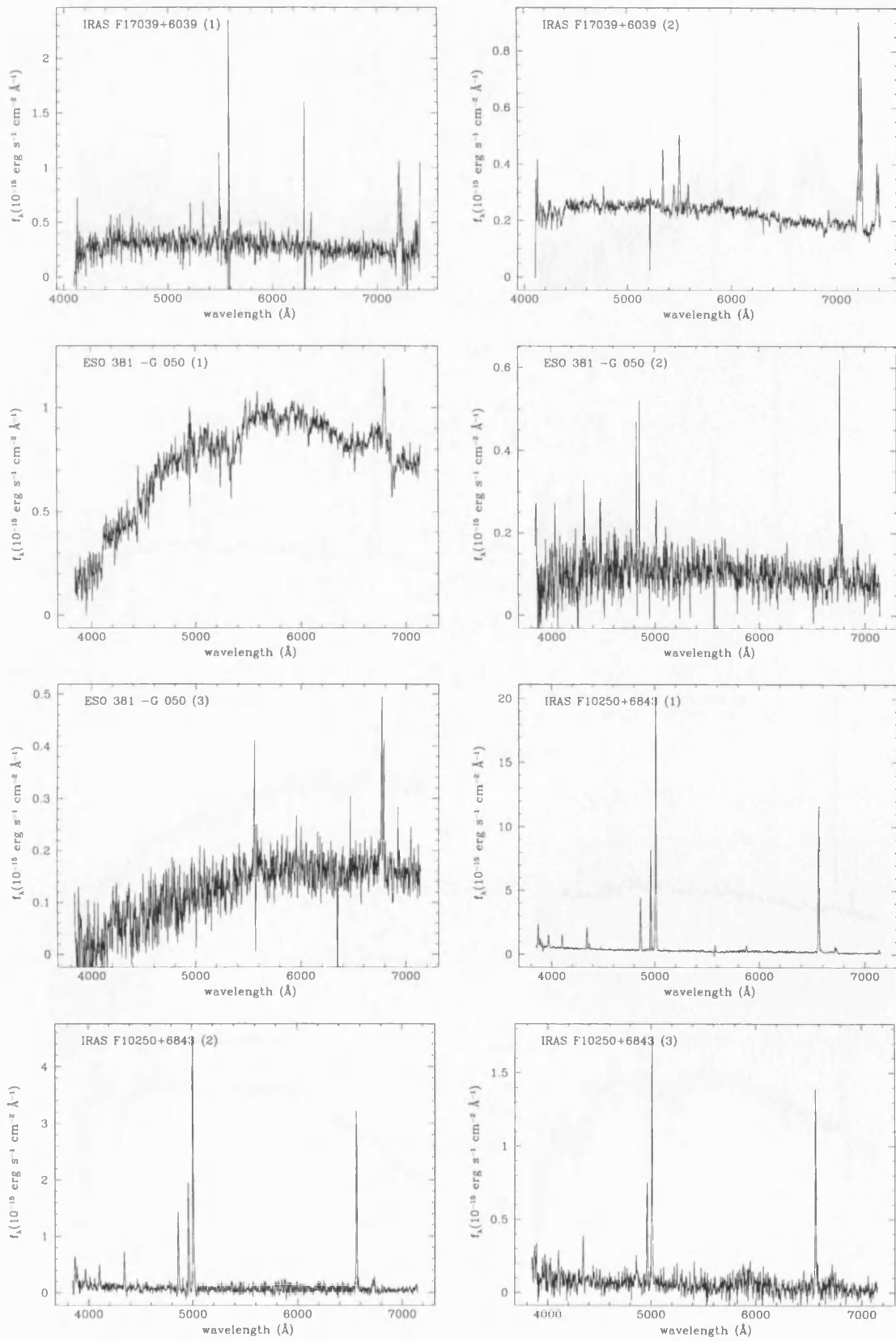


Figure 2.17: The optical spectra of the observed objects (North) *continued*

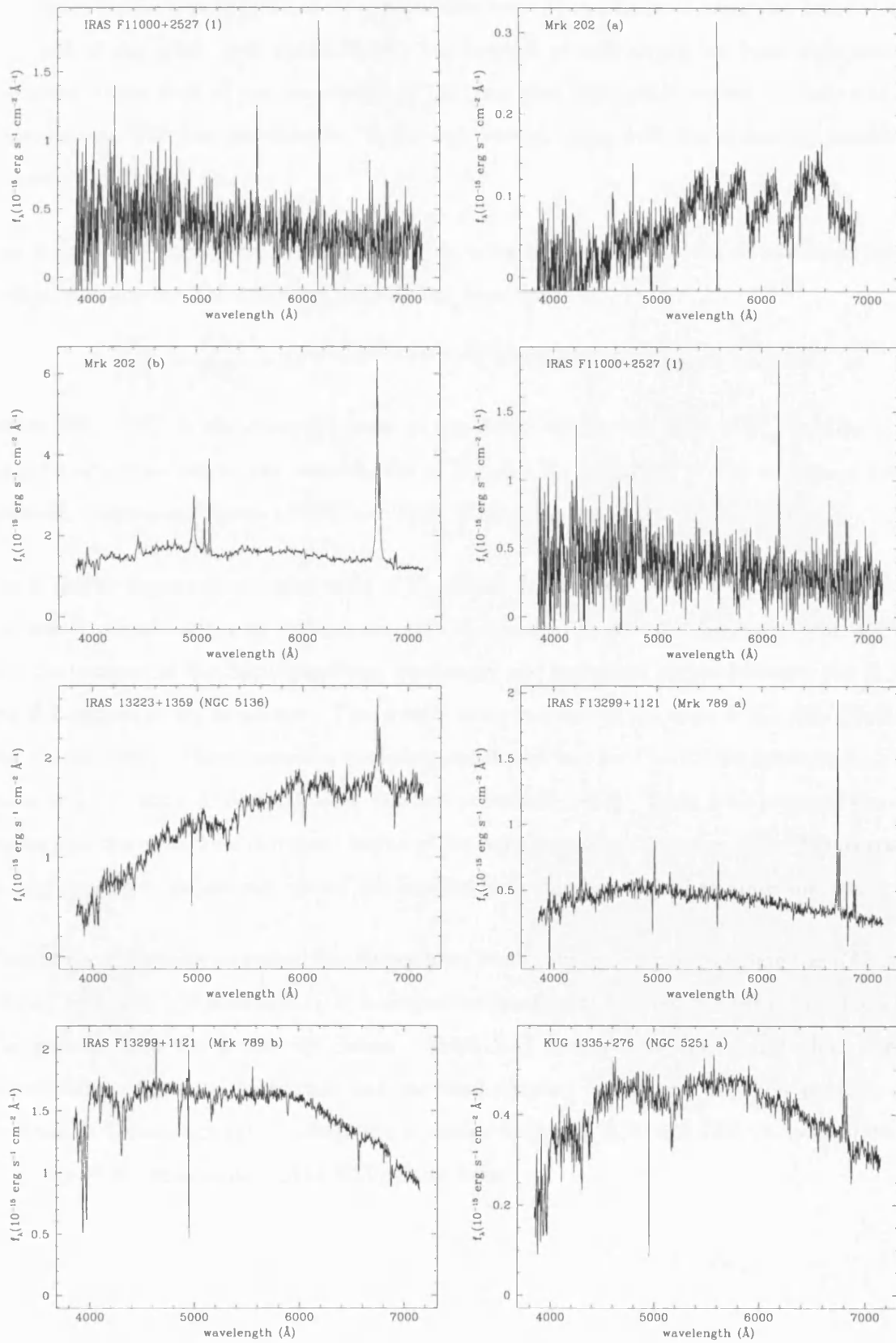


Figure 2.17: The optical spectra of the observed objects (North) *continued*

The emission line wavelengths, fluxes and widths have been measured using the line deconvolution task of the *splot* tool within IRAF. The redshift of each object has been estimated from the mean of the shift of the wavelength of the measured lines, with respect to their rest frame wavelengths. The line wavelengths, fluxes and widths, along with the estimated redshifts are presented in Table 2.10

The fluxes have been corrected for reddening using an extinction estimate obtained from the Balmer decrement. The following formula has been used:

$$\frac{IH_{\alpha}}{IH_{\beta}} = \frac{FH_{\alpha}}{FH_{\beta}} \times 10^{-\frac{E(B-V)}{0.77}[A(H_{\alpha})-A(H_{\beta})]} \quad (\text{Veilleux \& Osterbrock 1987}) \quad (2.1)$$

where FH_{α} / FH_{β} is the observed ratio of the fluxes of the two lines, $A(H_{\alpha}) - A(H_{\beta})$ is the interstellar extinction at the wavelengths of H_{α} and H_{β} according to the extinction curve of Cardelli, Clayton & Mathis (1989), and $I(H_{\alpha}) / I(H_{\beta})$ is the intrinsic flux ratio.

For H II type objects an intrinsic ratio of $H_{\alpha} / H_{\beta} \simeq 2.7$ has been used. This ratio is appropriate for case-B recombination in H II regions with $T \sim 10,000$ K and $n_e \sim 10^2 \text{ cm}^{-3}$. For AGN-type objects because of the harder ionising continuum the transition region between the H II and the H I regions is not as narrow. This results in an increase of the ratio of H_{α} / H_{β} (Veilleux & Osterbrock 1987). Photoionisation modeling has shown that for $\Gamma \sim 1.8$ the intrinsic H_{α} / H_{β} ratio is ~ 3.1 (Netzer & Ferland 1984, Gaskell & Ferland 1984). Table 2.10 presents the colour excess and the extinction corrected fluxes of the most important emission lines. The corrections is only applied to reddening correct the line fluxes for the high signal to noise spectra.

Finally the extinction corrected line fluxes have been used in order to calculate the $[OIII]/H\beta$, $[NII]/H\alpha$, $[SII]/H\alpha$ and $[OI]/H\alpha$ diagnostic line ratios. We then use these ratios to classify the galaxies into the 4 activity classes. Table 2.11 presents the line ratios along with the classifications based on each ratio and the final adopted classification. Their position in the Veilleux & Osterbrock (1987) diagrams is shown in figures 2.15 and 2.16. It is clear that the majority of the objects lie on the H II galaxy locus.

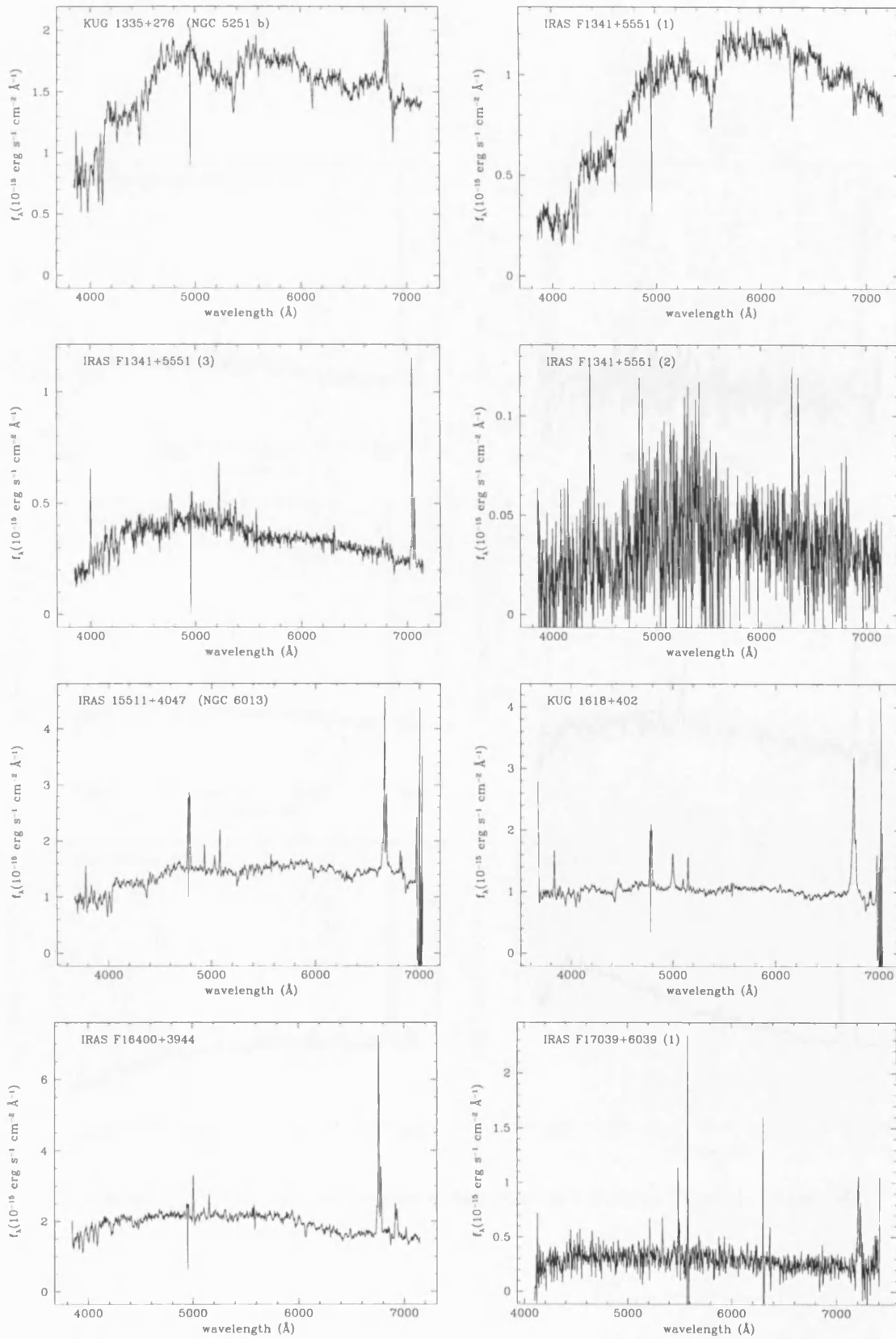


Figure 2.17: The optical spectra of the observed objects (North) *continued*

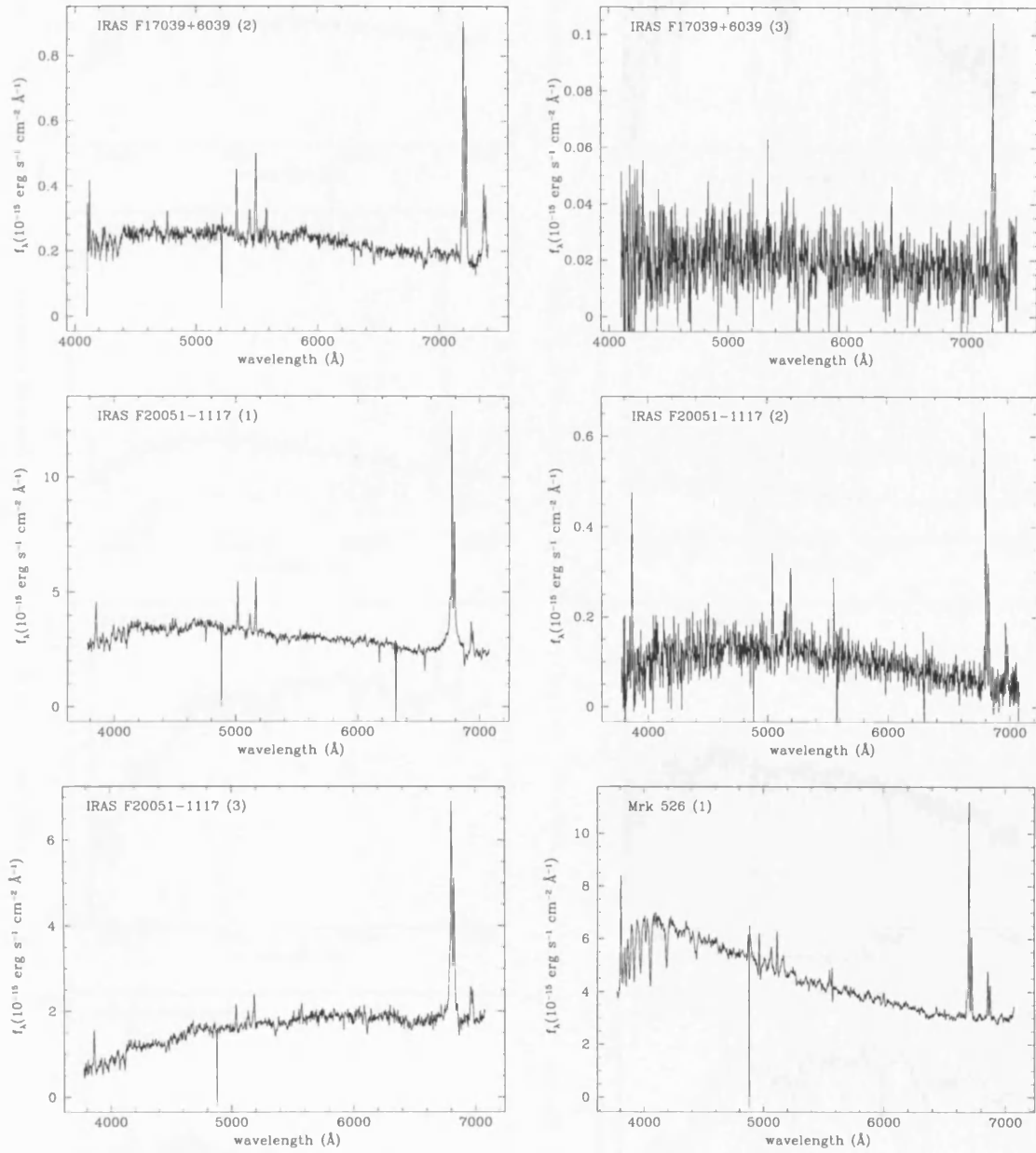


Figure 2.17: The optical spectra of the observed objects (North) *continued*

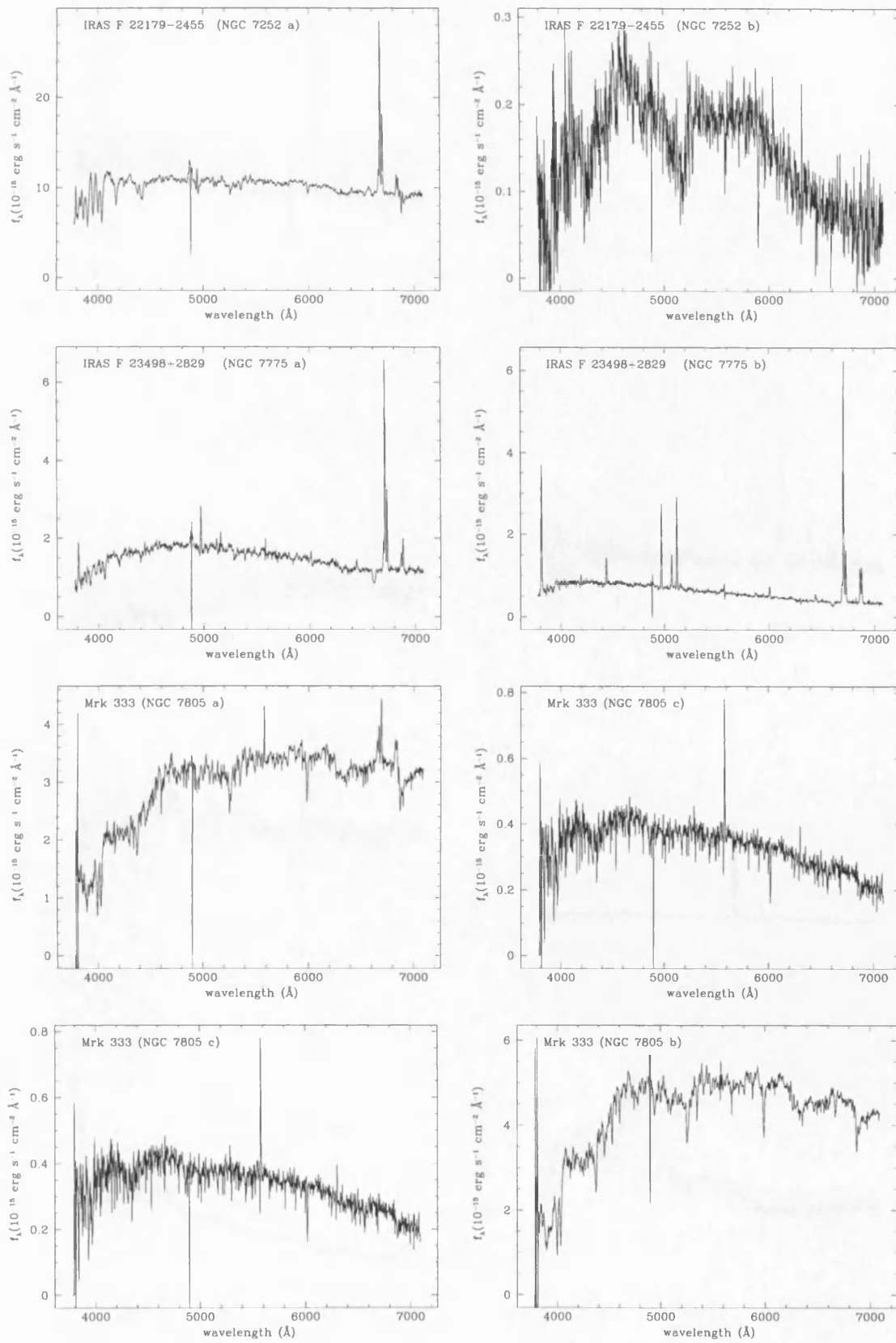


Figure 2.17: The optical spectra of the observed objects (North) *continued*

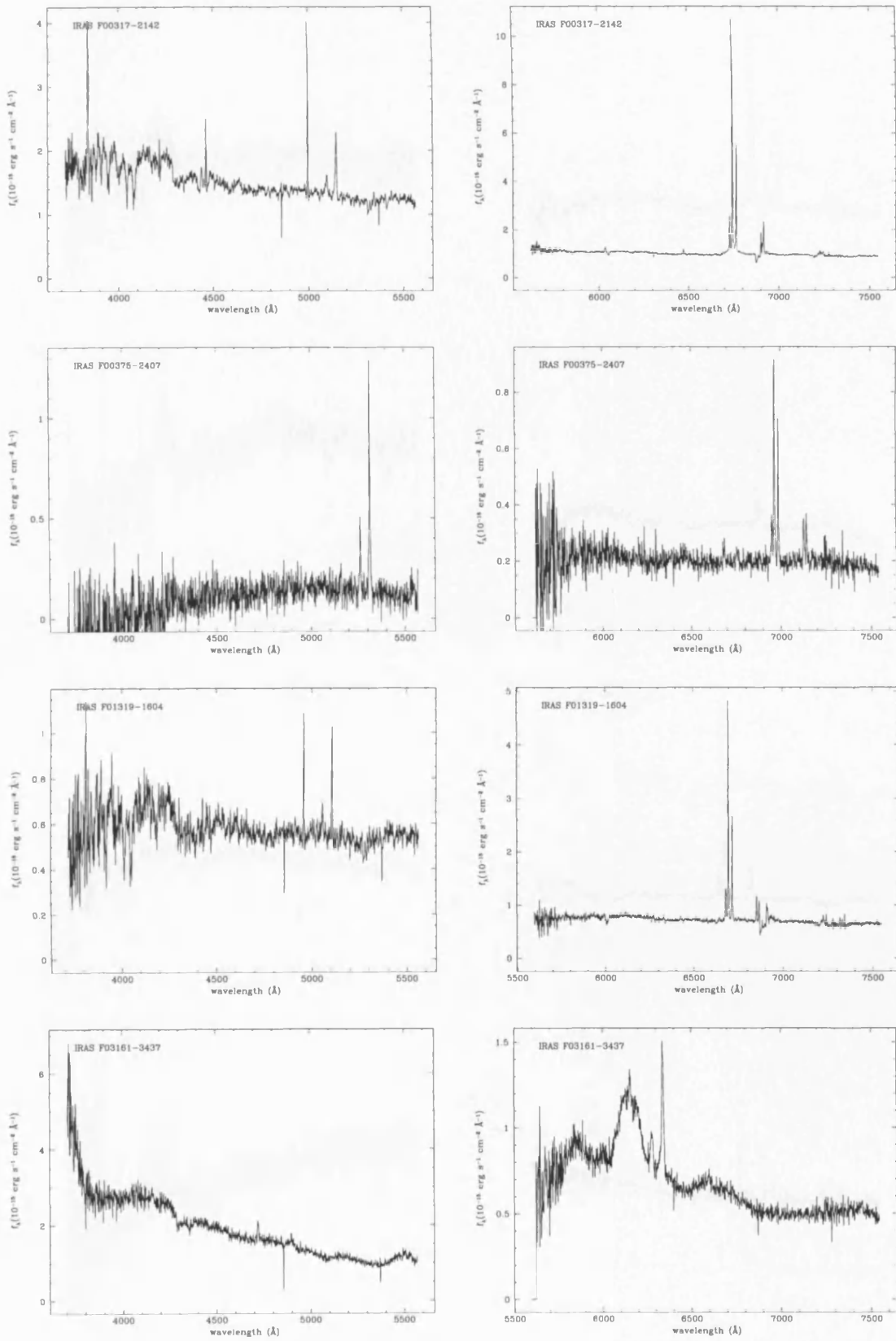


Figure 2.17: The optical spectra of the observed objects (South) *continued*

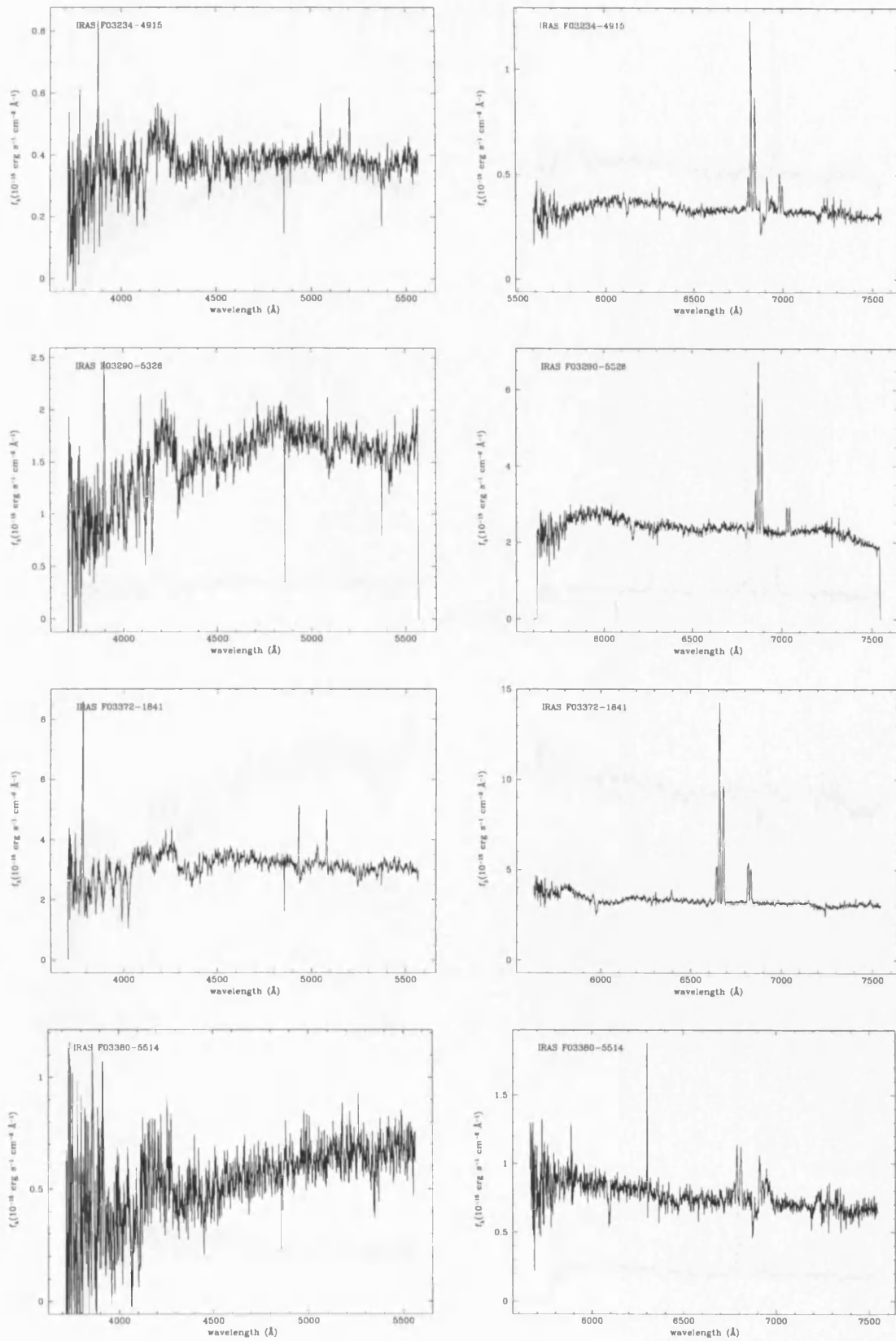


Figure 2.17: The optical spectra of the observed objects (South) *continued*

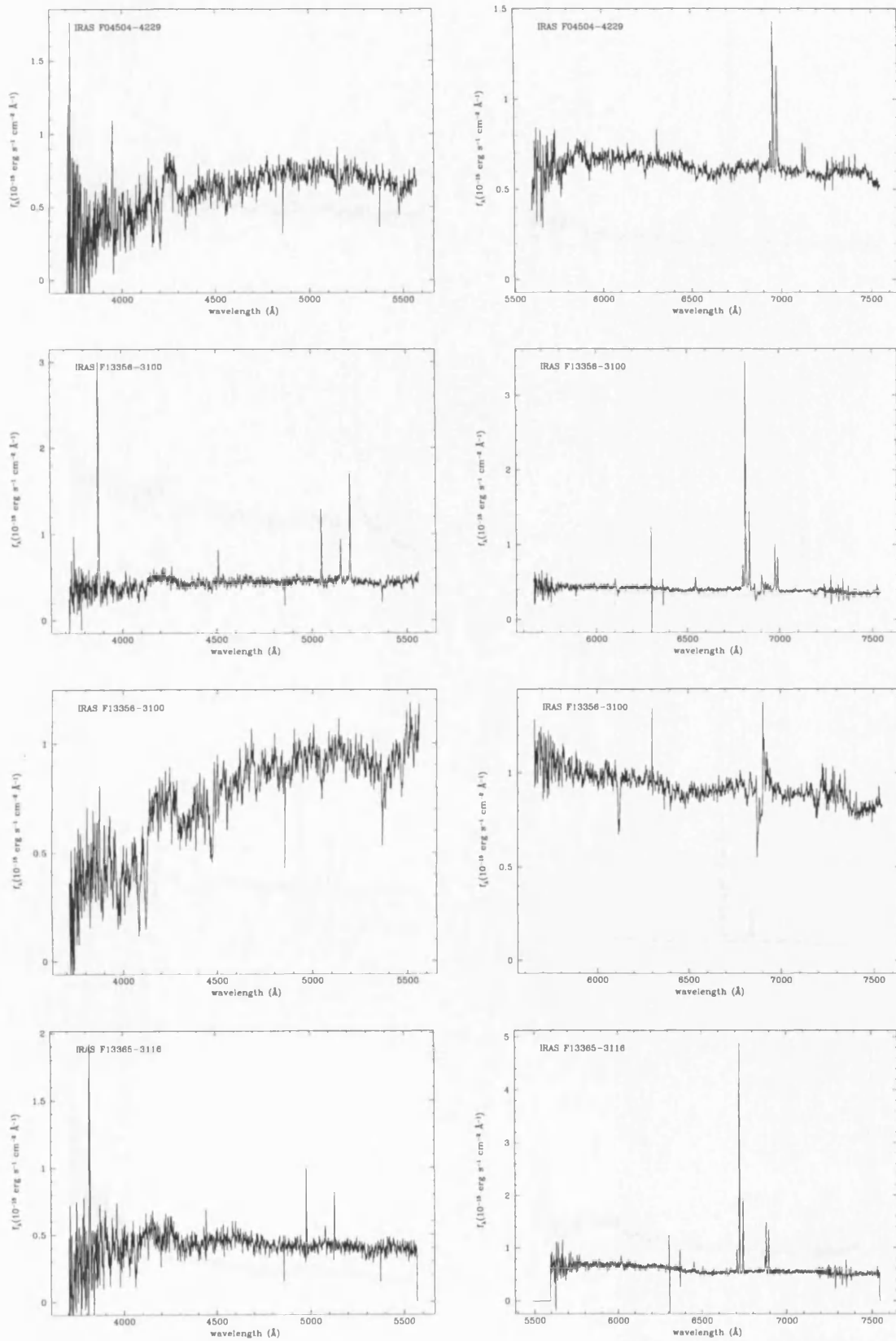


Figure 2.17: The optical spectra of the observed objects (South) *continued*

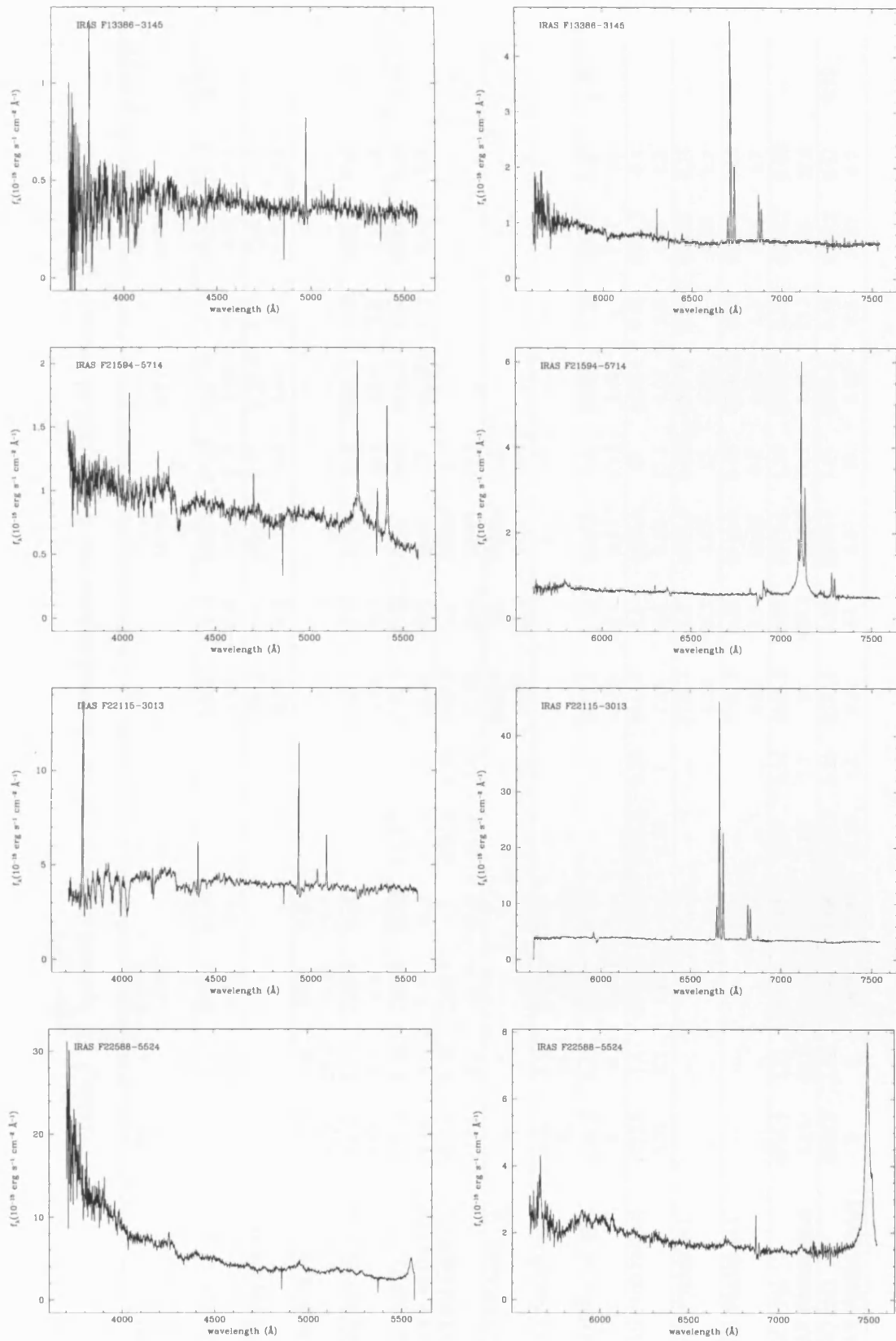


Figure 2.17: The optical spectra of the observed objects (South) *continued*

Table 2.10: Spectral properties of the observed objects which show optical emission lines

Name	H_{β}		[OIII] $\lambda 5007$		[OI] $\lambda 6300$		H_{α}	[NII] $\lambda 6583$		[SII] $\lambda 6716$		[SII] $\lambda 6731$		E(B-V)	
(1)	(2)	(3)	(4)	(5)	(6)	(7)	(8)	(9)	(10)	(11)	(12)	(13)	(14)	(15)	(16)
IRAS F00317-2142	4934.3	41.15	5082.1	14.73	6661	117.69	6682.2	50.27	6817.9	17.33	6832.6	15.02	0.76
	3.73	9.6	4.38	3.5	4.44	52.9	4.32	21.9	4.68	8.5	4.52	7.1	
IRAS F00375-2407	6966.2	0.47	6988.3	0.26	7129.6	0.11	7145	0.1	...
	6.29	22.6	5.16	12.4	6.81	5.6	5.58	4.9	
KUG 0128+328	5251.2	1.3	5358	0.98
	4.78	22.2	13.14	16.7
IRAS F01319-1604	4959	8.12	5107.1	8.02	6694.8	23.22	6716	11.5	6852.2	2.73	6866.4	1.92	1.07
	3.68	4.4	4.8	5	4.19	25.1	4.61	12.5	4.54	3.5	3.71	2.4	
Mkn 1027 (2)	5007.4	9.26	5157.3	10.06	6489.7	1.13	6759.9	26.49	6781	9.46	6918.5	4.96	6933.4	3.66	0.34
IRAS F 02114+0456	9.19	9.4	9.76	10.2	10.22	2.5	10.42	60.5	10.25	22	10.98	12.4	9.87	8.9	
KUG 0314-027 (1)	5211.6	0.78	5368.4	4.7	6759.9	0.29	7037.9	1.5	7059.7	1.4
	17.13	8.2	13.17	51.5	10.15	3.4	11.99	15.4	10.59	13.9
KUG 0314-027 (2)	7040.5	2.9	7062.6	1.3
	8.28	23.8	9.31	10.9
IRAS F03161-3437	6151	6.1	6339.9	0.95
	125	81	12.14	13.6
IRAS F03234-4915	5049.3	0.46	5200.7	0.41	6818.1	1.44	6839.8	0.9	6978.2	0.29	6993.1	0.23	0.36
	6	4	5.52	3.6	6.32	18.8	6.57	11.9	6.46	4	6.84	3.1	
IRAS F03372-1841	4932.8	1.4	5079.7	1.3	6393.9	0.34	6644.7	1.6	6659.8	10	6813.4	0.85	6832.3	0.9	
	5.33	5.1	6.02	4.2	6.59	1	7.35	4.8	8.58	31.1	4.04	2.6	4.63	2.8	
IRAS F03380-551	6788.3	1.3	6809.8	0.61	6947.6	0.22	6962.5	0.15	...
	4.22	24.7	4.67	12	4.23	4	4.32	2.7	
IRAS F03380-551	6789.3	0.28	6810.2	0.42	6884.3	0.08	6910.3	0.32	...
	6.63	3.9	10.26	6.1	5.59	1.3	8.44	4.7	
NGC 1741	4928.9	2.81	5076.4	7.65	6387	0.14	6653.2	8.03	6673.4	1.25	6808.5	0.96	6823.2	0.66	...
IRAS F04591-0416	9.12	94.2	9.01	240.9	8.29	7.7	9	457.4	10.04	71.2	8.97	51.7	8.56	37.6	
NGC 2341	4945.3	1.85	5093	1.08	6408.5	0.26	6675.4	5.29	6696.4	1.91	6831.3	0.81	6846.2	0.67	0.29
IRAS F07061+2041	8	9	8.2	5.2	14.23	2.5	8.74	54	9.47	20	8.78	8.2	10.57	6.7	

Table 2.10: Spectral properties of the observed objects *continued*

Name (1)	H β (2)	(3)	[OIII] (4)	(5)	[OI] (6)	(7)	H α (8)	(9)	[NII] (10)	(11)	[SII] (12)	(13)	[SII] (14)	(15)	E(B-V) (16)
NGC 2342 (1)	4950.3	8.12	5098.5	4.85	6414.2	1.99	6681.9	25.16	6702.9	15.39	6837.9	4.44	6852.8	5.06	0.68
IRAS F07063+2043	8.14	5.1	11.54	3.2	14.88	2.4	10.87	31.5	10.88	19.2	10.34	6	10.53	6.8	
NGC 2342 (2)	6686.4	0.85	6707.3	0.42	6843.4	0.2	6856.5	0.17	...
IRAS F07063+2043	7.73	25.4	9.43	12.3	7.27	6.1	9.22	5.3	
NGC 2342 (3)	4949.8	2.98	5096	3.75	6679.8	9.24	6701	3.18	6835.7	2.09	6851.1	1.61	0.54
IRAS F07063+2043	6.66	5.1	10.37	7.3	8.53	45.7	8.31	15.8	8.22	11	8.26	8.6	
ESO 381-G 050 (1)	6795.5	0.27	6805.4	0.26
	6.19	3.3	8.5	3.2
ESO 381-G 050 (2)	6767	0.46	6788	0.1	6926.2	0.07	6938.9	0.07	...
	7.79	46.4	6.74	9.9	7.42	12.1	7.17	10.6	
ESO 381-G 050 (3)	6766.4	0.28	6786.9	0.18	6924.2	0.07	6938.9	0.02	...
	8.62	16.2	6.98	10.7	4.16	4.4	2.72	1.6	
IRAS F10250+6843 (1)	4862.9	3.9	5008.4	19	6564.6	11	6586.1	0.17	6719.2	0.48	6732.8	0.36	...
	8.48	107.2	8.48	481.6	8.22	442.4	7.68	7.4	8.9	29.7	8.78	22.3	
IRAS F10250+6843 (2)	5008.4	41.22	6565	14.34	6583.6	0.61	6719.4	1.03	6733.8	0.53	0.7
	8.62	552.7	8.18	469.3	5.98	23.8	12.83	31	4.81	14.9	
IRAS F10250+6843 (3)	4858.8	27.5	5009.4	554.26	6566	78.64	6585.3	22.51	6719	10.11	6734.3	6.87	1.83
	4.08	5	9.25	200.7	7.89	409	32.6	70.6	8.42	165.4	7.81	128.4	
IRAS F11000+2527	5151.6	2.37	5308.2	2.5	6677	0.61	6955.1	6.76	6976.9	2.25	7116.4	1.91	7131.7	1.19	0.2
	8.29	11	4	9.8	8.61	5.2	7.87	55.5	7.38	17.9	9.66	19.2	7.2	12.8	
Mrk 202	4970.8	2.4	5122.1	2.2	6447.9	0.25	6716.1	3.5	6736.3	2.8	6874.1	0.28	6887.3	0.5	...
	22.9	14	8.4	14.1	17.56	1.9	9.55	23.4	12.31	18.3	7.1	2.5	9.62	4.4	
NGC 5136	6709.2	0.98	6730.8	0.51
IRAS F13223+1400	12.56	5.3	10.23	2.8	
Mrk 798	6441.8	0.05	6711.8	1.4	6733.1	0.44	6868.3	0.25	6883.4	0.15	...
IRAS 13299+1121	7.34	1.4	7.29	40.3	8.17	13.5	7.33	8.4	5.63	5.3	
NGC 5251 (1)	6808.2	0.19	6830.3	0.11
IRAS F 13351+2740	7.91	5.7	9.21	3.3	
NGC 5251 (2)	6804.8	0.59	6826.2	0.54	6966.1	0.31
IRAS F 13351+2740	9.69	3.8	9.72	3.5	17.85	2.2	

Table 2.10: Spectral properties of the observed objects *continued*

Name (1)	H β (2)	(3)	[OIII] (4)	(5)	[OI] (6)	(7)	H α (8)	(9)	[NII] (10)	(11)	[SII] (12)	(13)	[SII] (14)	(15)	E(B-V) (16)
IRAS F13356-310	4934.2 7.6	5.43 3.2	5081.9 7.87	7.46 4.8	6404 29.01	2.82 3.3	6661.9 8.37	15.52 17.3	6682.7 8.81	6.85 7.9	6817.5 7.87	2.08 2.7	6832.8 8.01	1.69 2.3	0.75
IRAS F13365-3116	4977.8 2.39	5.19 4.8	5127.6 2.8	3.3 3.2	6721.5 2.98	14.84 26.4	6742.6 3.21	5.25 9.4	6878.4 2.57	2.77 4.7	6893.2 3.2	2.66 4.6	1.01
IRAS F13386-3145	4971.7 3.16	21.46 6.6	5120.7 3.54	3.68 1.1	6712.6 4.97	61.37 36	6733.8 5.01	21.35 12.9	6869.6 5.42	12.14 7.5	6884.5 5.26	8.42 5.2	1.41
IRAS F13414+5551 (1)	5220.4 8.09	0.64 6	5374.9 13.05	0.37 3.7	6762.2 12.46	0.16 2.6	7046.8 8.99	1.82 39.4	7068.7 9.42	0.63 13.9	7142.5 0.63	...	0.31
NGC 6013	4934.2	5.43	5081.9	7.46	6404	2.82	6661.9	15.52	6682.7	6.85	6817.5	2.08	6832.8	1.69	0.75
IRAS F15511+4047	7.6	3.2	7.87	4.8	29.01	3.3	8.37	17.3	8.81	7.9	7.87	2.7	8.01	2.3	
KUG 1618+402	4998.7 17.46	0.96 8.1	5148.3 8.48	0.57 5.1	6478.1 3.52	0.03 -0.3	6749.4 12.81	2.73 24.4	6767.7 15.93	1.47 12.9	6906.9 9.57	0.24 2.8	6920.7 8.19	0.2 2.3	0.02
IRAS F1618+410	5042.8 23.81	1.4 16.9	5194.7 10.09	1.3 17.3	6538.9 23.56	0.13 1.8	6808.4 18.01	3.3 44.9	6827.1 31.56	2.6 36.2
KUG 1618+410	5043.7 18.67	0.9 5	5196.2 9.4	1.46 8.4	6811 17.58	2.58 21.2	6833.6 6.34	0.42 3.4	6969.1 9.61	0.12 1.1	0.29
IRAS F16400+3944	5006.4 8.1	9.63 5.7	5156.4 9.33	4.84 2.8	6758.7 10.09	27.54 36.5	6779.5 10.42	10.04 13.1	6916.3 9.37	4.22 6.2	6931.7 12.67	4.37 6.6	0.65
IRAS F16419+8213	5055.1 7.13	3.92 7.8	5207.3 6.35	1.96 4	6558.4 26.66	1.16 5	6825.7 9.04	11.21 50.1	6847.3 10.82	3.71 18.4	6985.4 10.59	1.36 6.9	7000.6 10.76	1.12 5.7	0.78
IRAS F17038+6038 (1)	5337.6 10.69	0.27 11.4	5497.5 13.2	0.38 16.6	7201 5.88	0.38 12.5	7207.6 5.91	0.46 14.9	7226.6 8.11	0.43 13.8
IRAS F17038+6038 (2)	5337.6 10.69	0.43 11.4	5497.5 13.2	0.59 16.6	6918.5 14.09	0.1 4	7205.1 11.62	1.33 57.1	7227.5 11.01	0.88 38.7	7373 11.76	0.34 13.6	7389.5 8.71	0.25 9.6	0.14

Table 2.10: Spectral properties of the observed objects *continued*

Name (1)	H β (2)	(3)	[OIII] (4)	(5)	[OI] (6)	(7)	H α (8)	(9)	[NII] (10)	(11)	[SII] (12)	(13)	[SII] (14)	(15)	E(B-V) (16)
IRAS F20051-1117	5014.5 7.05	7 4.6	5163.2 9.91	10.76 8.1	6497.5 9.72	1.07 1.5	6768.4 7.78	20.02 26.5	6789.7 8.12	10.11 13.5	6927.1 9.35	3.83 5.8	6942 9.57	2.62 4.2	0.44
IRAS F20069+5929 (1)	5040.1 9.42	0.23 22.6	5191.8 8.51	0.18 13.9	6806.1 8.63	0.58 138.7	6827.8 7.75	0.26 70	6965.8 5.46	0.09 17.3	6980.8 4.29	0.04 7.9	...
IRAS F20069+5929 (2)	5040.2 9.59	288.8 23.9	5191.6 8.43	... 13.7	6533.8 23.6	75.19 2.3	6804.4 11.03	825.93 26.6	6825.1 11.9	574.67 18.6	6963.6 12.3	155.94 6.6	6978.3 11.01	102.49 4.6	2.15
IRAS F22115-3013	5049.4 3.41	0.59 7.4	5200.4 4.33	1.05 12.4	6544.7 4.31	0.13 2.1	6817.3 3.52	1.7 24.1	6838.7 3.65	0.6 8.6	6977 4.26	0.38 6.2	6991.9 3.34	0.23 3.7	0.19
Mkn 526	4965.3 6.63	21.3 2.2	5114.1 8.49	25.96 3.2	6703.8 8.31	60.93 25.5	6725.1 8.61	24.66 10.3	6859.7 8.45	12.83 5.5	6877 7.92	8.26 3.8	0.89
NGC 7252	4942.9	94.17	6403.3	11.99	6670.8	269.32	6826.9	34.6	6841.4	28.84	1.16
IRAS F 22179-2455	7.11	2.1	10.48	18.7	9.05	9.4	9.19	2.7	8.45	2.3	
IRAS F23196+0805	5047.9 3.47	3.37 15.7	5200.1 3.66	1.84 8.3	6544.1 4.03	0.32 2.4	6817.3 3.75	9.64 72.5	6838.7 3.73	3.51 26.9	6976.9 3.9	1.53 12.3	6991.8 4	1.07 8.5	0.26
IRAS F23309-0215	5262 3.79	1.98 5.1	5419.1 6.32	2.74 10	7116.2 4.2	5.66 32.1	7138.5 4.64	2.82 16.4	7283.1 4.66	0.74 5.1	7298.7 4.69	0.63 4.4	0.45
NGC 7775 (1)	4971.1	4.25	5119.6	0.88	6441.4	0.64	6710.6	12.15	6731.7	4.6	6865.2	1.35	6882.8	1.89	0.38
IRAS F 23498+2829	8.55	7.6	7.77	1.5	12.04	2.1	8.16	41.4	8.32	15.7	11.45	4.8	8.24	6.8	
NGC 7775 (2)	4970.2	1.64	5118.9	1.82	6441.9	0.15	6709.6	4.69	6730.8	0.99	6866.2	0.73	6881.6	0.68	...
IRAS F 23498+2829	8.24	27.1	8.4	29.7	9.4	4.2	8.32	133.2	8.06	27.8	8.59	22.1	7.97	21.1	
NGC 7805	6667.7	0.63	6688.9	1.2	6824	0.9	6839.1	0.48	...
IRAS F 23589+3109	8.26	1.9	9.76	3.7	16.41	2.8	8.54	1.5	

Notes: (1) Name of the object, (2) Observed wavelength and FWHM of H β in Å, (3) Flux and equivalent width of H β in 10^{-14} erg cm $^{-2}$ s $^{-1}$ and Å respectively, (4) Observed wavelength and FWHM of [OIII] λ 5007, (5) Flux and equivalent width of [OIII] λ 5007, (6) Observed wavelength and FWHM of [OI] λ 6300, (7) Flux and equivalent width of [OI] λ 6300 (8) Observed wavelength and FWHM of H α , (9) Flux and equivalent width of H α , (10) Observed wavelength and FWHM of [NII] λ 6583, (11) Flux and equivalent width of [NII] λ 6583, (12) Observed wavelength and FWHM of [SII] λ 6716, (13) Flux and equivalent width of [SII] λ 6716, (14) Observed wavelength and FWHM of [SII] λ 6731, (15) Flux and equivalent width of [SII] λ 6731, (16) Colour excess E(B-V)

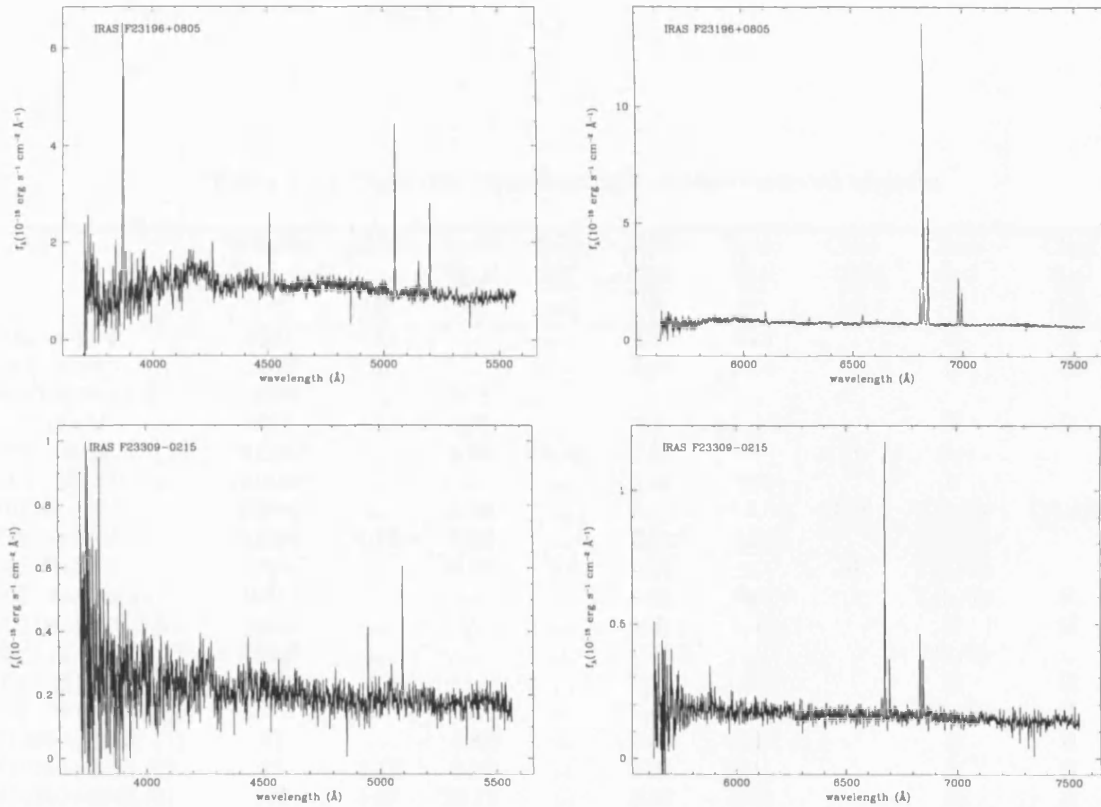


Figure 2.17: The optical spectra of the observed objects (South) *continued*

2.4 The X-ray luminous star-forming galaxies

2.4.1 Starformation Rate

The major objective of this project is to investigate whether the putative class of X-ray luminous starburst galaxies, which have X-ray luminosities much larger (more than 10 to 100 times) than the average for normal/starburst galaxies, really exists. A second objective is to study the origin of their powerful X-ray emission. In Table 2.12 the X-ray luminosities for all the star-forming galaxies in this sample which are detected by IRAS, are presented. It is clear that a significant number have X-ray luminosities above 10^{41} erg s $^{-1}$ in the 0.5-2.5 keV band (as is also clear from figures 2.3 to 2.14). The spectroscopic results suggest that the energy output of these galaxies is produced by a vigorous starburst. Next, these results will be used together with other properties of the galaxies in order to attempt to understand the origin of their powerful X-ray emission.

Using the calibration of Kennicutt (1998*b*), it is possible to estimate the SFR from the total

Table 2.11: Spectral classifications of the observed objects

Name	Velocity	(B-V)	Ratio	Ratio	Ratio	Ratio	Class	Class	Class	Adopted
(1)	(2)	(3)	$\frac{[OIII]}{H\beta}$	$\frac{[OI]}{H\alpha}$	$\frac{[NII]}{H\alpha}$	$\frac{[SII]}{H\alpha}$	$\frac{[OI]}{H\alpha}$	$\frac{[NII]}{H\alpha}$	$\frac{[SII]}{H\alpha}$	class
			(4)	(5)	(6)	(7)	(8)	(9)	(10)	(11)
F00317-2142	8231	1.11	0.45	0.19		H	H	H
F00375-2407	18457	0.55	0.44	H	H	H	H
KUG 0128+328	22556	...	0.75				
F01319-1604	6032	3.32	0.99	...	0.5	0.2 0.22		H	H	H
KUG 0314-027 (1)	21725	...	6.03	0.19	0.93	0	Sy	Sy		Sy
KUG 0314-027 (2)	21842	0.45	0		H		H
F03161-3437	78530	...	0.16	L/S	T/L/Sy	T/L/Sy	Sy
F03234-4915	11664	1.12	0.89	...	0.63	0.36		T/L/Sy		L/T
F03372-1841	5614	...	0.93	0.4	1.12	...	H	T/L/Sy		T/L/Sy
F03380-5514 (a)	10324	0.47	0.28		T/L/Sy	H	T
F03380-5514 (b)	9052	1.5	1.43		H	H	H
ESO 381-G 050 (1)	12785	0.96	...		T/L/Sy	...	T/L/Sy
ESO 381-G 050 (2)	9331	0.22	0.3		H	H	H
ESO 381-G 050 (3)	9289	0.64	0.33		T/L/Sy	H	T:
F10250+6843 [†] (1)	91	...	4.87	...	0.02	0.08		H	H	H
F10250+6843 (2)	98	2.17	8.22	...	0.04	0.11		H	H	H
F10250+6843 (3)	133	5.67	20.16	...	0.29	0.22		H	H	H
F11000+2527 (2)	17936	0.63	1.06	0.09	0.33	0.46	L/T	H	T/L	T/L
F13356-3100	11633	0.58	1.77	0.08	0.35	0.36	H	H	H	H:
F13365-3116	7239	3.13	0.64	...	0.35	0.37		T/L/Sy	T/L/Sy	Sy
F13386-3145	6839	4.36	0.17	0.03	0.35	0.33		H	H	H
F13414+5551 (3)	22096	0.95	0.59	0.09	0.35	...	T/H	H		H:
KUG 1618+402	8481	0.07	0.59	0.01	0.54	0.16	H	H	H	H
KUG 1618+410	11237	...	0.93	0.04	0.79	...	H	H		H
KUG 1618+410	11180	0.91	1.62	...	0.16	...		H	H	H
F16400+3944	8953	2.02	0.5	...	0.36	0.31		H	H	H
F16419+8213	12055	2.43	0.5	0.1	0.33	0.22	T	H	H	H:
F17039+6039 (1)	27848	...	1.41	...	1.21	1.13		T/L	T/L	T/L
F17039+6039 (2)	29382	0.43	1.38	0.08	0.67	0.44	H	T/L	T/L	T/L
F20051-1117 (1)	9411	1.38	1.54	0.05	0.51	0.32	H	H	H	H
F20069+5929 (1)	11114	...	0.78	...	0.45	0.23		H	H	H
F20069+5929 (2)	11058	6.65	...	0.09	0.7	0.31	H	H	H	H
F21594-5714	25137	1.38	1.39	0.03	0.5	0.24	H	H	H	H
F22115-3013	4515	2.35	0.36	0.02	0.43	0.27	H	H	H	H
F23196+0805	11612	0.82	0.55	0.03	0.36	0.27	H	H	H	H
F23309-0215	5305	1.8	2.02	...	0.17	0.42		H	T/L/Sy	H:
Mrk 202 (b)	6961	...	0.92	0.07	0.8	0.22	H	T/L	H	H
Mrk 798 (a)	6798	0.04	0.31	0.29	H	H	H	H:
Mkn 1027 (2)	9023	1.05	1.09	0.04	0.36	0.33	H	H	H	H
Mkn 526	5527	2.76	1.22	...	0.4	0.35		H	H	H

[†] This is most probably a Galactic H II region.

Table 2.11: Spectral classifications of the observed objects *continued*

Name	Velocity	E(B-V)	Ratio $\frac{[O_{III}]}{H\beta}$	Ratio $\frac{[O_I]}{H\alpha}$	Ratio $\frac{[N_{II}]}{H\alpha}$	Ratio $\frac{[S_{II}]}{H\alpha}$	Class $\frac{[O_I]}{H\alpha}$	Class $\frac{[N_{II}]}{H\alpha}$	Class $\frac{[S_{II}]}{H\alpha}$	Adopted class
NGC 1741	4139	-1.88	2.72	0.02	0.16	0.2	H	H	H	H
NGC 2341	5159	0.89	0.58	0.05	0.36	0.28	H	H	H	H
NGC 2342	5458	2.09	0.6	0.08	0.61	0.38	H	T/L	T/L	T:
NGC 2342	5647	0.49	0.44		H	T/L/Sy	T:
NGC 2342	5372	1.68	1.26	...	0.34	0.4		H	T/L	T:
NGC 7805	4814	1.9	2.19		T/L/Sy	T/L/Sy	T:
NGC 5136	6709	0.52	0		H	H	H
NGC 5251 (a)	11217	0.58	0.26		H/Sy	...	H/Sy
NGC 5251 (b)	11104	0.92	0.69		T/L/Sy	T/L/Sy	T/L:
NGC 7252 (a)	4954	3.59	...	0.04	0.49	0.24	H	H	H	H:
NGC 7775 (a)	6747	1.18	0.21	0.05	0.38	0.27	H	H	H	H
NGC 7775 (b)	6723	-0.14	1.11	0.03	0.21	0.3	H	H	H	H
NGC 6013	4585	2.32	1.37	0.18	0.44	0.24	L/Sy	H	H	H

Notes: (1) Name, (2) Recessional velocity in Km/s, (3) Color excess, (4),(5),(6),(7) Line ratios from the reddening corrected line fluxes, (8),(9),(10) Classifications based on the line ratios, (11) Adopted classification

H_α luminosity of a galaxy:

$$SFR(M_\odot yr^{-1}) = 7.9 \times 10^{-42} \times L(H\alpha) \quad (2.2)$$

(where the H_α luminosity is in erg s^{-1}), for a Salpeter IMF with $M_{\text{up}} = 100 M_\odot$ and $M_{\text{low}} = 0.1 M_\odot$. However, one must keep in mind that the H_α luminosity used here is measured from a very small aperture, whereas the X-ray luminosity may represent the integrated emission of the galaxy. Also the reddening estimate may be an underestimate of the extinction, because of the small wavelength distance between H_α and H_β . For these reasons the derived SFRs should be regarded only as lower limits.

An alternative method to calculate the SFR is to use the total FIR luminosity of each galaxy. This method relies on the assumption that all the stellar radiation is absorbed by intervening dust in the galaxy and is then reradiated in the FIR band. As Devereux & Young (1990) and Devereux & Hameed (1997) showed the 40-120 μ emission of spiral galaxies is dominated by heating from young stars. However, there are a few caveats: the dust coverage may not be uniform, resulting in *leakage* of stellar radiation, or the dust may be mixed with the emitting gas as is described by Buat & Xu (1996). Finally the interstellar radiation field may significantly contribute to the heating of the dust as is the case in elliptical galaxies (Devereux & Hameed 1997). With these complications in mind we will use the FIR luminosity in order to estimate the SFR. The advantages of this method are that it is unaffected by aperture effects and measurements of the IRAS fluxes are available for all the galaxies in the sample.

In general the SFRs of the starforming galaxies in this sample are much higher than the Galactic value. However, they are not much higher than those observed in other nearby starburst galaxies eg, Kennicutt (1998*a*), with the exception of a few extreme cases where it exceeds $100 M_{\odot} yr^{-1}$, reaching the values estimated for high redshift starforming galaxies in the Hubble Deep Field. Their redshifts are moderate (velocities less than $10,000 \text{ km s}^{-1}$) suggesting that they are local examples of the high redshift objects. Figure 2.19 shows their position in the $L_X - L_{IR}$ diagram (red circles) compared with the position of the nearby starforming galaxies from the sample of Ho, Filippenko & Sargent (1997*a*) (asterisks) which are studied in the next chapter.

2.4.2 The origin of the X-rays

Imaging soft X-ray studies of nearby starburst and normal galaxies have shown that their soft X-ray emission is extended arising from a component of diffuse gas, often forming a spectacular superwind (e.g. Watson et al. 1984, Dahlem 1997). This outflow is driven by the effect of the multiple supernova explosions and the stellar winds of evolved massive stars which heat the ambient interstellar medium (Heckman et al. 1990). In the first instance an expanding superbubble forms filled by hot gas ($T \sim 10^{6-7} \text{ K}$). When the radius of the bubble is a few times the minor axis of the galaxy, it breaks out under the effect of instabilities, forming a galactic scale superwind as is seen in nearby starbursts eg. Strickland & Stevens (1998). The superbubble or superwind can make a significant contribution to the soft X-ray emission of a starburst galaxy as shown by Suchkov et al. (1996), Strickland & Stevens (1998), and Read et al. (1997).

We can estimate the soft X-ray luminosity of such a superbubble from the FIR luminosity of the galaxy. We use the FIR luminosity with the calibration of Heckman et al. (1990):

$$(dE/dt)_{mech} = 7 \times 10^{42} L_{IR} \text{ erg s}^{-1} \quad (2.3)$$

which correlates the total infrared luminosity in the $8-1000\mu$ band (in units of $10^{11} L_{\odot}$) of a starburst with age greater than 10^7 yr with the kinetic energy deposition rate from supernovae and stellar winds, in order to calculate the deposition rate of mechanical energy by the supernovae and stellar winds of massive stars. Then from the formula of Heckman et al. (1995) which correlates the soft X-ray luminosity of a superbubble with the mechanical energy input:

$$L_X \simeq 5 \times 10^{39} L_{41}^{33/35} n^{17/35} t_7^{19/35} \text{ erg s}^{-1} \quad (2.4)$$

Table 2.12: Properties of the starforming galaxies with IRAS detections

IRAS name (1)	Other Name (2)	$L_{X_{obs}}$ (3)	$L_{FIR_{40-120\mu}}$ (4)	$L_{IR_{8-1000\mu}}$ (5)	$L_{X_{wind}}$ (6)	$L_{X_{bin}}$ (7)	SFR (8)	Classification
00006+2141	MRK 0334	18	4.06	8.95	0.18	8.11	40.3	H II
00124-3929	NGC 55	0.00008	0.016	0.026	0.001	0.032	0.12	H II
00276+2555		113.32	33.57	< 125.51	1.29	67.14	564.8	Comp
00317-2142	ESO 540- G 00	91.80	7.15	13.50	0.30	14.29	60.6	Comp
00342+2342	Arp 282	0.41	0.92	< 4.26	0.04	1.84	19.2	LINER
00375-2407	0037-2407	3.79	2.36	< 9.88	0.11	4.72	44.5	H II
00450-2533	NGC 0253	0.08	1.06	1.98	0.05	2.11	8.9	H II
00470+3200	NGC 266	0.89	0.71	< 1.56	0.03	1.41	7.0	LINER
01219+0331		0.15	3.71	6.44	0.16	7.42	29.0	H II
01220+0128	NGC 521	0.83	0.74	< 1.83	0.04	1.48	8.2	H II
01319-1604		22.72	1.93	3.67	0.09	3.87	16.5	H II
01403+1323	NGC 660	0.03	1.18	2.16	0.06	2.36	9.7	Comp
02069-1022	NGC 837	0.64	2.82	5.00	0.13	5.65	22.5	LINER
02071-1023	NGC 838	0.97	4.01	7.95	0.17	8.01	35.8	H II
02072-1025	NGC 839	0.29	4.74	9.40	0.20	9.48	42.3	H II
02078-1033	NGC 848	0.15	0.67	1.53	0.03	1.35	6.9	Comp
02194+4207	PGC9031	0.01	0.37	0.59	0.02	0.74	2.7	H II
02379-0838	PGC10122	0.02	0.11	0.21	0.01	0.23	0.9	H II
03176-6640	NGC 1313	0.22	0.10	0.16	0.01	0.20	0.7	H II
03207-3723	NGC 1316	0.99	0.28	0.56	0.01	0.56	2.5	LINER
03234-4925	PGC12774	5.18	1.53	3.80	0.07	3.05	17.1	LINER
03372-1841	PGC13467	0.46	2.02	4.03	0.09	4.04	18.1	Comp
03380-5514	0338-5514	2.63	1.22	< 3.19	0.06	2.44	14.3	Comp
03540-4230	NGC 1487	0.03	0.06	0.11	0.00	0.13	0.5	H II
04315-0840	NGC 1614	1.41	15.97	34.50	0.64	31.94	155.2	H II
04449-5920	NGC 1672	0.21	1.70	3.16	0.08	3.40	14.2	H II
04591-0419	PGC16571	0.55	1.62	3.00	0.07	3.24	13.5	H II
05059-3734	NGC 1808	0.27	2.19	4.43	0.10	4.39	19.9	H II
05365+6921	NGC 1961	0.75	3.55	6.54	0.16	7.11	29.4	LINER
06107+7822	PGC18797	0.15	2.51	4.85	0.11	5.02	21.8	H II
07062+2041	NGC 2341	0.83	< 7.68	< 12.99	0.32	15.36	58.5	H II
07063+2043	NGC 2342	1.15	< 8.42	< 14.84	0.35	16.84	66.8	Comp
09077+6014	NGC 2768	0.08	0.02	0.06	0.001	0.05	0.3	LINER
09186+5111	NGC 2841	0.03	0.07	0.11	0.004	0.13	0.5	LINER
09293+2143	NGC 2903	0.01	0.36	0.61	0.02	0.72	2.8	H II
09433-1408	PGC27991	0.38	1.66	3.15	0.08	3.33	14.2	H II
09517+6954	M82	0.31	1.08	2.42	0.05	2.17	10.9	H II
09593+6858	NGC 3077	0.02	0.41	0.76	0.02	0.82	3.4	H II
10153+2205	PGC30083	0.04	0.19	0.36	0.01	0.37	1.6	H II
10257-4339	NGC 3256	2.17	15.51	30.71	0.62	31.01	138.2	H II
10293+5439	ARP 233	0.04	0.22	0.47	0.01	0.45	2.1	H II
10356+5345	NGC 3310	0.28	0.70	1.35	0.03	1.40	6.1	H II
10356+5345	NGC 3310	0.53	0.70	1.33	0.03	1.40	6.0	H II
10413+1157	NGC 3351	0.06	0.28	0.51	0.01	0.57	2.3	H II
10422+5613	NGC 3353	0.03	0.11	0.21	0.01	0.21	0.9	H II
10433+6329	NGC 3359	0.03	0.16	0.26	0.01	0.31	1.2	H II
10516+5434	NGC 3448	0.17	0.28	0.51	0.01	0.57	2.3	H II
11000+2527		1.64	5.02	< 12.93	0.22	10.04	58.2	LINER

Table 2.12: Properties of the starforming galaxies *continued*

IRAS name (1)	Other Name (2)	$L_{X_{\text{obs}}}$ (3)	$L_{\text{FIR}_{40-120\mu}}$ (4)	$L_{\text{IR}_{8-1000\mu}}$ (5)	$L_{X_{\text{wind}}}$ (6)	$L_{X_{\text{bin}}}$ (7)	SFR (8)	Classification
11193+5921	PGC34889	0.21	0.13	0.23	0.007	0.25	1.0	LINER
11220+3902	NGC 3665	0.23	0.29	0.52	0.02	0.59	2.3	H II
11257+5850	ARP 299	2.39	22.02	46.41	0.87	44.04	208.8	H II
12056+6527	NGC 4125	0.24	0.03	0.08	0.002	0.07	0.3	Comp
12112+1510	NGC 4192	0.001	0.004	0.007	0.000	0.009	0.03	Comp
12131+1410	NGC 4212	0.02	0.14	0.26	0.01	0.28	1.2	H II
12133+1325	NGC 4216	0.001	0.001	0.002	0	0.002	0.01	Comp
12173+0537	NGC 4273	0.34	1.55	3.00	0.07	3.10	13.5	H II
12178+0539	NGC 4281	0.40	0.14	0.34	0.007	0.28	1.5	Comp
12193+0445	NGC 4303	0.40	1.86	3.15	0.08	3.72	14.2	H II
12200+3010	NGC 4314	0.06	0.10	0.17	0.005	0.19	0.8	LINER
12239+3130	NGC 4464	0.07	0.42	0.78	0.021	0.84	3.5	Comp
12259+1721	NGC 4450	1.18	0.20	0.36	0.01	0.41	1.6	LINER
12281+4155	NGC 4490	0.04	0.35	0.60	0.02	0.69	2.7	H II
12315+0758	NGC 4526	0.01	0.04	0.07	0.00	0.08	0.3	H II
12343+1326	NGC 4569	0.00	0.01	0.03	0.001	0.03	0.1	Comp
12374-1120	NGC 4594	0.56	0.16	0.31	0.008	0.32	1.4	LINER
12396+3249	NGC 4631	0.006	0.60	1.04	0.03	1.20	4.7	H II
12416+3228	NGC4656	0.003	0.03	< 0.05	0.00	0.05	0.2	H II
12593-3230	PGC44965	2.74	3.24	< 6.44	0.14	6.48	29.0	Comp
13022-4914		0.002	0.56	0.84	0.03	1.13	3.8	H II
13086+3719	NGC 5005	0.16	0.57	0.97	0.03	1.13	4.4	LINER
13135+4217	NGC 5055	0.03	0.28	0.48	0.014	0.55	2.1	Comp
13191-3622	NGC 5102	0.002	0.01	0.01	0	0.01	0.1	H II
13223+1400	NGC 5136	0.93	0.53	< 1.40	0.03	1.06	6.3	H II
13277+5840	NGC 5204	0.02	0.003	< 0.005	0	0.006	0.02	H II
13299+1121	Mrk 789	1.66	7.43	14.79	0.31	14.85	66.5	H II
13341-2936	M83	0.30	0.84	1.58	0.04	1.67	7.1	H II
13351+2740	NGC 5251	0.99	1.49	< 4.79	0.07	2.99	21.5	H II
13354+3924	1335+39	2.37	1.09	2.34	0.05	2.17	10.5	Comp
13356-3100	ESO 133535-3	1.84	1.24	< 4.89	0.06	2.48	22.0	H II
13362+4831	NGC 5256	7.75	12.77	23.49	0.52	25.53	105.7	H II
13370-3123	NGC 5253	0.006	0.11	0.29	0.006	0.21	1.3	H II
13386-3145	ESO 133836-3	1.34	0.75	< 2.11	0.04	1.49	9.5	H II
13414+5551	1341+5552	14.38	3.13	> 10.64	0.14	6.26	47.9	Comp
13475+6026	NGC 5322	0.16	0.04	< 0.12	0.002	0.08	0.5	LINER
13512+4036	NGC 5350	0.12	0.47	0.85	0.02	0.94	3.8	H II
14002-4108	NGC 5408	0.14	0.02	0.03	0.001	0.03	0.1	H II
15051+5557	NGC 5866	0.02	0.08	0.13	0.004	0.16	0.6	Comp
15140+5542	NGC 5905	0.12	0.93	1.75	0.04	1.86	7.8	H II
15153+5535	NGC 5908	0.21	1.72	3.14	0.08	3.43	14.1	LINER
15243+4150	NGC 5930	0.27	1.56	3.08	0.07	3.12	13.8	H II
15327+2340	Arp 220	0.65	67.68	109.97	2.50	135.36	494.9	H II
15511+4047	NGC 6013	3.11	0.26	< 0.65	0.01	0.52	2.9	H II

Table 2.12: Properties of the starforming galaxies *continued*

IRAS name (1)	Other Name (2)	$L_{X_{\text{obs}}}$ (3)	$L_{\text{FIR}_{40-120\mu}}$ (4)	$L_{\text{IR}_{8-1000\mu}}$ (5)	$L_{X_{\text{wind}}}$ (6)	$L_{X_{\text{bin}}}$ (7)	SFR (8)	Classification
16350+7817	NGC 6217	0.17	0.53	1.01	0.03	1.06	4.5	H II
16400+3944		1.75	3.07	5.85	0.14	6.14	26.3	H II
16419+8213		5.54	0.96	< 2.24	0.05	1.92	10.1	H II
17039+6039		8.77	8.47	23.78	0.35	16.94	107.0	LINER
20338+5958	NGC 6946	0.00	0.00	0.01	0.00	0.01	0.03	H II
22115-3013		0.22	1.85	3.82	0.08	3.70	17.2	H II
22179-2455	NGC 7252	0.65	2.29	4.37	0.10	4.58	19.6	Comp
22347+3409	NGC 7331	0.15	0.57	0.93	0.03	1.14	4.2	Comp
23133-4251	NGC 7552	0.67	4.35	8.55	0.19	8.70	38.5	H II
23135+2517	PGC70877	3.18	14.71	28.79	0.59	29.42	129.5	Comp
23179+1657	NGC 7625	0.13	0.67	1.29	0.03	1.35	5.8	H II
23196+0805		2.71	2.00	< 5.32	0.09	4.00	23.9	H II
23309-0215	PGC71737	0.66	1.62	3.18	0.07	3.23	14.3	Comp
23336+0152	NGC 7714	0.66	1.81	4.05	0.08	3.61	18.2	H II
23488+1949		0.82	9.95	17.51	0.41	19.90	78.8	H II
23487+1957	1E2348+1956	26.76	7.83	> 16.04	0.33	15.66	72.2	H II
23488+2018	Mrk 331	1.11	12.89	23.90	0.52	25.77	107.5	H II
23498+2829	NGC 7775	0.83	2.42	4.83	0.11	4.84	21.7	H II

Notes: (1) IRAS name, (2) Other name, (3) Observed X-ray luminosity in the 0.1-2.5keV band in units of $10^{41} \text{erg s}^{-1}$, (4) FIR luminosity in the $42\mu - 112\mu$ band in units of $10^{44} \text{erg s}^{-1}$ calculated from the 60μ and 100μ IRAS fluxes using the formula of Soifer, Sanders, Madore et al. (1987), (5) Total IR luminosity in the $8\mu - 1000\mu$ band calculated from the IRAS fluxes in all four bands using the formula of Kim & Sanders (1998) in units of $10^{44} \text{erg s}^{-1}$, (6) Estimated soft X-ray luminosity (0.5-2.5keV) of a super-wind component in units of $10^{40} \text{erg s}^{-1}$ - see text for details, (7) Estimated soft X-ray luminosity of X-ray binaries in units of $10^{40} \text{erg s}^{-1}$ - see text for details, (8) SFR from the IR luminosity - see text for details.

where L_{41} is the injection rate of mechanical energy into the bubble in units of $10^{41} \text{erg s}^{-1}$, n is the gas density and t_7 is the age of the bubble in units of 10Myrs, we can estimate the expected soft X-ray luminosity of such a bubble. Its formation begins after the effect of the stellar winds and we can assume that the age of the bubble is the same as the age of the starburst. In Column 6 of Table 2.12 the estimated X-ray luminosity from a superbubble is presented. It is clear that the X-ray emission of a superwind is not sufficient to reproduce the observed soft X-ray emission in most cases. This suggests that there is another component which could be a population of X-ray binaries. Indeed observations of nearby starforming galaxies show that only $\sim 50\% - 70\%$ of the 0.1-2.0keV emission from nearby starforming galaxies arises from a diffuse component (Read et al. 1997). It should be noted that these calculations are very uncertain as they rely on assumptions about the age of the starburst, the density of the material and the form of the IMF; all parameters which are very difficult to estimate.

The contribution of an X-ray binary component to the X-ray emission can be estimated in two ways: from the extinction corrected $H\alpha$ luminosity and assuming case B recombination we can

calculate the number of ionising photons. Then following Vacca *et al.* (1998) we can estimate the number of high mass stars (OB stars). From this number and using the calibration of Fabbiano *et al.* (1992) based on data for our Galaxy, they obtain that one in about every 500 high mass stars forms an X-ray binary. Assuming that a similar ratio is appropriate for star-forming galaxies, it is possible to estimate the number of high mass X-ray binaries in each galaxy. However, this method is extremely sensitive to aperture effects, unless the $H\alpha$ measurements are taken using large apertures.

In place of the $H\alpha$ luminosity we can use the FIR luminosity in order to estimate the number of high mass stars. This method is based on the assumption that the bulk of ionizing photons which are emitted by early-type stars are totally absorbed by the dust and are then re-emitted in the FIR part of the spectrum and that late-type stars do not contribute to the heating of the dust. Using this method we find a higher number of O stars compared to that using $H\alpha$ and therefore we infer a higher number of X-ray binaries. This discrepancy may arise because of the underestimated extinction from the Balmer decrement which gives a lower extinction corrected $H\alpha$ luminosity, or, as mentioned above, because of heating sources other than high mass stars, which may contribute to the overall far infrared emission of the galaxy. As seen from Table 2.12 the estimated X-ray luminosity from a population of high mass X-ray binaries (HMXRBs) assuming a mean luminosity of $10^{37} \text{ erg s}^{-1}$, is close to the measured soft X-ray luminosity and sometimes gives higher values. However, the X-ray luminosity of a population of high mass stars, depends on parameters such as the assumed Initial Mass Function (IMF), the upper and lower mass cutoffs and the mean luminosity of the HMXRBs. In addition it is noted that stars with sub-solar metallicities form higher luminosity X-ray binaries, as is found in the Magellanic clouds, (see van Paradijs & McClintock 1995, Griffiths & Padovani 1990).

Taking into account both components (the superwind and the X-ray binaries) we obtain luminosities close to those observed; in most cases within a factor of 5 (fig 2.18). It should be stressed that these calculations give only a rough idea of the contribution of each mechanism and therefore should be treated with caution. However, the fact that they reproduce the observed luminosities, even for the highest luminosity objects is an indication that X-ray luminous starforming galaxies may be simply extreme examples of nearby starburst galaxies like M82 and NGC253. The main difference is that they experience extremely intense bursts of starformation. Also from the same figure it is clear that in the case of LINERS and Composite objects the

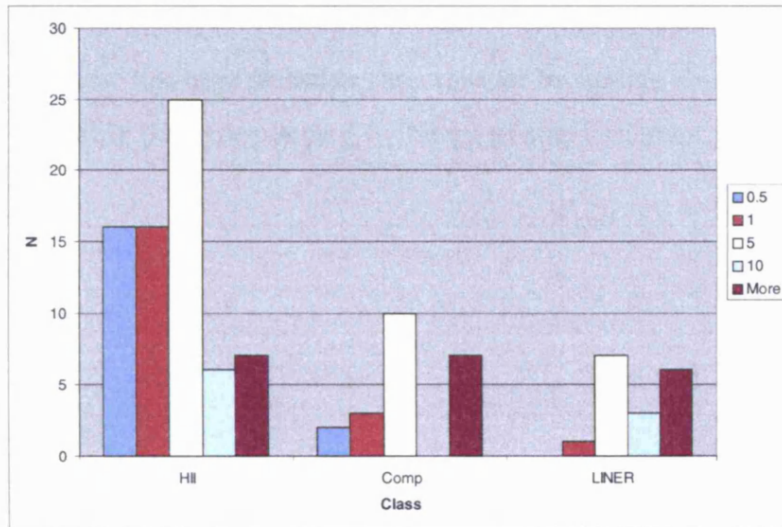


Figure 2.18: The fraction of the observed and the estimated X-ray emission for star-forming, composite and LINER objects in our sample.

predicted luminosities are systematically significantly lower than the observed, suggesting that there may be another component contributing to their X-ray emission. This could be either hot gas in the ISM or halo as is seen in elliptical galaxies (LINERs are found preferentially in elliptical hosts) or a low luminosity AGN. This is in agreement with the results of optical and near-IR spectroscopy which suggest that LINER and composite objects may be evolved starburst galaxies. In such a scenario a galactic driven superwind may form a halo around the galaxy or may trigger the formation of an AGN, as also has been suggested in some scenarios for the formation of AGNs.

Figure 2.19 shows a comparison between the star-forming galaxies in this sample and star-forming and other classes of galaxies in the sample of Moran et al. (1996) and Ho, Filippenko & Sargent (1997a). From the top figure it is clear that X-ray luminous star-forming galaxies follow the same trend as lower luminosity objects. This reinforces the conclusion that they are just scaled up examples of their lower luminosity counter-parts. The most striking feature of the bottom panel in the same figure is that the LX vs. LFIR relation has a different slope for AGN and star-forming galaxies, being flatter for star-forming galaxies. This has been previously

reported by Green et al. (1992) who found slopes of 0.82 ± 0.08 and 0.78 ± 0.07 for the LX vs. LFIR regression of broad line and narrow line objects, respectively. Another very interesting conclusion which can be drawn from this plot is that X-ray luminous star-forming galaxies follow the trend for the narrow-line objects rather than that for broad-line objects, which supports the view that most probably they are powered by bursts of star-formation rather than an AGN.

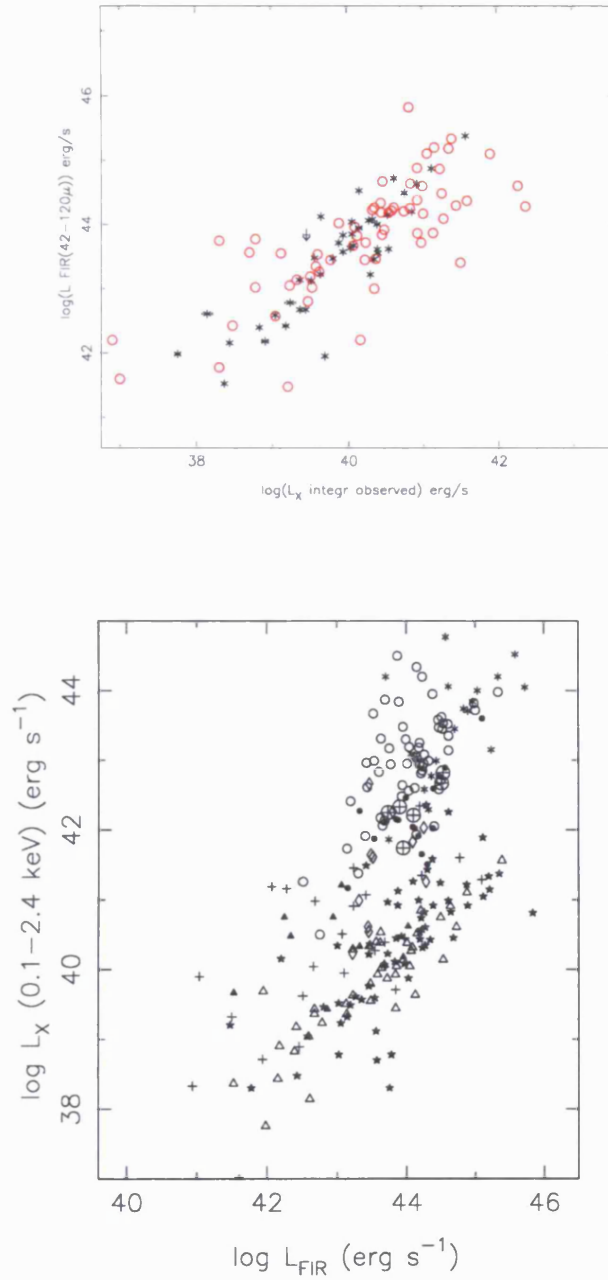


Figure 2.19: A comparison between the sample of star-forming galaxies presented here and the samples of Ho, Filippenko & Sargent (1997a) (top) and Moran et al. (1996)(bottom). In the top figure asterisks are the objects from Ho, Filippenko & Sargent (1997a) and red circles are the starbursts from this sample. In the bottom figure open and filled circles are Sy1-1.5 and Sy1.8-1.9, asterisks are NLS1, diamonds are Sy2, crossed circles are composite objects and star symbols are normal/star-forming galaxies from the sample of Moran et al. (1996). Filled stars and open triangles are star-forming galaxies from this survey and the survey of Ho, Filippenko & Sargent (1997a) respectively.

Chapter 3

A soft X-ray survey of star-forming galaxies

The nature of the X-ray emission of normal galaxies (ie. objects which do not host an AGN) has been the subject of detailed studies since their very first observations with Uhuru and Ariel V. However, it was with the launch of *Einstein* that it became possible to observe and study the properties of a large sample of these objects. The pioneering work of Fabbiano, Feigelson & Zamorani (1982) showed that there is a strong link between their X-ray emission and other properties (optical, IR, radio emission) of spiral galaxies. Similar results have been published by Green et al. (1992) and Read et al. (1997). The main disadvantage of these works is that the samples are not selected on the basis of the type of activity but on the basis of the morphology of the host galaxy; although the majority of nearby spiral galaxies are star-forming galaxies there are also a number which host Sy1 and Sy2 type nuclei. Therefore morphologically selected samples of galaxies are unsuitable to draw any general conclusions on the nature of star-forming galaxies.

ROSAT opened a new window to the study of the X-ray emission from nearby “low activity” galaxies. Its high sensitivity and better spectral and spatial resolution compared to those of earlier missions made it possible to obtain morphological and spectral information for a very large number of objects. Recently, Read et al. (1997) presented a multiwavelength study of nearby spiral galaxies based on *ROSAT* PSPC observations. Their results confirm the original findings of Fabbiano et al. (1982). Also they show that a large fraction ($\sim 50 - 60\%$) of the total soft X-ray (0.1-2.0keV) emission is associated with a diffuse component arising from hot

thermal gas ($kT \sim 0.3\text{keV}$). Stevens & Strickland (1998) presented a similar study of a small sample of Wolf-Rayet (WR) galaxies, where they find that in general WR galaxies follow the same trends as spiral galaxies regarding their multiwavelength properties. However, neither of these samples is suitable to draw any conclusions on the properties of star-forming galaxies. The main reason is that, as mentioned above, a sample of spiral galaxies may include other classes of galaxies apart from starbursts. Also Wolf-Rayet galaxies are a very distinct class of starburst galaxy which represent only a brief phase in their evolution, and therefore they are not typical examples of the whole class.

Here, we describe results of a study of a sample of 44 bona-fide star-forming galaxies (the largest such sample studied so far). Firstly the selection of the sample and the reduction of the data are described. Their X-ray images are then discussed, and finally their X-ray properties are linked with their emission in other wavebands.

3.1 Selection of the sample

The sample used for this study is selected from the compilation of Ho, Filippenko & Sargent (1995), Ho, Filippenko & Sargent (1997a). Their atlas contains high quality optical spectra and classifications for the nuclear regions of all northern galaxies in the Revised Shapley-Ames Catalogue of Bright Galaxies (de Vaucouleurs 1991) which are brighter than 12.5mag in the B band. The spectra cover the blue (4230-5110Å) and red (6210-6860Å) regions of the spectrum with spectral resolutions $\sim 4\text{Å}$ and $\sim 2.5\text{Å}$ FWHM respectively. A total number of 486 objects has been observed. They find that 14% of the objects in this sample do not show any kind of activity, whereas 42% are star-forming galaxies and 11% host an AGN (Sy1 or Sy2 type objects). There are also a number of LINERs (19%) and transition objects (13%). This means that the majority of the activity in nearby galaxies is in the form of star-formation rather than the more exotic form of accretion onto a supermassive black hole (Ho, Filippenko & Sargent 1997b).

This catalogue is ideal to select bona-fide star-forming galaxies because of the high quality of the spectral classifications. The X-ray sample consists of all the star-forming galaxies from this compilation which fall in the field of view of the publicly available *ROSAT* PSPC observations

(as of August 1998)¹. Only objects in the inner PSPC ring have been included in our sample as the *ROSAT* PSPC Point Spread Function significantly degrades and the vigneting becomes very important at large off-axis angles. In the cases of multiple observations of the same object, only the longest exposure, or the one with the object closest to the optical axis, has been selected for further analysis. NGC 598 has been excluded from the statistical analysis of the sample as its angular extent is much larger than the field of view of the PSPC and therefore its integrated emission would be underestimated. However, its X-ray image is shown together with the images of other galaxies for completeness. The final list together with some parameters of the galaxies is presented in Table 3.1.

3.2 Data reduction

For the reduction of the X-ray data the ASTERIX package (Allen & Vallance 1995) has been used. Initially periods of high background (master veto rate > 170) have been excluded as the particle background cannot be modeled accurately for these high background periods (Snowden, McCammon, Burrows & Mendenhall 1994). This resulted in a reduction of the original exposure time of the order of $\sim 10\%$ in most cases. Special care was taken in the subtraction of the background. The following procedure has been followed :

1. Images were extracted in the 0.5-2.0keV band (PI channels 52-201; B SASS band) in order to minimise the background. To investigate for supersoft sources, images at the 0.11-0.28keV band (PI channels 11-41; A SASS band) were also created. These images are referred to as the hard and the soft background images respectively.
2. The PSS algorithm (Allen 1997) has been employed in order to search these images for point sources down to a significance level of 4.0σ . The mean surface brightness measured from three source free regions has been used as an initial estimate of the background level.
3. A spectral image in the “hard band” (channels 52-201) with a pixel size of $20''$ has been extracted from the original event lists. From this image all the point sources detected using PSS in the two images have been removed. Then this source free image was used as input in the task XRTSUB in ASTERIX, to create a model of the background.

¹In the present form of the public catalogue of *ROSAT* PSPC observations data also exist for a few additional objects which are not included in this study.

Table 3.1: General properties of the galaxies

Name	Morph. type	T	Velocity km s ⁻¹	Distance Mpc	B	MB	MB bulge	i degrees	D25 arcmin
(1)	(2)	(3)	(4)	(5)	(6)	(7)	(8)	(9)	(10)
NGC 520	Pec	99	2215	27.8	11.89	-20.33		68	4.47
NGC 521	SB(r)bc	4	5039	67	12.29	-21.84	-19.87	24	3.16
NGC 598	SA(s)cd	6	-180	0.7	5.75	-18.48	-15.19	55	70.79
NGC 660	SB(s)a pec	1	852	11.8	11.44	-18.92	-17.9	70	8.32
NGC 891	SA(s)b? spin	3	528	9.6	9.37	-20.54	-19		13.49
NGC 1569	IBm	10	-89	1.6	9.42	-16.6		62	3.63
NGC 2146	SB(s)ab pec	2	890	17.2	10.58	-20.6	-19.37	57	6.03
NGC 2276	SAB(rs)c	5	2417	36.8	11.75	-21.08	-18.54	17	2.82
NGC 2342	S pec		5271	69.5	12.37	-21.84		21	1.38
NGC 2403	SAB(s)cd	6	129	4.2	8.43	-19.69	-16.4	57	21.88
NGC 2537	SB(s)m pec	9	446	9	12.02	-17.75	-10.9	32	1.74
NGC 2750	SABc	5	2671	38.4	12.09	-20.83	-18.29	27	2.19
NGC 2903	SAB(rs)bc	4	556	6.3	9.11	-19.89	-17.92	63	12.59
NGC 3034	IAO spin	90	213	5.2	8.86	-19.72		70	11.22
NGC 3077	IAO pec	90	13	2.1	10.32	-16.29		34	5.37
NGC 3184	SAB(rs)cd	6	591	8.7	10.34	-19.36	-16.07	21	7.41
NGC 3198	SB(rs)c	5	663	10.8	10.21	-19.96	-17.42	70	8.51
NGC 3310	SAB(r)bc pec	4	988	18.7	10.95	-20.41	-18.44	40	3.09
NGC 3319	SB(rs)cd	6	745	11.5	11.13	-19.17	-15.88	58	6.17
NGC 3359	SB(rs)c	5	1012	19.2	10.68	-20.74	-18.2	54	7.24
NGC 3395	SAB(rs)cd: pec	6	1618	27.4	12.09	-20.1	-16.81	55	2.09
NGC 3665	SA(s)0	-2	2061	32.4	11.69	-20.86	-20.25	34	2.46
NGC 3690	IBm pec	9	3033	40.4	11.85	-21.18	-14.33	41	2.04
NGC 4236	SB(s)dm	8	0	2.2	9.53	-17.18	-11.77	74	21.88
NGC 4245	SB(r)0/a:	0	890	9.7	12.01	-17.92	-17.06	41	2.88
NGC 4303	SAB(rs)bc	4	1569	15.2	10.12	-20.79	-18.82	27	6.46
NGC 4449	IBm	10	202	3	9.94	-17.45		46	6.17
NGC 4470	Sa ?	1	2340	31.4	12.95	-19.53	-18.51	44	1.29
NGC 4485	IB(s)m pec	10	496	9.3	12.22	-17.62		46	2.29
NGC 4490	SB(s)d pec	7	579	7.8	9.81	-19.65	-15.42	62	6.31
NGC 4526	SAB(s)0:	-2	462	16.8	10.53	-20.6	-19.99	74	7.24
NGC 4559	SAB(rs)cd	6	815	9.7	9.76	-20.17	-16.88	68	10.72
NGC 4631	SB(s)d spin	7	608	6.9	8.61	-20.58	-16.35		15.49
NGC 4647	SAB(rs)c	5	1415	16.8	11.81	-19.32	-16.78	38	2.88
NGC 4654	SAB(rs)cd	6	1035	16.8	10.75	-20.38	-17.09	56	4.9
NGC 4656	SB(s)m pec	9	641	7.2	10.1	-19.19	-12.34		15.14
NGC 5204	SA(s)m	9	203	4.8	11.48	-16.93	-10.08	54	5.01
NGC 5457	SAB(rs)cd	6	240	5.4	8.21	-20.45	-17.16	21	28.84
NGC 5775	SAB(rs)b? spin	3	1722	29.4	10.15	-22.19	-20.65		7.41
NGC 5905	SB(r)b	3	3388	44.4	12.22	-21.08	-19.54	50	3.98
NGC 5907	SA(s)c: spin	5	666	14.9	9.7	-21.17	-18.63		12.59
NGC 6236	SAB(s)cd	6	1279	23.3	12.06	-19.79	-16.5	56	2.88
NGC 6946	SAB(rs)cd	6	50	5.5	7.78	-20.92	-17.63	32	11.48
NGC 7448	SA(rs)bc	4	2194	30.3	11.5	-20.91	-18.94	65	2.69

Notes: (1) Name of the galaxy, (2) Hubble morphological type, (3) Numerical Hubble type, (4) Distance, (5) Recession velocity in km s⁻¹, (6) apparent B magnitude, (7) B band absolute magnitude corrected for extinction, (8) Estimated absolute B band magnitude of the bulge, (9) inclination in degrees, (10) Major axis of the D25 ellipse in degrees.

All the data are taken from Ho, Filippenko & Sargent (1997a).

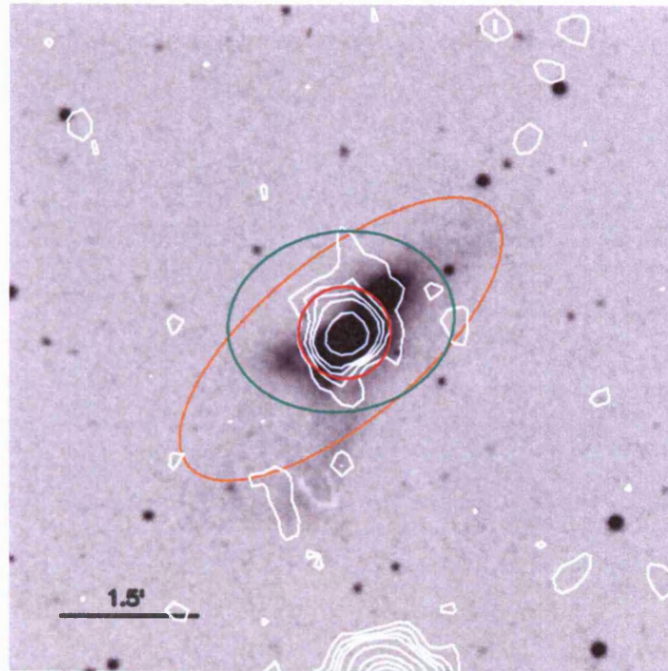
4. A second search using PSS on the hard image using as background the new more accurate background model (which takes into account the effect of vignetting) was then performed.
5. All the detected point sources have been excluded from a full band (0.11-2.04keV) high resolution (7.5'') spectral image. A source free annulus outside the inner support ring (after masking out the support grid) has been used as background. Any remaining diffuse emission in this region, which was not detected by PSS, was excluded by hand after a visual inspection.
6. The XRTSUB task was used to create a background subtracted spectral image. Finally this spectral image has been collapsed to form a two-dimensional image

3.3 Imaging analysis

Figures 3.1 to 3.22 show contours from the final background subtracted images overlaid onto B-band DSS images. The X-ray images have been smoothed using a two dimensional Gaussian with a FWHM of 2.25 pixels ($\sim 16.9''$). This gave an effective resolution of $\sim 20''$, whereas the on-axis resolution of the PSPC+XRT assembly is $\sim 25''$ (Hasinger, Turner, George & Boese 1992).

From these images it is clear that the X-ray morphologies of the objects in this sample are very diverse. There are objects which have emission extending over the optical extent of the galaxy, whereas others have only a point-like source in the nuclear region. In many cases the X-ray emission extends along the minor axis of the galaxy suggestive of a superwind, such as seen in the prototypical starbursts M82 and NGC253. Finally there are a few spectacular cases where numerous point-like sources are detected together with diffuse emission.

NGC 520



NGC 521

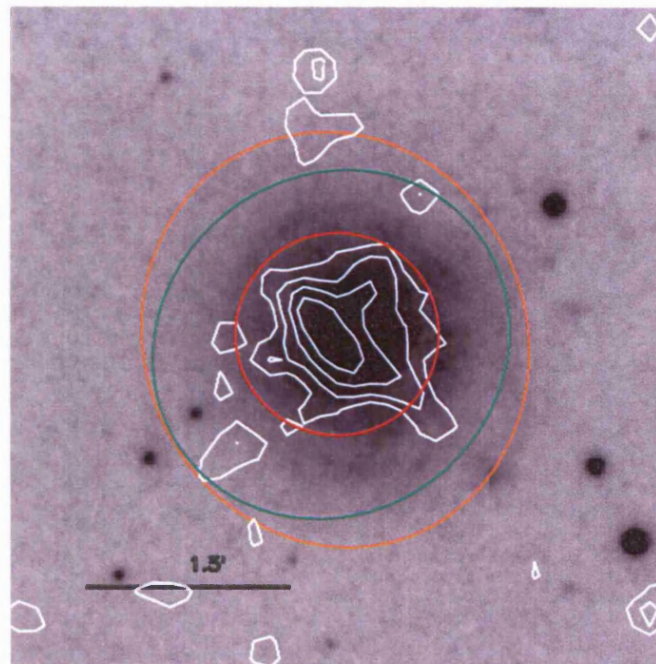
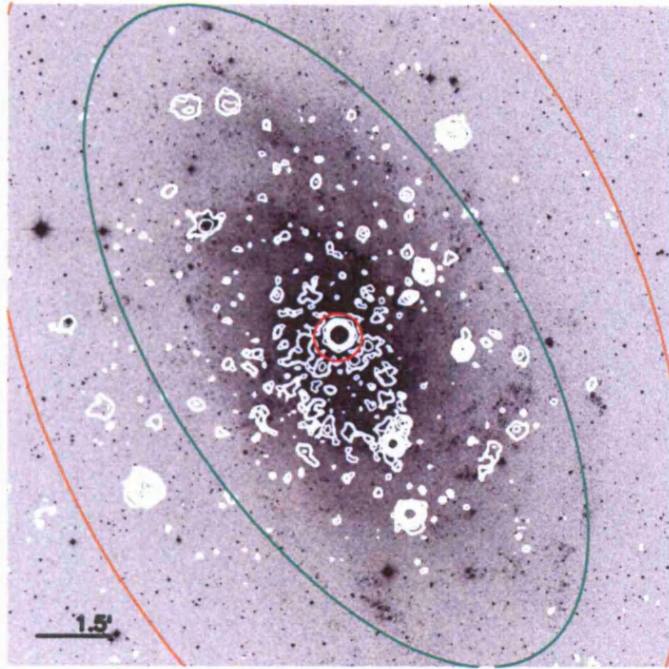


Figure 3.1: Overlay of contours from the PSPC observations of NGC520 and NGC521 on DSS images. In this and the following figures North is up and East is left. The bar in the bottom left corner is 1.5' long. The red circle corresponds to the nuclear region whereas the orange and the green ellipses are the D25 ellipse and the region used to measure the integrated emission respectively.

NGC 598



NGC 660

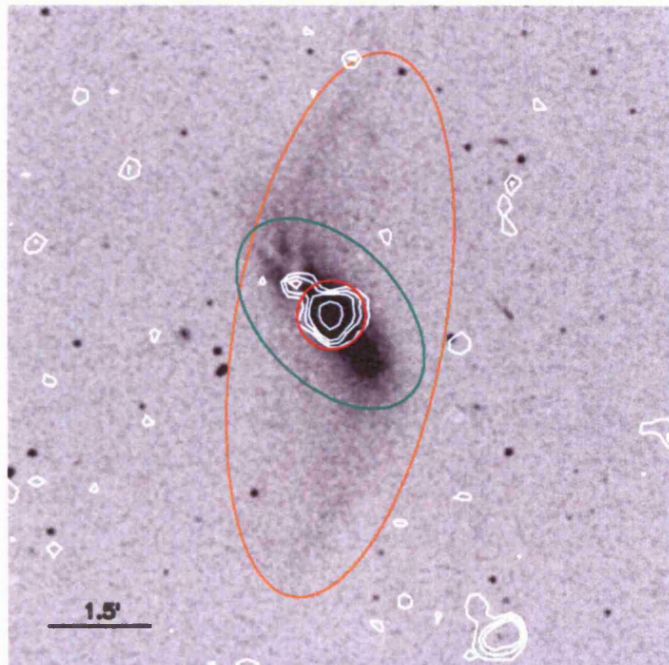
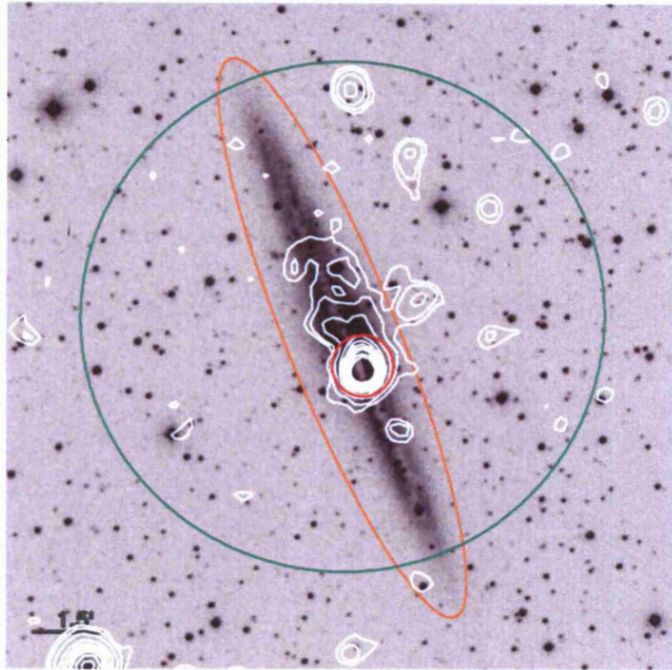


Figure 3.2: Overlay of contours from the PSPC observations of NGC598 and NGC660 on DSS images

NGC 891



NGC 1569

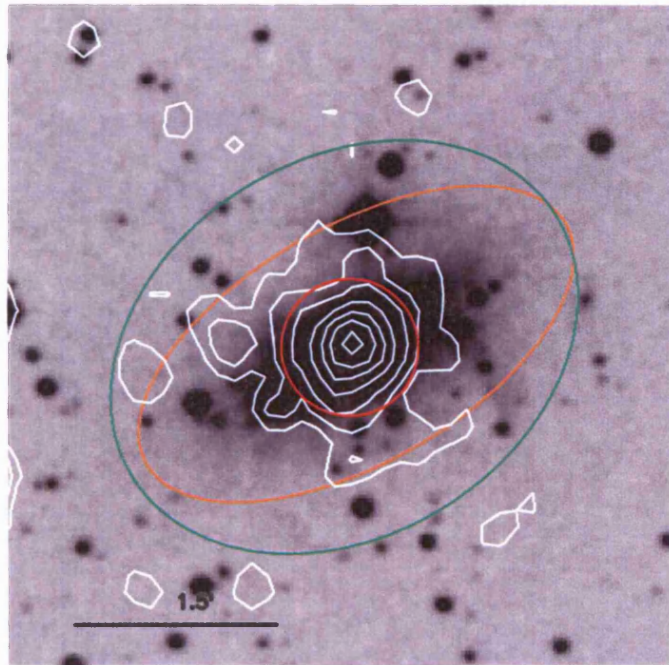
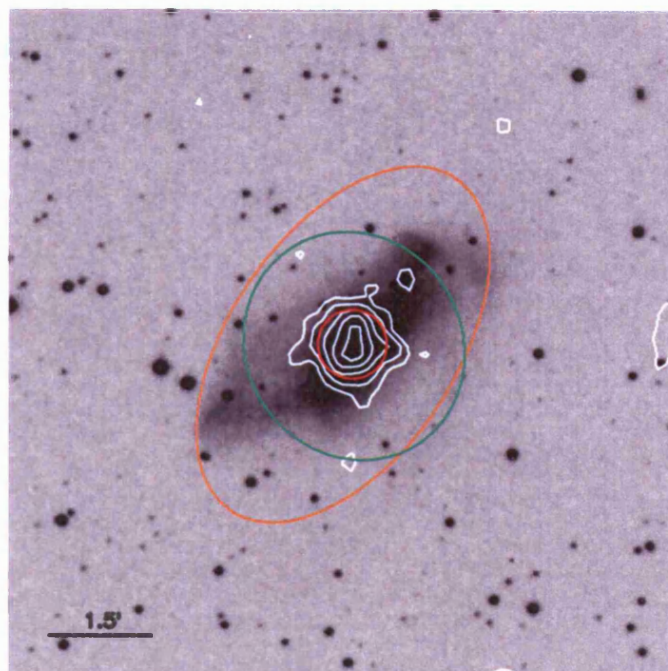


Figure 3.3: Overlay of contours from the PSPC observations of NGC891 and NGC1569 on DSS images

NGC 2146



NGC 2276

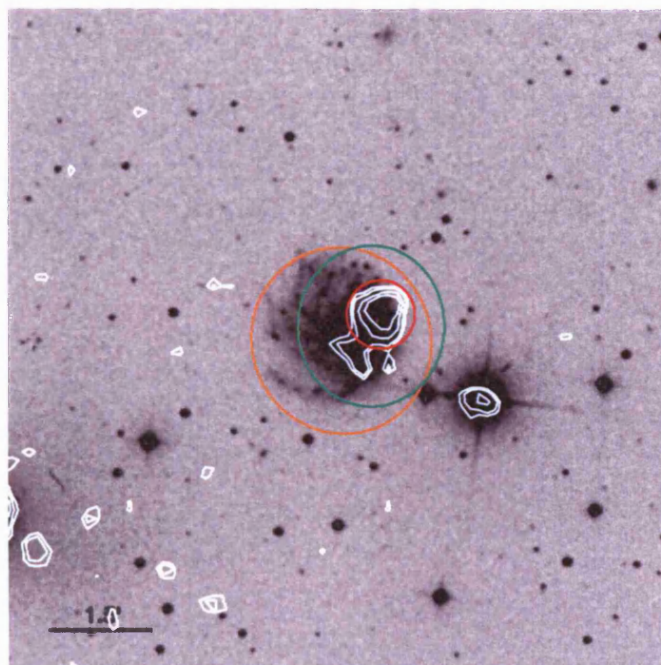
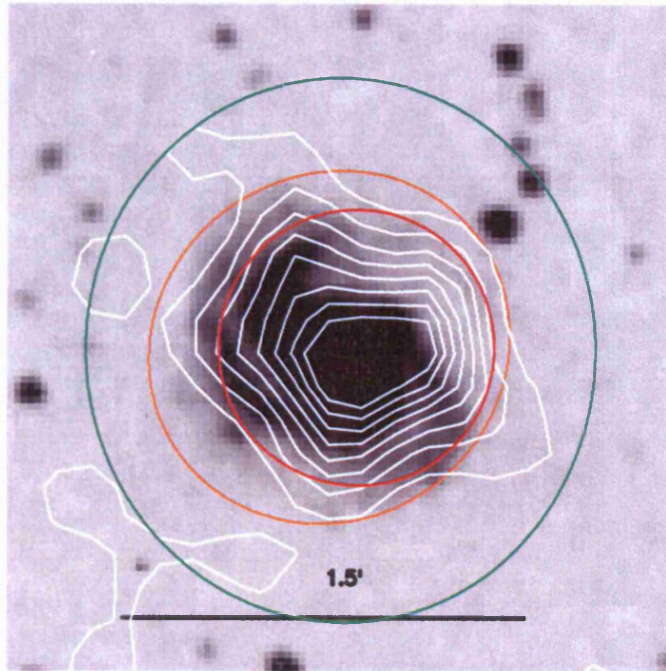


Figure 3.4: Overlay of contours from the PSPC observations of NGC2146 and NGC2276 on DSS images.

NGC 2342



NGC 2403

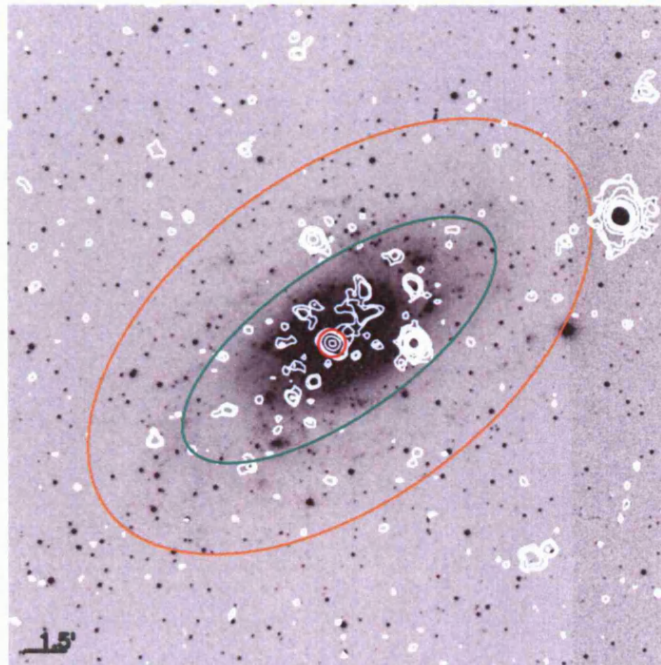
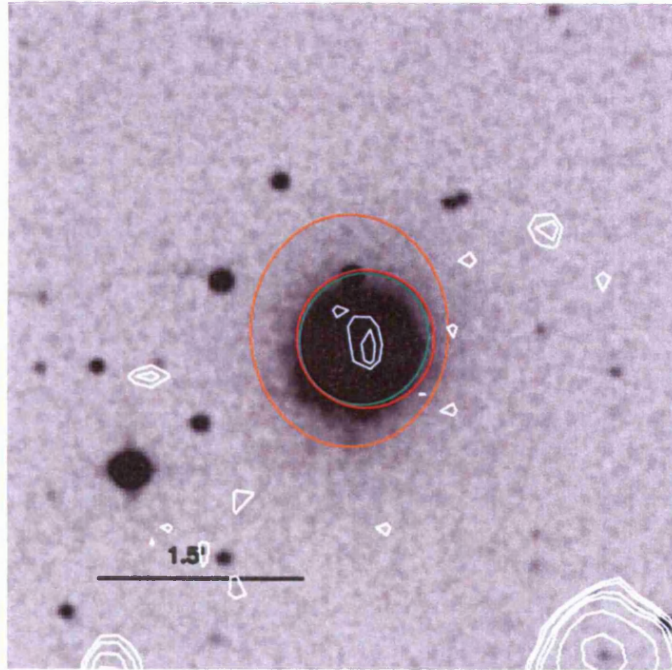


Figure 3.5: Overlay of contours from the PSPC observations of NGC2342 and NGC2403 on DSS images.

NGC 2547



NGC 2750

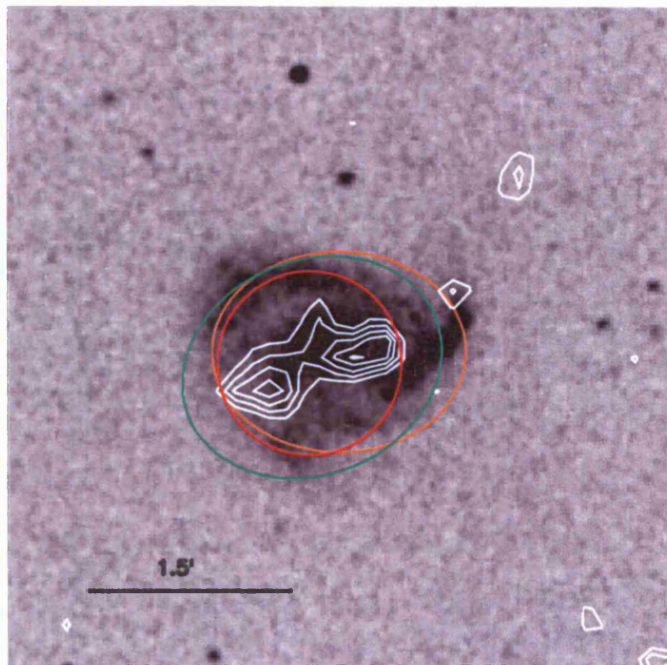
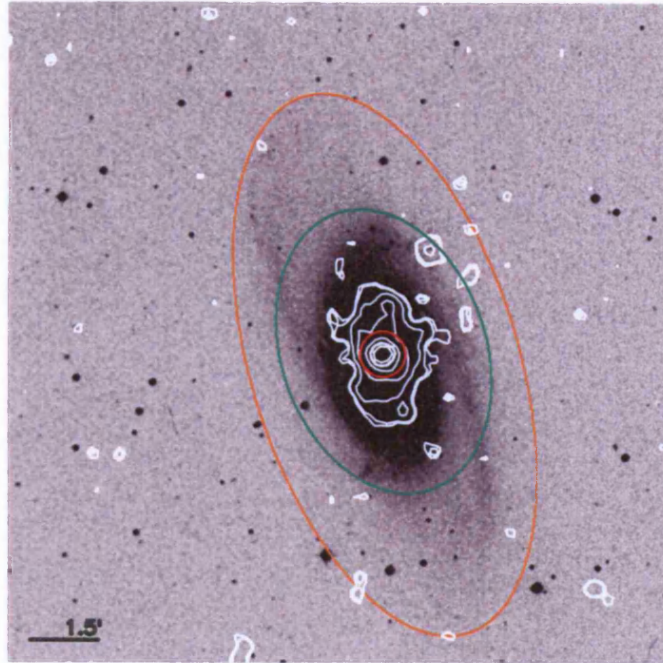


Figure 3.6: Overlay of contours from the PSPC observations of NGC2537 and NGC2750 on DSS images

NGC 2903



NGC 3034

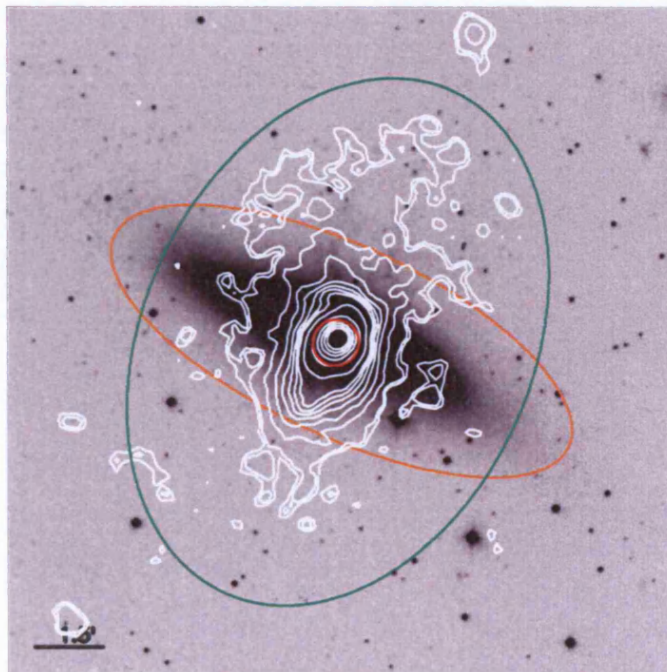
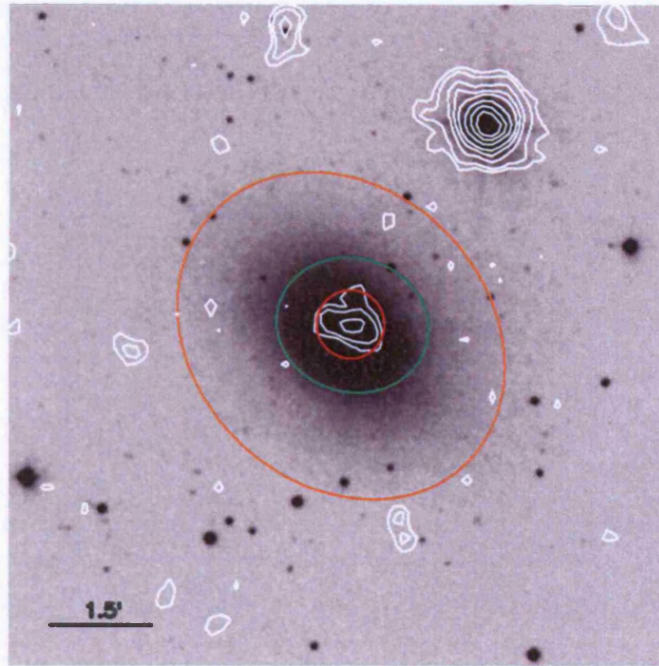


Figure 3.7: Overlay of contours from the PSPC observations of NGC2903 and NGC3034 on DSS images

NGC 3077



NGC 3184

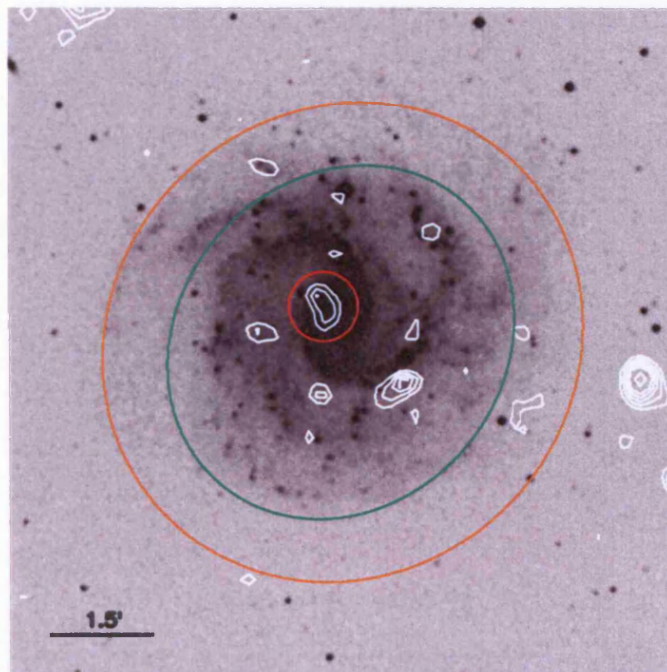
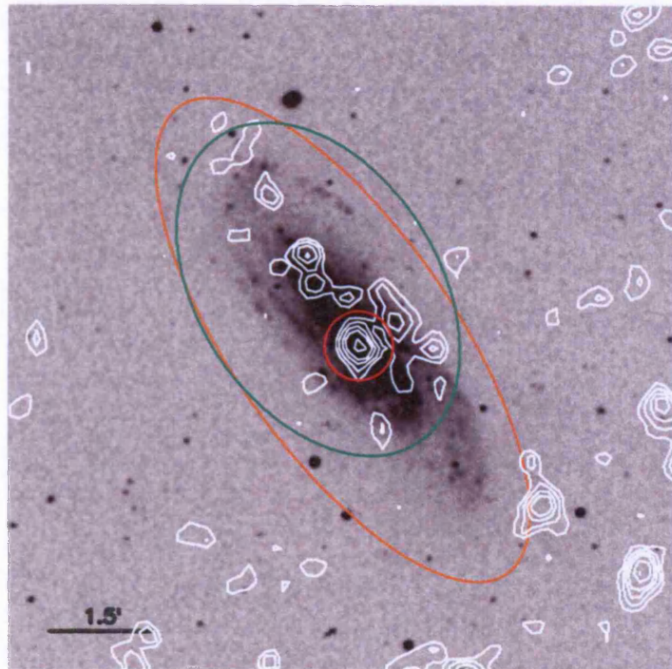


Figure 3.8: Overlay of contours from the PSPC observations of NGC3077 and NGC3184 on DSS images

NGC 3198



NGC 3310

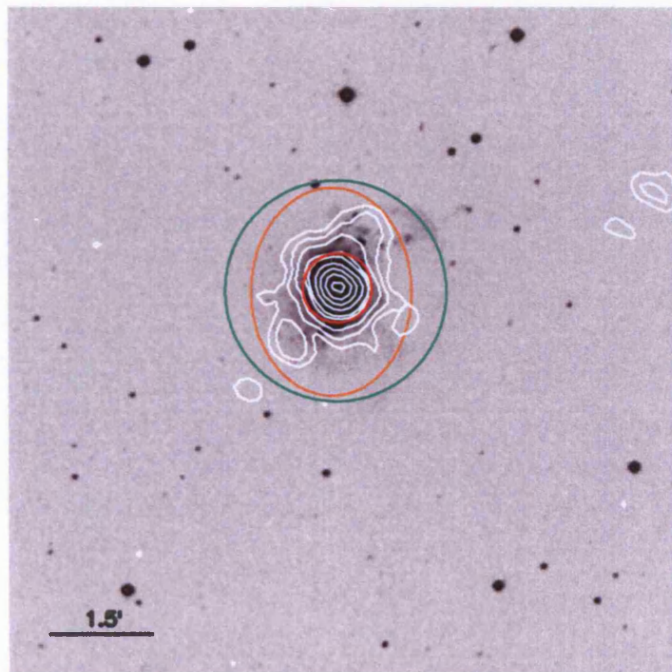
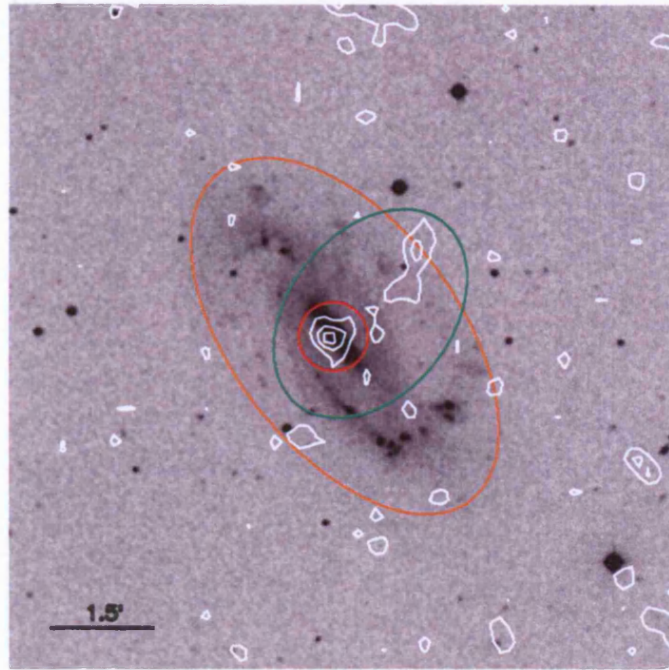


Figure 3.9: Overlay of contours from the PSPC observations of NGC3198 and NGC3310 on DSS images

NGC 3319



NGC 3359

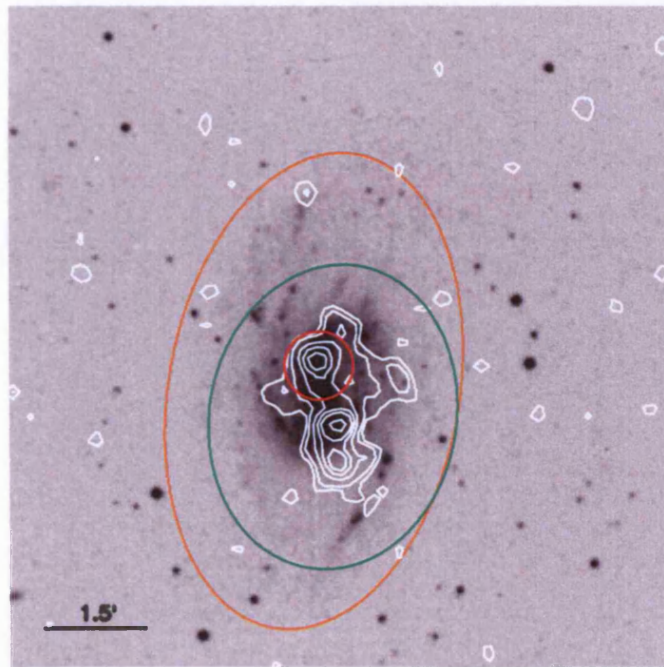
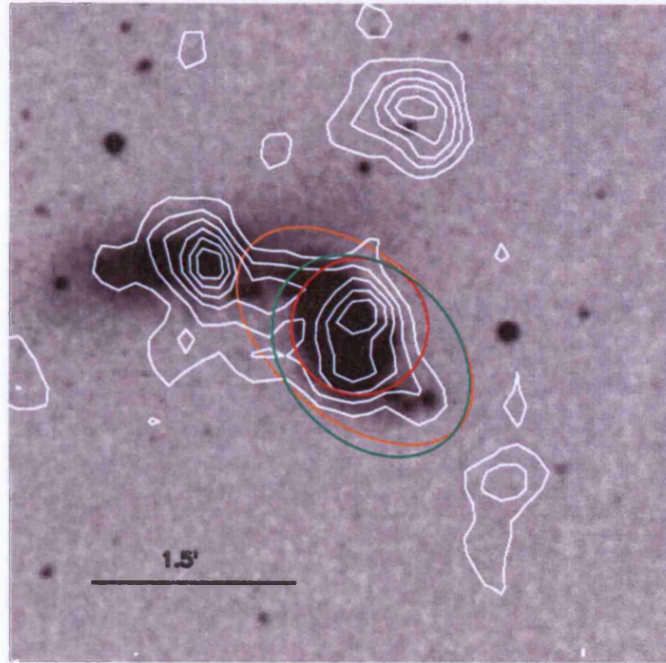


Figure 3.10: Overlay of contours from the PSPC observations of NGC3319 and NGC3359 on DSS images

NGC 3395



NGC 3665

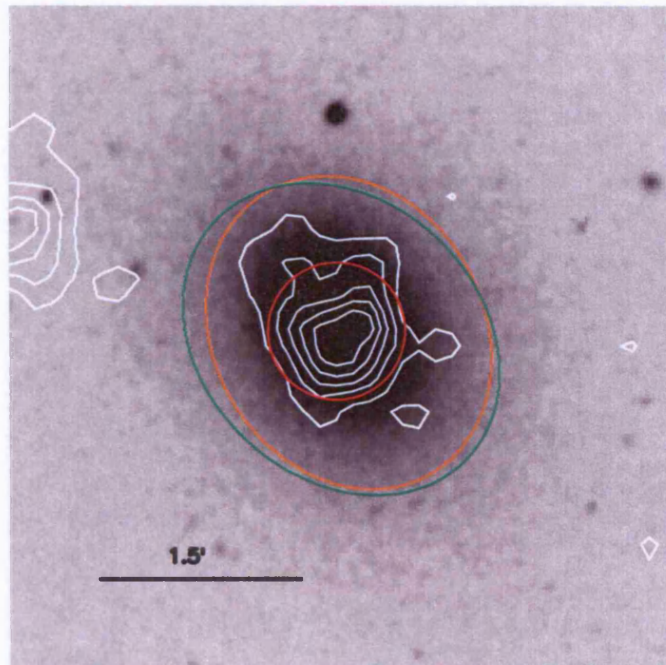
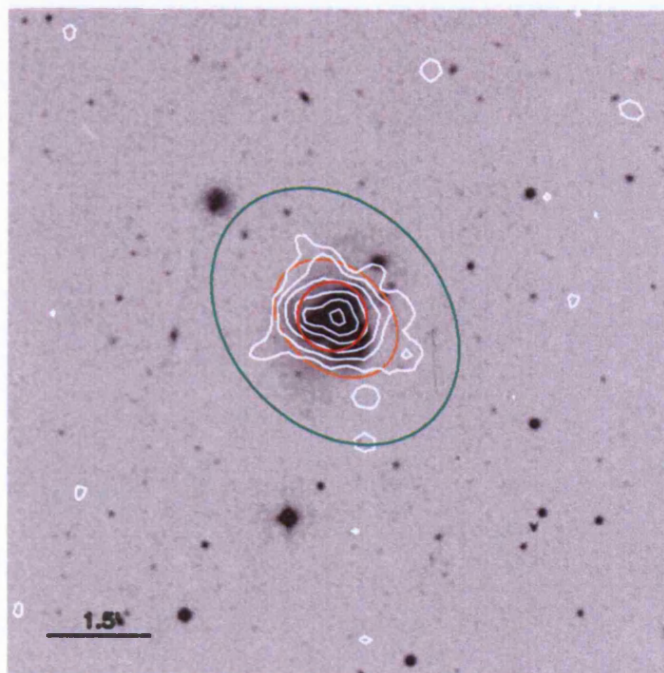


Figure 3.11: Overlay of contours from the PSPC observations of NGC3395 and NGC3665 on DSS images

NGC 3690



NGC 4236

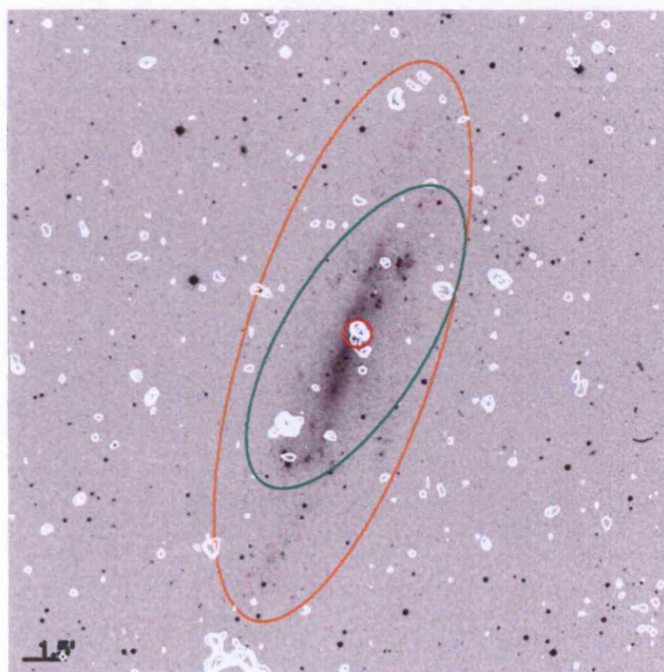
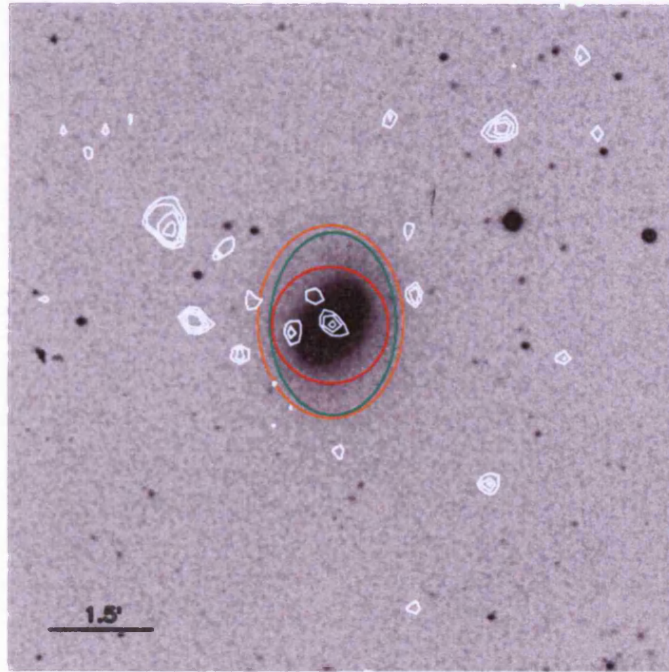


Figure 3.12: Overlay of contours from the PSPC observations of NGC3690 and NGC4236 on DSS images

NGC 4245



NGC 4303

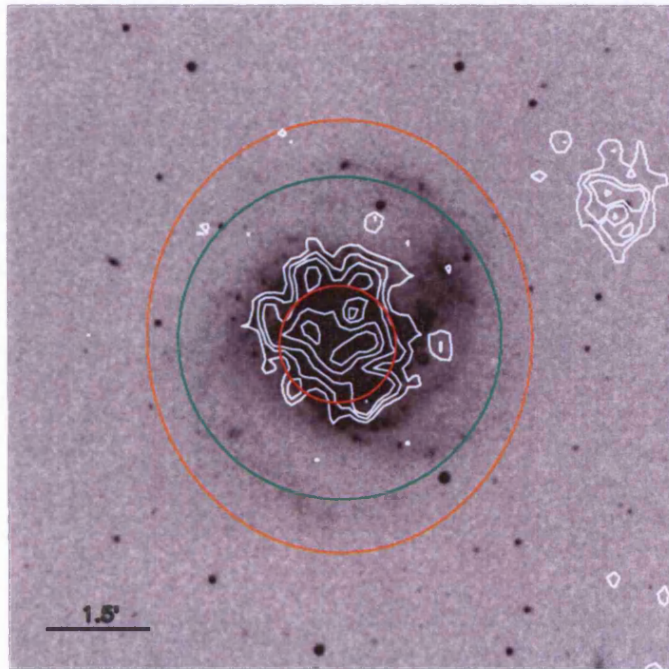
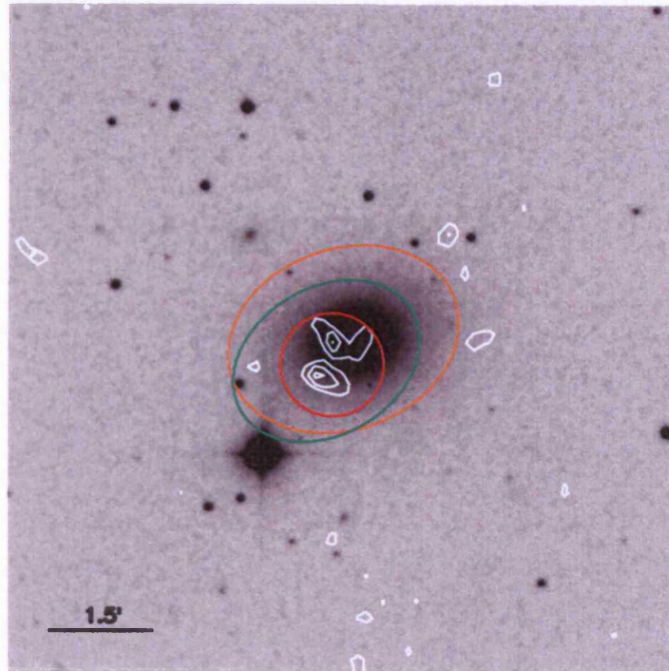


Figure 3.13: Overlay of contours from the PSPC observations of NGC4245 and NGC4303 on DSS images

NGC 4459



NGC 4470

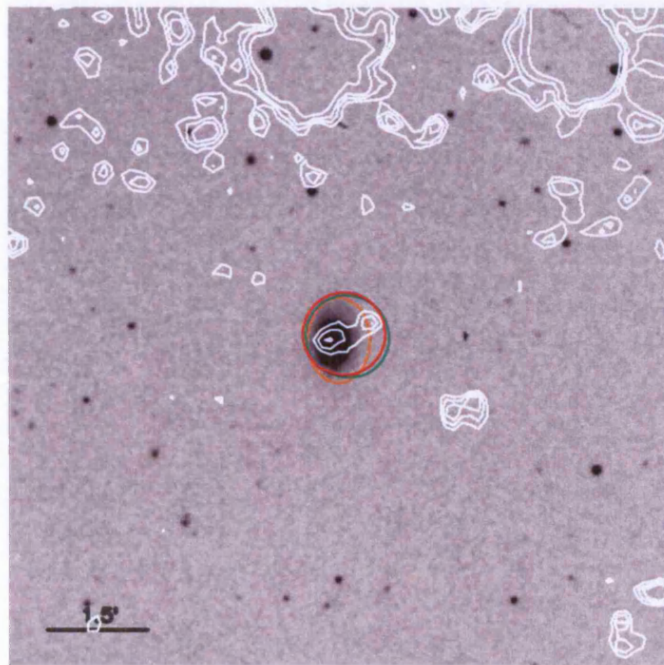
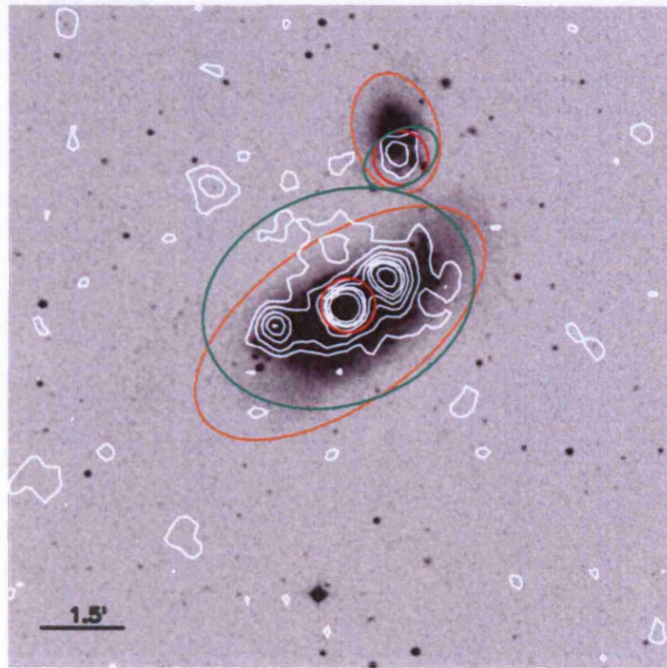


Figure 3.14: Overlay of contours from the PSPC observations of NGC4459 and NGC4470 on DSS images

NGC 4485/90



NGC 4526

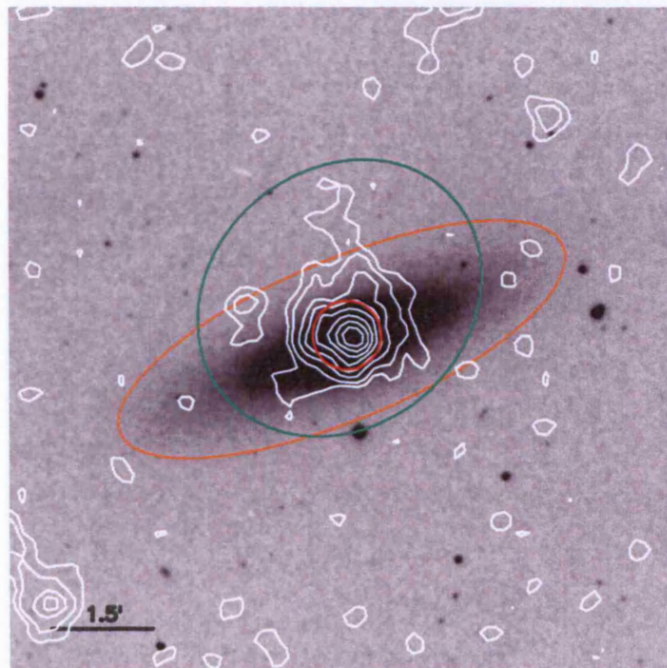
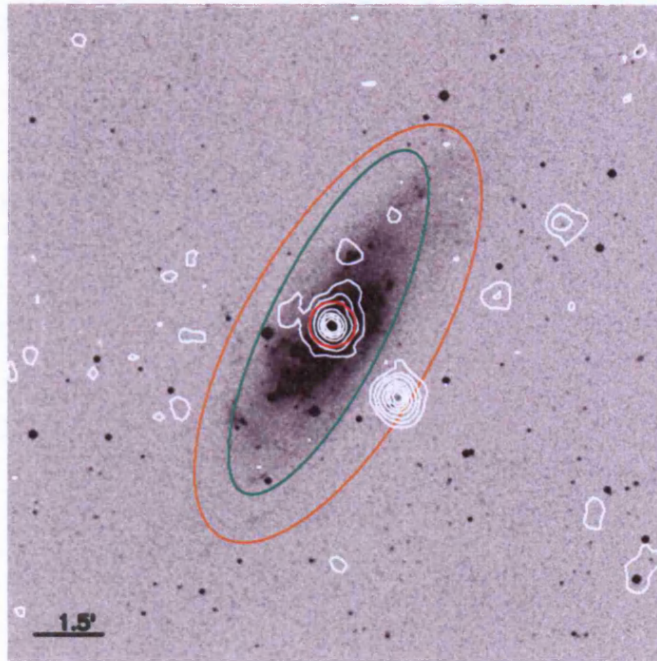


Figure 3.15: Overlay of contours from the PSPC observations of NGC4485/90 and NGC4526 on DSS images

NGC 4559



NGC 4631

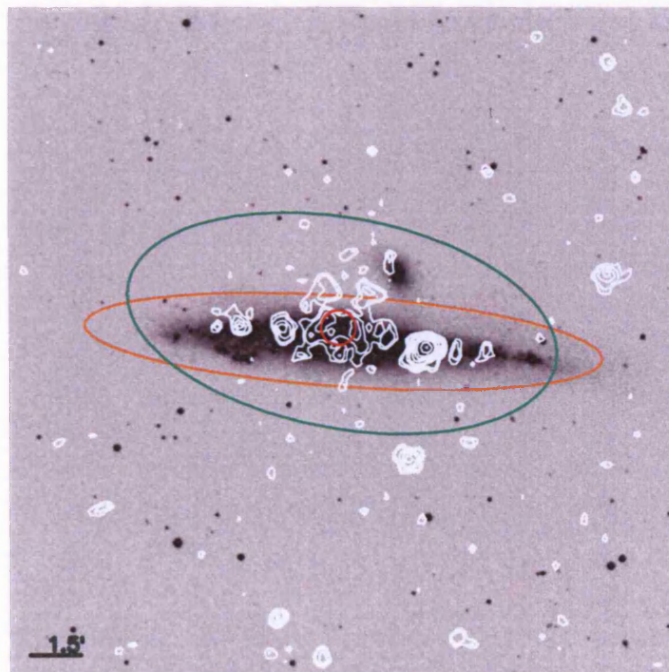
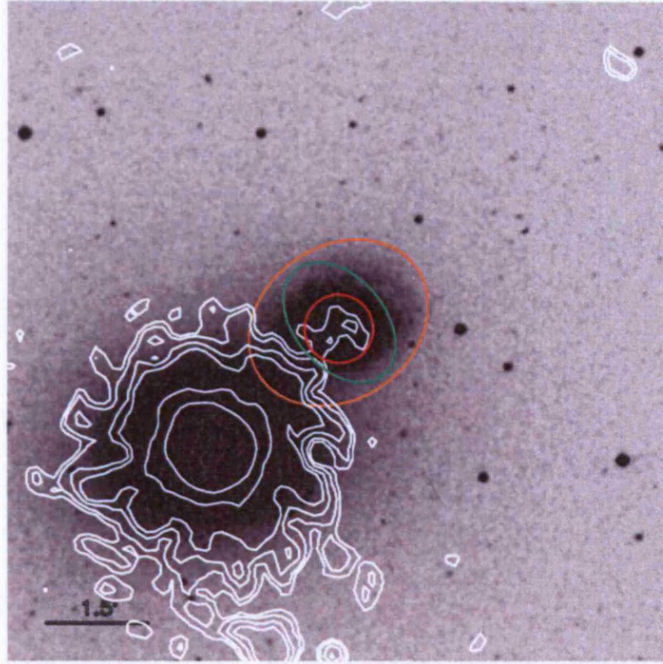


Figure 3.16: Overlay of contours from the PSPC observations of NGC4559 and NGC4631 on DSS images

NGC 4647



NGC 4654

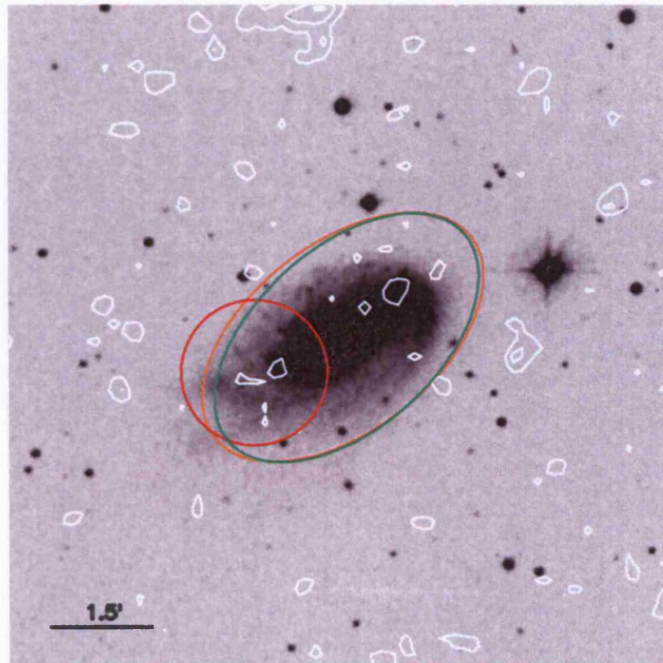
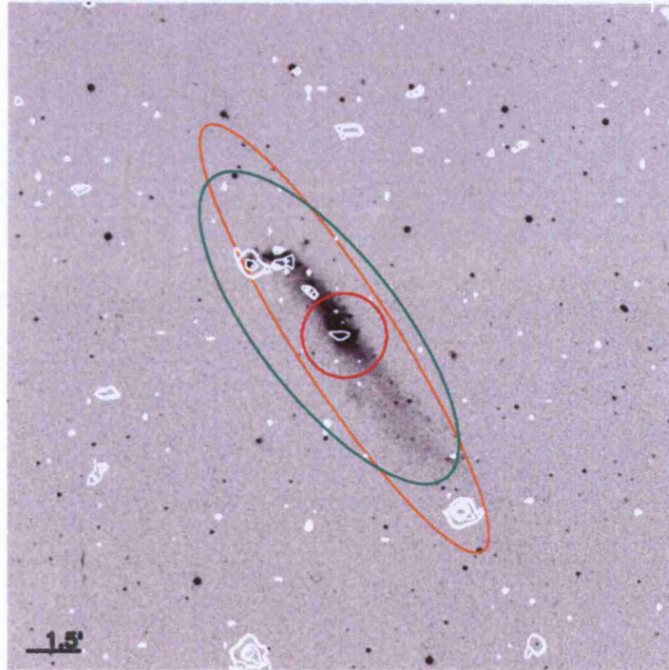


Figure 3.17: Overlay of contours from the PSPC observations of NGC4647 and NGC4654 on DSS images

NGC 4656



NGC 5204

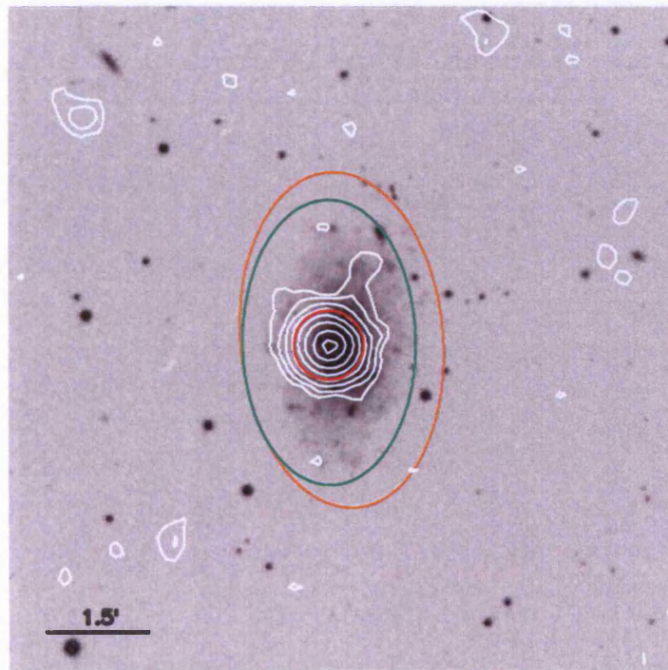
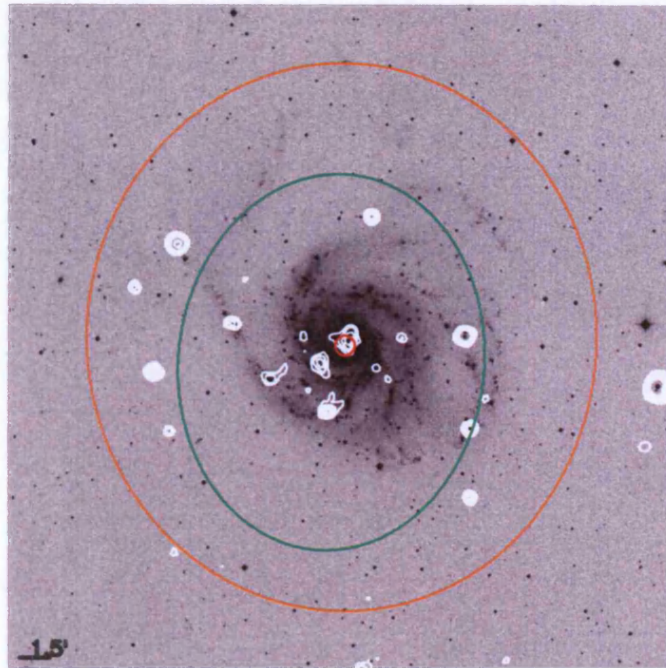


Figure 3.18: Overlay of contours from the PSPC observations of NGC4656 and NGC5204 on DSS images

NGC 5457



NGC 5775

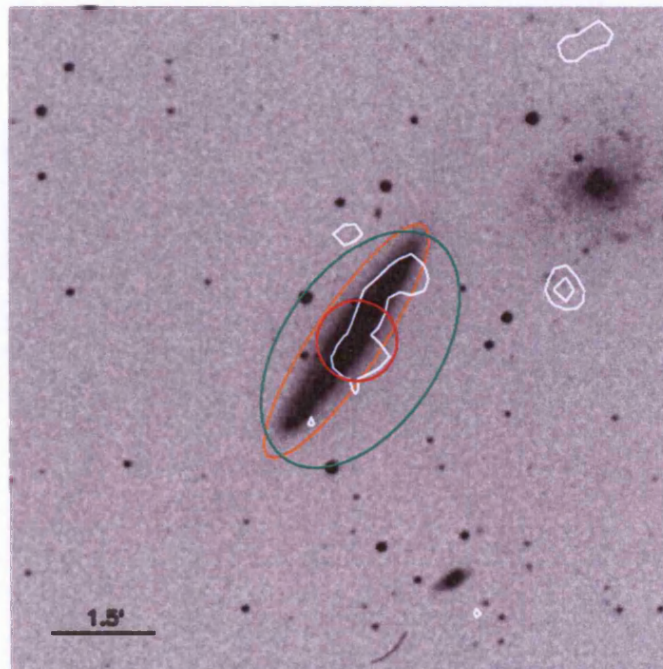
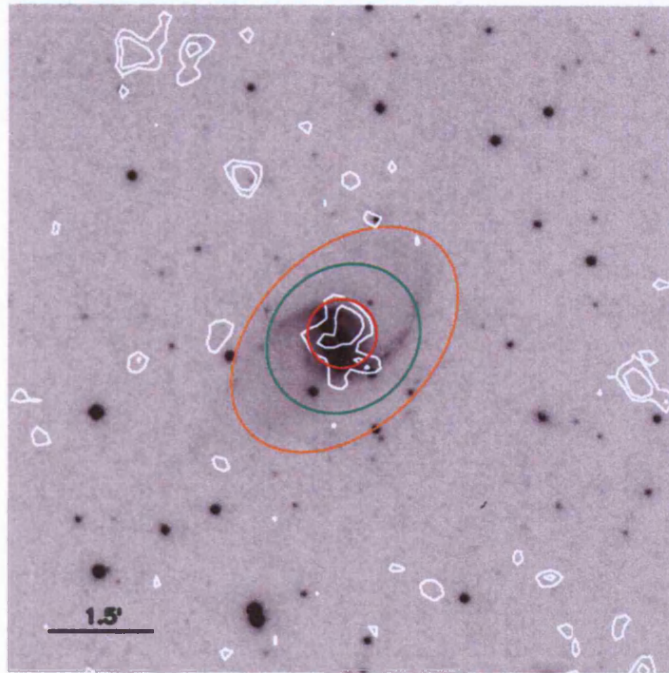


Figure 3.19: Overlay of contours from the PSPC observations of NGC5775 and NGC5866 on DSS images

NGC 5905



NGC 5907

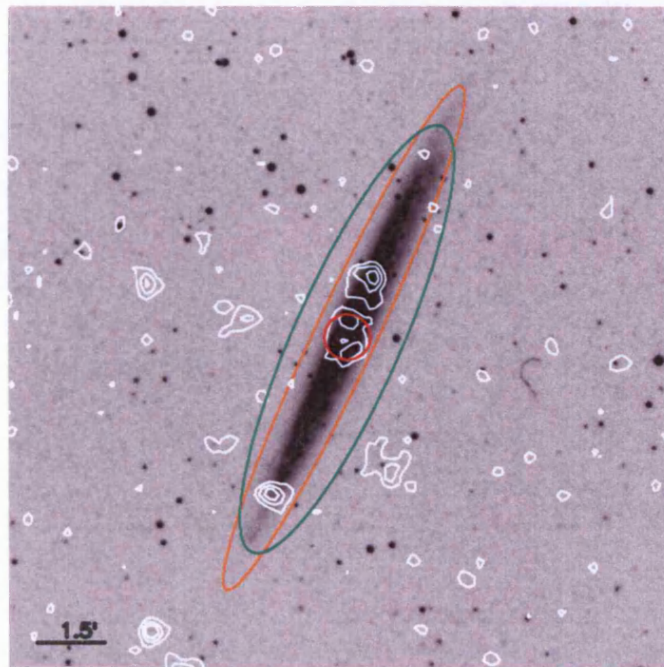
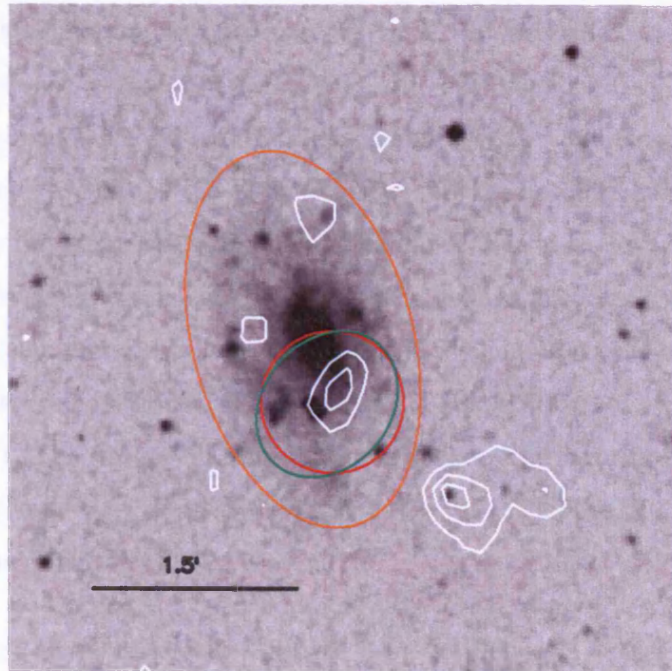


Figure 3.20: Overlay of contours from the PSPC observations of NGC5905 and NGC5907 on DSS images

NGC 6236



NGC 6946

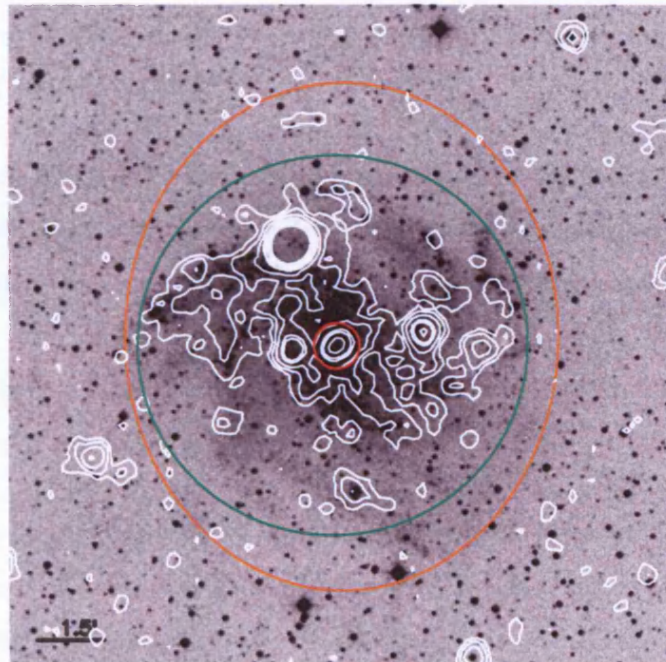


Figure 3.21: Overlay of contours from the PSPC observations of NGC6236 and NGC6946 on DSS images

3.3.1 X-ray measurements

The X-ray fluxes have been measured from three different regions. Firstly the D25 ellipse was used. This is defined as the isophotal ellipse at $\sim \mu_B = 25 \text{ mag arcsec}^{-2}$ (orange ellipse in figures 3.1 - 3.22). Although the D25 ellipse is a well defined objective way to measure the emission from a galaxy, it is not well suited for the X-ray emission of star-forming galaxies as there is often a strong superwind component extending along the minor axis of the galaxies. In these cases the D25 ellipse does not include this component as it is defined according to the optical isophotal profile of the galaxy. For this reason the integrated X-ray emission has been also measured using an arbitrarily defined region which includes all the X-ray emission of each object (green ellipse in figures 3.1 - 3.22). The fluxes (and luminosities) measured using this method have been used in all further analysis as they are more representative of the integrated emission of the galaxy than the measurements with the D25 ellipse.

Finally the nuclear emission has been measured using a circular aperture centered at the centroid of the X-ray source closest to the optical nucleus of the galaxy (red circle in figures 3.1 - 3.22). In the cases of galaxies which do not have a strong point source in the nuclear region the aperture was centered at the peak of the diffuse emission. The size of this aperture is the size of a circle which includes 75% of the total energy of a point source at the off-axis angle of each object. This is listed in column 7 of Table 3.3.

Table 3.4 presents the fluxes estimated from each of the three different regions. The factors used to convert the count rates to fluxes are calculated for a 0.8keV thermal plasma absorbed by a column density equal to the galactic at the line of sight of each galaxy, taken from Stark et al. (1992) (Table 3.3). This model is an adequate representation of the *ROSAT* spectra of other star-forming galaxies eg. Read et al. (1997). The absorption corrected fluxes are based on the same assumptions, but are corrected for the galactic absorption.

For the luminosities shown in Table 3.5 the fluxes from Table 3.4 have been used together with the distances given by Ho, Filippenko & Sargent (1997a). It is noted that these distances are determined assuming a Hubble constant of $75 \text{ km s}^{-1} \text{ Mpc}^{-1}$ and are corrected for the local group infall velocity.

Table 3.2: Multiwavelength properties of the galaxies (I. fluxes)

Name (1)	F60 μ (2)	FFIR (3)	H α (4)	H α EW (5)	H α integr (6)	FRAD (7)
NGC 520	31.55 \pm 0.049	-11.79	-13.64	33.22	-12.4	180
NGC 521	0.65 \pm 0.123	-13.22	-14.57	1.09		
NGC 598	419.65 \pm 62.95	-10.53	-14.7	2.36		3300
NGC 660	69.92 \pm 0.089	-11.45	-13.33	28.82	-11.64	387
NGC 891	61.1 \pm 9.164	-11.35	> -14.73		-11.68	701
NGC 1569	45.41 \pm 1.816	-11.68	-13.01	20.18	-10.64	411
NGC 2146	131 \pm 5.24	-11.18	-12.79	60.44	-11.27	1087
NGC 2276	14.39 \pm 0.058	-12.07	-13.34	67.51	-11.26	283
NGC 2342	7.96 \pm 0.045	-12.24	-12.83	63.37		
NGC 2403	51.55 \pm 7.732	-11.45	> -14.85	2.15		330
NGC 2537	3.24 \pm 0.194	-12.73	-13.07	98.61		
NGC 2750	3.96 \pm 0.035	-12.65	-12.65	69.11		
NGC 2903	52.38 \pm 7.857	-11.45	-12.63	68.9	-10.67	407
NGC 3034	1.27E+03 \pm 190.7	-10.23	> -11.8	166.84		7657
NGC 3077	14.66 \pm 0.039	-12.09	> -12.87	169	-11.22	33.2
NGC 3184	8.92 \pm 0.034	-12.18	-13.12	77.49	-11.12	55.9
NGC 3198	6.46 \pm 1.615	-12.36	-13.78	29.79		27.6
NGC 3310	34.13 \pm 0.052	-11.77	> -12.77	40.26		383
NGC 3319	0.61 \pm 0.091	< -13.13	-15.17	1.79		11.5
NGC 3359	6.27 \pm 0.03	-12.38	-14.46	6.09		50.1
NGC 3395	10.77 \pm 0.03	-12.24	> -13.56	28.52		29
NGC 3665	1.96 \pm 0.04	-12.83	-13.82	3.42		49
NGC 3690	121.64 \pm 0.069	-11.26	-12.67	64.49	-11.09	300
NGC 4236	3.98 \pm 0.596	-12.59	> -14.37			28.1
NGC 4245	0.81 \pm 0.04	-13.22	-14.3	1.55		
NGC 4303	41 \pm 3.28	-11.64	-12.84	12.32	-10.85	416
NGC 4449	37 \pm 0.099	-11.71	-12.62	44.01	-10.59	266
NGC 4470	1.9 \pm 0.152	-12.95	> -13.83	33.84		
NGC 4485	< 1.86 \pm	< -12.97	-14.79	4.18		
NGC 4490	47.79 \pm 0.063	-11.58	-14.08	5.32		774
NGC 4526	5.63 \pm 0.054	-12.42	-13.61	2.14		
NGC 4559	9.69 \pm 2.422	-12.18	-14	8.91		65.4
NGC 4631	82.9 \pm 0.111	-11.27	-14.33	233	-10.71	1200
NGC 4647	6.1 \pm 0.304	-12.4	-14.01	14.29	-11.67	
NGC 4654	14.7 \pm 0.734	-12.04	-13.46	42.08	-11.55	117
NGC 4656	5.9 \pm 0.885	-12.47	-13.85	40.6		62.6
NGC 5204	2.33 \pm 0.232	-12.84	> -14.53	29.2	-11.59	5
NGC 5457	88.04 \pm 13.2	-11.22	-13.33	19.6		750
NGC 5775	1.33 \pm 0.079	-12.81	> -14.17	5.97		190
NGC 5905	3.11 \pm 0.053	-12.72	-13.13	31.28		
NGC 5907	8.78 \pm 1.316	-12.06	-14.49	2.27	-11.48	89.5
NGC 6236	0.64 \pm 0.038	-13.38	-14.41	38.8		
NGC 6946	136.69 \pm 20.5	-11.06	> -13.01	34.32	-10.5	1395
NGC 7448	8.32 \pm 0.042	-12.31	-14.01	4.64	-11.58	

Notes: (1) Name of the galaxy, (2) IRAS 60 μ flux in Jy, (3) log of the 42-122 μ FIR flux in erg cm⁻² s⁻¹, (4) log of the nuclear H α flux in erg sec⁻¹ cm⁻², (5) Equivalent width of H α for the nucleus in Å, (6) log of the integrated H α flux in erg sec⁻¹ cm⁻² (from Kennicutt & Kent (1983) and Young, Allen, Kenney, Lesser & Rownd (1996)), (7) 1.42GHz integrated radio flux from Condon (1987) in mJy.

The data in columns (2),(3),(5) and (6) are taken (from Ho, Filippenko & Sargent 1997a).

Table 3.3: Conversion factors to X-ray fluxes

Name	Exposure	Column density cm ⁻²	Conv. factor observed	Conv. factor corrected	Off-axis angle degrees	Radius degrees
(1)	(2)	(3)	(4)	(5)	(6)	(7)
NGC 520	13235	3.27E+20	9.31	1.36	0.61	0.009
NGC 521	11587	3.13E+20	9.29	1.36	14.29	0.013
NGC 598	10594	5.58E+20	9.45	1.51	13.64	0.013
NGC 660	7465	4.86E+20	9.43	1.48	0.65	0.009
NGC 891	24137	7.64E+20	9.48	1.61	0.99	0.009
NGC 1569	4185	2.24E+21	9.56	2.43	0.19	0.009
NGC 2146	4930	7.30E+20	9.48	1.6	0.17	0.009
NGC 2276	4179	5.32E+20	9.45	1.49	0.51	0.009
NGC 2342	8852	8.93E+20	9.48	1.88	2.65	0.009
NGC 2403	8626	4.13E+20	9.39	1.42	0.31	0.009
NGC 2547	13370	4.64E+20	9.42	1.45	0.24	0.009
NGC 2750	7097	3.52E+20	9.34	1.38	13.06	0.011
NGC 2903	8511	3.14E+20	9.3	1.36	0.17	0.009
NGC 3034	12488	3.98E+20	9.38	1.41	0.19	0.009
NGC 3077	6386	3.88E+20	9.37	1.41	5.44	0.009
NGC 3184	8292	1.12E+20	8.72	1.15	0.35	0.009
NGC 3198	12510	1.02E+20	8.65	1.13	0.18	0.009
NGC 3310	7717	1.13E+20	8.72	1.15	0.19	0.009
NGC 3319	7626	1.36E+20	8.84	1.19	0.98	0.009
NGC 3359	7893	9.77E+19	8.62	1.13	1.01	0.009
NGC 3395	15125	1.94E+20	9.06	1.25	1.12	0.009
NGC 3665	6355	2.06E+20	9.09	1.27	0.17	0.009
NGC 3690	5609	9.86E+19	8.63	1.13	0.32	0.009
NGC 4236	11000	1.76E+20	9.00	1.23	0.62	0.009
NGC 4245	5911	1.71E+20	8.98	1.23	16.31	0.015
NGC 4303	7560	1.67E+20	8.97	1.23	16.50	0.015
NGC 4449	7440	1.37E+20	8.84	1.19	0.41	0.009
NGC 4470	24066	1.65E+20	8.96	1.22	10.89	0.010
NGC 4485	29941	1.78E+20	9.00	1.24	3.93	0.008
NGC 4485	29941	1.78E+20	9.00	1.24	1.67	0.009
NGC 4526	17785	1.65E+20	8.96	1.22	0.22	0.009
NGC 4559	16448	4.93E+19	8.23	1.01	0.28	0.009
NGC 4631	16988	1.27E+20	8.79	1.17	0.40	0.009
NGC 4647	12192	2.20E+20	9.13	1.28	2.97	0.009
NGC 4654	5272	2.32E+20	9.16	1.28	18.04	0.017
NGC 4656	5272	1.23E+20	8.77	1.17	19.00	0.018
NGC 5204	13868	1.39E+20	8.85	1.2	0.30	0.009
NGC 5457	32994	1.16E+20	8.73	1.16	0.83	0.009
NGC 5775	5904	3.48E+20	9.33	1.38	8.56	0.009
NGC 5905	7149	1.44E+20	8.88	1.2	0.19	0.009
NGC 5907	15824	1.44E+20	8.88	1.2	0.34	0.009
NGC 6236	6520	4.45E+20	9.41	1.44	8.98	0.009
NGC 6946	27955	2.11E+21	9.54	2.34	0.24	0.009
NGC 7448	6771	6.12E+20	9.46	1.54	6.52	0.008

Notes: (1) Name of the galaxy, (2) Effective exposure (after excluding high background intervals), (3) Galactic neutral hydrogen column density (from Stark et al. 1992), (4) Conversion factor for observed flux (see text) in units of 10^{-12} erg sec⁻¹ cm⁻² count⁻¹, (5) Conversion factor for absorption corrected flux (see text) in units of 10^{-11} erg sec⁻¹ cm⁻² count⁻¹, (6) Off axis angle of the nuclear source in degrees, (7) radius in degrees of the circle including 75% of the emission of a point source.

Table 3.4: Measured X-ray fluxes

Name (1)	D25 flux		Integrated flux		Nuclear flux	
	observed (2)	corrected (3)	observed (4)	corrected (5)	observed (6)	corrected (7)
NGC 520	0.73 ± 0.07	1.06 ± 0.10	0.67 ± 0.07	0.97 ± 0.10	0.53 ± 0.06	0.77 ± 0.09
NGC 521	0.72 ± 0.08	1.05 ± 0.11	0.69 ± 0.07	1.00 ± 0.11	0.53 ± 0.07	0.78 ± 0.10
NGC 598	80.97 ± 0.53	129.39 ± 0.84	82.87 ± 0.53	132.41 ± 0.85	45.30 ± 0.39	72.38 ± 0.63
NGC 660	1.24 ± 0.13	1.95 ± 0.20	1.15 ± 0.12	1.81 ± 0.19	0.79 ± 0.10	1.25 ± 0.16
NGC 891	4.63 ± 0.14	7.85 ± 0.23	4.47 ± 0.13	7.60 ± 0.23	2.30 ± 0.10	3.91 ± 0.16
NGC 1569	3.76 ± 0.29	9.56 ± 0.75	3.96 ± 0.30	10.08 ± 0.77	2.72 ± 0.25	6.92 ± 0.63
NGC 2146	5.42 ± 0.32	9.15 ± 0.55	5.09 ± 0.31	8.58 ± 0.53	2.91 ± 0.24	4.92 ± 0.40
NGC 2276	1.55 ± 0.19	2.45 ± 0.30	1.53 ± 0.19	2.41 ± 0.29	1.00 ± 0.15	1.58 ± 0.24
NGC 2342	0.86 ± 0.10	1.70 ± 0.19	0.98 ± 0.10	1.95 ± 0.20	0.79 ± 0.09	1.57 ± 0.18
NGC 2403	9.70 ± 0.33	14.66 ± 0.49	8.98 ± 0.31	13.58 ± 0.47	1.22 ± 0.12	1.85 ± 0.18
NGC 2547	0.08 ± 0.02	0.12 ± 0.04	0.06 ± 0.02	0.10 ± 0.03	0.07 ± 0.02	0.12 ± 0.04
NGC 2750	0.41 ± 0.07	0.61 ± 0.11	0.35 ± 0.07	0.51 ± 0.10	0.34 ± 0.07	0.50 ± 0.10
NGC 2903	8.08 ± 0.30	11.81 ± 0.43	7.94 ± 0.30	11.61 ± 0.43	3.74 ± 0.20	5.47 ± 0.30
NGC 3034	100.74 ± 0.87	151.43 ± 1.31	111.23 ± 0.91	167.19 ± 1.37	46.32 ± 0.59	69.63 ± 0.89
NGC 3077	0.51 ± 0.09	0.77 ± 0.13	0.48 ± 0.08	0.72 ± 0.13	0.42 ± 0.08	0.63 ± 0.12
NGC 3184	1.84 ± 0.14	2.43 ± 0.18	1.58 ± 0.13	2.08 ± 0.17	0.23 ± 0.05	0.30 ± 0.06
NGC 3198	0.64 ± 0.07	0.84 ± 0.09	0.73 ± 0.07	0.95 ± 0.09	0.19 ± 0.04	0.25 ± 0.05
NGC 3310	7.33 ± 0.29	9.67 ± 0.38	7.40 ± 0.29	9.76 ± 0.38	5.27 ± 0.24	6.95 ± 0.32
NGC 3319	0.51 ± 0.08	0.69 ± 0.10	0.42 ± 0.07	0.57 ± 0.09	0.20 ± 0.05	0.27 ± 0.07
NGC 3359	2.57 ± 0.17	3.37 ± 0.22	2.44 ± 0.16	3.20 ± 0.21	0.66 ± 0.09	0.87 ± 0.11
NGC 3395	0.83 ± 0.07	1.15 ± 0.10	0.92 ± 0.07	1.26 ± 0.10	0.56 ± 0.06	0.77 ± 0.08
NGC 3665	2.11 ± 0.17	2.95 ± 0.24	1.21 ± 0.13	1.69 ± 0.18	1.36 ± 0.14	1.91 ± 0.20
NGC 3690	6.60 ± 0.32	8.64 ± 0.42	8.33 ± 0.36	10.91 ± 0.47	4.58 ± 0.27	6.00 ± 0.35
NGC 4236	2.23 ± 0.14	3.04 ± 0.19	1.79 ± 0.12	2.44 ± 0.17	0.30 ± 0.05	0.42 ± 0.07
NGC 4245	0.34 ± 0.07	0.47 ± 0.10	0.32 ± 0.07	0.43 ± 0.10	0.28 ± 0.07	0.39 ± 0.09
NGC 4303	5.58 ± 0.26	7.65 ± 0.35	5.32 ± 0.25	7.30 ± 0.35	2.65 ± 0.18	3.63 ± 0.24
NGC 4449	10.66 ± 0.36	14.35 ± 0.48	11.13 ± 0.36	14.99 ± 0.49	2.10 ± 0.16	2.83 ± 0.21
NGC 4470	0.19 ± 0.03	0.26 ± 0.04	0.24 ± 0.03	0.32 ± 0.04	0.26 ± 0.03	0.36 ± 0.04
NGC 4485	0.30 ± 0.03	0.41 ± 0.04	0.29 ± 0.03	0.40 ± 0.04	0.26 ± 0.03	0.35 ± 0.04
NGC 4490	6.25 ± 0.14	8.61 ± 0.19	6.44 ± 0.14	8.88 ± 0.19	1.97 ± 0.08	2.71 ± 0.11
NGC 4526	2.91 ± 0.12	3.97 ± 0.17	2.86 ± 0.12	3.90 ± 0.16	1.41 ± 0.08	1.92 ± 0.12
NGC 4559	12.46 ± 0.25	15.30 ± 0.31	7.69 ± 0.20	9.44 ± 0.24	3.31 ± 0.13	4.06 ± 0.16
NGC 4631	5.53 ± 0.17	7.35 ± 0.23	7.75 ± 0.20	10.32 ± 0.25	0.41 ± 0.05	0.54 ± 0.06
NGC 4647	1.36 ± 0.10	1.91 ± 0.14	0.47 ± 0.06	0.65 ± 0.08	0.29 ± 0.05	0.41 ± 0.07
NGC 4654	0.39 ± 0.08	0.54 ± 0.11	0.37 ± 0.08	0.51 ± 0.11	0.21 ± 0.06	0.29 ± 0.08
NGC 4656	2.45 ± 0.11	3.27 ± 0.15	1.65 ± 0.09	2.20 ± 0.13	0.10 ± 0.02	0.13 ± 0.03
NGC 5204	7.87 ± 0.22	10.67 ± 0.30	7.87 ± 0.22	10.68 ± 0.30	7.23 ± 0.22	9.81 ± 0.29
NGC 5457	15.33 ± 0.20	20.37 ± 0.27	14.80 ± 0.20	19.66 ± 0.26	0.43 ± 0.03	0.57 ± 0.05
NGC 5775	1.00 ± 0.13	1.48 ± 0.19	1.06 ± 0.13	1.57 ± 0.19	0.25 ± 0.06	0.38 ± 0.09
NGC 5905	0.54 ± 0.08	0.73 ± 0.11	0.45 ± 0.08	0.61 ± 0.10	0.30 ± 0.06	0.40 ± 0.08
NGC 5907	1.15 ± 0.08	1.56 ± 0.11	1.25 ± 0.08	1.69 ± 0.11	0.29 ± 0.04	0.39 ± 0.05
NGC 6236	0.40 ± 0.08	0.62 ± 0.12	0.12 ± 0.04	0.18 ± 0.06	0.13 ± 0.04	0.20 ± 0.07
NGC 6946	14.09 ± 0.22	34.57 ± 0.54	13.76 ± 0.22	33.74 ± 0.53	0.83 ± 0.05	2.02 ± 0.13
NGC 7448	0.74 ± 0.10	1.20 ± 0.17	0.84 ± 0.11	1.37 ± 0.18	0.45 ± 0.08	0.73 ± 0.13

Notes: (1) Name of the galaxy, (2), (3) observed and absorption corrected fluxes estimated from the D25 ellipse in units of $10^{-13} \text{erg cm}^{-2} \text{s}^{-1}$ in the 0.1-2.4keV band, (4), (5) observed and absorption corrected integrated fluxes in units of $10^{-13} \text{erg cm}^{-2} \text{s}^{-1}$ in the 0.1-2.4keV band (see text), (6), (7) observed and absorption corrected nuclear fluxes in units of $10^{-13} \text{erg cm}^{-2} \text{s}^{-1}$ in the 0.1-2.4keV band (see text).

Table 3.5: Multiwavelength properties of the galaxies (II. luminosities)

Name (1)	X-ray D25 lum.		X-ray Integrated lum.		X-ray Nuclear lum.		H α	H α	L60 μ	LFIR	LRAD
	observed (2)	corrected (3)	observed (4)	corrected (5)	observed (6)	corrected (7)	(nucl) (8)	(integr) (9)	(10)	(11)	(12)
NGC 520	6.71 \pm 0.66	9.82 \pm 0.97	6.15 \pm 0.63	8.99 \pm 0.92	4.88 \pm 0.56	7.13 \pm 0.82	2.12	36.80	14.58 \pm 0.02	149.92	166.39
NGC 521	38.64 \pm 4.07	56.49 \pm 5.97	36.81 \pm 3.98	53.95 \pm 5.83	28.64 \pm 3.51	41.88 \pm 5.14	1.44		1.74 \pm 0.33	32.35	
NGC 598	0.47 \pm 0.003	0.76 \pm 0.005	0.49 \pm 0.003	0.78 \pm 0.005	0.27 \pm 0.002	0.42 \pm 0.004	0		0.12 \pm 0.02	1.73	1.93
NGC 660	2.07 \pm 0.21	3.24 \pm 0.33	1.92 \pm 0.2	3.02 \pm 0.32	1.32 \pm 0.17	2.07 \pm 0.26	0.78	38.15	5.82 \pm 0.01	59.09	64.45
NGC 891	5.09 \pm 0.15	8.65 \pm 0.25	4.93 \pm 0.15	8.38 \pm 0.25	2.54 \pm 0.1	4.32 \pm 0.18	> 0.02	23.03	3.37 \pm 0.50	49.24	77.28
NGC 1569	0.12 \pm 0.01	0.29 \pm 0.02	0.12 \pm 0.01	0.31 \pm 0.02	0.08 \pm 0.01	0.21 \pm 0.02	0.03	7.01	0.07 \pm 0.003	0.64	1.26
NGC 2146	19.19 \pm 1.14	32.36 \pm 1.93	17.99 \pm 1.11	30.34 \pm 1.87	10.3 \pm 0.84	17.42 \pm 1.41	5.74	190.04	23.18 \pm 0.93	233.80	384.65
NGC 2276	25.12 \pm 3.03	39.63 \pm 4.79	24.77 \pm 3.01	39.08 \pm 4.75	16.26 \pm 2.44	25.64 \pm 3.85	7.40	890.18	11.65 \pm 0.05	137.87	458.42
NGC 2342	49.55 \pm 5.53	98.4 \pm 10.99	56.62 \pm 5.92	112.46 \pm 11.75	45.71 \pm 5.32	90.57 \pm 10.54	85.46		22.99 \pm 0.13	332.47	
NGC 2403	2.05 \pm 0.07	3.09 \pm 0.1	1.9 \pm 0.07	2.86 \pm 0.1	0.26 \pm 0.02	0.39 \pm 0.04	> 0.003		0.54 \pm 0.08	7.49	6.96
NGC 2537	0.07 \pm 0.02	0.11 \pm 0.03	0.06 \pm 0.02	0.1 \pm 0.03	0.07 \pm 0.02	0.11 \pm 0.03	0.82		0.16 \pm 0.01	1.80	
NGC 2750	7.29 \pm 1.3	10.79 \pm 1.92	6.11 \pm 1.19	9.04 \pm 1.76	5.96 \pm 1.17	8.79 \pm 1.74	39.49		3.49 \pm 0.03	39.49	
NGC 2903	3.84 \pm 0.14	5.61 \pm 0.21	3.77 \pm 0.14	5.51 \pm 0.2	1.77 \pm 0.1	2.59 \pm 0.14	1.11	101.50	1.24 \pm 0.19	16.84	19.32
NGC 3034	32.58 \pm 0.28	48.98 \pm 0.42	35.97 \pm 0.3	54.08 \pm 0.44	15 \pm 0.19	22.54 \pm 0.29	> 5.13		20.54 \pm 3.08	190.45	247.65
NGC 3077	0.03 \pm 0.005	0.04 \pm 0.01	0.03 \pm 0.004	0.04 \pm 0.01	0.02 \pm 0.004	0.03 \pm 0.01	> 0.07	3.18	0.04 \pm 0.0001	0.43	0.17
NGC 3184	1.67 \pm 0.13	2.2 \pm 0.17	1.43 \pm 0.12	1.88 \pm 0.15	0.2 \pm 0.04	0.27 \pm 0.06	0.69	68.68	0.404 \pm 0.002	5.98	5.06
NGC 3198	0.89 \pm 0.09	1.17 \pm 0.12	1.01 \pm 0.1	1.32 \pm 0.13	0.26 \pm 0.05	0.35 \pm 0.07	0.23		0.45 \pm 0.11	6.09	3.85
NGC 3310	30.69 \pm 1.21	40.46 \pm 1.59	30.97 \pm 1.21	40.83 \pm 1.6	22.03 \pm 1.02	29.11 \pm 1.35	> 7.10		7.14 \pm 0.01	71.03	160.20
NGC 3319	0.81 \pm 0.12	1.09 \pm 0.16	0.67 \pm 0.11	0.9 \pm 0.15	0.32 \pm 0.08	0.43 \pm 0.1	0.011		0.05 \pm 0.08	< 1.17	1.82
NGC 3359	11.32 \pm 0.74	14.86 \pm 0.97	10.74 \pm 0.72	14.09 \pm 0.94	2.91 \pm 0.37	3.82 \pm 0.49	0.15		1.38 \pm 0.01	18.38	22.09
NGC 3395	7.48 \pm 0.63	10.3 \pm 0.87	8.22 \pm 0.67	11.35 \pm 0.92	4.98 \pm 0.52	6.87 \pm 0.71	> 2.47		4.84 \pm 0.01	51.67	26.04
NGC 3665	26.49 \pm 2.18	36.98 \pm 3.05	15.17 \pm 1.65	21.18 \pm 2.31	17.14 \pm 1.75	23.93 \pm 2.45	1.90		1.23 \pm 0.02	18.57	61.53
NGC 3690	128.82 \pm 6.22	168.66 \pm 8.15	162.55 \pm 7	212.81 \pm 9.16	89.33 \pm 5.18	116.95 \pm 6.79	41.74	1586.88	118.74 \pm 0.07	1072.86	585.68
NGC 4236	0.13 \pm 0.01	0.18 \pm 0.01	0.1 \pm 0.01	0.14 \pm 0.01	0.02 \pm 0.003	0.02 \pm 0.004	> 0.002		0.012 \pm 0.002	0.15	0.16
NGC 4245	0.38 \pm 0.08	0.53 \pm 0.11	0.36 \pm 0.08	0.49 \pm 0.11	0.32 \pm 0.07	0.44 \pm 0.1	0.06		0.046 \pm 0.002	0.68	
NGC 4303	15.42 \pm 0.71	21.13 \pm 0.97	14.69 \pm 0.7	20.18 \pm 0.95	7.33 \pm 0.49	10.05 \pm 0.67	3.99	390.363	5.66 \pm 0.45	63.31	114.96
NGC 4449	1.15 \pm 0.04	1.55 \pm 0.05	1.2 \pm 0.04	1.61 \pm 0.05	0.23 \pm 0.02	0.3 \pm 0.02	0.26	27.67	0.199 \pm 0.001	2.01	2.86
NGC 4470	2.28 \pm 0.32	3.1 \pm 0.43	2.78 \pm 0.35	3.78 \pm 0.48	3.09 \pm 0.37	4.21 \pm 0.5	> 1.74		1.12 \pm 0.09	13.23	
NGC 4485	0.31 \pm 0.03	0.43 \pm 0.04	0.3 \pm 0.03	0.41 \pm 0.04	0.26 \pm 0.03	0.36 \pm 0.04	0.02		< 0.096	< 1.11	
NGC 4490	4.55 \pm 0.1	6.27 \pm 0.14	4.69 \pm 0.1	6.46 \pm 0.14	1.43 \pm 0.06	1.98 \pm 0.08	0.06		1.74 \pm 0.002	19.14	56.33

Name (1)	X-ray D25 lum.		X-ray Integrated lum.		X-ray Nuclear lum.		H α	H α	L60 μ	LFIR	LRAD
	observed (2)	corrected (3)	observed (4)	corrected (5)	observed (6)	corrected (7)	(nucl) (8)	(integr) (9)	(10)	(11)	(12)
NGC 4526	9.84 \pm 0.41	13.4 \pm 0.56	9.66 \pm 0.41	13.15 \pm 0.55	4.76 \pm 0.28	6.49 \pm 0.39	0.83		0.95 \pm 0.01	12.83	
NGC 4559	14.03 \pm 0.28	17.22 \pm 0.35	8.65 \pm 0.22	10.62 \pm 0.27	3.72 \pm 0.14	4.57 \pm 0.18	0.11		0.54 \pm 0.14	7.44	7.36
NGC 4631	3.15 \pm 0.1	4.19 \pm 0.13	4.42 \pm 0.11	5.87 \pm 0.14	0.23 \pm 0.03	0.31 \pm 0.03	0.03	111.04	2.361 \pm 0.003	30.58	68.34
NGC 4647	4.59 \pm 0.34	6.43 \pm 0.48	1.57 \pm 0.2	2.21 \pm 0.28	0.99 \pm 0.16	1.38 \pm 0.22	0.33	72.17	1.03 \pm 0.051	13.44	
NGC 4654	1.3 \pm 0.28	1.82 \pm 0.39	1.24 \pm 0.27	1.73 \pm 0.38	0.7 \pm 0.2	0.98 \pm 0.28	1.17	95.15	2.48 \pm 0.12	30.79	39.50
NGC 4656	1.52 \pm 0.07	2.03 \pm 0.09	1.02 \pm 0.06	1.36 \pm 0.08	0.06 \pm 0.01	0.08 \pm 0.02	0.09		0.18 \pm 0.03	2.10	3.882
NGC 5204	2.17 \pm 0.06	2.94 \pm 0.08	2.17 \pm 0.06	2.94 \pm 0.08	1.99 \pm 0.06	2.7 \pm 0.08	> 0.008	7.08	0.032 \pm 0.003	0.40	0.14
NGC 5457	5.35 \pm 0.07	7.11 \pm 0.09	5.16 \pm 0.07	6.85 \pm 0.09	0.15 \pm 0.01	0.2 \pm 0.02	0.16		1.53 \pm 0.23	21.02	26.16
NGC 5775	10.35 \pm 1.3	15.31 \pm 1.92	10.96 \pm 1.34	16.22 \pm 1.98	2.62 \pm 0.65	3.88 \pm 0.97	> 0.70		0.69 \pm 0.04	16.013	196.44
NGC 5905	12.74 \pm 1.93	17.22 \pm 2.61	10.67 \pm 1.77	14.42 \pm 2.39	7.03 \pm 1.44	9.51 \pm 1.94	17.48		3.67 \pm 0.06	44.93	
NGC 5907	3.06 \pm 0.21	4.14 \pm 0.29	3.31 \pm 0.22	4.48 \pm 0.3	0.76 \pm 0.11	1.03 \pm 0.14	0.09	87.93	1.17 \pm 0.17	23.130	23.77
NGC 6236	2.61 \pm 0.49	4 \pm 0.76	0.76 \pm 0.27	1.17 \pm 0.41	0.85 \pm 0.28	1.3 \pm 0.43	0.25		0.21 \pm 0.01	2.707	
NGC 6946	5.11 \pm 0.08	12.5 \pm 0.19	4.98 \pm 0.08	12.22 \pm 0.19	0.3 \pm 0.02	0.73 \pm 0.05	> 0.35	114.42	2.47 \pm 0.37	31.51	50.48
NGC 7448	8.11 \pm 1.11	13.18 \pm 1.82	9.23 \pm 1.19	15 \pm 1.94	4.93 \pm 0.87	8.04 \pm 1.42	1.07	288.85	4.57 \pm 0.02	53.79	

Notes: (1) Name of the galaxy, (2),(3) observed and absorption corrected luminosities estimated from the D25 ellipse in units of 10^{39} erg s^{-1} in the 0.1-2.4keV band, (4),(5) observed and absorption corrected integrated luminosities in units of 10^{39} erg s^{-1} in the 0.1-2.4keV band, (6),(7) observed and absorption corrected nuclear luminosities in units of 10^{39} erg s^{-1} in the 0.1-2.4keV band, (8) nuclear H α luminosity in units of 10^{39} erg s^{-1} , (9) integrated H α in units of 10^{39} erg s^{-1} , (10) IRAS 60 μ luminosity in units of 10^{42} erg s^{-1} , (11) 42-122 μ luminosity in units of 10^{42} erg s^{-1} , (12) 1.49GHz integrated radio luminosity in units of 10^{27} erg s^{-1} Hz $^{-1}$.

3.3.2 Multiwavelength data

In order to connect the X-ray properties of the galaxies in this sample with their properties in other wavebands, data from various sources have been used. The main source for these data is the work of Ho, Filippenko & Sargent (1997a) who apart from the nuclear optical line measurements present some other parameters for the host galaxies. The nuclear H_α luminosities and equivalent widths are taken from this work, as well as the distances, the total and bulge B-band luminosities and the FIR fluxes.

The H_α luminosities were measured using a $2'' \times 4''$ aperture, centered on the optical nucleus (Ho et al. 1995). The asymptotic B-band magnitudes are corrected for internal and Galactic extinction. The internal absorption was estimated using the the method of Holmberg (1958) who expressed it as a function of the inclination angle parameterised as a/b :

$$A^{int} = \alpha + \beta \log(a/b) \quad (3.1)$$

where a/b is the ratio of the major and minor axes of the galaxy. The values of α and β as well as the maximum value of A^{int} depend on the morphological type and are determined by de Vaucouleurs (1991). The bulge luminosity is not measured using a bulge-disk decomposition but rather following the relation of Simien & de Vaucouleurs (1986) which gives the contribution of the disk component to the total luminosity as a function of the morphological type of the galaxy. Finally the FIR fluxes are integrated fluxes for each galaxy and were obtained from various sources (for more details see Ho, Filippenko & Sargent 1997a).

The integrated H_α luminosities are obtained from the work of Kennicutt & Kent (1983) and Young, Allen, Kenney, Lesser & Rownd (1996). They are derived from narrow band imaging and include the $[N_{II}]$ line emission. In these cases where no integrated photometry was available, the nuclear measurements have been used as lower limits.

The 1.49GHz radio data are mainly taken from the atlas of Condon (1987) who observed a large sample of spiral galaxies with the VLA in the D configuration. This has low spatial resolution ($\sim 0.9'$) but high sensitivity and is therefore ideal to measure the integrated radio emission of these galaxies.

3.4 Correlations

For the correlation tests and the linear regression the ASURV (Lavalley, Isobe & Feigelson 1992, Isobe, Feigelson & Nelson 1986) survival statistical analysis package has been used. This is necessary because of the existence of one upper limit in the X-rays and several upper and/or lower limits on other bands. More specifically, the Kendal τ (Isobe et al. 1986) and Spearman ρ (Akritas 1997) tests implemented in ASURV are used to quantify the significance of the correlations between different parameters. Both methods assume random censoring and accept both upper and lower limits in both axes. In the cases where a strong correlation, with probability higher than 99% is found the parameters of the best fit line are calculated using the Schmitt's linear regression method (Schmitt 1985). This method can deal with upper and lower limits on both variables, but only one type of censoring in each one. Whenever possible the regression results have been compared with the best fit parameters obtained using the Buckley-James and the EM algorithms, which can only be used with data censored in one variable. The agreement between the two methods in general was very good. Only in the case of the radio vs. X-ray emission correlation there was a significant discrepancy. In this case the BJ results are adopted following Lavalley et al. (1992). These results are presented in Table 3.6.

In order to investigate the effect of the upper and lower limits, the regression analysis is repeated but this time excluding all censored data points. The results of this regression analysis are presented in Table 3.7. It is clear that they are very similar to the results derived using the full sample (detections plus limits). Only in the case of the integrated H_α emission against the integrated absorption corrected X-ray emission there is a significant discrepancy. The slope is ~ 0.6 if we take lower limits into account and 0.97 if we include only detections. Because of the very large number of lower limits (almost 56% of the data) which are clustered at lower values of H_α and X-ray luminosities, the former result may be biased, therefore in the following analysis only the results from the detections will be considered.

In all cases the correlations have also been tested in flux space using a formal correlation test. Plots of flux against flux show that in most cases the correlations persist, although they are less significant. However, it should be noted that although the presence of a correlation in flux space is indicative of a genuine correlation between the two physical parameters its absence does not necessarily rule out this possibility (Fabbiano et al. 1982). Especially for this sample, given that

NGC 7448

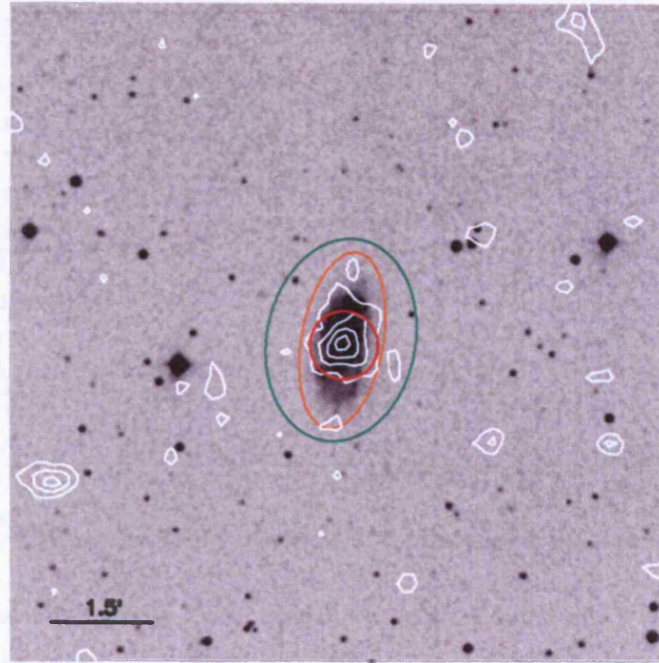


Figure 3.22: Overlay of contours from the PSPC observations of NGC7448 on DSS images

Table 3.6: The results of the correlations (bounds + detections)

Variables	Probability [†] %		Regression	
	Kendal τ	Spearman ρ	slope	intercept
logL α ,NUCL - logLX,NUCL	0.00	0.00	0.91 ± 0.15	3.1 ± 6.0
logLX,NUCL - logL α , NUCL	0.00	0.00	0.32 ± 0.10	18.8 ± 3.9
logL α ,INT - logLX,INT	0.00	0.02	1.00 ± 0.25	1.0 ± 9.9
logLX,INT - logL α ,INT	0.00	0.02	0.62 ± 0.11	14.2 ± 4.4
logLB,INT - logLX,INT	0.00	0.00	0.56 ± 0.05	6.2 ± 1.9
logLX,INT - logLB,INT	0.00	0.00	1.13 ± 0.15	7.3 ± 4.2
logLB,BULGE - logLX,NUCL	0.00	0.01	0.55 ± 0.55	5.9 ± 8.4
logLX,NUCL - logLB,BULGE	0.00	0.01	0.36 ± 0.17	29.2 ± 4.6
logL60 μ - logLX,INT	0.00	0.00	0.87 ± 0.09	7.1 ± 3.7
logLX,INT - logL60 μ	0.00	0.00	0.77 ± 0.08	7.2 ± 3.4
logLFIR - logLX,INT	0.00	0.00	0.85 ± 0.09	9.1 ± 3.6
logLX,INT - logLFIR	0.00	0.00	0.82 ± 0.08	4.0 ± 3.5
logLRAD - logLX,INT	0.00	0.00	1.24 ± 0.16	-21.0 ± 6.5
logLX,INT - logLRAD	0.00	0.00	$0.67 \pm 0.06^{\ddagger}$	20.7^{\ddagger}

[†] Probability that a correlation is not present.

[‡] These values are calculated with the BJ method.

Table 3.7: The results of the correlations (only detections)

Variables	BJ Regression			Schmitt's Regression	
	slope	intercept	std dev	slope	intercept
logL α ,NUCL - logLX,NUCL	1.00 \pm 0.17	-0.4	0.85	1.00 \pm 0.16	-0.9 \pm 6.5
logLX,NUCL - logL α , NUCL	0.52 \pm 0.09	19.1	0.61	0.53 \pm 0.09	18.8 \pm 3.7
logL α ,INT - logLX,INT	0.75 \pm 0.10	10.8	0.36	0.73 \pm 0.08	11.6 \pm 3.4
logLX,INT - logL α ,INT	1.01 \pm 0.14	-1.5	0.41	0.97 \pm 0.17	-0.2 \pm 7.1
logLB,INT - logLX,INT	0.61 \pm 0.06	4.45	0.32	5.6 \pm 0.05	2.0 \pm 2.0
logLX,INT - logLB,INT	1.15 \pm 0.11	6.69	0.44	1.14 \pm 0.15	7.3 \pm 4.2
logLB,BULGE - logLX,NUCL	0.59 \pm 0.19	4.04	0.92	0.56 \pm 0.20	5.1 \pm 8.03
logLX,NUCL - logLB,BULGE	0.73 \pm 0.12	29.16	0.73	0.37 \pm 0.16	29.1 \pm 4.6
logL60 μ - logLX,INT	0.19 \pm 0.09	4.4	0.46	0.92 \pm 0.11	5.4 \pm 4.2
logLX,INT - logL60 μ	0.77 \pm 0.07	7.2	0.42	0.65 \pm 0.10	21.3 \pm 2.9
logLFIR - logLX,INT	0.93 \pm 0.08	6.2	0.42	0.89 \pm 0.09	7.9 \pm 3.5
logLX,INT - logLFIR	0.82 \pm 0.07	4.2	0.39	0.80 \pm 0.09	5.11 \pm 4.0
logLRAD - logLX,INT	1.13 \pm 0.11	-16.7	0.49	1.12 \pm 0.08	-16.3 \pm 3.15
logLX,INT - logLRAD	0.68 \pm 0.07	20.5	0.38	0.73 \pm 0.07	8.6 \pm 3.5

all the objects are nearby, with a maximum distance of ~ 100 Mpc the effect of the Malmquist bias will be small. Moreover, as Fabbiano (1988) points out the Malmquist effect would only give a correlation with a slope of 1, whereas most of the correlations found are non linear Finally the fact that the limits follow the trend of the detections suggest that this is not the result of a selection effect. In figures 3.23-3.31 the nuclear and integrated fluxes/luminosities are plotted against the respective optical, IR and radio fluxes/luminosities. The scatter in the plots between integrated luminosities is much less than in the plots involving nuclear and integrated emission. This is a clear indication that there is a significant non nuclear component either in the form of resolved sources or diffuse emission as is shown in figures 3.1-3.22 and is suggested by other studies (Read et al. 1997).

3.4.1 Optical vs. X-ray emission

The optical continuum emission in star-forming galaxies is mainly of stellar origin, although there is a smaller component which arises in the interstellar medium (ISM). More specifically continuum emission in the blue band is dominated by young massive stars whereas the red band is dominated by older stars. On the other hand the line emission mainly arises by reprocessing of stellar radiation by the ISM, which is photoionised by early type stars of OB spectral types. There is also a line component produced in supernova remnants which are mainly shock excited.

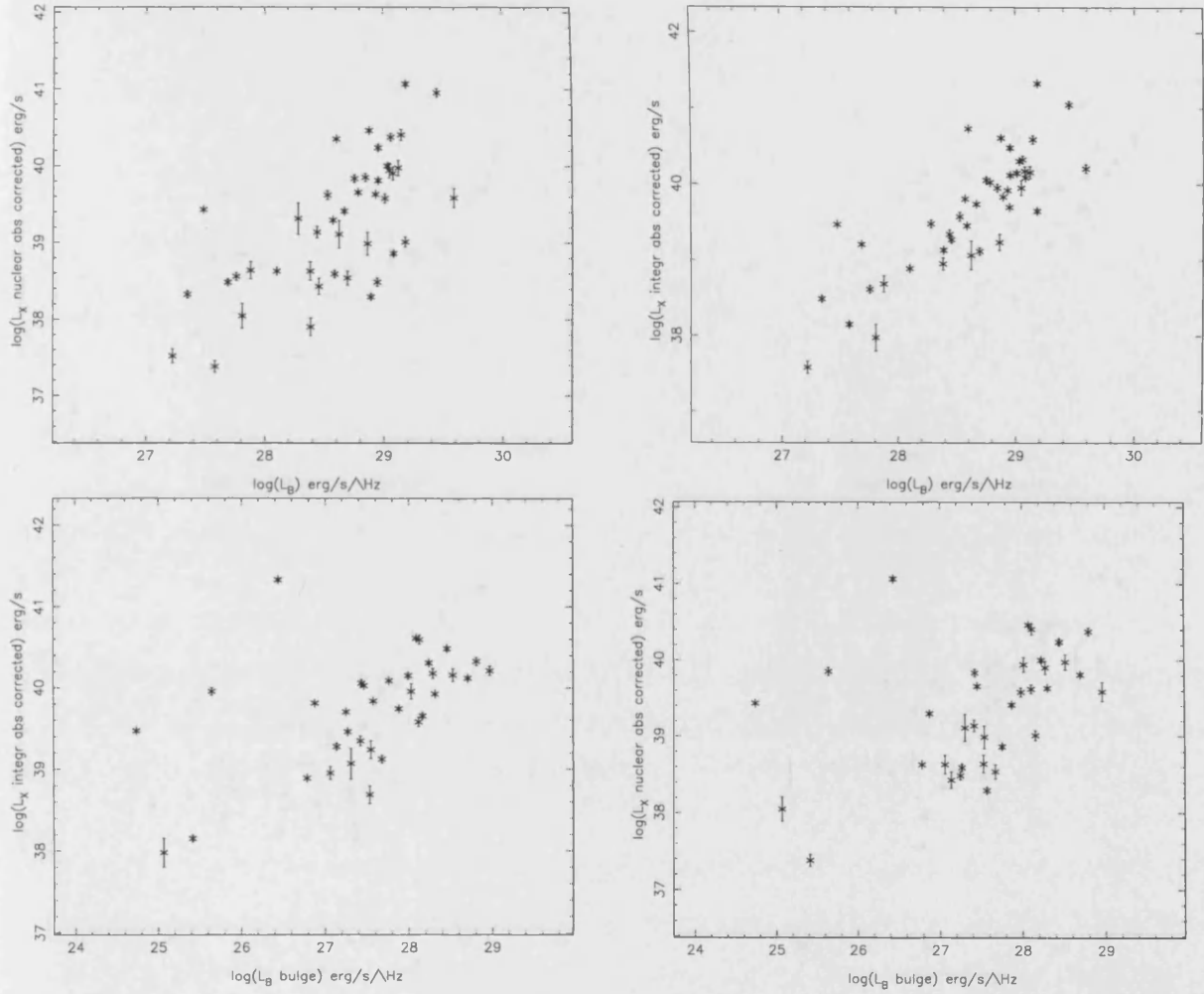


Figure 3.23: Scatter plots of LB-LX,NUCL, LB-LX,INT, LB,BULGE-LX,INT and LB,BULGE-LX,NUCL

Given that the soft X-ray emission is associated with a the population of early type stars either directly (HMXRBs) or indirectly (SNRs, superwind) one expects to find a strong correlation between the blue optical light and soft X-ray emission in star-forming galaxies. We note that LMXRBs do not make a significant contribution to the X-ray emission of a young starburst as their X-ray emitting phase begins after filling their Roche lobe, which takes much longer than the lifetimes of massive stars (Iben, Tutukov & Yungelson 1995). In the case where the bulk of the X-ray emission arises from a superwind its luminosity depends almost linearly with the injection rate of mechanical energy ($L_X \propto L_{mech}^{33/35}$ Heckman et al. 1990), which in turn is a constant fraction of the B-band luminosity, given that the latter is produced by high mass stars which drive the superwind.

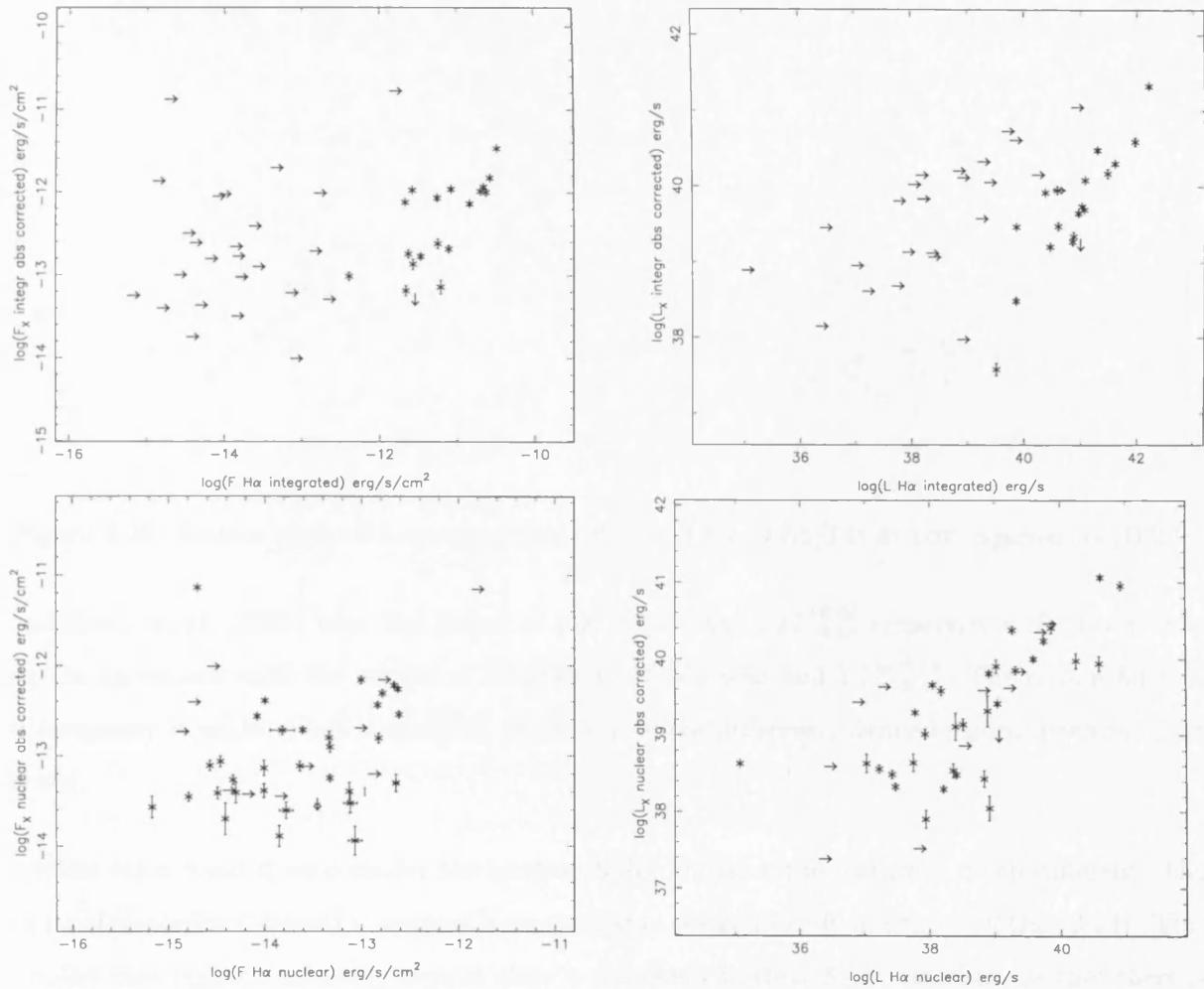


Figure 3.24: Scatter plots of $f_{H\alpha,INT}$ - $f_{X,INT}$, $L_{H\alpha,INT}$ - $L_{X,INT}$, $F_{H\alpha,NUCL}$ - $F_{X,NUCL}$ and $L_{H\alpha,NUCL}$ - $L_{X,NUCL}$

Indeed, there is an almost linear correlation between the X-ray and blue continuum emission of starforming galaxies (fig. 3.23) which suggests that a constant fraction of the stellar population contributes to the X-ray emission as has been previously proposed by Fabbiano (1988). The same argument also holds for the integrated H α versus the integrated X-ray emission (fig. 3.24). The resulting slope is also linear (taking into account only the detections). This again is a direct indication that the X-rays are related to massive stars. This holds either in the case when they arise from HMXRBs (which are a constant number fraction of massive stars) or type Ib/II SNRs (which have massive stars as their precursors) or finally a superwind which is formed after the effect of stellar winds and/or SNRs.

The slope found for this sample is in excellent agreement with the result of Fabbiano et al. (1988)

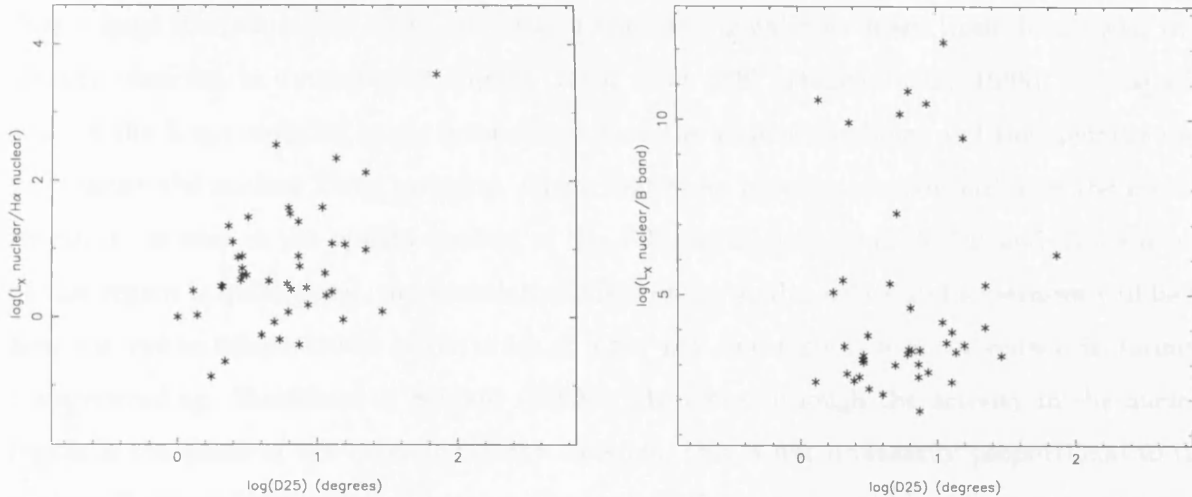


Figure 3.25: Scatter plots of $L_{X,NUCL}/L_{H\alpha,NUCL}$ and $L_{X,NUCL}/L_{B,BULGE}$, against $\log(D25)$.

and David et al. (1992) who find slopes of 1.07 ± 0.08 and $1.12^{+0.06}_{-0.08}$ respectively. However, it is not in agreement with the results of Read et al. (1997) who find $1.77^{+0.18}_{-0.16}$. The reason for this discrepancy is unclear, but it could be attributed to the differently defined sample used for their study.

On the other hand if we consider the nuclear/bulge emission the picture is much different. The slope of the bulge B-band vs. nuclear X-ray emission is significantly less than 1.0 (fig. 3.23). This implies that higher luminosity objects show a deficiency in their X-ray emission, or that there is an additional non X-ray emitting component which contributes to the blue continuum emission of the bulge. Similar results are obtained for the nuclear H_{α} vs. nuclear X-ray emission. The slope of the best fit line is very flat, although not as flat as in the case of the B-band luminosity. However, this result *could* be an aperture effect. The size of the H_{α} emitting region may be much smaller than the size of the X-ray emitting region listed in Table 3.3. This becomes more evident if we plot the ratio of the nuclear X-ray luminosity over the H_{α} luminosity against the D25 radius which is a measure of the size of the galaxy (fig 3.25). From this plot there is a clear trend for larger systems to have a higher excess of X-ray emission. This means that in larger systems the optical aperture does not sample the whole emitting region, whereas the X-ray aperture (which is much larger) samples the whole nuclear region, and may even include some circumnuclear emission.

On the other hand, the flat slope of the $L_{BULGE}-L_{X,NUCL}$ correlation could be an indication

that a large fraction of the X-ray emission of starforming galaxies arises from diffuse gas, as is already observed in a handful of objects (Read et al. 1997, Dahlem et al. 1998). The spatial scale of the X-ray emitting gas is much larger than the scale of the bulge and the aperture used to measure the nuclear X-ray emission. Given that there is active star-formation in the nuclear region (as is seen in the optical spectra of Ho, Filippenko & Sargent 1997*a*) and that the size of this region is quite small, the cumulative effect of the stellar winds and supernova will be to heat the gas to temperatures of the order of a few keV and force it to move outwards, forming a superwind eg. Strickland & Stevens (1998). Therefore although the activity in the nuclear region is the cause of the extended X-ray emission, this is not necessarily proportional to the nuclear X-ray emission. This is because the nuclear X-ray emission depends on the number of X-ray binaries present and the amount of the hot gas, whereas the luminosity of the extended emission depends on the density and temperature of the gas and its mass. Moreover, the more optically luminous the object is, on average the more intense the star-formation and therefore the stronger the superwind component for starbursts of ages $\sim 10^7$ Myr as the mechanical energy injection rate depends on the strength of the starburst (Leitherer, Robert & Drissen 1992). This fact may explain the deficiency of nuclear X-ray emission in more optically luminous objects.

3.4.2 Infrared vs. X-ray emission

The FIR emission mainly arises by reprocessing of the ionising stellar radiation by interstellar dust (Devereux & Young 1990, Cox et al. 1986). The absorption cross-section of the FIR emitting dust particles peaks in the UV region of the spectrum which means that the major contribution to the FIR emission of a normal (non AGN) galaxy comes from early type stars with strong UV continuum. However, a component of cooler dust heated by later type stars cannot be ruled out (Devereux & Hameed 1997, Buat & Xu 1996) In the case of the Milky Way there are two major components: cold dust heated by the general radiation field which produces about 37% of the total IR (8-1000 μ) emission and warm dust, heated by O and B stars (in a ratio 2:1) which makes $\sim 50\%$ of the emission (Cox et al. 1986). According to this model stars with masses as low as $3 M_{\odot}$ (A type) can contribute to this component and stars as late as F-type can heat the cold dust through the general radiation field (Devereux & Hameed 1997).

It is clear that the FIR emission is directly related to the current star-formation, therefore one

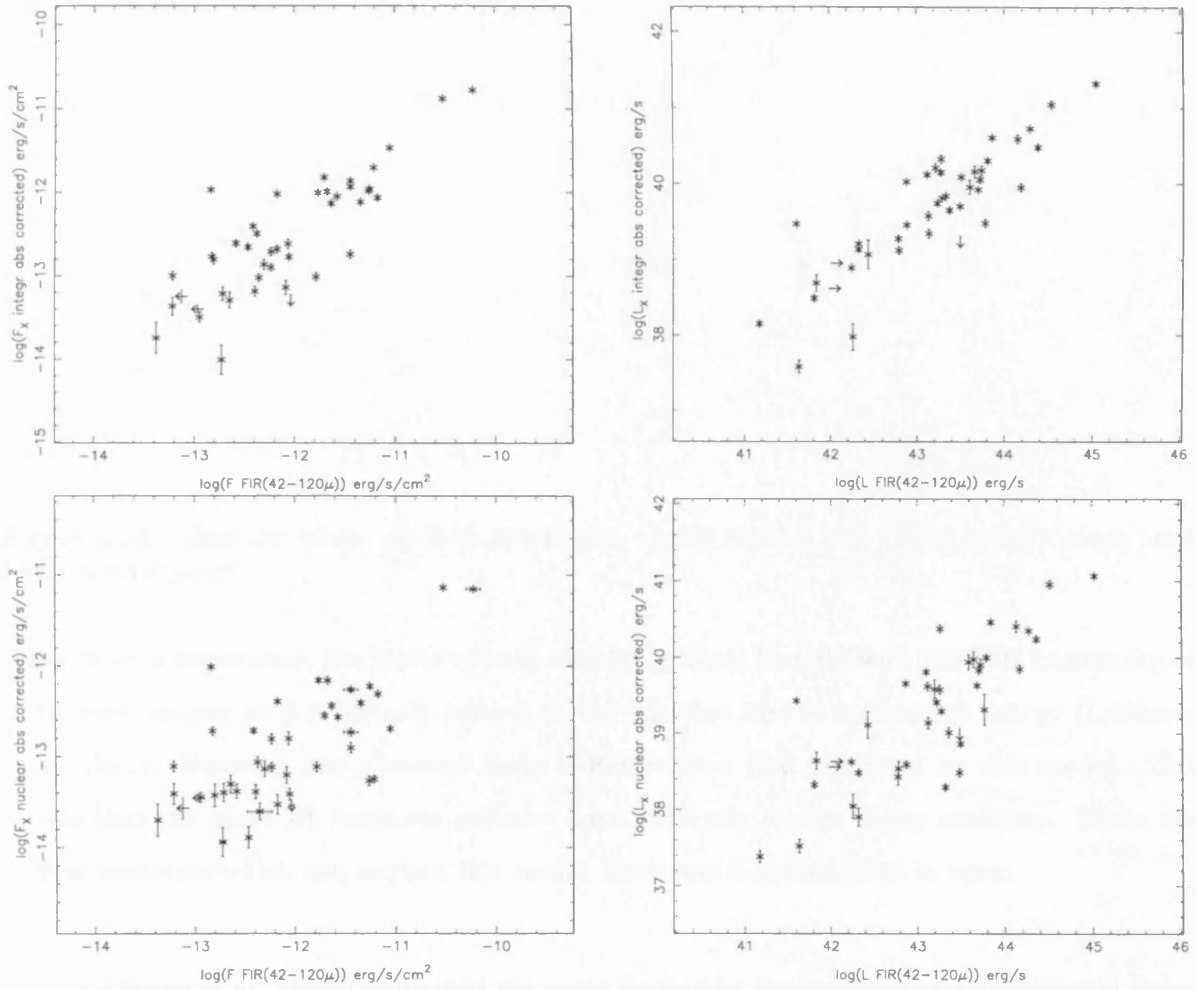


Figure 3.26: Scatter plots of FFIR,INT-FX,INT, LFIR,INT-LX,INT, FFIR,INT-FX,NUCL and LFIR,INT-LX,NUCL

would expect a good correlation between the FIR and X-ray luminosity of starburst galaxies. Indeed, a very tight correlation has been found in the past by Fabbiano et al. (1988) and Green et al. (1992) using *Einstein* data. This result was recently confirmed by the *ROSAT* survey of nearby spiral galaxies carried out by Read et al. (1997) and (Stevens & Strickland 1998). This correlation, not surprisingly, is present in this sample as well (figs. 3.26,3.27) The best fit slope is ~ 0.8 which is in very good agreement with that found by Read et al. (1997), and David et al. (1992) ($0.88^{+0.06}_{-0.05}$ and $0.95^{+0.06}_{-0.05}$ respectively) and marginally consistent with that of Fabbiano (1988) ($0.65^{+0.05}_{-0.07}$). Also the 60μ vs. X-ray correlation is in good agreement with the results of Green et al. (1992).

According to the simple model presented earlier, which assumes that the soft X-ray emission

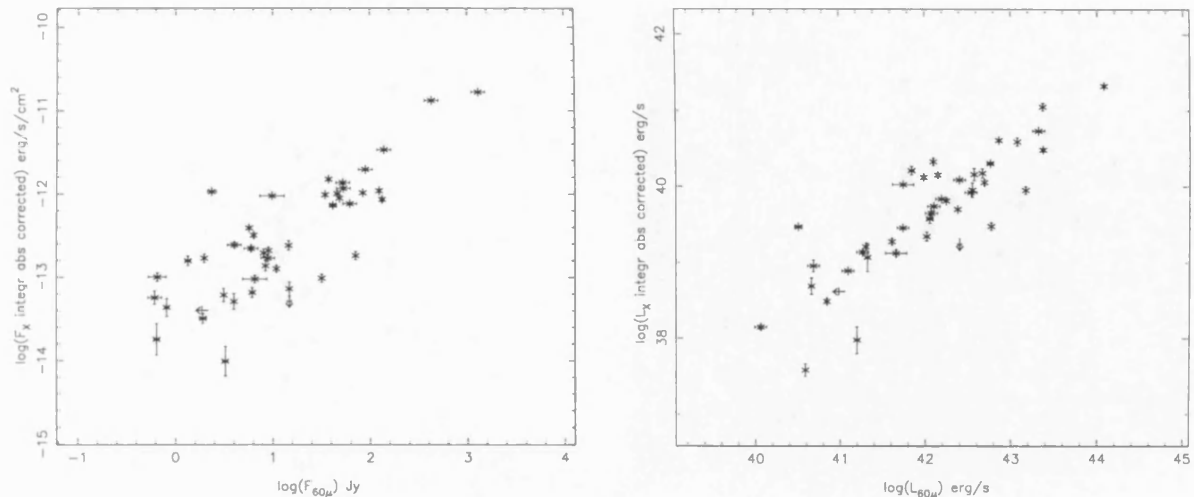


Figure 3.27: Scatter plots of $f_{60,INT}-f_{X,INT}$, $L_{F60,INT}-L_{X,INT}$, $F_{F60,INT}-F_{X,NUCL}$ and $L_{F60,INT}-L_{X,NUCL}$.

arises from a superwind, the latter should correlate almost linearly with the FIR luminosity of a starburst galaxy as it is linearly related to the injection rate of mechanical energy (Leitherer et al. 1992). However, the observed slope is flatter than that predicted by this model. This means that the more IR luminous galaxies have relatively weaker X-ray emission. There are several scenarios which can explain this result. Each one is investigated in turn:

1. Fabbiano et al. (1988) explained the same finding by the presence of an additional warm starburst component, which contributes to the FIR but is highly obscured so it is absorbed in the optical and X-ray wavebands. According to the same work, support for this model comes from the increase in the F_{60}/F_{100} colour ratio with increasing L_{FIR} and L_B/L_{FIR} . However, such a trend is not present in this sample (fig 3.28). One possibility is that the sample of Fabbiano et al. (1988) includes a few AGN which in general have warmer colours than star-forming galaxies (de Grijp et al. 1992); the same reason may explain the flatter slope of their L_X-L_{IR} relation. This is supported by the work of Veilleux, Kim & Sanders (1999) on the IRAS 1Jy sample. Figure 3.28 also presents the F_{60}/F_{100} ratio against the L_B/L_{FIR} for galaxies in the BGS sample of Veilleux et al. (1995) and the IRAS 1Jy sample; the correlation disappears when bright starbursts from the 1Jy sample are included.
2. Another possibility is that the IMF evolves with luminosity, as has been suggested by Fabbiano et al. (1988). If more luminous objects have steeper IMF then the number of early type stars could be lower, and therefore the X-ray emission would be weaker. On the

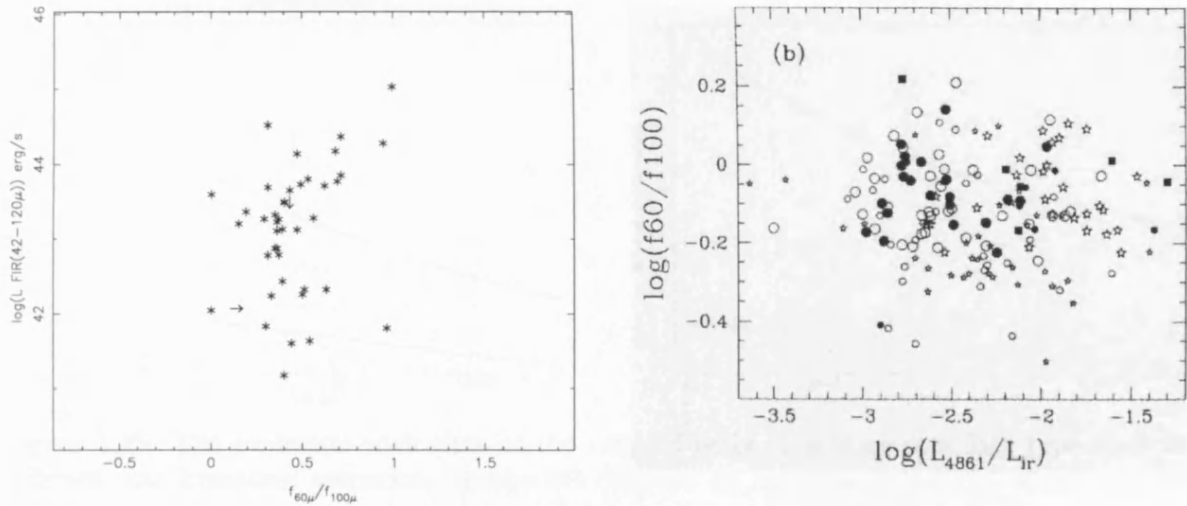


Figure 3.28: Scatter plots of the FIR luminosity against the F_{60}/F_{100} colour for this sample (left) and plots of the F_{60}/F_{100} colour against the L_B/L_{FIR} ratio from Veilleux, Kim & Sanders (1999) (right). The H II galaxies are denoted by stars. Large symbols are from the 1Jy sample, whereas small symbols are from the Bright galaxy sample of Veilleux et al. (1995).

other hand the relative number of intermediate/late type stars increases producing higher FIR emission. The effect of different IMF on the relative numbers of early and late type stars is illustrated in figure 3.29. It is clear that a steeper IMF results in a significant decrease in the relative numbers of early and late type stars. A different upper mass cutoff does not affect this ratio significantly as stars with very high mass (in this case above $30 M_{\odot}$) have very short lifetimes and they are only present in the very early stages of a star-burst assuming a non-continuous star-formation law. Although this is a plausible scenario it is very difficult to test as only in very few cases it is possible to determine accurately the parameters of the IMF in other galaxies, particularly at the low-mass end.

3. This effect can be explained if we take into account the different lifetimes of the various spectral types. In this case, while the short lived massive stars, which form the HMXRBs and drive the superwind, die, the intermediate mass stars which live longer accumulate and therefore make a larger contribution to the FIR emission. So if the SFR is constant, the number of HMXRBs will be constant whereas the number of lower mass stars (and thus the FIR luminosity) will increase. This is clear from figure 3.29 which shows the ratio of the early type and late type stars as a function of time for different star-formation scenarios. It is clear that this ratio can change dramatically over a timescale of $\sim 10^7$ yr, which is the estimated age of most observed star-forming galaxies. In the case of continuous

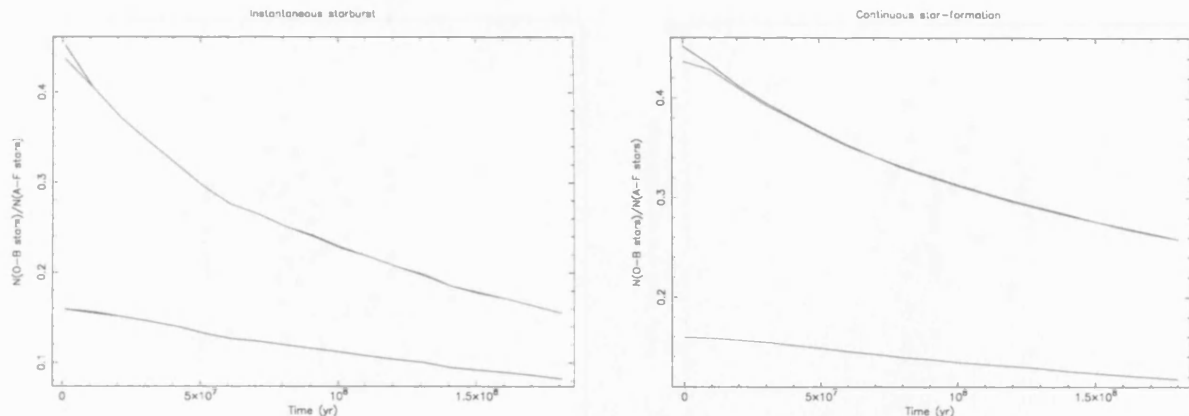


Figure 3.29: The evolution with time of the ratio of early type stars over late type stars for different star-formation scenarios. In the left diagram an instantaneous burst which converts $10^6 M_{\odot}$ into stars is assumed whereas the right diagram assumes continuous star-formation with a rate of $1 M_{\odot} yr^{-1}$. The dark blue line corresponds to a Salpeter IMF ($\alpha = 2.35$) with an upper mass cutoff at $100 M_{\odot}$, and the light blue line is for the same IMF but with an upper mass cutoff of $30 M_{\odot}$. The green and the red lines are for a Miller-Scalo IMF ($\alpha = 2.35$) with upper mass cutoffs of $100 M_{\odot}$ and $30 M_{\odot}$ respectively.

star-formation the age dependence of this ratio is not very significant as the number of early type stars becomes constant after $\sim 10^7$ yr. The increasing number of late type stars, compared to the number of early type stars would result in an increase of the EW of stellar absorption lines typical of these spectral types. However, such a trend is very difficult to see given the diversity of star-formation histories, dust content and metallicities observed in star-forming galaxies. This could be the reason for the large scatter observed in all the plots of luminosity against stellar activity indicators (H_{α} EW, B-V, U-B colours; fig. 3.30).

4. Finally, the excess of FIR emission could be simply related to shock heating of the dust. Although small dust grains are very easily destroyed via sputtering by shocks with velocities larger than $\sim 50 \text{ km s}^{-1}$ (Whittet 1992), if their number density is high enough a fraction of the larger grains can survive in the postshock region of even faster shocks, and be heated by the shock-heated gas. Indeed a study of the properties of dust in star-forming galaxies by Gordon, Calzetti & Witt (1997) showed that starburst galaxies have very different extinction curves compared to those of 30 Dor or Orion. They attribute this difference to the more important effect of shocks in starburst galaxies. This results in a larger number of small dust grains through the sputtering of the larger ones.

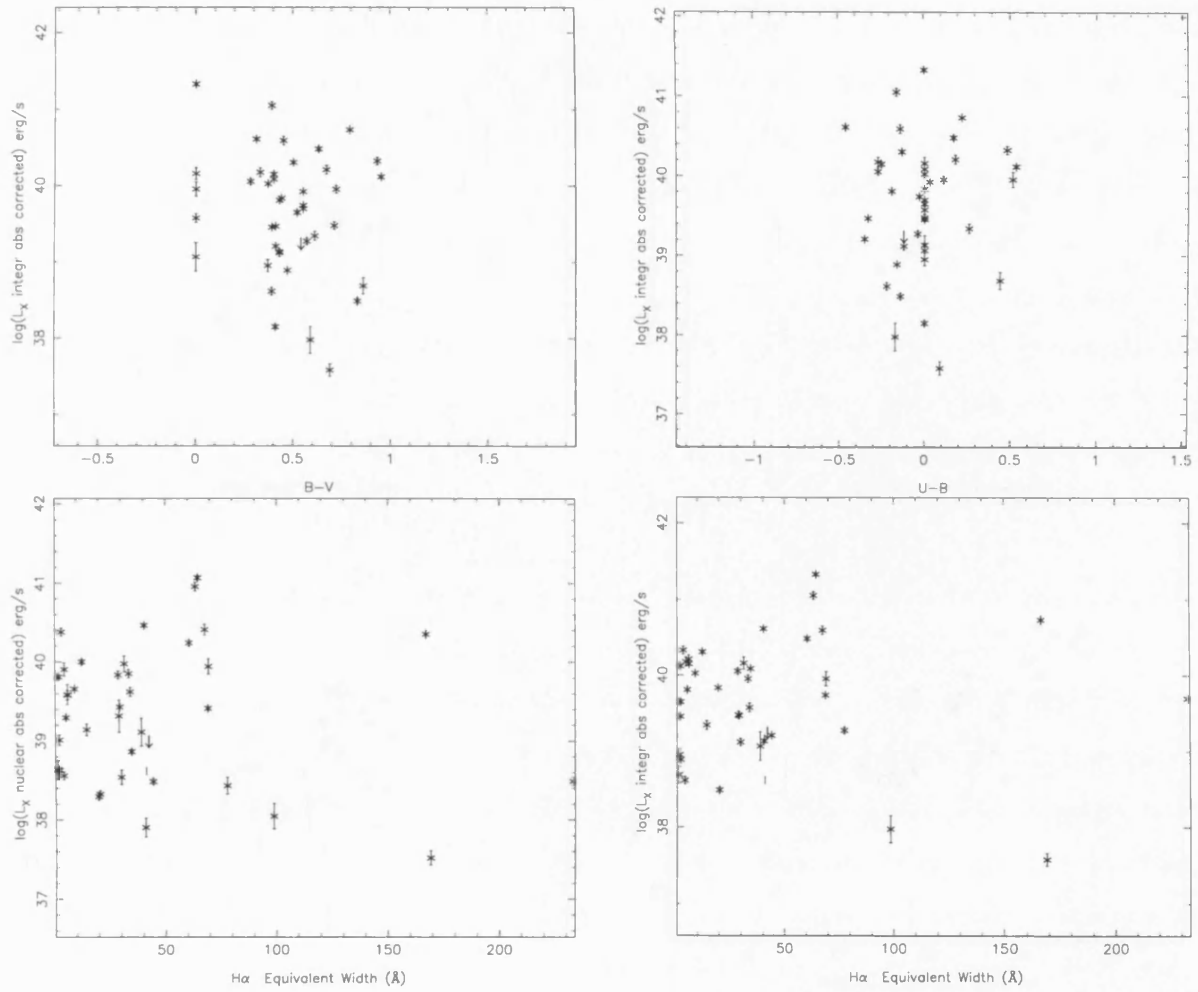


Figure 3.30: Scatter plots of the absorption corrected X-ray luminosity against the EW of the nuclear H α emission line (bottom panel) and the B-V and U-B colours of the galaxy (top panel).

3.4.3 Radio vs. X-ray emission

The continuum radio emission in star-forming/normal galaxies can be of thermal or non-thermal origin. In the first case it is either free-free or free-bound radiation in H II regions. The bulk of the non thermal emission is synchrotron radiation by relativistic cosmic ray electrons (accelerated by supernovae) moving in the galactic magnetic field (Condon 1992). Also there is a small component produced in SNRs but this is minimal compared to the cosmic ray component. Figure 1.7 shows the contribution of these different components in the radio emission of M82. At the frequency of 1.49GHz used in this study the relative contribution of the continuum thermal and non-thermal components is 1:10 therefore the emission at this frequency is mainly

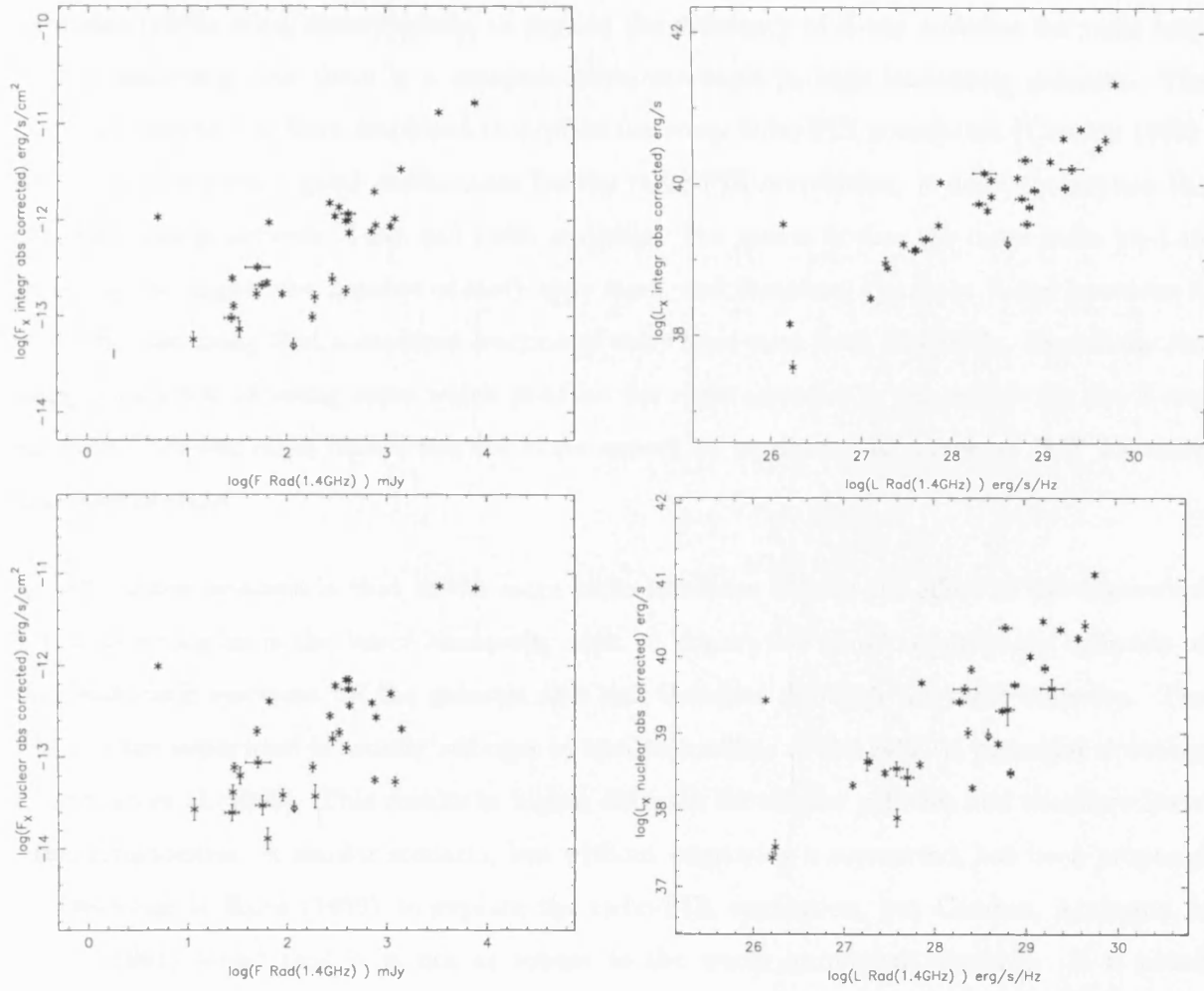


Figure 3.31: Scatter plots of FRAD,INT-FX,INT , LRAD,INT-LX,INT , FRAD,INT-FX,NUCL and LRAD,INT-LX,NUCL .

non thermal (Condon 1992).

Given that the electrons are accelerated by SN explosions, the radio emission should be very well correlated with the FIR and X-ray emission. Indeed there is a very tight correlation between the FIR and radio emission in galaxies (Condon 1992). Fabbiano et al. (1988) have also found a very good correlation between the X-ray and radio emission in spiral galaxies. Moreover, between the FIR vs. X-ray and radio vs. X-ray correlation the latter is considered to be the primary correlation based on a Spearman partial rank test. Their best fit slope is ~ 0.7 in very good agreement with the result of this work (0.67 ± 0.06), i.e. the L_x/L_{rad} ratio decreases with increasing radio power..

Fabbiano (1988) tried, unsuccessfully, to explain the deficiency of X-ray emission for radio loud objects assuming that there is a compact warm starburst in high luminosity galaxies. The same component has been employed to explain the steep radio-FIR correlation (Condon 1992). Although this gives a good explanation for the radio-FIR correlation, it does not explain the flat relationship between X-ray and radio emission. The reason is that the more radio loud an object is, the higher the number of early type stars, and therefore, the more X-ray luminous it would be, assuming that a constant fraction of early type stars form HMXRBs. Essentially the same population of young stars which produce the radio emission is responsible for the X-ray emission. For the same reason the flat slope cannot be attributed to a steeper IMF for more luminous objects.

An alternative scenario is that in the more radio luminous objects the effect of the superwind is not as strong as in the lower luminosity ones. A superwind would result in the diffusion of the relativistic electrons off the galactic disk and therefore diminish the radio emission. The effect of the superwind is usually stronger in smaller systems as the galactic potential is weaker (Heckman et al. 1995). This results in higher diffusion for smaller galaxies and therefore lower radio luminosities. A similar scenario, but without employing a superwind, has been proposed by Devereux & Eales (1989) to explain the radio-FIR correlation, but Condon, Anderson & Helou (1991) found that it is not as robust as the warm component scenario. It is noted that the more X-ray luminous objects do not necessarily have a stronger superwind component (compared to the X-ray binary component) as there is no evidence for an increase of the fraction of diffuse/point source component for more luminous objects. However, for a definite answer to this question, high spatial resolution X-ray observations are needed and *Chandra* will help to resolve this issue.

The flat X-ray vs. radio relation can also be explained by the evolution of the ratio of early/late type stars, assumed to explain the X-ray-FIR correlation. In this case the supernova generated electrons accumulate in the galactic disk increasing their numbers with time, while the high mass stars, which are their progenitors, remain at a constant number. The lifetime of a relativistic electron depends on the dominant energy loss mechanism; either synchrotron or Inverse Compton scattering. In the case of synchrotron radiation the energy loss is (Longair 1992) :

$$\left(\frac{dE}{dt}\right)_{synch} = -4/3 \sigma_T c \gamma^2 U_{mag} = 6.6 \times 10^4 \gamma^2 B^2 \quad (3.2)$$

and therefore for a typical galactic magnetic field of 10^{-1}T and a few GeV electrons their lifetime will be $\sim 10^8\text{yr}$. In the case of IC scattering the energy loss depends on the density of the radiation field:

$$\left(\frac{dE}{dt}\right)_{IC} = -4/3 \sigma_T c \gamma^2 U_{rad} \text{(Longair 1992)} \quad (3.3)$$

For an ULIRG with $L_{IR} = 11.5 L_{\odot}$ and assuming that the radiation is emitted in a region of radius $\sim 100\text{pc}$, Condon, Huang, Yin & Thuan (1991) find that a relativistic electron can live for $\sim 10^4\text{yr}$. With a more realistic assumption on the size of the IR emitting region this age can be $\sim 10^5\text{yr}$, which is still slightly less than the lifetime of massive stars. Therefore this mechanism can account for the excess of radio emission in lower luminosity objects but not for the extremely high luminosity ones where the IC losses dominate over the synchrotron losses. The electrons do not live long enough to accumulate, unless the region where the starburst takes place is large enough so that the radiation field energy density is low.

3.5 The multiwavelength properties of star-forming galaxies - The origin of the soft X-ray emission

The correlations between the X-ray emission and the emission in other wavebands, which are presented in the last section can be summarised by the following: a) there is a linear correlation between the integrated optical continuum and H_{α} radiation and X-ray emission and b) there is a non linear (relatively flat) relationship between X-ray and FIR/radio emission. These results are in very good agreement with other previously published work. Two of the most plausible explanations for the observed correlations are:

- *An “age effect”*

In this case the different lifetimes of early and late type stars are taken into account. Therefore, whereas the number of massive stars is constant (or rapidly decreasing for an instantaneous burst), the late type stars, which live much longer gradually increase in number (or in the case of an evolved instantaneous starburst they decrease with a very low rate). This results in constant X-ray emission but enhanced FIR and radio emission as the supernova generated relativistic electrons and the intermediate type stars, which also contribute to the heating of the dust, pile-up. This also explains the steep slope

of the radio-FIR slope as the number of intermediate type stars is much larger than the number of high mass stars which produce the relativistic electrons. According to this model one expects to observe an increase of the EW of stellar absorption lines typical for A-F stars or a decrease of the EW of the H_α emission line in the more IR luminous objects. However, using the available data this is very difficult to test because of the diversity of star-formation rates, metallicities and star-formation histories observed. One way to test this model would be to use spectral evolutionary synthesis modeling together with good quality integrated optical and IR spectra in order to deconvolve the stellar populations and study the star-formation properties in each object.

- *Evolution of the IMF*

A more exotic scenario is one in which the IMF is steeper for more luminous objects. In this case more luminous objects have higher star-formation rates, but the relative numbers of high and low mass stars will not scale proportionally with their SFR. Therefore for increasing FIR luminosity the X-ray emission will increase but by a smaller factor, as the number of OB stars which form HMXRBs will be smaller. As the number of OB stars will be smaller a superwind will be weaker resulting in reduced diffusion of the relativistic electrons from the disk and therefore increased radio emission, which also explains the radio-FIR correlation. As in the previous model it is very hard to test these assumptions with the available data. Detailed evolutionary synthesis modeling of good quality optical and IR spectra is required in order to determine the parameters of the IMF.

3.6 Implications for the soft X-ray background

The previously discussed results will now be used in order to constrain the contribution of star-forming galaxies to the soft (0.1-2.4keV) extragalactic X-ray background. As mentioned in the introduction this is a long standing problem. Observational attempts to classify the optical counterparts of the faint X-ray sources found in deep surveys are hampered by their faintness and the poor spatial resolution of the previous satellites, which made it very difficult to pinpoint the optical counterparts of the X-ray sources because of their high spatial density (Lehmann et al. 2000). On the other hand theoretical modeling depends on *a priori* assumptions about the evolution of these sources, which is unknown. Here, we consider this problem from a different

perspective: knowing the evolution of the cosmic SFR and the correlation of the X-ray luminosity of starburst galaxies with their FIR and H_α emission it is possible to estimate their contribution to the XRB based on the correlation between the SFR and the FIR and H_α luminosity.

3.6.1 Modelling

The SFR of a galaxy is directly linked to its emission in various wavebands such as H_α , FIR and radio. For this work only the H_α and FIR emission will be used as they are the best calibrated. However, H_α is heavily affected by obscuration and therefore careful extinction correction is needed to account for it. As the extinction correction is determined from the reddening of the H_α with respect to H_β , it may not account for the total obscuration because of the short wavelength distance between H_α and H_β and therefore the SFRs estimated in this way should be regarded only as lower limits. The calibration of Kennicutt (1998b) and Madau et al. (1998) will be used:

$$SFR(M_\odot \text{ yr}^{-1}) = 7.9 \times 10^{-42} L(H\alpha)(\text{erg s}^{-1}) \quad (3.4)$$

According to Schaerer (1999) this calibration is accurate to within 0.7dex. This error includes uncertainties in the IMF slope and upper mass limits and the metallicity.

On the other hand the FIR emission may be contaminated by a population of later type stars, although the dominating populations are massive stars which emit the bulk of the ionising continuum as discussed in the previous section. For this reason this method applies only to young starbursts with ages less than 10^8 yr. Therefore this method may overestimate the current SFR for older systems. The calibration used here is that of Kennicutt (1998b):

$$SFR(M_\odot \text{ yr}^{-1}) = 4.5 \times 10^{-44} L(FIR)(\text{erg s}^{-1}) \quad (3.5)$$

where LFIR is the total (8-1000 μ) IR luminosity. Schaerer (1999) has determined that all the published calibrations lie within 30% of this relation.

From these two relations, and using the correlation of the X-ray luminosity with the IR and the H_α luminosity, it is possible to calculate a relation between the X-ray emission and the rate of star-formation. In order to obtain more realistic estimates of the uncertainties of the intercept in the range of X-ray luminosities of interest (i.e. greater than 10^{36} erg/s), we recalculate the parameters of the linear fits to the $\log(L_X) = f(\log(L_{IR}))$ and $\log(L_X) = f(\log(L_{H_\alpha}))$, by

shifting both the X-ray and optical/IR axes so the first data point is close to the origin. Also we use the bolometric IR luminosity (8-1000 μ) calculated with the formula given by Kim & Sanders (1998), in order to be consistent with the FIR luminosity used in eq. 3.6.1. In the case of the H α correlation again, we use only the detections. The resulting correlation is

$$(\log(L_X) - 36.0) = (0.81 \pm 0.11) \times (\log(L_{IR}) - 40.0) + (0.91 \pm 0.45) \quad (3.6)$$

for the X-ray - FIR luminosity correlation, and

$$(\log(L_X) - 36.0) = (1.04 \pm 0.0.19) \times (\log(L_{H\alpha}) - 34.0) + (-3.7 \pm 1.38) \quad (3.7)$$

for the X-ray - H α correlation. In both cases the luminosities are in erg/s.

Then we can obtain the relation between the star-formation rate and the X-ray luminosity:

$$\log(L_X(\text{erg s}^{-1})) = (0.81 \pm 0.11) \times \log(\text{SFR}(M_{\odot} \text{ yr}^{-1}) + 3.35) + 36.0 + (0.91 \pm 0.45) \quad (3.8)$$

for the IR calibration, and

$$\log(L_X(\text{erg s}^{-1})) = (1.04 \pm 0.0.19) \times (\log(\text{SFR}(M_{\odot} \text{ yr}^{-1}) + 7.1) + 36.0 + (-3.7 \pm 1.38) \quad (3.9)$$

for the H α calibration.

Convolving these relationships with the evolution of the SFR with redshift it is possible to calculate the soft X-ray emissivity of starburst galaxies for each redshift bin. Figure 3.32 shows the evolution of the cosmic starformation rate with redshift. The blue points are based on estimates from the Hubble Deep Field whereas the red points are based on measurements in the optical, IR and sub-mm bands respectively. Figures 3.33 and 3.34 show the X-ray emissivity of starforming galaxies calculated as described above. For this calculation it is assumed that the SFR remains constant for each redshift bin. In order to account for the uncertainties in the slope, intercept and the SFR we perform a Monte Carlo simulation assuming that the errors in these quantities are distributed normally. For each set of these parameters we calculate the X-ray luminosity. Then the mode of the distribution of the simulated luminosities gives its most probable value. The uncertainty is given by the standard deviation of the same distribution. We use the mode because the resulting distribution is not necessarily Gaussian and the mean value will overestimate the luminosity.

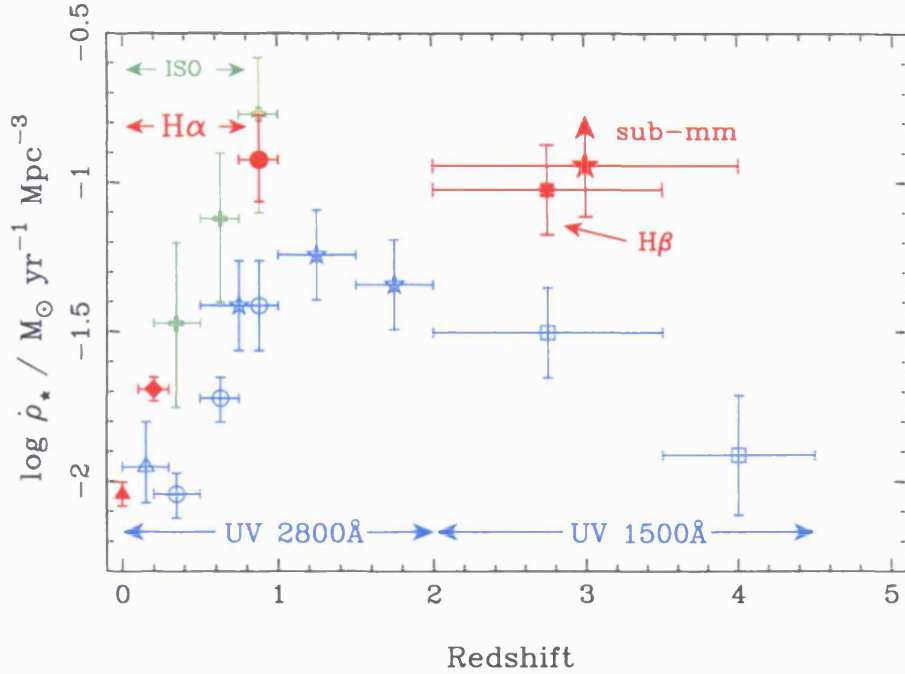


Figure 3.32: The evolution of the cosmic star-formation rate with redshift (from Glazebrook et al. 1999). The blue points are from UV measurements (open triangle Treyer et al. (1998), open circles Lilly et al. (1996), open stars Connolly et al. (1997), open squares Madau et al. (1998)). The red and green points are from Balmer lines and IR/sub-mm measurements (filled triangle Gallego et al. (1995), filled diamond Tresse & Maddox (1998), filled circle Glazebrook et al. (1999), open crosses Flores et al. (1999), filled square Pettini et al. (1998) and filled star Hughes et al. (1998)).

Integrating over redshift, the X-ray emissivity for each redshift bin we can estimate the intensity of the X-ray emission arising from starburst galaxies at different redshifts and finally adding all these contributions we can calculate the total X-ray emission due to starformation. From Longair (1995) we have:

$$I = \frac{c}{4\pi H_0} \int_{z_1}^{z_2} \frac{j_x}{(1+z)^{(2+\alpha_x)}(1+\Omega_0 z)^{1/2}} dz \quad (3.10)$$

$$I(\text{erg s}^{-1} \text{sr}^{-1}) = 5.013 \times 10^{-47} \int_{z_1}^{z_2} \frac{j_x(\text{erg s}^{-1} \text{Mpc}^{-3})}{(1+z)^{(2+\alpha_x)}(1+\Omega_0 z)^{1/2}} dz \quad (3.11)$$

where j_x is the X-ray emissivity, α_x is the spectral index in the X-ray band assumed to be 0.7 in agreement with results for other starburst galaxies (eg. Ptak et al. 1999), and Ω_0 is assumed to be 1.0.

Figures 3.33 and 3.34 show the intensity of the X-ray emission from starburst galaxies in each redshift bin. It is clear that the bulk of the contribution to the XRB comes from objects at redshifts up to 1.5.

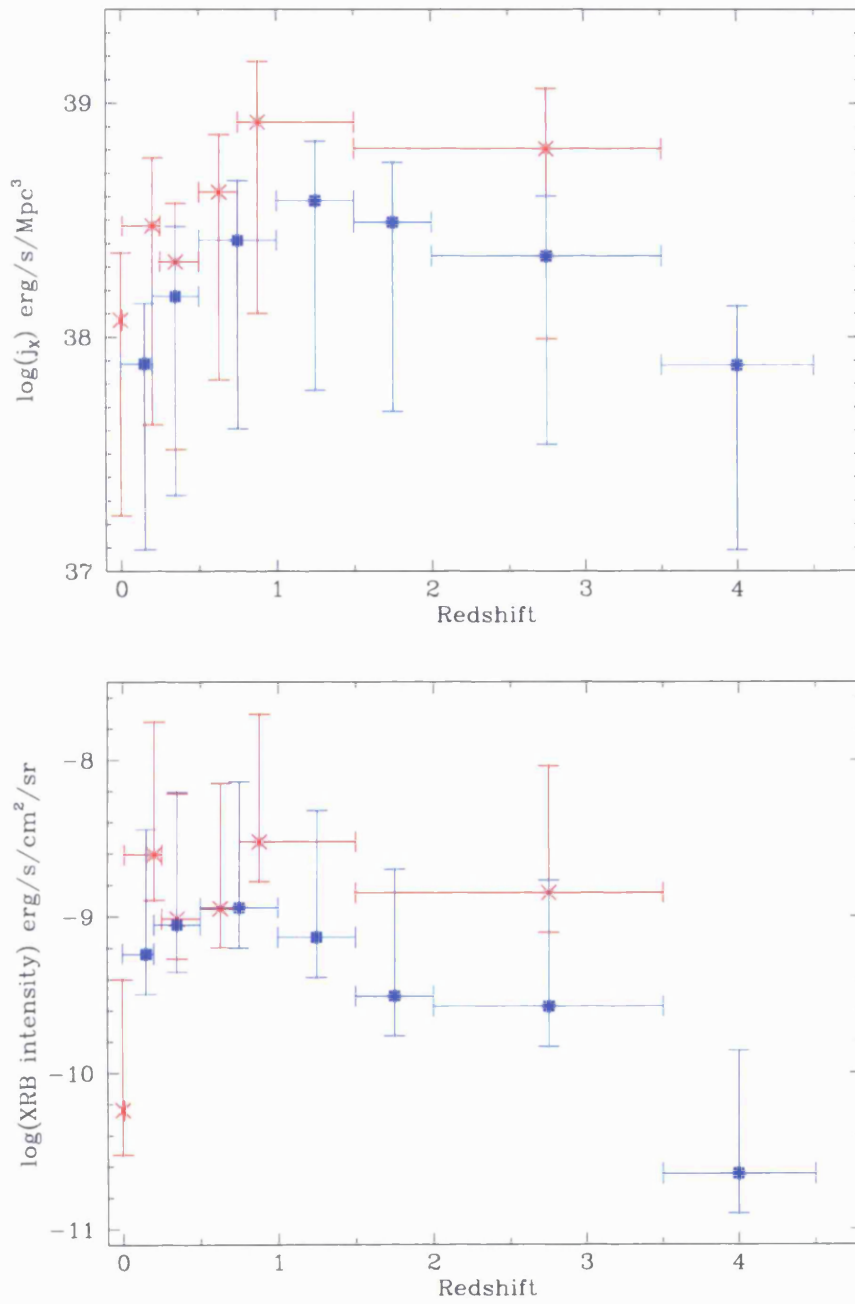


Figure 3.33: X-ray emissivity and intensity of the X-ray emission of star-forming galaxies calculated using the X-ray- H_α correlation. Red points are from the optical/IR determination of the SFR history, and blue points are from the HDF.

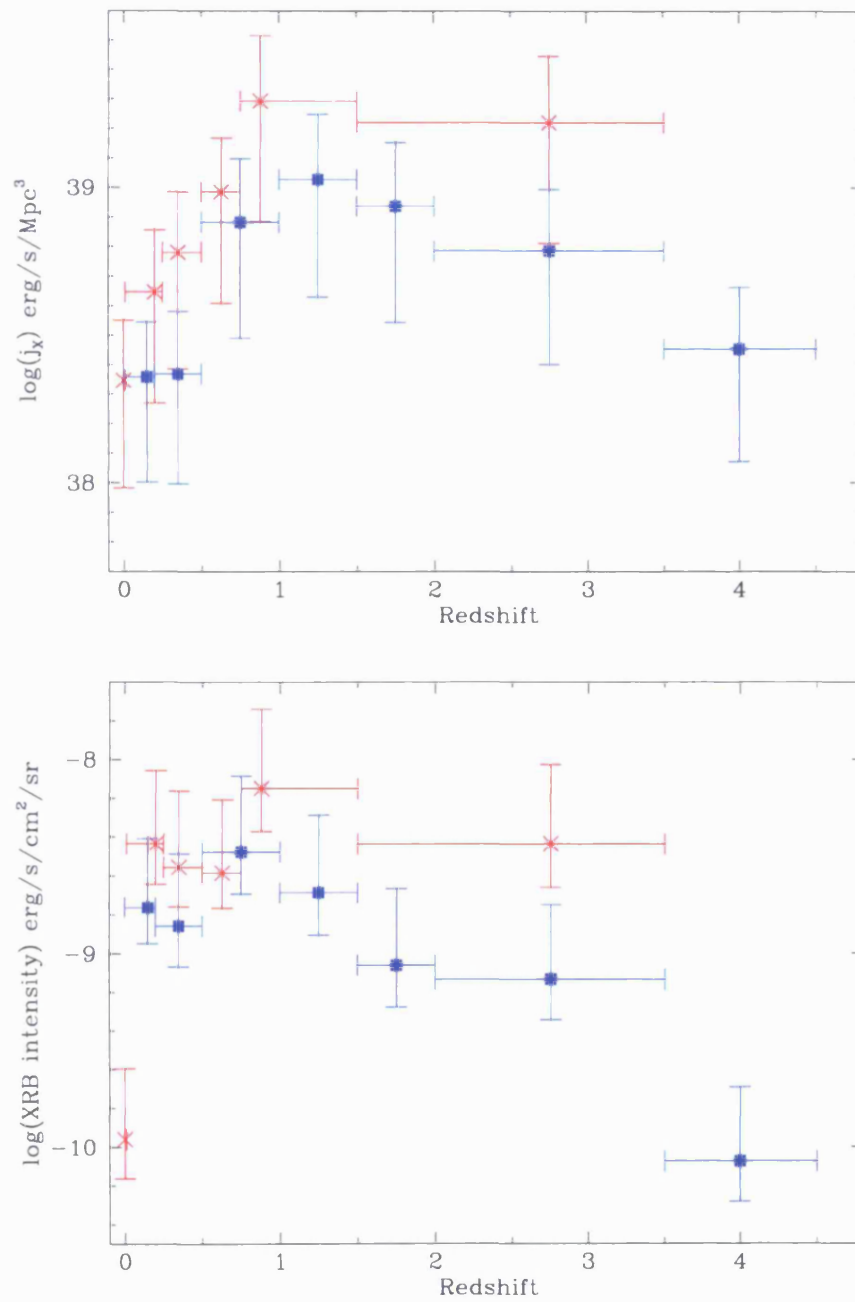


Figure 3.34: X-ray emissivity and intensity of the X-ray emission of star-forming galaxies calculated using the X-ray-FIR correlation. Red points are from the optical/IR determination of the SFR history, and blue points are from the HDF.

3.6.2 Starbursts vs. AGN

Adding the contributions from the different redshift bins gives the total X-ray background emission due to star-formation. This is $48.5^{+29.2}_{-29.1}\%$ and $24.7^{+14.13}_{-14.5}\%$ for the optical/IR and the UV determinations of the SFR history respectively, using the FIR calibration. In the case of the H_α calibration the result is $22.1^{+17.9}_{-16.4}\%$ and $9.5^{+9.6}_{-8.0}\%$ for the optical/IR and the UV determinations of the SFR history. However, because of the large uncertainties of the H_α calibration the latter results are essentially unconstrained. These results suggest that star-forming galaxies can account for a non negligible fraction of the extragalactic X-ray background. This fraction can be larger if the X-ray emission of star-forming galaxies evolves with redshift. This could arise because of lower metallicities at earlier epochs (Pei & Fall 1995) and therefore increased luminosity of X-ray binaries.

These numbers are in excellent agreement with the estimates of Griffiths & Padovani (1990) who find a contribution of 20%-30% for moderate evolution and of Green et al. (1992) who find 5%-25% at 2keV. Also David et al. (1992) find 30%-40% contribution in the *Einstein* band. Their results are based on the convolution of the FIR luminosity function of normal galaxies with the LX-LFIR relation. From the *ROSAT* Deep Survey is found that 11%-36% of the 2keV XRB down to a flux limit of $4 \times 10^{-15} \text{erg cm}^{-2} \text{s}^{-1}$ in the 0.5-2.0keV band arises from NELXGs (Griffiths et al. 1996). From a much longer Deep Survey McHardy et al. (1998) calculate a contribution of NELGs of $\sim 8\%$ in the 1-2keV background down to a flux level of $2.0 \times 10^{-15} \text{erg cm}^{-2} \text{s}^{-1}$. Extrapolating these results down to a flux level of $0.5 \times 10^{-15} \text{erg cm}^{-2} \text{s}^{-1}$ they find a contribution of 15%-30%, in very good agreement with the results of this work. Recently, Hasinger et al. (1998) resolved 70-80% of the soft extragalactic X-ray background down to a flux limit of $5.5 \times 10^{-15} \text{erg cm}^{-2} \text{s}^{-1}$. Follow up optical spectroscopy of these sources shows that almost all of them are AGN: $\sim 80\%$ broad line AGN and $\sim 20\%$ show only narrow-lines (Lehmann et al. 2000). The fact that Lehmann et al. (2000) do not observe any obvious star-forming galaxies may be due to their faintness as in general they are less luminous and they have lower surface brightness than AGN, and their emission arises from the whole galaxy rather than in the very nuclear region. Therefore it is possible that they are present at lower flux limits. Indeed McHardy et al. (1998) estimated that NELGs may have much higher contribution at fluxes below $5 \times 10^{-15} \text{erg cm}^{-2} \text{s}^{-1}$. Moreover, the first results from a Deep Survey with

Chandra showed that there is a very large number of optically faint sources at X-ray fluxes $3 \times 10^{-16} \text{erg cm}^{-2} \text{s}^{-1}$ in the 0.5-2.0keV band (Mushotzky, Cowie, Barger & Arnaud 2000). Some of these sources may be related to star-forming galaxies; however, careful optical and X-ray observations are needed in order to draw any definite conclusions.

Chapter 4

Study of selected X-ray luminous starburst galaxies¹

This chapter describes in detail the data analysis and interpretation of the X-ray properties of three examples of nearby X-ray luminous starburst galaxies. The aim is to investigate whether they have the same properties as their lower luminosity counterparts. The first two galaxies are selected from the sample of Ho, Filippenko & Sargent (1997*a*) which is reported in Chapter 2, on the basis of their high X-ray luminosity. The third object (UGC 4305) is selected from the work of Moran et al. (1996) on the basis of its very high ratio X-ray to FIR luminosity.

4.1 NGC3310

4.1.1 Overview

NGC3310 is a well studied nearby galaxy of Sbc(r)pec type (Mulder & Van Driel 1996). Its recession velocity is 980 km s⁻¹ (de Vaucouleurs 1991) implying a distance of 19.6 Mpc . Its optical image presents some very interesting morphologies, like a jet-like structure in the north-west of the nucleus which points towards an arc about 100 arcsec from the nucleus. There are various suggestions for the nature of this structure. For example Bertola & Sharp (1984)

¹The work presented in this chapter has been done in collaboration with M.J. Ward and I. Georgantopoulos and is published in MNRAS.

proposed that this can be the remnant of an old jet and the part of a spiral arm. In the other hand Balick & Heckman (1981) suggest that this is the remnant from an older collision between two galaxies. This seems to be the most probable explanation as the anomalies found in its rotation curve imply that it has undergone a collision with another galaxy (Mulder & Van Driel 1996). However, infrared and high resolution radio images do not reveal any double nucleus structure (Telesco & Gatley 1984, Balick & Heckman 1981). This could mean that the merger phase is almost complete and the system is now relaxing (Balick & Heckman 1981). Another very interesting morphological structure is a giant H II region located in the South-East of the nucleus. Its size is about $6''$ ($\sim 570\text{pc}$), comparable to the largest extragalactic H II regions known.

The optical spectrum of the galaxy exhibits the typical signatures of starburst activity. The position of the line ratios in the standard diagnostic diagrams of Veilleux & Osterbrock (1987) lies well in the H II locus. This gives confidence that it is a bona-fide starburst galaxy without any activity arising from accretion onto a super-massive black-hole. The spectrum of the 'jumbo' H II region is dominated by the signatures of Wolf-Rayet stars like the WR bump at 4640\AA , (Pastoriza, Dottori, Terlevich et al. 1993).

Evolutionary synthesis modeling of the starburst in NGC3310 has shown that the age of the starburst is between 10^7 and 10^8 years, whereas there is the possibility that another starburst event has occurred in the past which produced the population of old stars observed now (Pastoriza et al. 1993).

NGC3310 has been previously observed with the Imaging Proportional Counter (IPC) on board the *Einstein* observatory yielding an X-ray flux $f_x = 1.1 \times 10^{-12} \text{erg cm}^{-2} \text{s}^{-1}$ in the 0.3-3.5 keV band for a 5keV bremsstrahlung model and Galactic absorption (Fabbiano et al. 1992). This corresponds to an X-ray luminosity of $5.0 \times 10^{40} \text{erg s}^{-1}$.

4.1.2 The data

NGC3310 has been observed in the soft X-rays with PSPC and *HRI* on board *ROSAT* (Trumper 1984). The details of the observations are presented in Table 4.1.

Table 4.1: Summary of the observations of NGC3310

Satellite	Instrument	Date Observation started	Exposure Time Ksec
<i>ROSAT</i>	PSPC	1991-11-16	9.114
<i>ROSAT</i>	HRI	1995-04-17	41.842
<i>ROSAT</i>	HRI	1994-11-23	4095
<i>ASCA</i>	SIS/GIS	1994-04-17	GIS: 10.4, SIS:10.4
<i>ASCA</i>	SIS/GIS	1994-11-13	GIS:11.6, SIS:10.2

For the reduction of the PSPC data we have followed the procedure described in Chapter 3. We excluded those data with Master Veto rates higher than $170 \text{ counts s}^{-1}$ as the particle background cannot be accurately modeled for higher background time intervals. We extracted a PSPC spectral image (channels 11 to 201) with a pixel size of $15''$. To obtain an X-ray spectrum we extracted data from a circular region of $1.5'$ radius around the X-ray centroid. The background was estimated from an annular region between radii of $15'$ and $8.8'$ from the centroid, after exclusion of all the discrete sources detected with the PSS algorithm (Allen 1997) down to the 5σ level.

From the HRI observations only the longest one has been used. HRI covers a field of $38'$ diameter and it has a spatial resolution of about $5''$ (the FWHM of the XRT+HRI Point Spread Function). We note that the HRI has very limited spectral resolution so it is not useful in spectral analysis (David et al. 1997). The screening of the data has been carried out using the *ASTERIX* package. We have rejected all data with aspect errors greater than 2.

NGC3310 has been also observed with the *ASCA* satellite (Tanaka et al. 1994) see Table 4.1 for the details of the observations. For the screening of the data we have followed the standard procedure and used the *ASCACLEAN* program in the *FTOOLS* package with the parameters described in the ABC *ASCA* Guide (Yaqoob 1997). After the standard processing we inspected the light curves and removed time intervals with unusually high numbers of counts, which may result from background particle contamination. The extraction of the source and the background spectra has been carried out using the *XSELECT* program within the *FTOOLS* package. We extract the source spectrum using a circular region of 2.7 and 5.5 arcmin radius for the SIS and GIS respectively. For the background regions we have selected ten source free zones, each of area about 6 and 10 arcmin² for the SIS and GIS respectively. Following extraction of the source and

background spectra, we ran the SISrmg program to create the SIS response matrices for each SIS source spectral file. For the GIS spectral files we used the gis2v4.0.rmf and gis3v4.0.rmf for GIS2 and GIS3 respectively. We created the Ancillary Response Matrices for each file by running the ASCAarf programs within the FTOOLS package.

4.1.3 Soft X-ray imaging

We used the archival *HRI* observations to obtain information on the morphology of the X-ray emitting regions and compared these with images of these galaxies at other wavelengths. First we searched for extended emission by comparing the background subtracted radial profile of the galaxies with the radial profile of a point source. For this purpose we used as a reference the point source corresponding to the star AR-Lac. We retrieved archival data for an on-axis observation of AR-Lac, and applied the same extraction process as used for the galaxy. The comparison of the radial profiles of NGC3310, and the radial profile of AR-Lac is shown in figure 4.1. This figure clearly shows that the X-ray source has a radius of ~ 0.5 arcmin (at larger radii the emission from the galaxy begins to blend with the profile of AR-Lac, within the 2σ error bars). Although this is a somewhat arbitrary point at which to define the extent of the emission, it gives a lower limit to the source size. At the distance of NGC3310 this corresponds to ~ 3 kpc. We note that fitting a Gaussian function to the radial profile gives a similar source size (FWHM=1.6 arcmin).

In order to compare the distribution of the X-ray emitting gas with the optical image we have resampled the X-ray image with a pixel size of 1.5 arc-seconds and then smoothed this image using a two-dimensional Gaussian of FWHM=3.5 arc-seconds (2.3 pixels) following Della Ceca, Griffiths, Heckman & Mackenty (1996). The effective resolution is $5.4''$, equal to the XRT+HRI PSF. Then we obtained contours from this image corresponding to 2.2, 2.0, 1.7, 1.33, 0.88, 0.44, 0.35, 0.26, 0.17 counts arcsec⁻² and overlaid these onto an optical image obtained from the Digitized Sky Survey. This image is shown in figure 4.2. The main problem we faced in attempting to overlay the two images is that of frame registration. There are no X-ray sources within the HRI image which have an obvious optical counterpart. Thus in order to overlay the X-ray contour plot onto the optical image, we are forced to assume that the centroid of the X-ray source corresponds to that of the optical nucleus. In the X-ray image of NGC3310 we detect

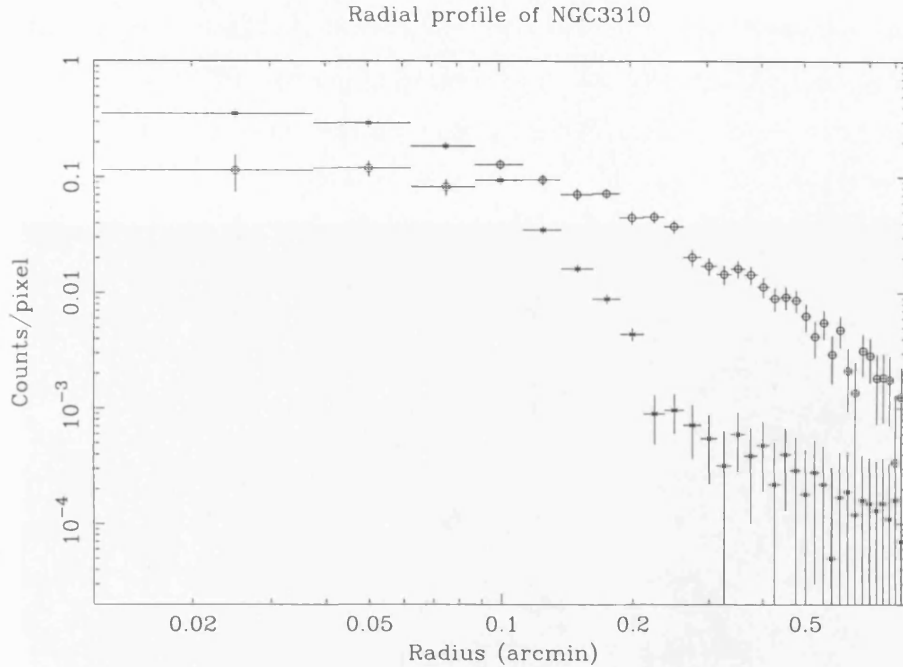


Figure 4.1: The HRI radial profile of NGC3310 (circles) overlaid on the radial profile of AR Lac (stars).

Table 4.2: Sources in the *HRI* field of NGC3310

RA (J2000)	Dec (J2000)	Count rate count s ⁻¹	Flux erg cm ⁻² s ⁻¹	Significance
10 38 43.2	+53 31 07	$2.0 \pm 0.27 \times 10^{-3}$	2.3×10^{-14}	15.5
10 38 46.7	+53 30 38	$2.8 \pm 0.26 \times 10^{-3}$	3.07×10^{-14}	23.4

two other sources in addition to the nucleus, at a significance above 10σ . The details concerning these sources are presented in Table 4.2. The fluxes have been calculated from the background subtracted count rates and a 0.8 keV thermal plasma model absorbed by the galactic column density. These point sources may correspond to luminous X-ray binaries or young supernova remnants. Unfortunately there are no identified optical counterparts for these X-ray sources on the POSS plates.

4.1.4 Spectral analysis

The *ROSAT* and *ASCA* spectra of NGC3310 were extracted as described previously, and analysed with the *XSPEC* package (v10). In order to use χ^2 statistics the spectra have been binned

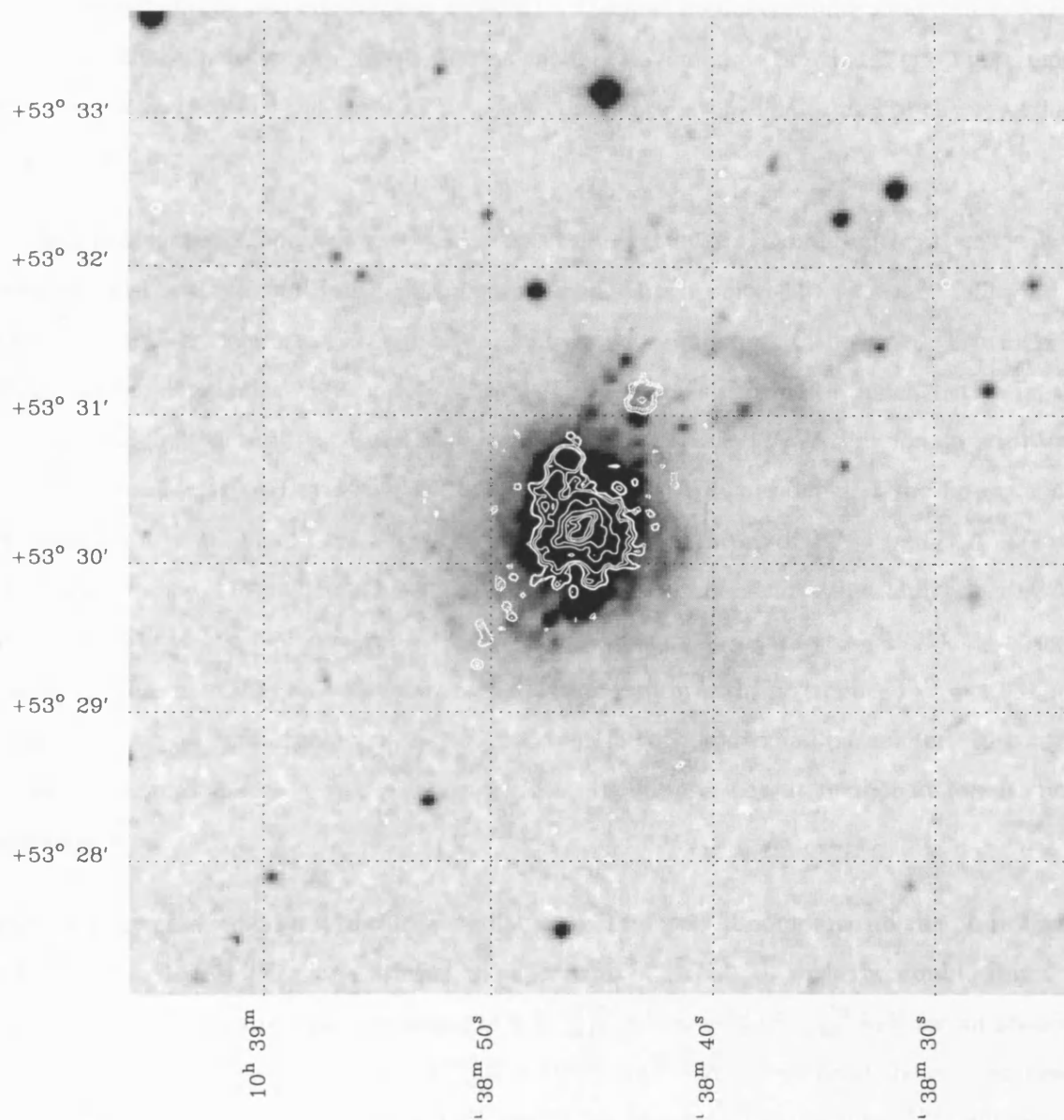


Figure 4.2: X-ray contours from the HRI observation of NGC3310 overlaid on a POSS image. The contours are in levels of 2.2, 2.0, 1.7, 1.33, 0.88, 0.44, 0.35, 0.26, 0.17 counts arcsec⁻².

in order to have at least 20 counts in each bin. All *ROSAT* points below 0.1 keV and above 2.0 keV have been rejected because of the limitations of the detector. We have used only *ASCA* data in the range 0.6 to 8.0 keV for SIS and 0.7 to 7.0 keV for GIS.

We first fitted simple one-component models: a thermal bremsstrahlung model, a power-law model and finally a Raymond-Smith plasma model (Raymond & Smith 1977). These models were rejected at greater than the 99.9 per cent confidence level. The results of the spectral fits are given in 4.3.

We then fitted two component models: a two temperature Raymond-Smith plasma (ray-ray hereafter) and a Raymond-Smith plasma combined with a power-law (po-ray), following the results of Moran & Lehnert (1997) and Ptak, Serlemitsos, Yaqoob, Mushotzky & Tsuru (1997) on the starburst galaxies M82 and NGC253. These models provided a much better fit than the simple models described above, at a confidence level over 90 per cent for an addition of two free parameters (eg Bevington & Robinson (1992)). We consider first the po-ray model. We obtained a photon index of $\Gamma = 1.44_{-0.11}^{+0.20}$ and a temperature of $kT = 0.81_{-0.12}^{+0.09}$ keV with a reduced $\chi^2 = 1.115$, where the abundance is fixed to the solar value and the absorbing column density to the Galactic value, $N_H = 0.7 \times 10^{20} \text{ cm}^{-2}$, (Stark et al. 1992). Leaving the absorbing column density as a free parameter further improves the fit (reduced $\chi^2 = 1.031$); this is significant at a confidence level of > 99 per cent for one additional parameter. In contrast, leaving the abundance as a free parameter does not improve the fit further at a statistically significant level.

In the ray-ray case we do not obtain a significantly improved fit compared to the po-ray model (reduced $\chi^2 = 1.022$). Figure 4.3 shows the spectrum of NGC3310 with the double Raymond-Smith model. We obtained temperatures of $0.80_{-0.04}^{+0.07}$ keV and $14.98_{-4.88}^{+13.52}$ keV for an absorbing hydrogen column density of $N_H = 1.37_{-0.32}^{+0.50} \times 10^{20} \text{ cm}^{-2}$. When we fixed the column density to the Galactic value ($N_H \approx 1.0 \times 10^{20} \text{ cm}^{-2}$) we obtained $kT_1 = 0.84_{-0.07}^{+0.05}$, whereas the temperature of the hard component was pegged at the upper limit imposed by the model ($kT_2 \approx 64$ keV). We also introduced two different absorbing column densities, for the soft and the hard components, following the analysis of M82 by Moran & Lehnert (1997) who showed that the hard X-ray component is obscured by $N_H \sim 10^{22} \text{ cm}^{-2}$.

Table 4.3: Spectral fitting results for NGC 3310

Parameter	Power-law	Single Temperature Raymond-Smith	Double Temperature Raymond Smith	Raymond Smith + Power-law
kT (KeV)		$7.35^{+1.24}_{-1.18}$	$0.80^{+0.07}_{-0.04}$ $14.98^{+13.52}_{-4.88}$	$0.81^{+0.09}_{-0.12}$
Γ	$1.68^{+0.08}_{-0.08}$			$1.44^{+0.20}_{-0.11}$
$N_H(10^{20} \text{cm}^{-20})$	$3.15^{+0.63}_{-0.52}$	$1.90^{+0.45}_{-0.36}$	$1.37^{+0.50}_{-0.32}$	$1.74^{+0.68}_{-0.40}$
$\chi^2 / \text{d.o.f.}$	222.9/175	239.3/175	168.7/165	170.2/165
Flux [†] small (0.1-2.0keV)	0.95	0.86	0.9	1.09
Flux [†] (2.0-10.0keV)	1.88	2.12	2.10	2.10
Total Luminosity [‡] (0.1-10keV)	1.3	1.4	1.4	1.5

[†]All the fluxes are in units of $10^{-12} \text{erg s}^{-1} \text{cm}^{-2}$. [‡]The luminosity is in units of $10^{41} \text{erg s}^{-1}$.

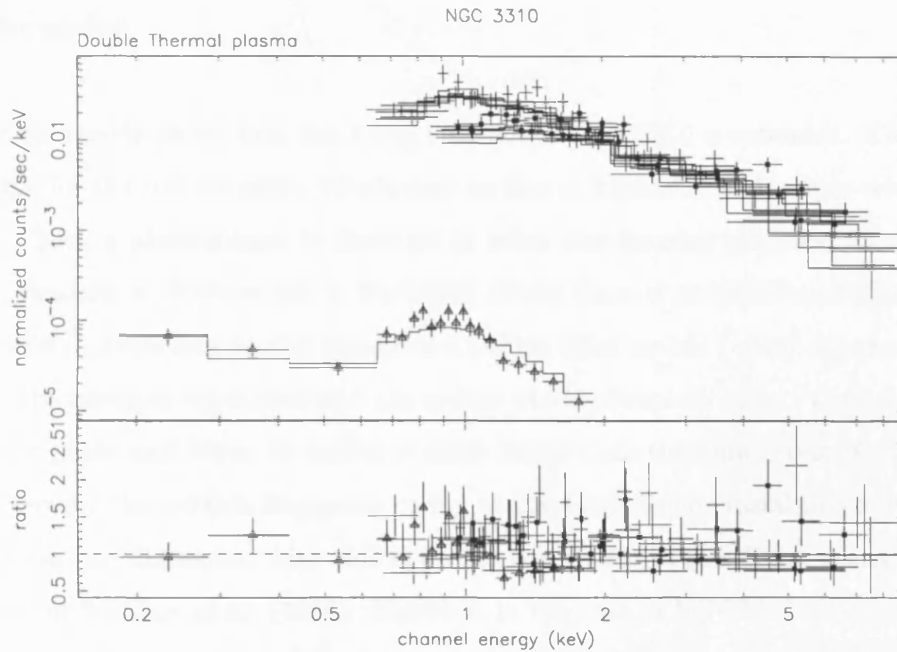


Figure 4.3: The top panel shows *ROSAT* and *ASCA* spectra of NGC3310 with the best fit double Raymond Smith model. The bottom panel shows the ratio of the data points to the model. The SIS data are marked with dots while the PSPC data are marked with triangles.

However, we do not find similar evidence here, since the hard component column has a value of $N_H \approx 1.77 \times 10^{20} \text{ cm}^{-2}$. Finally, we attempted to measure the element abundance in order to compare it with that for other star-forming galaxies (Sansom et al. 1996, Serlemitsos et al. 1996), which appear to show a systematic trend towards sub-solar abundances. Unfortunately the data for NGC 3310 are not able to set any useful constraint on the abundances.

We do not detect the FeK_α line at 6.7 keV as would be expected for a hot thermal plasma. The low signal/noise data above $\sim 5\text{keV}$, do not allow us to set a useful upper limit on the line equivalent width. The lack of a strong FeK line could be explained by lower than solar abundances, as is probably the case in other well-studied starbursts such as NGC253, (Ptak et al. 1997), and the Antennae, (Sansom et al. 1996).

We note that a previous preliminary analysis of *ASCA* data by Serlemitsos et al. (1996), find a spectral slope consistent with our value. However, they derive a considerably higher column density, but without the benefit of using the lower energy *ROSAT* data.

4.1.5 Discussion

The HRI image clearly shows that the X-ray emission in NGC3310 is extended. This supports a thermal origin for the soft emission, which may be due to a galactic scale super-wind (Heckman et al. 1990). Such a phenomenon is observed in other star-forming galaxies, for example M82 (Strickland, Ponman & Stevens 1997), NGC1569 (Della Ceca et al. 1996) and NGC4449 (Della Ceca et al. 1997). According to this scenario, a bubble filled by hot ($\sim 10^8$ K) gas is formed by the effect of the multiple supernova and the stellar winds of evolved stars. The bubble expands in the galactic plane and when its radius is much larger than the minor axis of the galaxy, the dense shell around the bubble fragments owing to Rayleigh-Taylor instabilities and forms the optical emission line filaments. Also this is probably a source of soft X-ray emission according to the studies of Suchkov et al. (1996). However, in the case of NGC3310 we cannot draw any definite conclusion because its low inclination angle ($\theta \approx 32^\circ$) makes detection of any outflow along the galaxy's minor axis very difficult.

In order to further check the validity of this model we can take the expected X-ray luminosity of a superbubble and compare it to the observed luminosity of the soft Raymond-Smith component. First we relate the X-ray luminosity of the gas contained in a superbubble with the basic properties of the starburst; its bolometric luminosity and age. Heckman et al. (1995) have calculated the total X-ray luminosity from a superbubble by integrating over its volume, and using the expressions for the gas density and the bubble radius derived by Mac Low & McCray (1988). They find that

$$L_X \simeq 5 \times 10^{39} L_{41}^{33/35} n^{17/35} t_7^{19/35} \text{ erg s}^{-1} \quad (4.1)$$

where L_{41} is the injection rate of mechanical energy into the bubble in units of $10^{41} \text{ erg s}^{-1}$, n is the gas density and t_7 is the age of the bubble in units of 10Myrs. Considering that the formation of the bubble begins, as a result of strong winds from O stars following the starburst, we can assume that the age of the bubble is almost the same as the age of the starburst. Using the relation

$$dE/dt = 7 \times 10^{42} L_{IR,11} \text{ erg s}^{-1} \quad (\text{Heckman et al. 1990}) \quad (4.2)$$

which correlates the total infrared luminosity (in units of $10^{11} L_\odot$) of a starburst with age greater than 10^7 yr with the kinetic energy deposition rate from supernovae and stellar winds, we can

estimate the X-ray luminosity. Using the IRAS data from Soifer et al. (1987), the IR luminosity of NGC3310 is $5.5 \times 10^{10} L_{\odot}$. Assuming a gas density of $\sim 1 \text{cm}^{-3}$ and a typical starburst age of 10 Myr we obtain an X-ray luminosity $L_x = 1.5 \times 10^{41} \text{erg s}^{-1}$ in the ROSAT band. This luminosity is larger than the measured luminosity in the same energy band of ($L_X = 4.7 \times 10^{40} \text{erg s}^{-1}$), but considering the large uncertainties in the model parameters involved, we conclude that the super-wind model remains a possible scenario for the origin of the soft X-ray emission. More support for the superbubble scenario comes from the soft X-ray spectrum of NGC3310. Its spectrum is well fitted by a warm thermal plasma of temperature 0.8 keV, consistent with the soft X-ray spectra of the prototypical starburst galaxies NGC253 and M82 where the superwind phenomenon is clearly detected. It is also similar to the temperature found in other star-forming galaxies like NGC1569 (Della Ceca et al. 1996), NGC4449 (Della Ceca et al. 1997) and NGC2782.

In the other hand the hard X-ray emission is consistent with a point-like source in the resolution of ASCA ($\sim 2'$). The spectrum can be fitted with either a high temperature Raymond-Smith component of temperature $\sim 15 \text{keV}$ or a power-law with a slope $\Gamma = 1.44$. The origin of the hard X-ray emission is more uncertain than that of the soft X-rays. There are four possible mechanisms which can produce the observed emission. Namely :

- Inverse Compton scattering of the IR photons produced in the starburst by electrons from the numerous supernova remnants (eg Schaaf et al. (1989)).
- Emission from a low-luminosity AGN as is the case in NGC3628 (Yaqoob, Serlemitsos, Ptak, Mushotzky, Kunieda & Terashima 1995).
- Thermal emission from a very hot gas ($T \sim 10^8 \text{K}$).
- Emission from X-ray binaries (Griffiths & Padovani 1990)

We discuss each of these possibilities in turn. We consider first the possibility, that the hard X-ray emission arises from Inverse Compton (IC) scattering of the copious infrared photons off of the relativistic electrons generated by the numerous supernovae. Support for this, especially in the case of NGC3310, comes from the similarity (within the errors) of the spectral index of the hard X-rays and the spectral index of the radio emission ($\alpha_{rad} = 0.61_{-0.03}^{+0.03}$ Niklas, Klein & Wielebinski (1997)). Following Schaaf et al. (1989) we can estimate the X-ray luminosity from

Inverse Compton scattering. From Vallee (1993) we have that the “minimum energy” magnetic field (see (Longair 1992)) is $B = 0.47 \times 10^{-5}$ Gauss. Then the minimum energy density is

$$u = (7/3)(B^2/8\pi) \text{ erg cm}^{-3} = 2.05 \times 10^{-12} \text{ erg cm}^{-3} \quad (4.3)$$

Following (Schaaf et al. 1989) we have that

$$L_{IC} = (1/3)\sigma_T R_{IC} L_{IR} \frac{\epsilon_e}{mc^2} \gamma_2^{0.8} \gamma_1^{0.2} \quad (4.4)$$

where σ_T , R_{IC} , L_{IR} and mc^2 , ϵ_e are the Thomson cross-section, the thickness of the disk, the far-IR luminosity, the rest mass of the electron and the energy density of the relativistic electrons, respectively. For a typical galactic disk $R_{IC} \sim 1\text{kpc}$ (we cannot measure the actual thickness of the disk since NGC3310 is almost face on) and for a typical value of the low frequency cut-off $\nu = 0.01\text{GHz}$ we have $\gamma_1 = 150$ for the lower limit of the Lorentz factor, and $\gamma_2 = 10^3$ for the maximum Lorentz factor, in order to have IC emission at 10keV (Schaaf et al. 1989). So for the Inverse Compton X-ray luminosity we predict a value of $2.5 \times 10^{38} \text{ erg s}^{-1}$, much lower than the detected hard X-ray luminosity of NGC3310, which is thus implying that IC can be only a minor component of the total X-ray emission from this galaxy. We caution that this result is quite uncertain as the calculation depends on parameters like the volume of the source and the thickness of the disk which are poorly known.

However, the hard X-ray power-law spectrum is nevertheless consistent with the presence of an active nucleus. In order to test this possibility further, we use the L_X/L_{H_α} relation from Elvis, Soltan & Keel (1984), where L_{H_α} is the luminosity of the broad component of the H_α line and L_X is the hard X-ray luminosity (2-10 keV). $L_X/L_{H_\alpha} \simeq 40$, for low-luminosity AGN and thus we estimate $f(H_\alpha) \sim 5.3 \times 10^{-14} \text{ erg cm}^{-2} \text{ s}^{-1}$. A broad component of this strength would be easily detectable at the spectra of Ho, Filippenko & Sargent (1997a), but is not seen. The absorbing columns found from the X-ray spectral fitting (ray-po model in Table 4.3) imply low extinction, $A_V \sim 0.1 \text{ mag}$ (Bohlin, Savage & Drake 1978). Hence a BLR reddened by this amount would still be observed.

The next possibility is the presence of a very hot thermal component. A Raymond-Smith model

with $kT > 10$ keV provides a good fit to the data. However, the strong FeK line at 6.7 keV which should accompany the thermal emission is not observed. This could be attributed to a low metallicity, but unfortunately we cannot check this as the abundances are not well constrained using the present X-ray data. Alternatively, the lack of a FeK line could be explained by a low contribution of type Ia supernovae to the enrichment of the Interstellar Medium (Sansom et al. 1996).

Finally we consider high mass X-ray binaries as a possible origin of the hard X-ray component. High mass binaries will form as a consequence of the starburst, and indeed many such systems have been identified in nearby star-forming galaxies (Read et al. (1997), Fabbiano (1995) and references therein). Assuming that a typical X-ray luminosity of these systems is 10^{37-38} erg s⁻¹, we can estimate the total number of binaries. As the X-ray luminosity of the hard component is $L_X \sim 10^{41}$ erg s⁻¹, we estimate a range of between 1,000-10,000 X-ray binaries. Now we can compare this with the number of ionising OB stars determined from the integrated far-infrared luminosity. Making the assumption that it is mostly these stars that heat the dust, which then re-radiates in the mid-far infrared, we estimate $\sim 2 \times 10^5$ OB stars for NGC3310. If, following Fabbiano et al. (1992), 0.2 percent of these are massive X-ray binaries, then there are 400, and 7000 such systems, respectively. For the upper range of binary luminosities the predicted X-ray luminosity is comparable to that observed in both cases. Indeed, if the hard X-ray emission arises from binaries with low-metallicity and thus high X-ray luminosity ($L_X \sim 10^{38-39}$ erg s⁻¹) like those observed in the Magellanic Clouds (van Paradijs & McClintock 1995), then they could easily produce the observed luminosity.

4.2 Arp 299

4.2.1 Overview

Arp 299 is also a merging system, but in contrast to NGC3310 it is in an earlier merger phase. The system is composed of NGC3690, which is the western part of the merger and IC694, the eastern component. It is in the original catalogue of peculiar galaxies of Arp (1966), and it is also catalogued in the list of UV-excess galaxies of Markarian. Casoli, Combes, Augarde, Figon & Martin (1989) propose that there is a third component in the system thus forming an interacting

triplet. Its recession velocity is 3159 km s^{-1} (Sanders & Mirabel 1985), implying a distance of 63.2 Mpc. At that distance the projected separation of $22.5''$ of the two components corresponds to 6.9 kpc. The infrared surface brightness of NGC3690 is at least twice that of IC694 (Friedman, Cohen, Jones et al. 1987). The total mass of gas calculated from radio observations is about $2 \times 10^{11} M_{\odot}$ (Casoli et al. 1989)

The high IR luminosity ($L_{FIR} = 1.2 \times 10^{12} L_{\odot}$) (Soifer et al. 1987), results from re-radiating dust heated by the starburst activity. This is supported by multi-wavelength studies (Gehrz, Sramek & Weedman 1983), (Friedman et al. 1987), (Nakagawa, Nagata, Geballe, Okuda, Shibai & Matsuhara 1989). Detailed analysis of emission line ratios using the diagnostic diagrams of (Veilleux & Osterbrock 1987) clearly indicate a stellar origin of the ionising continuum (Friedman et al. 1987). The infrared emission is extended over a region of several kpc, but the main sources are located close to the two nuclei (Friedman et al. 1987).

Modeling of the starburst has been carried out by (Gehrz et al. 1983) and (Nakagawa et al. 1989). The latter find a starburst age of about 10 Myrs. An interesting point is that the two nuclei have different properties, implying either a different age and/or a different Initial Mass Function (IMF) for each starburst event.

Arp 299 has been previously observed with the High Resolution Imager (HRI) on board the *Einstein* observatory. 17 counts were detected implying an X-ray flux $f_x = 4.8 \times 10^{-13} \text{ ergs}^{-1} \text{ cm}^{-2}$ in the 0.2-4.0 keV band, for a 5 keV bremsstrahlung model and Galactic absorption (Fabbiano et al. 1992). This corresponds to an X-ray luminosity of $2.3 \times 10^{41} \text{ erg s}^{-1}$.

4.2.2 The data

Arp 299 has been observed on four occasions with the *ROSAT* satellite; one with *HRI* and three with *PSPC*. All the details about the observations are presented in Table 4.4. From these only the shortest *PSPC* observation has not been used. It has also been observed twice with *ASCA* (see Table 4.4) and both observations has been used in the data analysis.

Table 4.4: Summary of the observations of NGC3690

Satellite	Instrument	Date Observation started	Exposure Time† Ksec
<i>ROSAT</i>	PSPC	1993-04-22	3.534
<i>ROSAT</i>	PSPC	1991-11-18	6.391
<i>ROSAT</i>	HRI	1993-04-18	6.751
<i>ASCA</i>	SIS/GIS	1994-04-06	GIS:5.7, SIS:5.3
<i>ASCA</i>	SIS/GIS	1994-12-01	GIS:38.2, SIS:35.5

4.2.3 Soft X-ray imaging

The HRI analysis of Arp 299 followed the same procedure as for NGC3310. The image pixels were binned to a size of $1.5''$ and then smoothed using a two-dimensional Gaussian of FWHM $3.5''$. Finally, we overlaid the X-ray contours on a POSS plate image obtained from the Digitized Sky Survey, figure 4.4; the contours correspond to 0.57, 0.44, 0.40, 0.35, 0.31, 0.27, 0.22, 0.18, 0.13 and $0.11 \text{ counts arcsec}^{-2}$ respectively. The most striking feature is the existence of three separate sources in the X-ray image. The two most luminous sources correspond to the two merging nuclei. Their X-ray fluxes are given in Table 4.5. The third X-ray source is very close to a hot spot seen in the infrared and radio images to the north of NGC3690 (the western component), but they are not spatially coincident as is seen from the comparison between the X-ray image and a narrow band Fabry-Perrot $\text{Pa}\alpha$ image (Alonso-Herrero et al. 2000) (figs. 4.5, 4.6). In the same image H-band continuum and $[\text{FeII}]\lambda 1.644$ continuum subtracted NICMOS images of NGC3690 and IC 694 are presented.

Apart from these three sources there are marginal detections of other sources, but at a low level of significance (below 3σ), and will not be discussed further. It is worth to note that the relative strengths of the three main X-ray sources follow quite well the relative strengths of the near infrared sources, suggesting a possible common origin for the IR and the X-ray emission.

We have searched for extended emission from the two resolved nuclei. From figure 4.4 it is clear that the emission from the two resolved nuclei is extended and not symmetrical. Fitting a Gaussian function to the radial profiles of NGC3690 and IC694 yields a FWHM of 1.5 and 1.8 arcmin respectively.

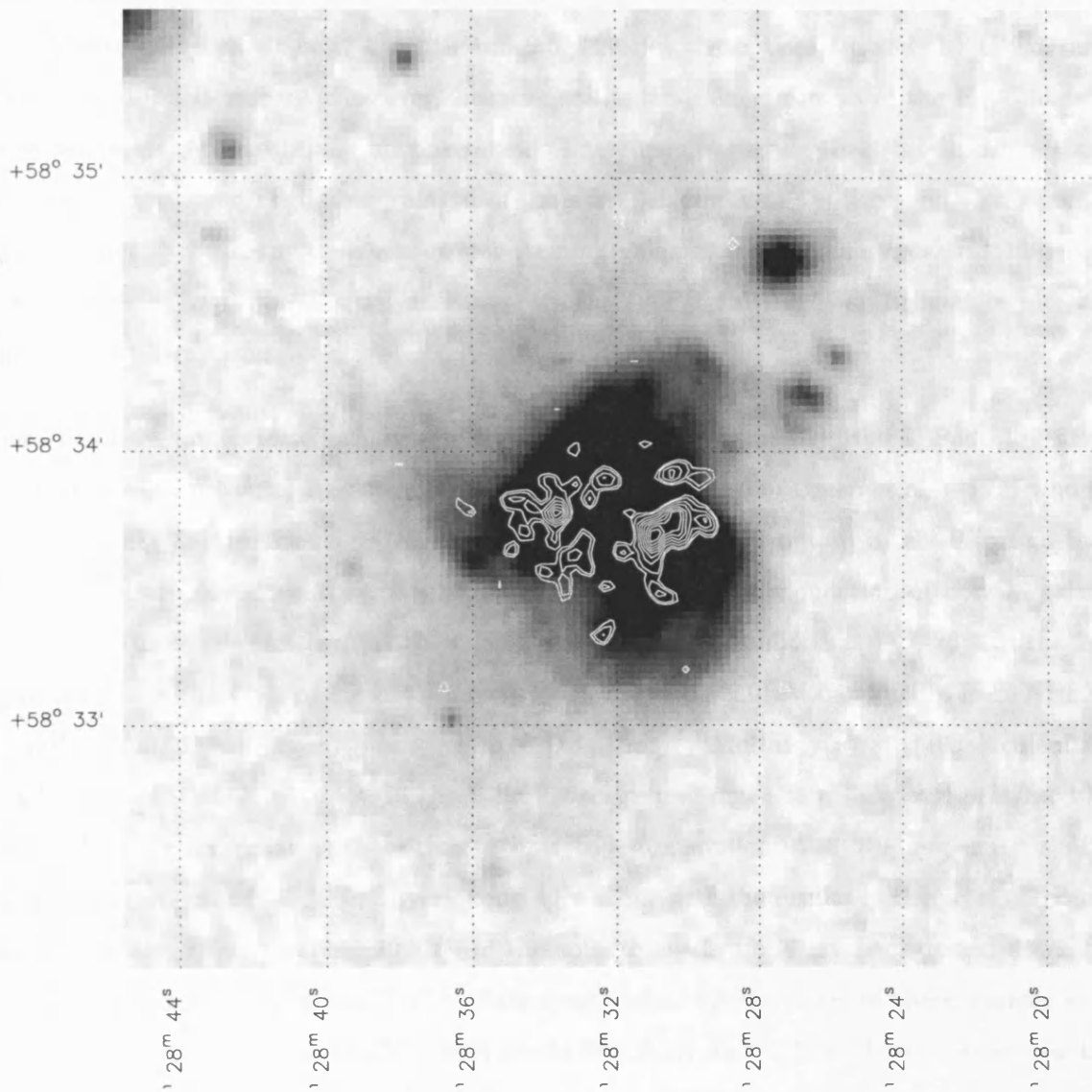


Figure 4.4: X-ray contours from the HRI observation of Arp 299 overlaid on a POSS image. The contours are in levels of 0.57, 0.44, 0.4, 0.35, 0.31, 0.26, 0.22, 0.18, 0.13, 0.11 counts arcsec⁻².

3.6.2 Starbursts vs. AGN

Adding the contributions from the different redshift bins gives the total X-ray background emission due to star-formation. This is $48.5^{+29.2}_{-29.1}\%$ and $24.7^{+14.13}_{-14.5}\%$ for the optical/IR and the UV determinations of the SFR history respectively, using the FIR calibration. In the case of the H_α calibration the result is $22.1^{+17.9}_{-16.4}\%$ and $9.5^{+9.6}_{-8.0}\%$ for the optical/IR and the UV determinations of the SFR history. However, because of the large uncertainties of the H_α calibration the latter results are essentially unconstrained. These results suggest that star-forming galaxies can account for a non negligible fraction of the extragalactic X-ray background. This fraction can be larger if the X-ray emission of star-forming galaxies evolves with redshift. This could arise because of lower metallicities at earlier epochs (Pei & Fall 1995) and therefore increased luminosity of X-ray binaries.

These numbers are in excellent agreement with the estimates of Griffiths & Padovani (1990) who find a contribution of 20%-30% for moderate evolution and of Green et al. (1992) who find 5%-25% at 2keV. Also David et al. (1992) find 30%-40% contribution in the *Einstein* band. Their results are based on the convolution of the FIR luminosity function of normal galaxies with the LX-LFIR relation. From the *ROSAT* Deep Survey is found that 11%-36% of the 2keV XRB down to a flux limit of $4 \times 10^{-15} \text{erg cm}^{-2} \text{s}^{-1}$ in the 0.5-2.0keV band arises from NELXGs (Griffiths et al. 1996). From a much longer Deep Survey McHardy et al. (1998) calculate a contribution of NELGs of $\sim 8\%$ in the 1-2keV background down to a flux level of $2.0 \times 10^{-15} \text{erg cm}^{-2} \text{s}^{-1}$. Extrapolating these results down to a flux level of $0.5 \times 10^{-15} \text{erg cm}^{-2} \text{s}^{-1}$ they find a contribution of 15%-30%, in very good agreement with the results of this work. Recently, Hasinger et al. (1998) resolved 70-80% of the soft extragalactic X-ray background down to a flux limit of $5.5 \times 10^{-15} \text{erg cm}^{-2} \text{s}^{-1}$. Follow up optical spectroscopy of these sources shows that almost all of them are AGN: $\sim 80\%$ broad line AGN and $\sim 20\%$ show only narrow-lines (Lehmann et al. 2000). The fact that Lehmann et al. (2000) do not observe any obvious star-forming galaxies may be due to their faintness as in general they are less luminous and they have lower surface brightness than AGN, and their emission arises from the whole galaxy rather than in the very nuclear region. Therefore it is possible that they are present at lower flux limits. Indeed McHardy et al. (1998) estimated that NELGs may have much higher contribution at fluxes below $5 \times 10^{-15} \text{erg cm}^{-2} \text{s}^{-1}$. Moreover, the first results from a Deep Survey with

Chandra showed that there is a very large number of optically faint sources at X-ray fluxes $3 \times 10^{-16} \text{erg cm}^{-2} \text{s}^{-1}$ in the 0.5-2.0keV band (Mushotzky, Cowie, Barger & Arnaud 2000). Some of these sources may be related to star-forming galaxies; however, careful optical and X-ray observations are needed in order to draw any definite conclusions.

Chapter 4

Study of selected X-ray luminous starburst galaxies¹

This chapter describes in detail the data analysis and interpretation of the X-ray properties of three examples of nearby X-ray luminous starburst galaxies. The aim is to investigate whether they have the same properties as their lower luminosity counterparts. The first two galaxies are selected from the sample of Ho, Filippenko & Sargent (1997*a*) which is reported in Chapter 2, on the basis of their high X-ray luminosity. The third object (UGC 4305) is selected from the work of Moran et al. (1996) on the basis of its very high ratio X-ray to FIR luminosity.

4.1 NGC3310

4.1.1 Overview

NGC3310 is a well studied nearby galaxy of Sbc(r)pec type (Mulder & Van Driel 1996). Its recession velocity is 980 km s^{-1} (de Vaucouleurs 1991) implying a distance of 19.6 Mpc . Its optical image presents some very interesting morphologies, like a jet-like structure in the north-west of the nucleus which points towards an arc about 100 arcsec from the nucleus. There are various suggestions for the nature of this structure. For example Bertola & Sharp (1984)

¹The work presented in this chapter has been done in collaboration with M.J. Ward and I. Georgantopoulos and is published in MNRAS.

proposed that this can be the remnant of an old jet and the part of a spiral arm. In the other hand Balick & Heckman (1981) suggest that this is the remnant from an older collision between two galaxies. This seems to be the most probable explanation as the anomalies found in its rotation curve imply that it has undergone a collision with another galaxy (Mulder & Van Driel 1996). However, infrared and high resolution radio images do not reveal any double nucleus structure (Telesco & Gatley 1984, Balick & Heckman 1981). This could mean that the merger phase is almost complete and the system is now relaxing (Balick & Heckman 1981). Another very interesting morphological structure is a giant H II region located in the South-East of the nucleus. Its size is about $6''$ ($\sim 570\text{pc}$), comparable to the largest extragalactic H II regions known.

The optical spectrum of the galaxy exhibits the typical signatures of starburst activity. The position of the line ratios in the standard diagnostic diagrams of Veilleux & Osterbrock (1987) lies well in the H II locus. This gives confidence that it is a bona-fide starburst galaxy without any activity arising from accretion onto a super-massive black-hole. The spectrum of the 'jumbo' H II region is dominated by the signatures of Wolf-Rayet stars like the WR bump at 4640\AA , (Pastoriza, Dottori, Terlevich et al. 1993).

Evolutionary synthesis modeling of the starburst in NGC3310 has shown that the age of the starburst is between 10^7 and 10^8 years, whereas there is the possibility that another starburst event has occurred in the past which produced the population of old stars observed now (Pastoriza et al. 1993).

NGC3310 has been previously observed with the Imaging Proportional Counter (IPC) on board the *Einstein* observatory yielding an X-ray flux $f_x = 1.1 \times 10^{-12} \text{erg cm}^{-2} \text{s}^{-1}$ in the 0.3-3.5 keV band for a 5keV bremsstrahlung model and Galactic absorption (Fabbiano et al. 1992). This corresponds to an X-ray luminosity of $5.0 \times 10^{40} \text{erg s}^{-1}$.

4.1.2 The data

NGC3310 has been observed in the soft X-rays with PSPC and *HRI* on board *ROSAT* (Trumper 1984). The details of the observations are presented in Table 4.1.

Table 4.1: Summary of the observations of NGC3310

Satellite	Instrument	Date Observation started	Exposure Time Ksec
<i>ROSAT</i>	PSPC	1991-11-16	9.114
<i>ROSAT</i>	HRI	1995-04-17	41.842
<i>ROSAT</i>	HRI	1994-11-23	4095
<i>ASCA</i>	SIS/GIS	1994-04-17	GIS: 10.4, SIS:10.4
<i>ASCA</i>	SIS/GIS	1994-11-13	GIS:11.6, SIS:10.2

For the reduction of the PSPC data we have followed the procedure described in Chapter 3. We excluded those data with Master Veto rates higher than $170 \text{ counts s}^{-1}$ as the particle background cannot be accurately modeled for higher background time intervals. We extracted a PSPC spectral image (channels 11 to 201) with a pixel size of $15''$. To obtain an X-ray spectrum we extracted data from a circular region of $1.5'$ radius around the X-ray centroid. The background was estimated from an annular region between radii of $15'$ and $8.8'$ from the centroid, after exclusion of all the discrete sources detected with the PSS algorithm (Allen 1997) down to the 5σ level.

From the HRI observations only the longest one has been used. HRI covers a field of $38'$ diameter and it has a spatial resolution of about $5''$ (the FWHM of the XRT+HRI Point Spread Function). We note that the HRI has very limited spectral resolution so it is not useful in spectral analysis (David et al. 1997). The screening of the data has been carried out using the *ASTERIX* package. We have rejected all data with aspect errors greater than 2.

NGC3310 has been also observed with the *ASCA* satellite (Tanaka et al. 1994) see Table 4.1 for the details of the observations. For the screening of the data we have followed the standard procedure and used the *ASCACLEAN* program in the *FTOOLS* package with the parameters described in the ABC *ASCA* Guide (Yaqoob 1997). After the standard processing we inspected the light curves and removed time intervals with unusually high numbers of counts, which may result from background particle contamination. The extraction of the source and the background spectra has been carried out using the *XSELECT* program within the *FTOOLS* package. We extract the source spectrum using a circular region of 2.7 and 5.5 arcmin radius for the SIS and GIS respectively. For the background regions we have selected ten source free zones, each of area about 6 and 10 arcmin² for the SIS and GIS respectively. Following extraction of the source and

background spectra, we ran the SISrmg program to create the SIS response matrices for each SIS source spectral file. For the GIS spectral files we used the gis2v4_0.rmf and gis3v4_0.rmf for GIS2 and GIS3 respectively. We created the Ancillary Response Matrices for each file by running the ASCAarf programs within the FTOOLS package.

4.1.3 Soft X-ray imaging

We used the archival *HRI* observations to obtain information on the morphology of the X-ray emitting regions and compared these with images of these galaxies at other wavelengths. First we searched for extended emission by comparing the background subtracted radial profile of the galaxies with the radial profile of a point source. For this purpose we used as a reference the point source corresponding to the star AR-Lac. We retrieved archival data for an on-axis observation of AR-Lac, and applied the same extraction process as used for the galaxy. The comparison of the radial profiles of NGC3310, and the radial profile of AR-Lac is shown in figure 4.1. This figure clearly shows that the X-ray source has a radius of ~ 0.5 arcmin (at larger radii the emission from the galaxy begins to blend with the profile of AR-Lac, within the 2σ error bars). Although this is a somewhat arbitrary point at which to define the extent of the emission, it gives a lower limit to the source size. At the distance of NGC3310 this corresponds to ~ 3 kpc. We note that fitting a Gaussian function to the radial profile gives a similar source size (FWHM=1.6 arcmin).

In order to compare the distribution of the X-ray emitting gas with the optical image we have resampled the X-ray image with a pixel size of 1.5 arc-seconds and then smoothed this image using a two-dimensional Gaussian of FWHM=3.5 arc-seconds (2.3 pixels) following Della Ceca, Griffiths, Heckman & Mackenty (1996). The effective resolution is $5.4''$, equal to the XRT+HRI PSF. Then we obtained contours from this image corresponding to 2.2, 2.0, 1.7, 1.33, 0.88, 0.44, 0.35, 0.26, 0.17 counts arcsec⁻² and overlaid these onto an optical image obtained from the Digitized Sky Survey. This image is shown in figure 4.2. The main problem we faced in attempting to overlay the two images is that of frame registration. There are no X-ray sources within the HRI image which have an obvious optical counterpart. Thus in order to overlay the X-ray contour plot onto the optical image, we are forced to assume that the centroid of the X-ray source corresponds to that of the optical nucleus. In the X-ray image of NGC3310 we detect

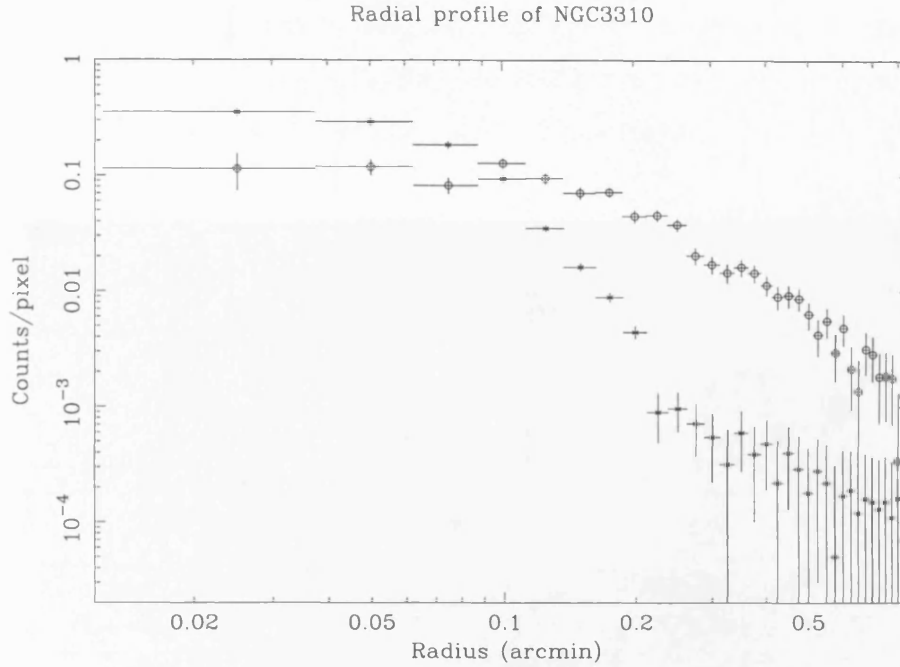


Figure 4.1: The HRI radial profile of NGC3310 (circles) overlaid on the radial profile of AR Lac (stars).

Table 4.2: Sources in the *HRI* field of NGC3310

RA (J2000)	Dec (J2000)	Count rate count s ⁻¹	Flux erg cm ⁻² s ⁻¹	Significance
10 38 43.2	+53 31 07	2.0±0.27×10 ⁻³	2.3 × 10 ⁻¹⁴	15.5
10 38 46.7	+53 30 38	2.8±0.26×10 ⁻³	3.07 × 10 ⁻¹⁴	23.4

two other sources in addition to the nucleus, at a significance above 10σ . The details concerning these sources are presented in Table 4.2. The fluxes have been calculated from the background subtracted count rates and a 0.8 keV thermal plasma model absorbed by the galactic column density. These point sources may correspond to luminous X-ray binaries or young supernova remnants. Unfortunately there are no identified optical counterparts for these X-ray sources on the POSS plates.

4.1.4 Spectral analysis

The *ROSAT* and *ASCA* spectra of NGC3310 were extracted as described previously, and analysed with the *XSPEC* package (v10). In order to use χ^2 statistics the spectra have been binned

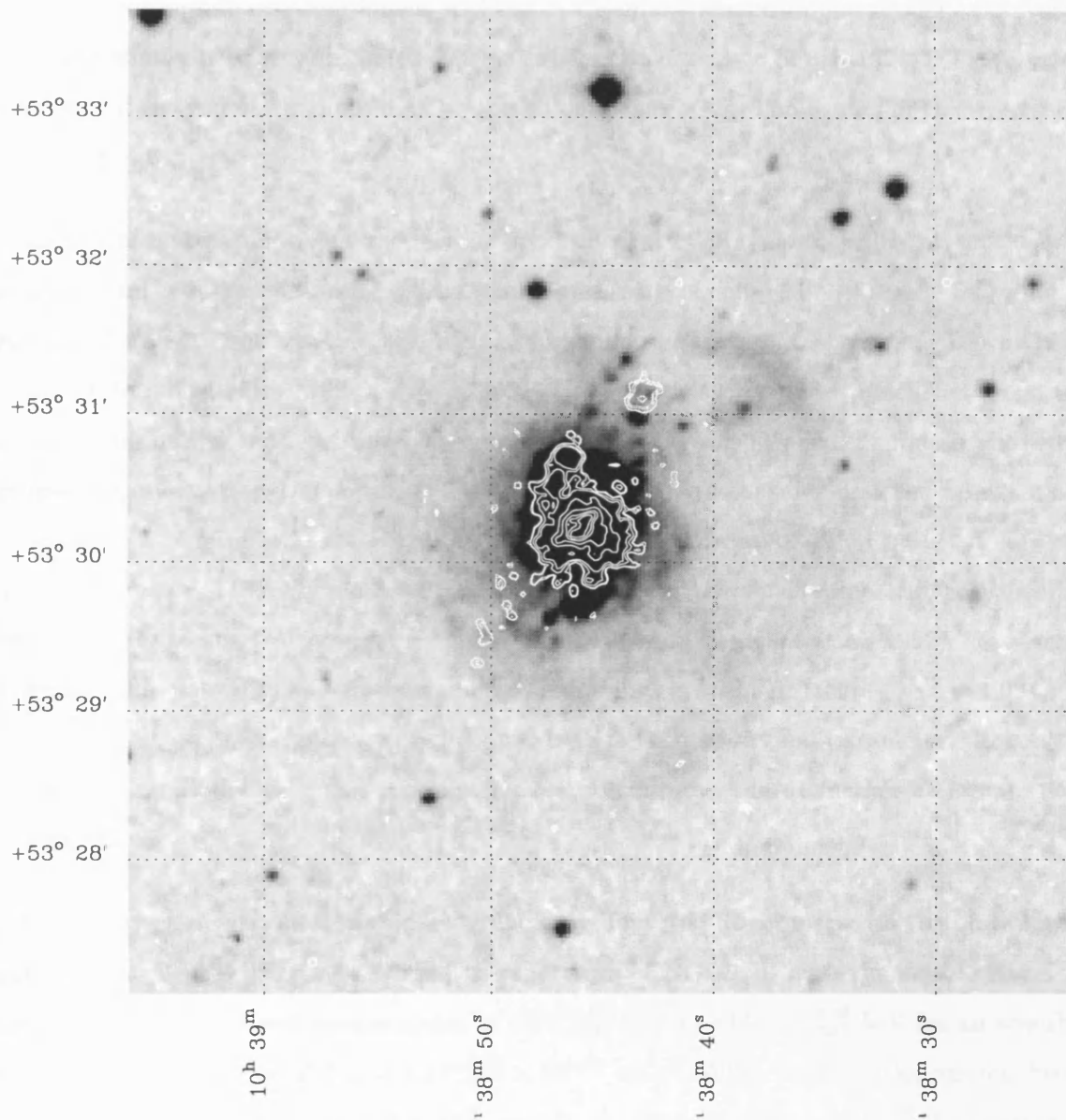


Figure 4.2: X-ray contours from the HRI observation of NGC3310 overlaid on a POSS image. The contours are in levels of 2.2, 2.0, 1.7, 1.33, 0.88, 0.44, 0.35, 0.26, 0.17 counts arcsec⁻².

in order to have at least 20 counts in each bin. All *ROSAT* points bellow 0.1 keV and above 2.0 keV have been rejected because of the limitations of the detector. We have used only *ASCA* data in the range 0.6 to 8.0 keV for SIS and 0.7 to 7.0 keV for GIS.

We first fitted simple one-component models: a thermal bremsstrahlung model, a power-law model and finally a Raymond-Smith plasma model (Raymond & Smith 1977). These models were rejected at greater than the 99.9 per cent confidence level. The results of the spectral fits are given in 4.3.

We then fitted two component models: a two temperature Raymond-Smith plasma (ray-ray hereafter) and a Raymond-Smith plasma combined with a power-law (po-ray), following the results of Moran & Lehnert (1997) and Ptak, Serlemitsos, Yaqoob, Mushotzky & Tsuru (1997) on the starburst galaxies M82 and NGC253. These models provided a much better fit than the simple models described above, at a confidence level over 90 per cent for an addition of two free parameters (eg Bevington & Robinson (1992)). We consider first the po-ray model. We obtained a photon index of $\Gamma = 1.44_{-0.11}^{+0.20}$ and a temperature of $kT = 0.81_{-0.12}^{+0.09}$ keV with a reduced $\chi^2 = 1.115$, where the abundance is fixed to the solar value and the absorbing column density to the Galactic value, $N_H = 0.7 \times 10^{20} \text{ cm}^{-2}$, (Stark et al. 1992). Leaving the absorbing column density as a free parameter further improves the fit (reduced $\chi^2 = 1.031$); this is significant at a confidence level of > 99 per cent for one additional parameter. In contrast, leaving the abundance as a free parameter does not improve the fit further at a statistically significant level.

In the ray-ray case we do not obtain a significantly improved fit compared to the po-ray model (reduced $\chi^2 = 1.022$). Figure 4.3 shows the spectrum of NGC3310 with the double Raymond-Smith model. We obtained temperatures of $0.80_{-0.04}^{+0.07}$ keV and $14.98_{-4.88}^{+13.52}$ keV for an absorbing hydrogen column density of $N_H = 1.37_{-0.32}^{+0.50} \times 10^{20} \text{ cm}^{-2}$. When we fixed the column density to the Galactic value ($N_H \approx 1.0 \times 10^{20} \text{ cm}^{-2}$) we obtained $kT_1 = 0.84_{-0.07}^{+0.05}$, whereas the temperature of the hard component was pegged at the upper limit imposed by the model ($kT_2 \approx 64$ keV). We also introduced two different absorbing column densities, for the soft and the hard components, following the analysis of M82 by Moran & Lehnert (1997) who showed that the hard X-ray component is obscured by $N_H \sim 10^{22} \text{ cm}^{-2}$.

Table 4.3: Spectral fitting results for NGC 3310

Parameter	Power-law	Single Temperature Raymond-Smith	Double Temperature Raymond Smith	Raymond Smith + Power-law
kT (KeV)		$7.35^{+1.24}_{-1.18}$	$0.80^{+0.07}_{-0.04}$ $14.98^{+13.52}_{-4.88}$	$0.81^{+0.09}_{-0.12}$
Γ	$1.68^{+0.08}_{-0.08}$			$1.44^{+0.20}_{-0.11}$
$N_H(10^{20} \text{cm}^{-20})$	$3.15^{+0.63}_{-0.52}$	$1.90^{+0.45}_{-0.36}$	$1.37^{+0.50}_{-0.32}$	$1.74^{+0.68}_{-0.40}$
$\chi^2 / \text{d.o.f.}$	222.9/175	239.3/175	168.7/165	170.2/165
Flux [†] small (0.1-2.0keV)	0.95	0.86	0.9	1.09
Flux [†] (2.0-10.0keV)	1.88	2.12	2.10	2.10
Total Luminosity [†] (0.1-10keV)	1.3	1.4	1.4	1.5

†All the fluxes are in units of $10^{-12} \text{erg s}^{-1} \text{cm}^{-2}$. ‡The luminosity is in units of $10^{41} \text{erg s}^{-1}$.

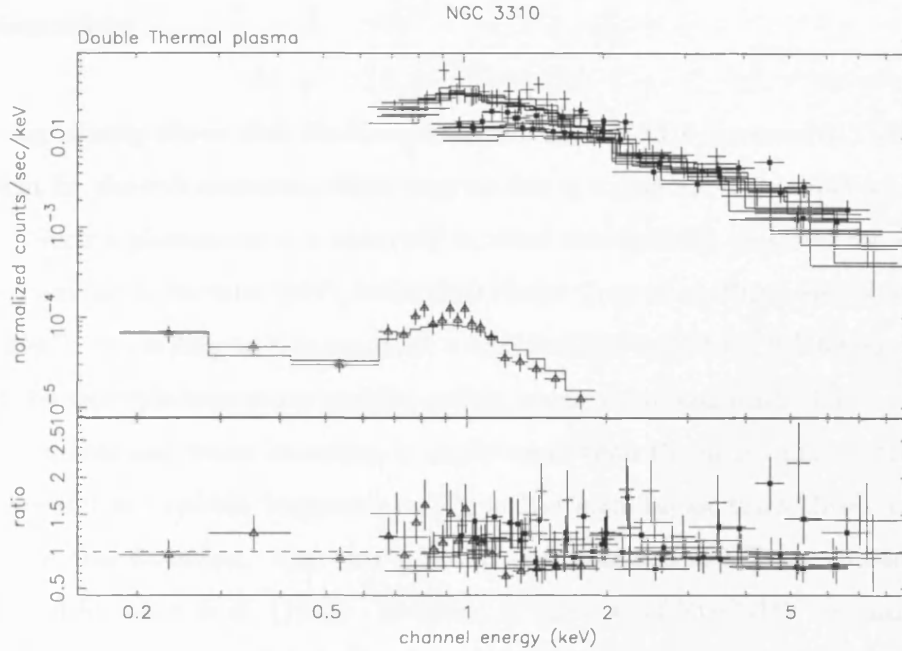


Figure 4.3: The top panel shows *ROSAT* and *ASCA* spectra of NGC3310 with the best fit double Raymond Smith model. The bottom panel shows the ratio of the data points to the model. The SIS data are marked with dots while the PSPC data are marked with triangles.

However, we do not find similar evidence here, since the hard component column has a value of $N_H \approx 1.77 \times 10^{20} \text{ cm}^{-2}$. Finally, we attempted to measure the element abundance in order to compare it with that for other star-forming galaxies (Sansom et al. 1996, Serlemitsos et al. 1996), which appear to show a systematic trend towards sub-solar abundances. Unfortunately the data for NGC 3310 are not able to set any useful constraint on the abundances.

We do not detect the FeK_α line at 6.7 keV as would be expected for a hot thermal plasma. The low signal/noise data above $\sim 5\text{keV}$, do not allow us to set a useful upper limit on the line equivalent width. The lack of a strong FeK line could be explained by lower than solar abundances, as is probably the case in other well-studied starbursts such as NGC253, (Ptak et al. 1997), and the Antennae, (Sansom et al. 1996).

We note that a previous preliminary analysis of *ASCA* data by Serlemitsos et al. (1996), find a spectral slope consistent with our value. However, they derive a considerably higher column density, but without the benefit of using the lower energy *ROSAT* data.

4.1.5 Discussion

The HRI image clearly shows that the X-ray emission in NGC3310 is extended. This supports a thermal origin for the soft emission, which may be due to a galactic scale super-wind (Heckman et al. 1990). Such a phenomenon is observed in other star-forming galaxies, for example M82 (Strickland, Ponman & Stevens 1997), NGC1569 (Della Ceca et al. 1996) and NGC4449 (Della Ceca et al. 1997). According to this scenario, a bubble filled by hot ($\sim 10^8$ K) gas is formed by the effect of the multiple supernova and the stellar winds of evolved stars. The bubble expands in the galactic plane and when its radius is much larger than the minor axis of the galaxy, the dense shell around the bubble fragments owing to Rayleigh-Taylor instabilities and forms the optical emission line filaments. Also this is probably a source of soft X-ray emission according to the studies of Suchkov et al. (1996). However, in the case of NGC3310 we cannot draw any definite conclusion because its low inclination angle ($\theta \approx 32^\circ$) makes detection of any outflow along the galaxy's minor axis very difficult.

In order to further check the validity of this model we can take the expected X-ray luminosity of a superbubble and compare it to the observed luminosity of the soft Raymond-Smith component. First we relate the X-ray luminosity of the gas contained in a superbubble with the basic properties of the starburst; its bolometric luminosity and age. Heckman et al. (1995) have calculated the total X-ray luminosity from a superbubble by integrating over its volume, and using the expressions for the gas density and the bubble radius derived by Mac Low & McCray (1988). They find that

$$L_X \simeq 5 \times 10^{39} L_{41}^{33/35} n^{17/35} t_7^{19/35} \text{ erg s}^{-1} \quad (4.1)$$

where L_{41} is the injection rate of mechanical energy into the bubble in units of $10^{41} \text{ erg s}^{-1}$, n is the gas density and t_7 is the age of the bubble in units of 10Myrs. Considering that the formation of the bubble begins, as a result of strong winds from O stars following the starburst, we can assume that the age of the bubble is almost the same as the age of the starburst. Using the relation

$$dE/dt = 7 \times 10^{42} L_{IR,11} \text{ erg s}^{-1} \quad (\text{Heckman et al. 1990}) \quad (4.2)$$

which correlates the total infrared luminosity (in units of $10^{11} L_\odot$) of a starburst with age greater than 10^7 yr with the kinetic energy deposition rate from supernovae and stellar winds, we can

estimate the X-ray luminosity. Using the IRAS data from Soifer et al. (1987), the IR luminosity of NGC3310 is $5.5 \times 10^{10} L_{\odot}$. Assuming a gas density of $\sim 1 \text{cm}^{-3}$ and a typical starburst age of 10 Myr we obtain an X-ray luminosity $L_x = 1.5 \times 10^{41} \text{erg s}^{-1}$ in the ROSAT band. This luminosity is larger than the measured luminosity in the same energy band of ($L_X = 4.7 \times 10^{40} \text{erg s}^{-1}$), but considering the large uncertainties in the model parameters involved, we conclude that the super-wind model remains a possible scenario for the origin of the soft X-ray emission. More support for the superbubble scenario comes from the soft X-ray spectrum of NGC3310. Its spectrum is well fitted by a warm thermal plasma of temperature 0.8 keV, consistent with the soft X-ray spectra of the prototypical starburst galaxies NGC253 and M82 where the superwind phenomenon is clearly detected. It is also similar to the temperature found in other star-forming galaxies like NGC1569 (Della Ceca et al. 1996), NGC4449 (Della Ceca et al. 1997) and NGC2782.

In the other hand the hard X-ray emission is consistent with a point-like source in the resolution of ASCA ($\sim 2'$). The spectrum can be fitted with either a high temperature Raymond-Smith component of temperature $\sim 15 \text{ keV}$ or a power-law with a slope $\Gamma = 1.44$. The origin of the hard X-ray emission is more uncertain than that of the soft X-rays. There are four possible mechanisms which can produce the observed emission. Namely :

- Inverse Compton scattering of the IR photons produced in the starburst by electrons from the numerous supernova remnants (eg Schaaf et al. (1989)).
- Emission from a low-luminosity AGN as is the case in NGC3628 (Yaqoob, Serlemitsos, Ptak, Mushotzky, Kunieda & Terashima 1995).
- Thermal emission from a very hot gas ($T \sim 10^8 \text{ K}$).
- Emission from X-ray binaries (Griffiths & Padovani 1990)

We discuss each of these possibilities in turn. We consider first the possibility, that the hard X-ray emission arises from Inverse Compton (IC) scattering of the copious infrared photons off of the relativistic electrons generated by the numerous supernovae. Support for this, especially in the case of NGC3310, comes from the similarity (within the errors) of the spectral index of the hard X-rays and the spectral index of the radio emission ($\alpha_{rad} = 0.61^{+0.03}_{-0.03}$ Niklas, Klein & Wielebinski (1997)). Following Schaaf et al. (1989) we can estimate the X-ray luminosity from

Inverse Compton scattering. From Vallee (1993) we have that the “minimum energy” magnetic field (see (Longair 1992)) is $B = 0.47 \times 10^{-5}$ Gauss. Then the minimum energy density is

$$u = (7/3) (B^2/8\pi) \text{ erg cm}^{-3} = 2.05 \times 10^{-12} \text{ erg cm}^{-3} \quad (4.3)$$

Following (Schaaf et al. 1989) we have that

$$L_{IC} = (1/3)\sigma_T R_{IC} L_{IR} \frac{\epsilon_e}{mc^2} \gamma_2^{0.8} \gamma_1^{0.2} \quad (4.4)$$

where σ_T , R_{IC} , L_{IR} and mc^2 , ϵ_e are the Thomson cross-section, the thickness of the disk, the far-IR luminosity, the rest mass of the electron and the energy density of the relativistic electrons, respectively. For a typical galactic disk $R_{IC} \sim 1\text{kpc}$ (we cannot measure the actual thickness of the disk since NGC3310 is almost face on) and for a typical value of the low frequency cut-off $\nu = 0.01\text{GHz}$ we have $\gamma_1 = 150$ for the lower limit of the Lorentz factor, and $\gamma_2 = 10^3$ for the maximum Lorentz factor, in order to have IC emission at 10keV (Schaaf et al. 1989). So for the Inverse Compton X-ray luminosity we predict a value of $2.5 \times 10^{38} \text{ erg s}^{-1}$, much lower than the detected hard X-ray luminosity of NGC3310, which is thus implying that IC can be only a minor component of the total X-ray emission from this galaxy. We caution that this result is quite uncertain as the calculation depends on parameters like the volume of the source and the thickness of the disk which are poorly known.

However, the hard X-ray power-law spectrum is nevertheless consistent with the presence of an active nucleus. In order to test this possibility further, we use the $L_X/L_{H\alpha}$ relation from Elvis, Soltan & Keel (1984), where $L_{H\alpha}$ is the luminosity of the broad component of the $H\alpha$ line and L_X is the hard X-ray luminosity (2-10 keV). $L_X/L_{H\alpha} \simeq 40$, for low-luminosity AGN and thus we estimate $f(H\alpha) \sim 5.3 \times 10^{-14} \text{ erg cm}^{-2} \text{ s}^{-1}$. A broad component of this strength would be easily detectable at the spectra of Ho, Filippenko & Sargent (1997a), but is not seen. The absorbing columns found from the X-ray spectral fitting (ray-po model in Table 4.3) imply low extinction, $A_V \sim 0.1 \text{ mag}$ (Bohlin, Savage & Drake 1978). Hence a BLR reddened by this amount would still be observed.

The next possibility is the presence of a very hot thermal component. A Raymond-Smith model

with $kT > 10$ keV provides a good fit to the data. However, the strong FeK line at 6.7 keV which should accompany the thermal emission is not observed. This could be attributed to a low metallicity, but unfortunately we cannot check this as the abundances are not well constrained using the present X-ray data. Alternatively, the lack of a FeK line could be explained by a low contribution of type Ia supernovae to the enrichment of the Interstellar Medium (Sansom et al. 1996).

Finally we consider high mass X-ray binaries as a possible origin of the hard X-ray component. High mass binaries will form as a consequence of the starburst, and indeed many such systems have been identified in nearby star-forming galaxies (Read et al. (1997), Fabbiano (1995) and references therein). Assuming that a typical X-ray luminosity of these systems is 10^{37-38} erg s⁻¹, we can estimate the total number of binaries. As the X-ray luminosity of the hard component is $L_X \sim 10^{41}$ erg s⁻¹, we estimate a range of between 1,000-10,000 X-ray binaries. Now we can compare this with the number of ionising OB stars determined from the integrated far-infrared luminosity. Making the assumption that it is mostly these stars that heat the dust, which then re-radiates in the mid-far infrared, we estimate $\sim 2 \times 10^5$ OB stars for NGC3310. If, following Fabbiano et al. (1992), 0.2 percent of these are massive X-ray binaries, then there are 400, and 7000 such systems, respectively. For the upper range of binary luminosities the predicted X-ray luminosity is comparable to that observed in both cases. Indeed, if the hard X-ray emission arises from binaries with low-metallicity and thus high X-ray luminosity ($L_X \sim 10^{38-39}$ erg s⁻¹) like those observed in the Magellanic Clouds (van Paradijs & McClintock 1995), then they could easily produce the observed luminosity.

4.2 Arp 299

4.2.1 Overview

Arp 299 is also a merging system, but in contrast to NGC3310 it is in an earlier merger phase. The system is composed of NGC3690, which is the western part of the merger and IC694, the eastern component. It is in the original catalogue of peculiar galaxies of Arp (1966), and it is also catalogued in the list of UV-excess galaxies of Markarian. Casoli, Combes, Augarde, Figon & Martin (1989) propose that there is a third component in the system thus forming an interacting

triplet. Its recession velocity is 3159 km s^{-1} (Sanders & Mirabel 1985), implying a distance of 63.2 Mpc. At that distance the projected separation of $22.5''$ of the two components corresponds to 6.9 kpc. The infrared surface brightness of NGC3690 is at least twice that of IC694 (Friedman, Cohen, Jones et al. 1987). The total mass of gas calculated from radio observations is about $2 \times 10^{11} M_{\odot}$ (Casoli et al. 1989)

The high IR luminosity ($L_{FIR} = 1.2 \times 10^{12} L_{\odot}$) (Soifer et al. 1987), results from re-radiating dust heated by the starburst activity. This is supported by multi-wavelength studies (Gehrz, Sramek & Weedman 1983), (Friedman et al. 1987), (Nakagawa, Nagata, Geballe, Okuda, Shibai & Matsuhara 1989). Detailed analysis of emission line ratios using the diagnostic diagrams of (Veilleux & Osterbrock 1987) clearly indicate a stellar origin of the ionising continuum (Friedman et al. 1987). The infrared emission is extended over a region of several kpc, but the main sources are located close to the two nuclei (Friedman et al. 1987).

Modeling of the starburst has been carried out by (Gehrz et al. 1983) and (Nakagawa et al. 1989). The latter find a starburst age of about 10 Myrs. An interesting point is that the two nuclei have different properties, implying either a different age and/or a different Initial Mass Function (IMF) for each starburst event.

Arp 299 has been previously observed with the High Resolution Imager (HRI) on board the *Einstein* observatory. 17 counts were detected implying an X-ray flux $f_x = 4.8 \times 10^{-13} \text{ ergs}^{-1} \text{ cm}^{-2}$ in the 0.2-4.0 keV band, for a 5 keV bremsstrahlung model and Galactic absorption (Fabbiano et al. 1992). This corresponds to an X-ray luminosity of $2.3 \times 10^{41} \text{ erg s}^{-1}$.

4.2.2 The data

Arp 299 has been observed on four occasions with the *ROSAT* satellite; one with *HRI* and three with PSPC. All the details about the observations are presented in Table 4.4. From these only the shortest PSPC observation has not been used. It has also been observed twice with *ASCA* (see Table 4.4) and both observations has been used in the data analysis.

Table 4.4: Summary of the observations of NGC3690

Satellite	Instrument	Date Observation started	Exposure Time† Ksec
<i>ROSAT</i>	PSPC	1993-04-22	3.534
<i>ROSAT</i>	PSPC	1991-11-18	6.391
<i>ROSAT</i>	HRI	1993-04-18	6.751
<i>ASCA</i>	SIS/GIS	1994-04-06	GIS:5.7, SIS:5.3
<i>ASCA</i>	SIS/GIS	1994-12-01	GIS:38.2, SIS:35.5

4.2.3 Soft X-ray imaging

The HRI analysis of Arp 299 followed the same procedure as for NGC3310. The image pixels were binned to a size of $1.5''$ and then smoothed using a two-dimensional Gaussian of FWHM $3.5''$. Finally, we overlaid the X-ray contours on a POSS plate image obtained from the Digitized Sky Survey, figure 4.4; the contours correspond to 0.57, 0.44, 0.40, 0.35, 0.31, 0.27, 0.22, 0.18, 0.13 and $0.11 \text{ counts arcsec}^{-2}$ respectively. The most striking feature is the existence of three separate sources in the X-ray image. The two most luminous sources correspond to the two merging nuclei. Their X-ray fluxes are given in Table 4.5. The third X-ray source is very close to a hot spot seen in the infrared and radio images to the north of NGC3690 (the western component), but they are not spatially coincident as is seen from the comparison between the X-ray image and a narrow band Fabry-Perrot $\text{Pa}\alpha$ image (Alonso-Herrero et al. 2000) (figs. 4.5, 4.6). In the same image H-band continuum and $[\text{FeII}]\lambda 1.644$ continuum subtracted NICMOS images of NGC3690 and IC 694 are presented.

Apart from these three sources there are marginal detections of other sources, but at a low level of significance (below 3σ), and will not be discussed further. It is worth to note that the relative strengths of the three main X-ray sources follow quite well the relative strengths of the near infrared sources, suggesting a possible common origin for the IR and the X-ray emission.

We have searched for extended emission from the two resolved nuclei. From figure 4.4 it is clear that the emission from the two resolved nuclei is extended and not symmetrical. Fitting a Gaussian function to the radial profiles of NGC3690 and IC694 yields a FWHM of 1.5 and 1.8 arcmin respectively.

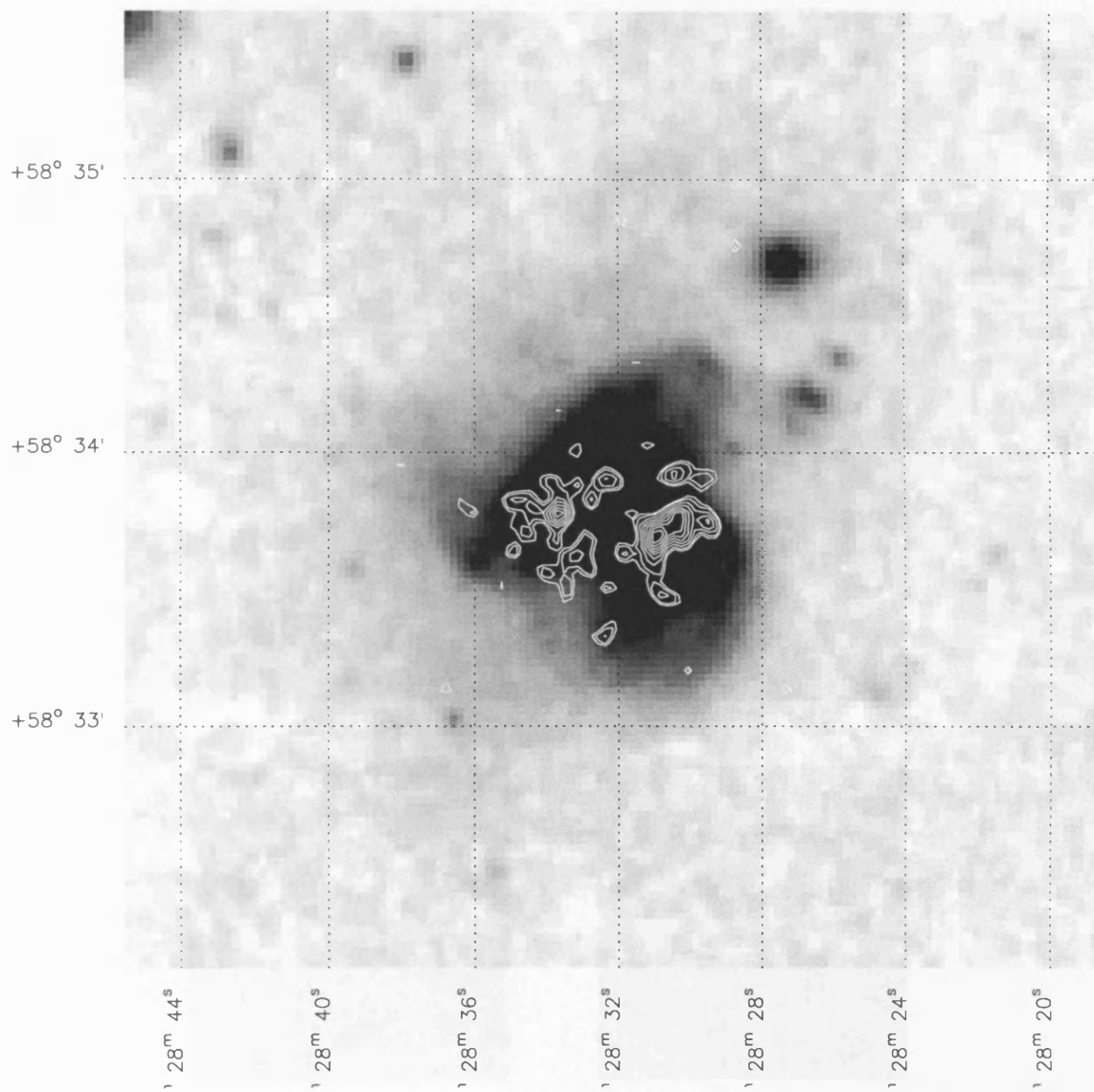


Figure 4.4: X-ray contours from the HRI observation of Arp 299 overlaid on a POSS image. The contours are in levels of 0.57, 0.44, 0.4, 0.35, 0.31, 0.26, 0.22, 0.18, 0.13, 0.11 counts arcsec⁻².

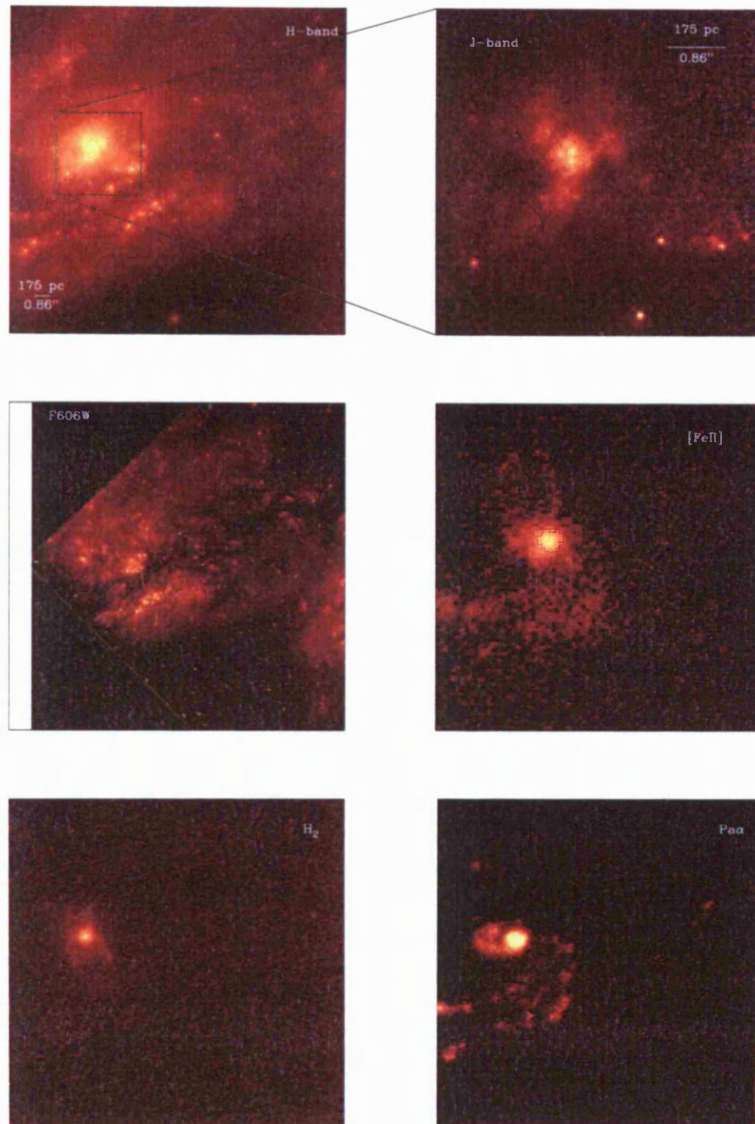


Figure 4.5: NICMOS and WFPC2 observations of IC694. North is up and East to the left. The size of all the images except the inset is $19.5'' \times 19.5''$. From Alonso-Herrero et al. (2000).

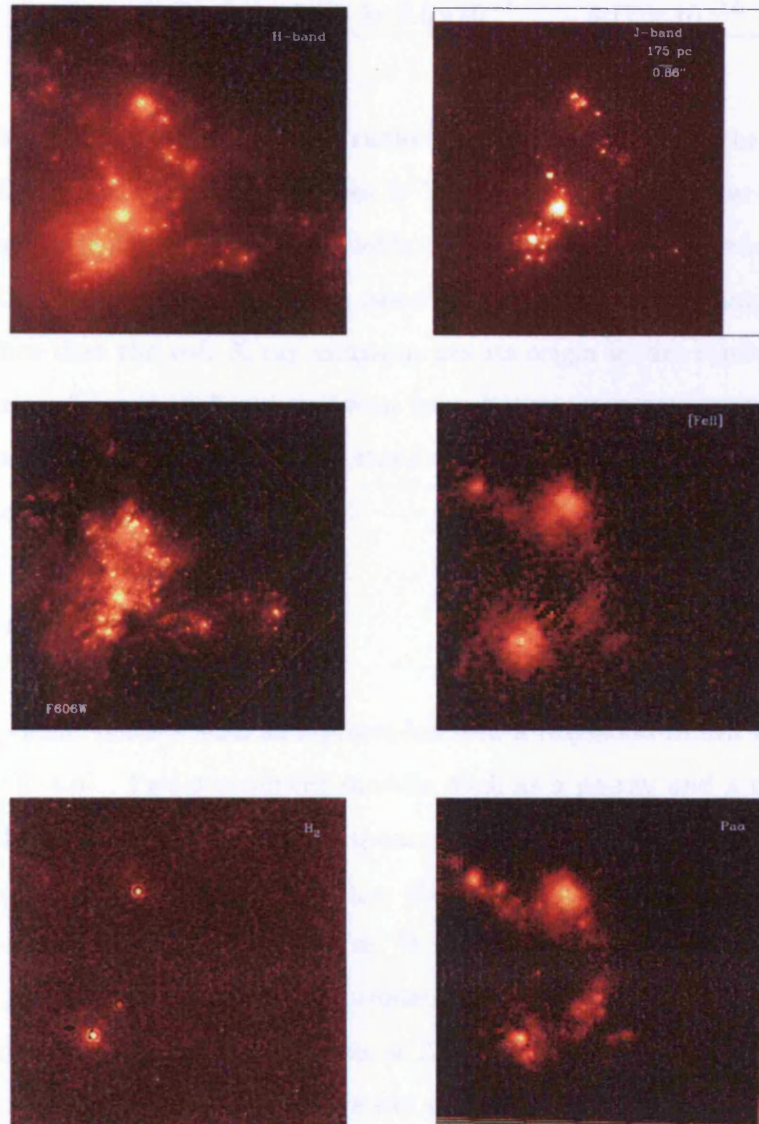


Figure 4.6: NICMOS and WFPC2 observations of NGC3690. Orientation and size same as fig. 4.5. From Alonso-Herrero et al. (2000).

Table 4.5: Sources in the *HRI* field of NGC3690

RA (J2000)	Dec (J2000)	Count rate count s ⁻¹	Flux (0.1-2.5keV) erg cm ⁻² s ⁻¹
11 28 30.7	+58 33 50	10±1.2×10 ⁻³	1.18 × 10 ⁻¹³
11 28 34.1	+58 33 51	15±1.5×10 ⁻³	1.72 × 10 ⁻¹³
11 28 30.0	+58 34 03	3±0.6×10 ⁻³	3.17 × 10 ⁻¹⁴

Comparison between the X-ray images and radio (VLA-A observation of the H92 α radio recombination line, (Zhao, Anantharamaiah, Goss & Viallefond 1997) and near-IR images (Wynn-Williams, Hodapp, Joseph et al. 1991), available in the literature, shows some clear similarities. As the radio and near-IR emission is clearly associated with the star-forming regions, the spatial coincidence implies that the soft X-ray emission has its origin in the starburst. We note that we do not see any evidence of X-ray emission from hot gas connecting the two galaxies, unlike the situation in some other interacting star-forming galaxies e.g. the Antennae, (Fabbiano, Schweizer & Mackie 1997).

4.2.4 X-ray spectroscopy

Simple one-component models such as a power-law and a Raymond-Smith plasma are similarly rejected (see Table 4.6). Two-component models, such as a po-ray and a ray-ray model (with the hydrogen column density as a free component) give $\Gamma = 1.56_{-0.11}^{+0.11}$, $kT = 0.83_{-0.04}^{+0.02}$, $N_H = 2.4_{-0.5}^{+0.6} \times 10^{20} \text{ cm}^{-2}$ and $kT_1 = 0.83_{-0.03}^{+0.03}$, $kT_2 = 10.3_{-2.44}^{+5.95}$, $N_H = 1.6_{-0.4}^{+0.4} \times 10^{20} \text{ cm}^{-2}$ respectively (the Galactic absorption is $N_H = 1 \times 10^{20} \text{ cm}^{-2}$). In the above model the abundance was fixed to solar. When the abundance is a free parameter, it cannot be usefully constrained. Figure 4.7 shows the *ROSAT* and *ASCA* spectrum of Arp 299 with the best fit double temperature Raymond-Smith thermal plasma model. We can clearly see from the spectrum that there is no evidence for an Fe line at ~ 6.7 keV. The upper limit to the Fe line equivalent width is ~ 860 eV. We also tried to fit the models using a different absorbing column for the hard component. We obtain $N_H = 1.7_{-0.8}^{+0.1} \times 10^{20} \text{ cm}^{-2}$, which is comparable to the previous best fit values, while the χ^2 is not significantly improved for one additional parameter. Thus there is no evidence for excess absorption in the hard component, in contrast to the results for M82 (Moran & Lehnert 1997). We also note that both the ray-ray and the po-ray models do not provide an

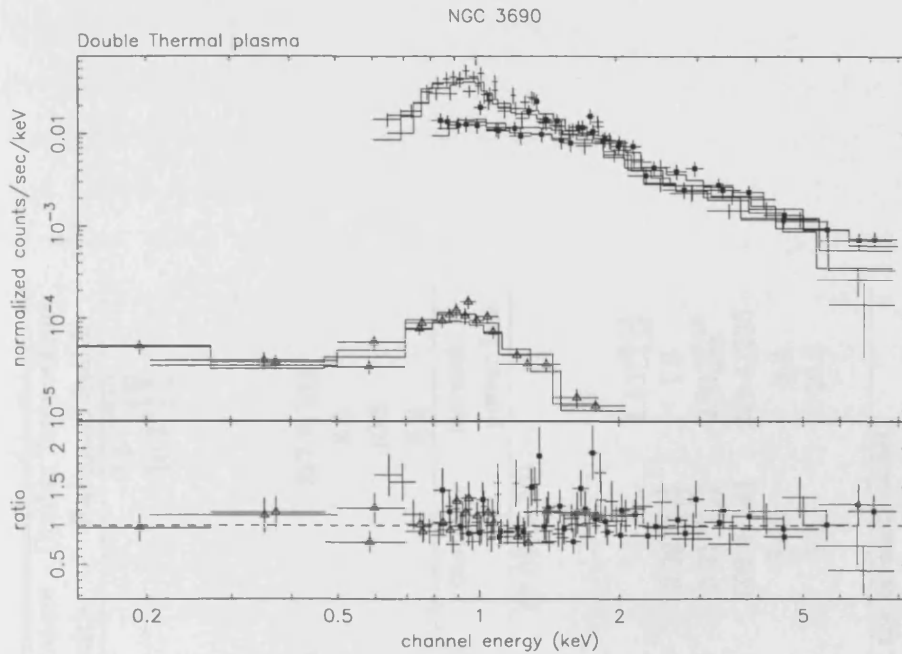


Figure 4.7: The top panel shows *ROSAT* and *ASCA* spectra of Arp 299 with the best fit double Raymond Smith model. The bottom panel shows the ratio of the data points to the model. The SIS data are marked with dots, while the PSPC data are marked with triangles.

adequate fit to the data as they can be rejected at over the 99 per cent level of confidence using a χ^2 goodness of fit. The inclusion of one additional thermal component slightly improves the fit but not in a statistically significant level.

We therefore attempted to fit more complicated models, such as multi-temperature components, and a power-law distribution of temperatures. This is model 'cevmekl' in XSPEC, (see Done & Osborne (1997) for details on the version of the model we used). This model gives a best fit of reduced $\chi^2 = 1.286$, with a maximum temperature of ~ 57 keV, a power-law index of the temperature distribution of $\alpha = 0.22^{+0.11}_{-0.10}$ and $N_H = 3.21^{+0.73}_{-0.48} \times 10^{20} \text{ cm}^{-2}$. A combination of a power-law and the multi-temperature model gives a slightly better fit (reduced $\chi^2 = 1.211$) with $\Gamma = 1.52^{+0.13}_{-0.12}$, $T_{\text{max}} = 1.17^{+0.25}_{-0.16}$ and α fixed to 1.

Table 4.6: Spectral fitting results for NGC3690.

Parameter	Power-law	Single Temperature Raymond-Smith	Double Temperature Raymond Smith	
kT (KeV)		$4.25^{+0.36}_{-0.45}$	$0.83^{+0.03}_{-0.03}$	$10.3^{+5.9}_{-2.4}$
Γ	$2.23^{+0.12}_{-0.12}$			
$N_H(10^{20} \text{ cm}^{-2})$	$5.50^{+0.7}_{-0.7}$			
$2.11^{+0.38}_{-0.33}$	$1.60^{+0.42}_{-0.40}$			
$\chi^2 / \text{d.o.f.}$	490.0/242	624.5/242	287.8/235	
Flux [†] (0.1-2.0keV)	9.72	8.85	8.5	
Flux [†] (2.0-10.0keV)	7.68	9.59	10.8	
Total Luminosity* (0.1-10.0keV)	8.3	8.8	9.2	
Parameter	Raymond Smith + Power-law	Triple temperature Raymond Smith	cevmekl	cevmekl + power-law
kT (KeV)	$0.83^{+0.02}_{-0.04}$	$0.29^{+0.19}_{-0.06}$ $0.87^{+0.43}_{-0.68}$ $11.17^{+6.96}_{-3.13}$	57.08(> 30)	
Γ	$1.56^{+0.11}_{-0.11}$			$1.52^{+0.13}_{-0.12}$
α^\dagger			$0.22^{+0.11}_{-0.01}$	1.0
$N_H(10^{20} \text{ cm}^{-2})$	$2.42^{+0.63}_{-0.46}$	$2.03^{+0.28}_{-0.47}$	$3.21^{+0.73}_{-0.48}$	$2.91^{+0.68}_{0.55}$
$\chi^2 / \text{d.o.f.}$	291.5/235	290.3/237	309.9/241	286.4/235
Flux [†] (0.1-2.0keV)	9.0	8.95	8.62	8.2
Flux [†] (2.0-10.0keV)	10.8	10.3	9.9	10.8
Total Luminosity*	9.46	9.2		

† The slope of power-law distribution of temperatures in the cevmekl model.

‡ The fluxes are in units of $10^{-13} \text{ erg s}^{-1} \text{ cm}^{-2}$.

* The luminosity is in units of $10^{41} \text{ erg s}^{-1}$. in the 0.1 to 10.0 keV band.

Finally, we considered using a non-equilibrium-ionization model (NEI), such as that applied to hot gas resulting from supernova explosions (Hughes & Singh 1994). This model assumes that the gas is instantaneously shock heated, and then applies corrections to the Raymond-Smith thermal plasma code to account for the non-equilibrium ionization fraction. An additional variable in the NEI model is nt , which is the product of the electron density and the time elapsed since the passage of the shock wave and is a quantitative measure of the offset from equilibrium. In principle the results from fitting NEI models can be used to estimate the characteristic timescale over which the gas reaches ionization equilibrium. Clearly for a situation in which multiple supernova occur over an extended time period, it will not be possible to identify a unique timescale. However, NEI models have been applied to the optically thin plasma in galactic scale superwinds, such as observed in M82, (Tsuru, Awaki, Koyama & Ptak 1997). Unfortunately in the case of Arp 299, we do not have the benefit of measurements of the low energy lines of silicon and magnesium needed to quantify the importance of non-equilibrium effects. For Arp 299 the NEI models give a best fit with a combination of a power-law and a NEI model. However the reduction in the χ^2 is not statistically significant at a level above 90%, and so we conclude that our data do not justify further consideration of the NEI models. However, if new soft X-ray emission line data become available, it would be worthwhile returning to this question.

4.2.5 Discussion

As in the case of NGC3310 the soft X-ray emission most probably arises from diffuse hot gas. This is indicated by the extension of the soft X-ray emission and its spectral shape which is consistent with a thermal plasma of temperature ~ 0.8 keV . The optical data also support this model. In the case of Arp 299 the H_α images show plumes and filaments extending out to several kpc (Armus, Heckman, Weaver & Lehnert 1995). Additional evidence comes from the extended synchrotron radio emission which may arise from the electrons produced by supernova remnants in the starburst regions, (Gehrz et al. 1983).

Next we estimate the expected X-ray luminosity from an expanding bubble filled with hot gas as we did in the case of NGC3310. However, in NGC3690/IC694 the situation is more complex, as there are at least three distinct starburst components (Nakagawa et al. 1989) which are unresolved by IRAS. In order to obtain an estimate of the mechanical energy input for each

component, we used the ground based mid-IR data (10-32 microns) of Wynn-Williams et al. (1991). These observations have sufficient spatial resolution to separate the three components. We then make the reasonable assumption that the fractions of the total IRAS flux which arise from each of the three star-forming components, are similar to the fractions in the mid-IR band. Using the formulae of Heckman et al. (1995) as in the analysis of NGC3310 above, and assuming a starburst age of 10 Myr and an ambient gas density of $n = 1 \text{ cm}^{-3}$, we predict $L_x = 1.3 \times 10^{42}$, 1.1×10^{42} and $3.2 \times 10^{41} \text{ erg s}^{-1}$ for the A,B and C components respectively (following the notation of Gehrz et al. (1983)). Again the predicted luminosity is higher than the measured soft (0.1-2.5keV) X-ray luminosity ($4.7 \times 10^{41} \text{ erg s}^{-1}$). This could possibly result from the fact that some fraction of the far-infrared emission measured by IRAS, may arise from regions more extended than those producing the X-rays. Another possibility is that an additional source of heating may be present, perhaps due to stars of later spectral type than those producing the winds.

The soft X-ray spectrum of Arp 299 is very similar to the spectra of the prototypical starburst galaxies eg. M82 (Strickland et al. 1997), NGC1569 (Della Ceca et al. 1996) and NGC4449 (Della Ceca et al. 1997). However, our SIS spectral fits yield a relatively poor χ^2 fit. This could be suggestive of a hot tenuous gas component. Indeed, if the expanding gas has not had time to reach thermal equilibrium, its spectrum will not be well represented by the Raymond-Smith model. The use of a non-equilibrium code developed by Hughes & Singh (1994) improved the fit, but again the χ^2 is not accepted at the 98 per cent confidence level. This is not surprising as even a non-equilibrium model may be inadequate to fit an ensemble of supernova remnants occurring in several star-forming regions as is the case for NGC3690/IC694.

The hard X-ray spectrum of Arp 299 is very similar to the hard X-ray spectrum of NGC3310 and other well known starburst galaxies. Again there are three possibilities for the origin of the hard X-ray emission: a) Inverse Compton scattering of the IR photons produced in the starburst by electrons from the numerous supernova remnants b) emission from a low-luminosity AGN as is the case in NGC3628 c) thermal emission from a very hot gas ($T \sim 10^8 \text{ K}$) and d) emission from X-ray binaries.

Unfortunately we cannot investigate the validity of the IC scattering case as the available radio data do not allow such a sophisticated analysis as in the case of NGC3310.

However, we can exclude the possibility that the hard X-rays arise from an AGN on the grounds of the non detection of broad wings in the H_α line. Using the L_X/L_{H_α} relation from Elvis et al. (1984), where L_{H_α} is the luminosity of the broad component of the H_α line and L_X is the hard X-ray luminosity (2-10 keV), we can estimate the expected intensity of the broad wings of the H_α line. It is $L_X/L_{H_\alpha} \simeq 40$, for low-luminosity AGN and thus we estimate $f(H_\alpha) \sim 2.7 \times 10^{-14}$ erg cm^{-2} s^{-1} . A broad component of this strength is easily detectable, but is not seen (Ho, Filippenko, Sargent & Peng 1997). The absorbing columns found from the X-ray spectral fitting (ray-po models in Table 4.6) imply low extinction, $A_V \sim 0.1$ mag (Bohlin et al. 1978) and hence a BLR reddened by this amount would still be observed.

The next possibility is the presence of a very hot thermal component. A Raymond-Smith model with $kT > 10$ keV provides a good fit to the data. However, the strong $\text{FeK}\alpha$ line at 6.7 keV which is expected from hot gas at this temperature is not observed. This could be attributed to low metallicity, but unfortunately we cannot check this possibility as the abundances cannot be well constrained by the available X-ray data. Alternatively, as in the case of NGC3310 the lack of a $\text{FeK}\alpha$ line could be explained by a low contribution of type Ia supernovae to the enrichment of the Interstellar Medium (Sansom et al. 1996).

Finally the hard X-ray emission may be produced by a population of HMXRBs. For a typical X-ray luminosity of these systems of 10^{37-38} erg s^{-1} and given that the hard X-ray luminosity of Arp299 is $L_X \sim 5 \times 10^{41}$ erg s^{-1} we estimate that a number of 5,000-50,000 HMXRBs is needed in order to reproduce the observed luminosity. Now we can compare this with the number of ionising OB stars determined from the integrated far-infrared luminosity. Making the assumption that it is mostly these stars that heat the dust, which then re-radiates in the mid-far infrared, we estimate $\sim 3.5 \times 10^6$ OB stars. We can also determine the number of ionising OB stars from the hydrogen radio recombination lines measurements of Zhao et al. (1997) which are similar to the results from Pa_α NICMOS observations of the system (Alonso-Herrero et al. 2000). They find that the number of Lyman continuum photons in NGC3690 and IC694 lies between 1.5×10^{53} s^{-1} to 8.8×10^{53} s^{-1} and 4.8×10^{54} s^{-1} to 8.7×10^{54} s^{-1} respectively depending on the density and the excitation parameters used for the modeling. Assuming a mean Lyman continuum photon production rate of 2×10^{48} s^{-1} which is appropriate for O7-O9 stars we estimate a number in the range of 75,000 to 450,000 and 2.5×10^6 to 4.3×10^6 O type stars for each case. These numbers are consistent with the estimate from the total IR luminosity, given the

very broad range of the parameters used in the modeling of Zhao et al. (1997). If, following Fabbiano et al. (1992), we assume that 0.2 percent of these are massive X-ray binaries, then there are between 5,000 and 10,000 such systems. For the upper range of binary luminosities ($L_x \sim 10^{37-38} \text{ erg s}^{-1}$) the predicted X-ray luminosity is therefore comparable to that observed. This result suggests that there is no need to invoke an energy source other than star-formation in order to explain the extreme X-ray luminosity of Arp299.

4.3 UGC4305 (Holmberg II)

Holmberg II one of the most luminous dwarf irregular galaxies in the sample of Moran et al. (1996), with an X-ray luminosity of $10^{40} \text{ erg s}^{-1}$ in the 0.5-2.0 keV band. This sample is constructed by the cross-correlation of the IRAS Point Source catalogue with the ROSAT All Sky Survey which was carried out during the first years of the operation of ROSAT. Holmberg II is also one of the most X-ray luminous dwarf starbursts for its mass. The ratio of L_X/M_{gal} is about $4 \times 10^{30} \text{ erg s}^{-1} M_{\odot}^{-1}$. This is almost an order of magnitude higher than in other dwarf starbursts making its X-ray luminosity exceptionally high when compared to the X-ray luminosity of other dwarf starbursts (Strickland et al. 1997, Hensler, Dickow & Junkes 1997).

H α observations (Hodge, Strobel & Kennicutt 1994) clearly demonstrate that there is intense star-forming activity in this galaxy. It is composed of many HII regions (their size ranging from 96 pc up to 525 pc) which appear as bright knots in optical images. The star-formation rate per unit area in Holmberg II is found to be $1.32 \times 10^{-3} M_{\odot} \text{ yr}^{-1} \text{ kpc}^{-2}$ (Hunter, Elmegreen & Baker 1998). Most of the HII regions are coincident with “holes” found in the surface density of atomic hydrogen with VLA observations at 21cm (Puche, Westpfahl, Brinks & Roy 1992). This suggests that the HII regions excavate the interstellar medium of the galaxy forming these “holes”. VLA radio continuum observations (Tongue & Westpfahl 1995) show that most of the bright HII regions present intense radio emission. Some regions have typical (non-thermal) supernova remnant spectrum while others present a thermal bremsstrahlung spectrum.

The powerful X-ray luminosity $L_X \sim 10^{40} \text{ erg s}^{-1}$ in combination with the proximity of Holmberg II (3.2 Mpc), make it an ideal case for the study of the X-ray emission mechanisms in dwarf star-forming galaxies.

Table 4.7: Summary of the observations of UGC 4305.

Instrument	Date Observation started	Net Exposure time (s)
PSPC	14-4-1992	2827
PSPC	29-9-1992	8223
PSPC	14-3-1993	5449
<i>HRI</i>	17-10-1994	7863

4.3.1 The *ROSAT* data

Holmberg II has been observed on three occasions with PSPC (Pfeffermann et al. 1987) and HRI (David et al. 1997) on board *ROSAT* (Trumper 1984). The details of the observations are given in Table 4.7. The data have been reduced following the standard procedures presented in Chapter 1 and in the previous section.

4.3.2 X-ray imaging

In order to study the spatial distribution of the X-ray emission, we have extracted PSPC and HRI images with pixel size of 5.0 and 1.5 arcseconds respectively. Figure 4.8 shows the HRI map overlaid on an O-band POSS image retrieved from the Digitised Sky Survey database located at Leicester. The HRI map was created from the original 1.5'' pixel image after smoothing with a Gaussian (3.5'' FWHM). The contours correspond to levels of 0.09, 0.13, 0.18, 0.22, 0.44, 1.11, 2.22, 6.67, 8.0 cnts arcsec⁻². As there are no other X-ray sources in the HRI field, the registration of the X-ray contour on to the POSS image was achieved by assuming that errors in the pointing accuracy and the aspect solution of the HRI are negligible. In reality, there is a scatter of $\sim 6'$ in the difference between the HRI and optical positions of SIMBAD sources, probably originating in residual star-tracker errors (Briel et al. 1994). As a check of the pointing accuracy we have compared the coordinates of the centroids of the point source from the different PSPC and HRI pointings. We found that the coordinates were the same to within 3.8' apart from the shortest PSPC exposure where the distance between the centroids was $\sim 10'$.

The most striking result is that the X-ray image shows only one source. Comparing the radial profile of the source with the radial profile of a point source (in this case is the star AR-Lac, see figure 4.9) we see that it is slightly extended. Actually, the source appears elongated in

UGC 4305

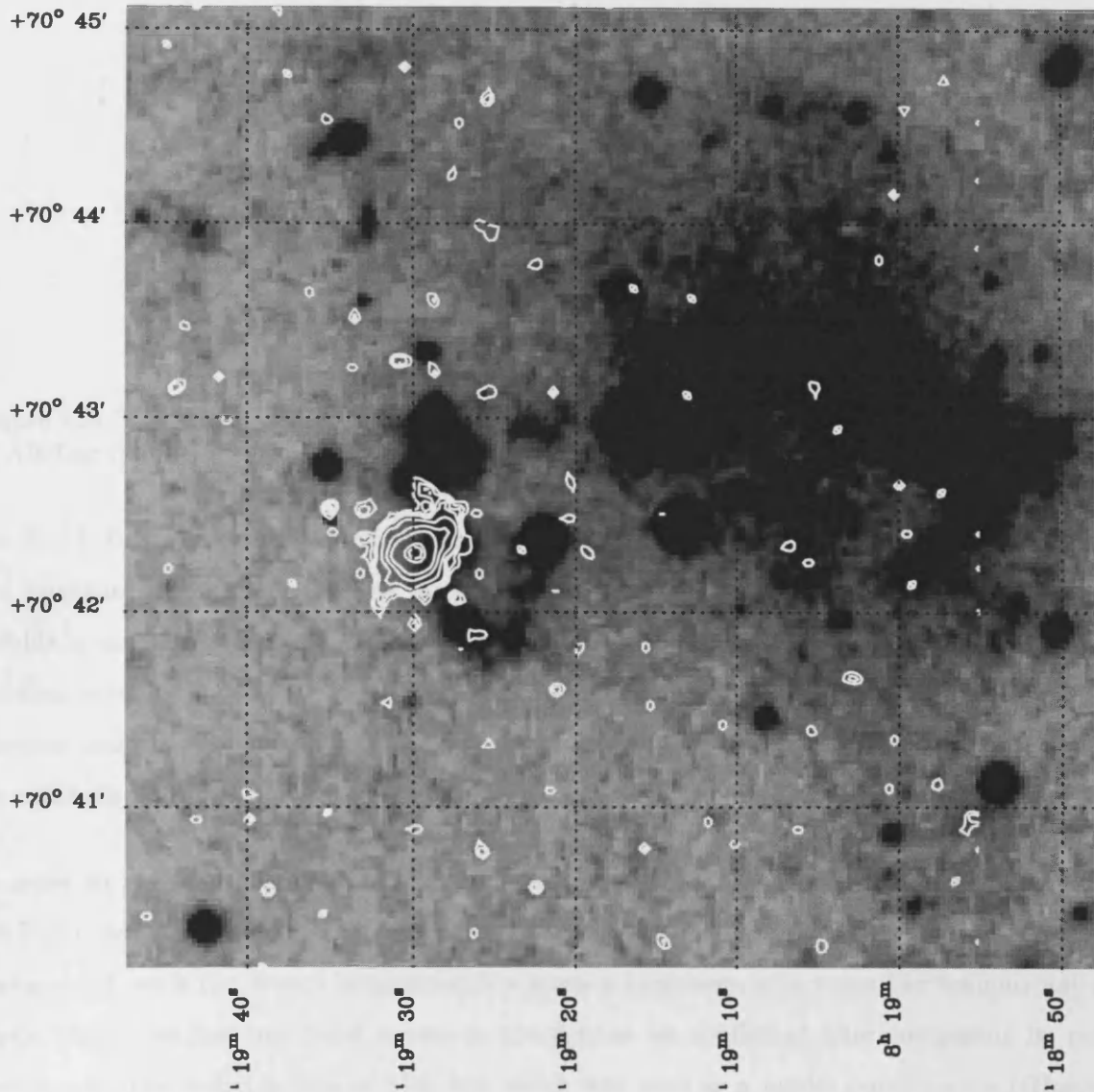


Figure 4.8: Contours from the HRI observation overlaid on a POSS image of the galaxy. The contours correspond to levels of 0.09, 0.13, 0.18, 0.22, 0.44, 1.11, 2.22, 6.67, 8.0 cts arcsec⁻². The epoch of the coordinates is J2000.0, and the positional error of the X-ray coordinates with respect to the optical is $\sim 6''$. The position of the X-ray centroid is $08^{\text{h}}19^{\text{m}}29.9^{\text{s}} + 70^{\circ}42'18.0''$ J2000.0

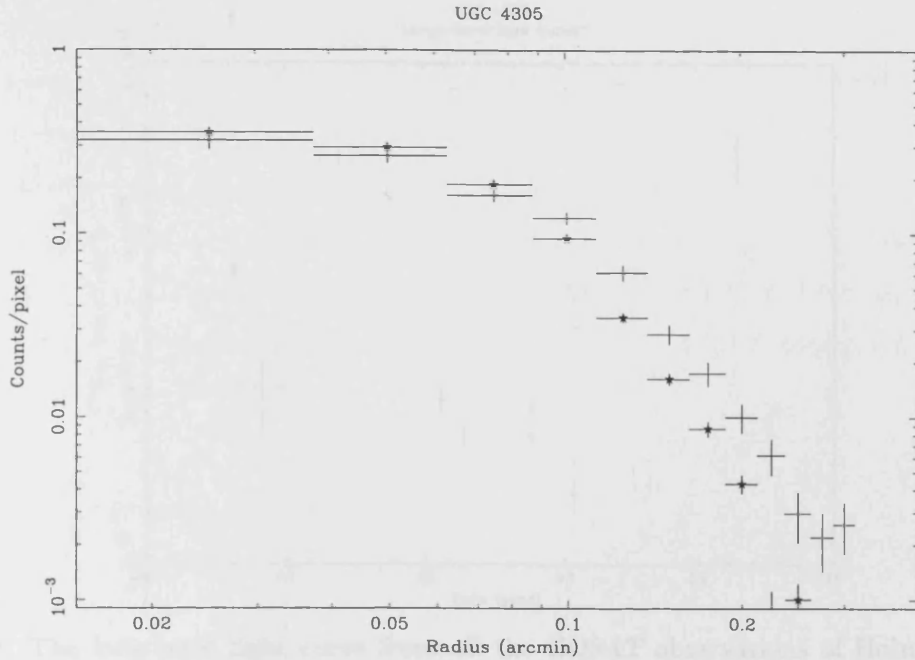


Figure 4.9: The HRI radial profile of the source in Holmberg II compared with the radial profile of AR-Lac (stars).

the South East - North West direction. However, as the satellite wobbles in order to smooth the quantum efficiency variations on the microchannel plates (see Briel et al. (1994)). The wobble is not always appropriately taken into account into the aspect solution and thus some residual extent is possible. In order to check this possibility, we extracted the HRI image in detector coordinates. It appears that the elongation is along the wobble direction and therefore we conclude that most probably our source is unresolved by the HRI.

In order to investigate for low surface brightness extended X-ray emission, we have smoothed the PSPC image with a $15''$ two-dimensional Gaussian. PSPC has the advantage of low internal background; so it can detect large-scale, low surface brightness structures like tenuous hot gas. Again there was just one point source in the field as we confirmed after comparing its radial profile with the radial profile of Mrk 509 which was used as a model point source ((Hasinger et al. 1992)). The X-ray source is coincident with one of the most luminous HII regions of Holmberg II having $L_{H\alpha} = 3 \times 10^{38} \text{ erg s}^{-1}$. Its diameter is 23 arcsec, which in the galaxy's distance (3.2 Mpc) translates to 352 pc (Hodge et al. 1994). Using the $\log N - \log S$ relation in the soft X-ray band (0.5-2.0keV) of (Georgantopoulos, Stewart, Shanks et al. 1996), we expect 0.07 sources deg^{-2} to be brighter than $10^{-12} \text{ erg s}^{-1} \text{ cm}^{-2}$. In the area covered by the X-ray

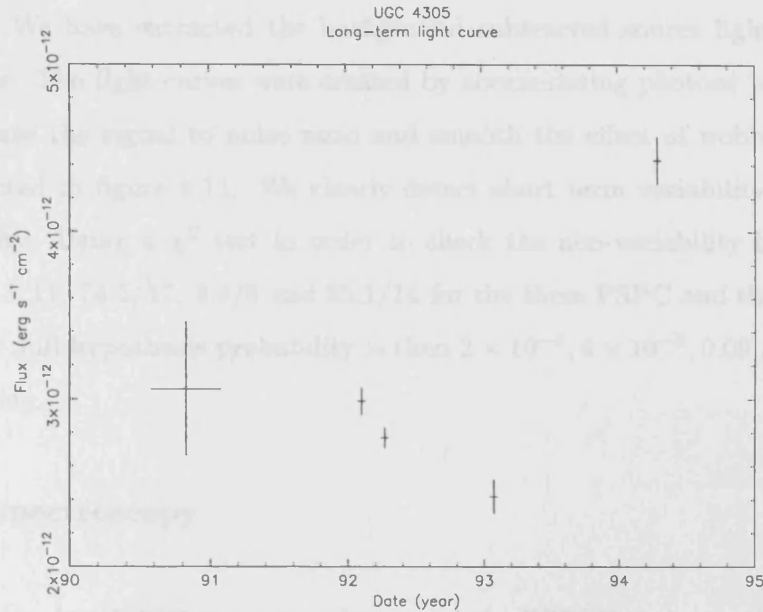


Figure 4.10: The long-term light curve from all the *ROSAT* observations of Holmberg II. the first point corresponds to the RASS detection of the galaxy while the last point to the HRI observation.

source we expect to find 3×10^{-6} X-ray sources brighter than $10^{-12} \text{ erg s}^{-1} \text{ cm}^{-2}$ by chance, giving us confidence that a confusing foreground or background source is improbable.

4.3.3 Variability

In order to investigate the nature of the X-ray source, further we have constructed a long-term light curve from all four observations of Holmberg II (figure 4.10). We have used the background subtracted count rates and assumed a power-law model with $\Gamma = 2.7$ and absorbing column density $N_{\text{H}} = 1.2 \times 10^{21} \text{ cm}^{-2}$ as found from our spectral fits (see Table 4.8 below). The points are in chronological order; the first point corresponds to the RASS detection and the other four are from the pointed observations with the last one being from the HRI observation. The errors on the PSPC observations are based on counting statistics only. In contrast, the error on the HRI observation includes the 1σ uncertainty on the absorbing column density (see section below). This is necessary in order to compare PSPC and HRI fluxes as the derived HRI flux is very sensitive on the assumed column density owing to the soft energy response of the HRI. From this figure it is clear that Holmberg II is variable by approximately a factor of 2.

Next we extracted light curves from the four pointed observations in order to check for short

term variability. We have extracted the background subtracted source light-curves using the FTOOLS package. The light curves were created by accumulating photons in 800 seconds bins in order to increase the signal to noise ratio and smooth the effect of wobble. All four light-curves are presented in figure 4.11. We clearly detect short term variability, but without any obvious periodicity. Using a χ^2 test in order to check the non-variability hypothesis we find reduced χ^2 of 41.3/11, 74.5/17, 9.4/5 and 35.1/14 for the three PSPC and the one HRI dataset respectively. The null hypothesis probability is then 2×10^{-5} , 4×10^{-9} , 0.09 and 0.001 for each dataset respectively.

4.3.4 X-ray spectroscopy

For the fitting of the two PSPC spectra we have used the XSPEC package, after binning-up the spectra in order to obtain at least 20 counts in each bin. We have fitted the three spectra from the pointed PSPC observations simultaneously (the normalizations were allowed to vary freely between the observations) using various models. The results are presented in Table 4.8 . All the single model fits with absorbing column density fixed at the Galactic value, $3.4 \times 10^{20} \text{cm}^{-2}$, (Stark et al. 1992) were rejected at above the 99 per cent confidence level.

UGC 4305 Light curve

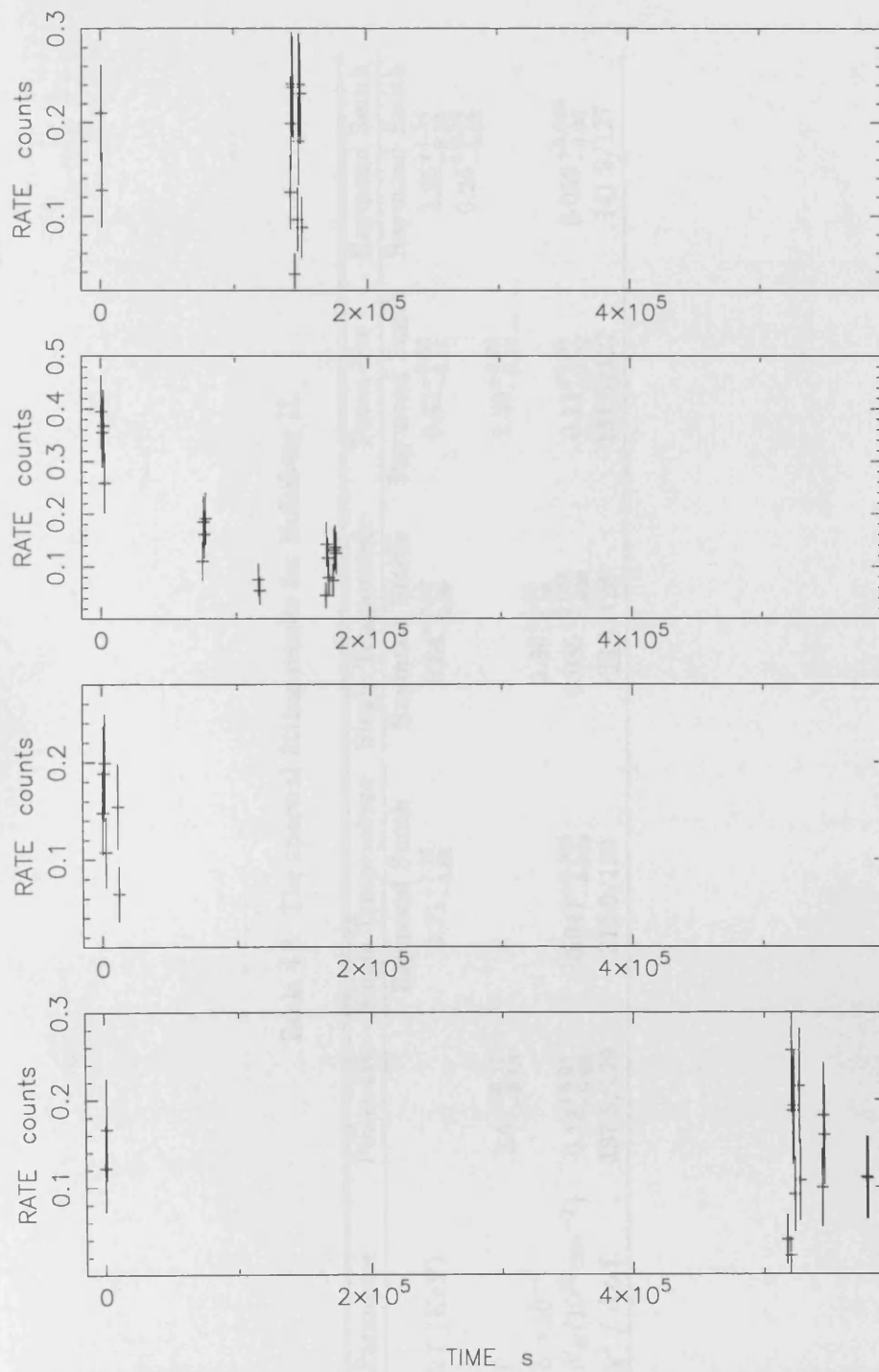


Figure 4.11: The light curves for each observation of Holmberg II. The first three panels correspond to the three PSPC observations in chronological order and the last panel corresponds to the HRI observation.

Table 4.8: The spectral fitting results for Holmberg II.

Parameter	Power-law	Single Temperature	Single Temperature	Power-law	Raymond Smith
		Raymond Smith	Raymond Smith	Raymond Smith	Raymond Smith
kT (KeV)		$3.71^{+1.16}_{-0.68}$	$0.84^{+0.12}_{-0.09}$	$0.83^{+0.31}_{-0.21}$	$2.25^{+1.54}_{-0.53}$ $0.25^{+0.04}_{-0.03}$
Γ	$2.68^{+0.17}_{-0.13}$			$2.59^{+0.29}_{-0.26}$	
$Z \times 10^{-3}$			$3.36^{+1.25}_{-3.36}$		
$N_H (10^{22} \text{ cm}^{-2})$	$0.12^{+0.01}_{-0.02}$	$0.047^{+0.004}_{-0.003}$	$0.085^{+0.011}_{-0.009}$	$0.11^{+0.01}_{-0.02}$	$0.059^{+0.009}_{-0.06}$
$\chi^2 / \text{d.o.f.}$	137.5/129	312.9/129	133.4/128	131.5/127	141.3/127

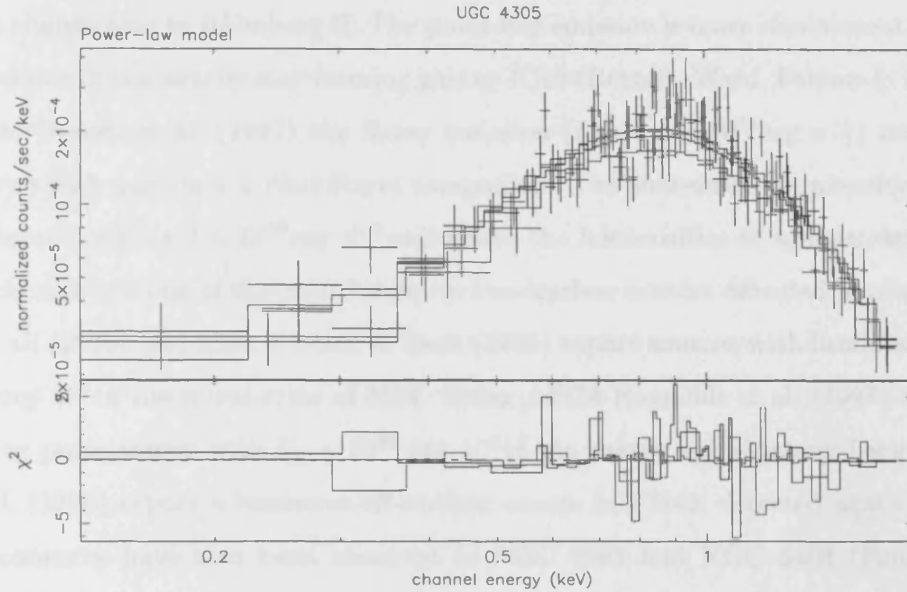


Figure 4.12: The best fit power-law spectrum for Holmberg II. The top panel shows the data with the model and the bottom panel shows the $\Delta\chi^2$.

However, a power-law fit with free absorbing column density gave a good fit with a very steep slope ($\Gamma = 2.68_{-0.13}^{+0.17}$) and a high column density of $12.0_{-2.0}^{+1.0} \times 10^{20} \text{cm}^{-2}$. An even lower reduced χ^2 was achieved with a Raymond-Smith thermal plasma with free abundances and absorption. However, when compared to the power-law model, this improvement is statistically significant at less than the 90 per cent confidence level. The best-fit power law model along with the residuals is presented in figure 4.12.

We have also tried double component models of Raymond Smith thermal plasma (R-S) combined with another R-S or a power-law model, which give the same or slightly better reduced χ^2 compared to the best-fit single component models. According to the F-test the addition of a power-law component to the R-S (free abundance) spectrum is not statistically significant at a level of confidence above 90 per cent.

4.3.5 Discussion

The most striking result of our study of Holmberg II is that the X-ray emission comes from a single point source which is found to be variable. Therefore, we are not dealing with the integrated emission from a superbubble, as is the case for NGC1569 and NGC4449. The X-ray emission from these two galaxies is clearly extended although they are situated at distances of

2-5 Mpc ie. comparable to Holmberg II. The point-like emission is more reminiscent of the point-like X-ray source in the nearby star-forming galaxy IC10 (Brandt, Ward, Fabian & Hodge 1997). According to Brandt et al. (1997) the X-ray emission ($L_X \sim 4 \times 10^{38} \text{ erg s}^{-1}$) comes from an X-ray binary which may have a Wolf-Rayet companion. The unabsorbed luminosity of the X-ray source in Holmberg II is $2 \times 10^{40} \text{ erg s}^{-1}$ well above the luminosities of sources detected in our Galaxy. This makes it one of the most luminous non-nuclear sources detected in nearby galaxies. Marston et al. (1995) and Ehle, Pietsch & Beck (1995) report sources with luminosities of a few times $10^{39} \text{ erg s}^{-1}$ in the spiral arms of M51. Using *ASCA* Reynolds et al. (1997) detect an off-nuclear X-ray point source with $L_x \sim 10^{39} \text{ erg s}^{-1}$ in the nearby spiral galaxy Dwingeloo-1, and Okada et al. (1998) report a luminous off-nuclear source in IC342, detected again using *ASCA*. Point-like sources have also been observed in NGC 4961 and NGC 5408 (Fourniol, Pakull & Motch 1996, Fabian & Ward 1993) using *ROSAT* PSPC, with luminosities $\sim 10^{40} \text{ erg s}^{-1}$. These highly luminous X-ray sources are believed to be associated with supernova remnants, superbubbles or X-ray binaries (Fabbiano 1995).

Single supernovae in a dense environment can also reach high luminosities: Fabian & Terlevich (1996) report the detection of SN1988Z with a luminosity of $L_X \approx 10^{41} \text{ erg s}^{-1}$. Our source is spatially coincident with one of the large HII regions in Holmberg II. It also coincides with a strong radio source (Tongue & Westpfahl 1995). The spectral index of the radio emission is typical of supernovae remnants. However, the presence of significant long-term (years) and short term variability (days) in X-rays rules out the possibility that the bulk of the X-ray emission comes from diffuse hot gas either in a supernova or in a superbubble. Hence, most probably our source is associated with an accreting compact object.

The X-ray spectrum of this source adds further clues on the origin of the X-ray emission. The spectrum is well-fit either by a single power-law with a absorption ($N_H \sim 0.1 \times 10^{22} \text{ cm}^{-2}$) well above the Galactic values ($N_H \sim 4 \times 10^{20} \text{ cm}^{-2}$) or a Raymond-Smith spectrum with relatively low temperature ($kT \sim 1 \text{ keV}$), very low metallicity and absorption again in excess of the Galactic value. The spectrum of our source is much harder than the typical *ROSAT* spectra of supernovae remnants in nearby spiral galaxies, which have temperatures of $\sim 0.36 \text{ keV}$ with a wide dispersion of 0.2 keV (Read et al. 1997). On the other hand, the temperature is softer than that of the luminous sources detected in M51, $kT \sim 1.3-1.7 \text{ keV}$ (Marston et al. 1995) and of X-ray binary sources detected in other nearby spiral galaxies, $kT \approx 1.8 \text{ keV}$ with a dispersion of

0.13 keV (Read et al. 1997). Interestingly, the spectrum of Holmberg II is very similar to that observed in nearby Wolf-Rayet galaxies (young star-forming galaxies) by Stevens & Strickland (1998). Their X-ray spectra have $kT \sim 0.5\text{--}1$ keV, and their luminosities range from few times 10^{38} up to 10^{41} erg s $^{-1}$ while the metallicities of the X-ray gas are very low, typically $Z = 0.01$. Most of these galaxies have X-ray emission unresolved in *ROSAT* PSPC observations. According to Stevens & Strickland (1998) the emission originates in a superbubble. As there are no timing observations of these galaxies, we consider it likely that a large fraction of their X-ray emission, at least in the cases of the compact dwarf galaxies, may originate from the same process as in Holmberg II. As Stevens & Strickland (1998) point out the ultrasoft components of some black hole candidates have roughly similar spectral characteristics (Inoue 1991) to Wolf-Rayet galaxies and consequently to Holmberg II. The same result is also found for galaxies in the sample of Fourniol et al. (1996), but they cannot distinguish between a binary or a hot gas origin of the X-ray emission in the absence of timing data. Assuming that the putative binary accretes at its Eddington limit, the mass of the central object must be $\sim 200M_{\odot}$, well in excess of the mass limit for a black hole formed by the collapse of a normal star. It is difficult to envisage how these high mass off-nuclear black holes originally formed. However, there are several ways to reduce the required mass.

- Accretion at a rate in excess of the Eddington limit: strong magnetic fields may channel the mass onto the accreting object and thus may reduce the mass by a factor of a few.
- The emission may be anisotropic as proposed by Reynolds et al. (1997) for Dwingeloo X1: one candidate class of objects could be the transient X-ray sources with radio jets displaying superluminal motion eg. GRS1915+105.
- Finally, the low metallicities derived could result in the increase in the X-ray luminosity of an X-ray binary by as much as an order of magnitude eg. van Paradijs & McClintock (1995).

As mentioned in the introduction there is now increasing evidence for the existence of a population of extranuclear sources with X-ray luminosities $\sim 10^{40\text{--}41}$ erg s $^{-1}$ (Roberts & Warwick 2000, Lira 1999). Some of these sources could be black-hole binaries with black-hole masses much larger than typical for stellar black-holes (Ptak & Griffiths 1999). Another possibility is that

these sources are accreting at super-Eddington rates. Detailed studies of individual objects such as UGC 4305 will help to determine the true nature of these sources. If they are high mass black-hole binaries then stellar population synthesis models will be challenged to explain their formation.

Chapter 5

Conclusions and future work

5.1 An overview of the presented work

One of the major debates in X-ray astronomy over the last 10 year has been whether X-ray luminous star-forming galaxies exist. The debate was initiated by the discovery of a few X-ray luminous galaxies (in the luminosity range $10^{41} - 10^{42} \text{erg s}^{-1}$) in samples of *Einstein* and *ROSAT* sources which had H II -type spectra. However, more careful follow-up optical spectroscopy showed that most of these objects were faint obscured AGN or composite objects hosting both an AGN and a starburst (Moran et al. 1996). A further reason for this work was the claim by some workers that a class of narrow emission line galaxies were optical counterparts of X-ray sources found in Deep X-ray surveys, and that such objects might be related to star-forming galaxies.

5.1.1 Do X-ray luminous star-forming galaxies exist ?

The survey presented in Chapter 2 was undertaken in order to investigate whether X-ray luminous star-forming galaxies exist. The samples were selected in order to have a high content of candidates for potential star-forming galaxies. The results of the survey suggest that there is a number of star-forming galaxies with soft X-ray luminosities above $10^{41} \text{erg s}^{-1}$, although there are very few with luminosities higher than $10^{42} \text{erg s}^{-1}$. Even at this level these objects are 10 to 100 times more luminous than nearby “normal” and starburst galaxies. Moreover, their X-ray emission can be easily explained assuming a population of X-ray binaries and/or a

superwind component. This means that there is no need for a more exotic energy source such as a supermassive black hole. One important question is how X-ray luminous can star-forming galaxies be ? The X-ray versus FIR luminosity relation is relatively flat suggesting that more FIR luminous objects (ie. with more intense star-formation) present a deficiency in their X-ray luminosities. The results of this survey show that they can reach the luminosities of Seyfert-2 galaxies. This result can have very important implications for star-formation models, and models of the X-ray background as will be discussed later. However, even if they do not produce a significant fraction of the soft XRB they are still of considerable interest in their own right.

5.1.2 The properties of X-ray luminous starbursts

Arp 299 and NGC 3310

One important question about X-ray luminous star-forming galaxies is whether their X-ray properties are different than the properties of their less luminous counterparts. For this reason two examples of X-ray luminous star-forming galaxies (namely Arp299 (NGC3690+IC694) and NGC 3310) have been studied in detail. Their X-ray spectral parameters are very similar to the parameters of other star-forming galaxies like M82 and NGC253, or dwarf starbursts (NGC1569, NGC4449). This is an indication that the same physical mechanisms are responsible for the production of the X-ray emission in starburst galaxies spanning over 3 orders of magnitude in luminosity. In general the soft X-ray emission is produced by diffuse thermal gas as is suggested by its extent and its spectrum, which is well modeled with a thermal component of temperature of $\sim 0.8\text{keV}$. On the other hand the origin of their hard X-ray emission is still unclear. The hard X-ray spectrum can be fitted equally well with a relatively steep power-law ($\Gamma \sim 1.8$) or a thermal plasma with $kT \sim 10 - 15\text{keV}$. From the available data there is no indication for excess absorption either in the soft or the hard component. Therefore the hard X-rays may be produced by another, much hotter thermal component, a population of X-ray binaries, Inverse Compton scattering of IR photons or perhaps by a hidden AGN.

UGC 4305 (Holmberg II)

Apart from these two galaxies another dwarf irregular galaxy with very strong X-ray emission ($L_X \sim 10^{40}\text{erg s}^{-1}$ when corrected for absorption) has been studied. The most striking result is that all the X-ray emission is produced by a single source. This is one of

the very first X-ray luminous off-nuclear sources discovered. Long and short term temporal variations suggest that it is an X-ray binary. Its extreme X-ray luminosity can be explained either by super-Eddington accretion rate or accretion onto a massive black hole with a mass of $\sim 200 M_{\odot}$. There is increasing evidence that such objects are not uncommon. Recently Lira (1999) and Roberts & Warwick (2000) showed that a large number of nearby galaxies host extranuclear sources with X-ray luminosities up to $\sim 10^{40} \text{erg s}^{-1}$. The source in UGC4305 lies at the upper end of the luminosity function of these objects as calculated by Roberts & Warwick (2000). A population of such sources could easily explain the X-ray luminosity of star-forming galaxies up to X-ray luminosities as high as $\sim 10^{42} \text{erg s}^{-1}$. However, the existence of such massive black-holes poses challenges for star-formation and binary evolution models.

5.1.3 The link between X-rays and other wavelengths

In order to investigate the soft X-ray properties of star-forming galaxies, a well defined sample of bona-fide star-forming galaxies from the compilation of Ho, Filippenko & Sargent (1997*a*) has been studied. In general it has found that the very good correlation between the X-ray emission and the optical, IR and radio emission of spiral galaxies (including some with AGN activity) reported by earlier studies (Fabbiano et al. 1988, Green et al. 1992, David et al. 1992, Read et al. 1997) hold for bona-fide star-forming galaxies as well, although with slightly different correlation parameters in some cases. Also, a regression for the H_{α} against X-ray luminosity of star-forming galaxies is presented for the first time. These correlations are usually non-linear (apart from the X-ray against H_{α} and X-ray versus B-band correlation) showing a deficiency of X-ray emission for the more luminous objects. This non-linearity can be explained in terms of an age effect or evolution of the IMF with luminosity. It should be possible to test both scenarios with detailed optical and IR spectroscopy.

5.1.4 The contribution of star-forming galaxies to the XRB

Since its discovery, the origin of the extragalactic soft X-ray background has remained a mystery. It is now been demonstrated by numerous Deep X-ray surveys that most or all of it is produced by a population of unresolved sources. However, the nature of these sources is still unclear.

Several models involving QSOs and AGNs with different degrees of obscuration, and star-forming galaxies have been suggested. Optical follow-up of the majority of these sources is very difficult because of their faintness. Only recently Lehmann et al. (2000) obtained optical spectra for all the sources into which 70%-80% of the soft X-ray background is resolved (Hasinger et al. 1998). Almost all of these are reported to be AGN.

In Chapter 3 we attempt to constrain the contribution of star-forming galaxies to the soft extragalactic XRB, and see whether it is consistent with the recent results from the *ROSAT* Deep Surveys of the Lockman Hole (Hasinger et al. 1998). The very good correlations between the X-ray versus FIR and X-ray versus H_α emission is used in order to calculate the correlation between star-formation rate and soft X-ray emission. Then the latter has been convolved with the evolution of the cosmic SFR (as determined by UV HDF data and measurements in the optical, IR and sub-mm bands), in order to estimate the total soft X-ray emission produced by star-formation. This gives a contribution of $\sim 27\%$ if the optical/IR determination of the SFR history is used and $\sim 14\%$ for the UV determination. This result suggests that star-forming galaxies cannot produce a significant fraction of the extragalactic XRB as has been claimed in the past. This is then in agreement with the recent results of Lehmann et al. (2000). However, there may be significant numbers of star-forming galaxies at fainter fluxes (as suggested by McHardy et al. 1998) which may produce a fraction of the still unresolved soft XRB.

5.2 Future work

5.2.1 Surveys

As the optical spectroscopic survey of the X-ray selected samples of galaxies is still incomplete (mainly for the southern objects) it is crucial to obtain spectroscopic classifications for the remaining sample. In order to make sure that the candidate X-ray luminous star-forming galaxies do not host a hidden AGN, follow-up IR and radio observations will be performed. After the completion of this survey, we will be able to calculate the X-ray luminosity functions for different classes of objects. The large size of the samples used, will give very good statistics and will provide an accurate determination of their luminosity function. However, careful consideration will need to be given to the possible influence of the faintest objects for which it has not been

possible to obtain optical spectra.

A sample of star-forming galaxies drawn from this survey can be used to extend the luminosity function of nearby star-forming galaxies calculated by Georgantopoulos et al. (1999) at luminosities above $10^{41} \text{erg s}^{-1}$. This will provide an independent way of estimating the contribution of star-forming galaxies to the XRB.

The soft X-ray survey of the star-forming galaxies from the sample of Ho et al. (1995) will be extended to include LINER and Transition objects in order to investigate if their multiwavelength properties are different from those of star-forming galaxies. As is shown in figure 2.19 star-forming galaxies and AGN have different trends in their L_X/L_{IR} ratios, with star-forming galaxies being relatively under-luminous in the X-ray band. An interesting task will be to see whether LINERs and Transition objects follow the AGN or the starburst branch of the correlation. This is not possible with the previously available data because of the small size of the samples. The results will provide a test for models which suggest that LINER and Transition objects are evolved star-bursts. In the cases where multiple individual sources are detected their luminosities will be measured in order to extend the sample of extranuclear X-ray sources in nearby galaxies of Lira (1999) and Roberts & Warwick (2000). Also in these cases we will determine the fraction of the total soft X-ray emission arising from discrete sources and diffuse emission, and compare this with other parameters of the galaxy such as the age of the starburst and radio and IR luminosity.

5.2.2 High resolution imaging

The *Chandra* observatory can deliver X-ray images of unprecedented spatial resolution ($\sim 0.5''$) in the 0.2-10.0 keV band. This is a very powerful tool to study the different populations of sources which produce the X-ray emission in star-forming galaxies. Also it will provide us the first opportunity to disentangle the diffuse and point source components and measure their contribution in different energy bands.

The exciting results from the pilot study of M82 with ACIS-I on board *Chandra*, showed that whereas the bulk of the soft (0.2-2.5keV) X-ray emission arises from diffuse gas (almost 80% of the total), this contribution drops to $\sim 50\%$ in the 2.5-10.0keV band (see fig. 5.1). There are

16 discrete sources with luminosities up to $\sim 10^{40} \text{erg s}^{-1}$. Many of these sources are variable in X-rays on a timescale of a few months as deduced from a comparison between HRC and ACIS-I observations of M82 taken a few months apart.

The *Chandra* results on M82 show the discovery potential from extremely high spatial resolution observations. Similar studies for more X-ray luminous star-forming galaxies will allow us to investigate whether their X-ray emission arises by a population of a few super-luminous sources such as the ones found in UGC4305 and in other nearby galaxies. The large number of sources which will become available will allow us to compare the properties of sources in galaxies of different morphology, evolutionary stage and metallicity. Also spatially resolved spectroscopy of the extended emission will allow us to test different models for the superwind formation and evolution. In the hard X-ray regime, comparison between the distribution of the diffuse emission and the radio morphology will be a crucial test for the IC hypothesis.

5.2.3 High quality spectroscopy

Whereas *Chandra* offers very good quality images, *XMM* with its very large effective area will deliver extremely high S/N spectra. Figure 5.2 shows a simulated spectrum for a 20Ks exposure of Arp299. With spectra of this quality it will be possible to study the soft and the hard component and measure the parameters of the hot gas. Specially in the case of superwinds it will be possible to accurately determine the parameters at different positions, although with not as high positional resolution as with *Chandra*. Moreover the very high effective area of *XMM* will allow us to detect large numbers of galaxies as serendipitous sources and thereby create large samples of star-forming galaxies, which will be used for subsequent studies which will extend the work presented in Chapters 2 and 3.

These two major observatories will revolutionarise the study of X-ray emission from star-forming galaxies, as well as many other areas and will provide answers to many long standing problems such as:

- What is the contribution of diffuse emission to the total emission of star-forming galaxies and what is its origin ?

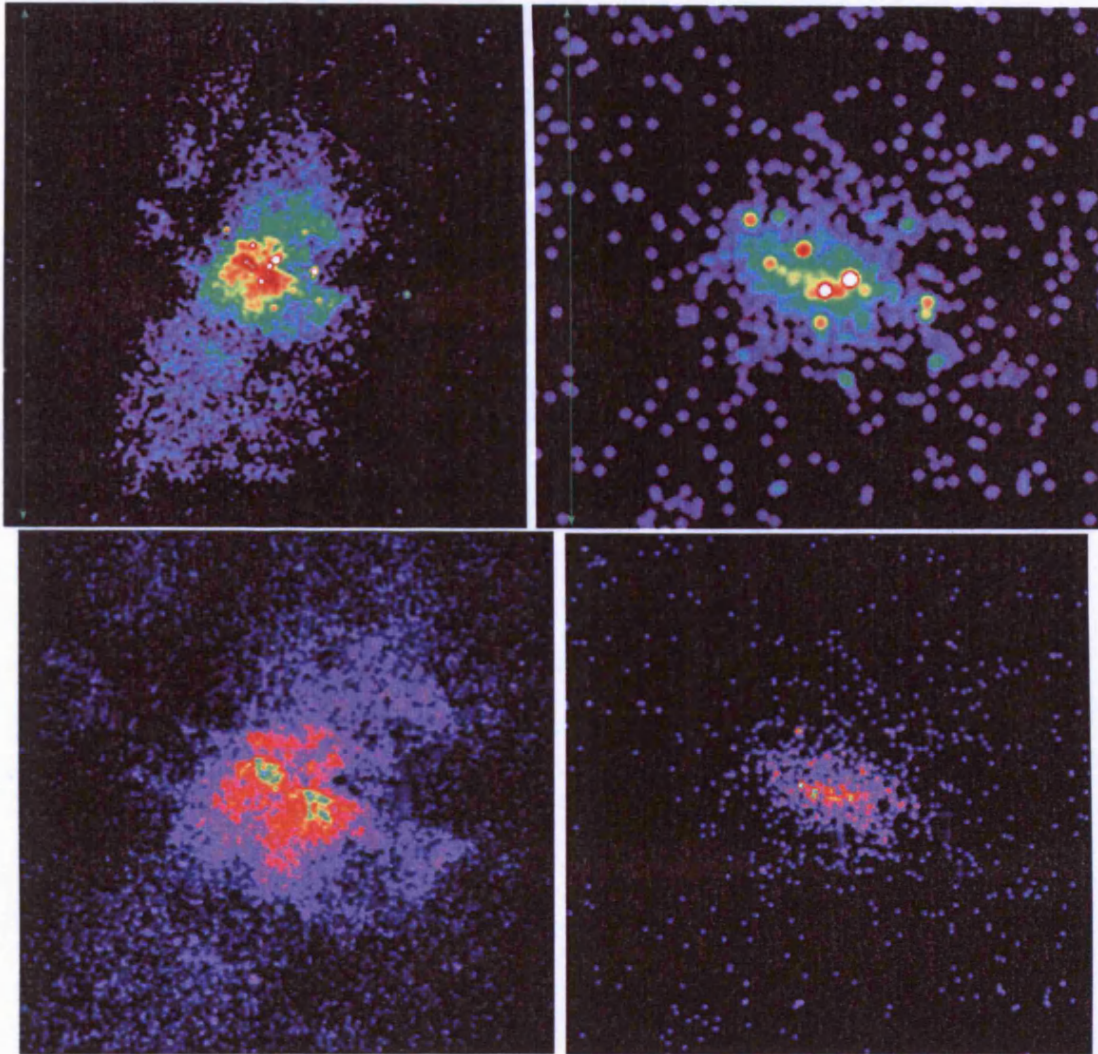


Figure 5.1: Chandra ACIS-I observations of M82. Top left: soft band (0.2-2.5keV) image; top right: hard band (2.5-10.0keV) image; bottom left: diffuse emission in the soft band; bottom right: diffuse emission in the hard band. The bar in the top right image is 4.2' long whereas in the top left image is 2.1' long. The scale of the bottom images is the also 2.1' \times 2.1'

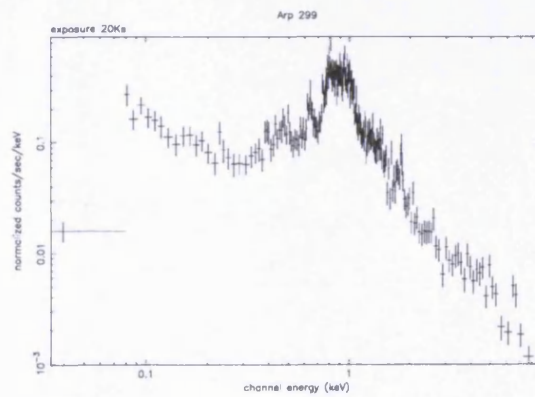


Figure 5.2: A simulated 20Ks observation of Arp299 with XMM (EPIC-MOS). The assumed model is the best fit double thermal model from the *ASCA* + *ROSAT* fits.

- What is the origin of their hard X-ray emission ?
- The physical parameters of the hot gas.
- The nature of the discrete extranuclear sources - are they a new class of binary systems ?
- The statistics of the various populations of discrete X-ray sources in different classes of galaxies
- The relationship between star-formation and AGN activity in the same galaxy

Bibliography

- Akritis, M. (1997), *Aligned Rank tests for Regression with censored data*, Penn State Dept. of Statistics Technical Report, 1989.
- Allen, D. (1997), *The PSS algorithm*, STARLINK.
- Allen, D. & Vallance, R. (1995), *ASTERIX - X-ray data processing system*, STARLINK.
- Alonso-Herrero, A., Rieke, M. J. & Rieke, G. H. (2000), *Astrophys. J.* **in press**.
- Antonucci, R. (1993), *Ann. Rev. Astron. Astrophys.* **31**, 473–521.
- Antonucci, R. R. J. & Miller, J. S. (1985), *Astrophys. J.* **297**, 621–632.
- Armus, L., Heckman, T. M., Weaver, K. A. & Lehnert, M. D. (1995), *Astrophys. J.* **445**, 666.
- Arp, H. (1966), *Atlas of Peculiar galaxies*, California Insitute of Technology.
- Athanassoula, E. (1992), *Mon. Not. R. astr. Soc.* **259**, 328–344.
- Augarde, R., Chalabaev, A., Comte, G., Kunth, D. & Maehara, H. (1994), *Astr. Astrophys. Suppl.* **104**, 259–270.
- Babul, A. & Rees, M. J. (1992), *Mon. Not. R. astr. Soc.* **255**, 346–350.
- Bade, N., Fink, H. H., Engels, D., Voges, W., Hagen, H. J., Wisotzki, L. & Reimers, D. (1995), *Astr. Astrophys. Suppl.* **110**, 469+.
- Baldwin, J. A., Phillips, M. M. & Terlevich, R. (1981), *Pub. Astr. Soc. Pacific.* **93**, 5–19.
- Balick, B. & Heckman, T. (1981), *Astr. Astrophys.* **96**, 271.
- Barnes, J. E. & Hernquist, L. (1992), *Ann. Rev. Astron. Astrophys.* **30**, 705–742.

- Bertola, F. & Sharp, N. A. (1984), *Mon. Not. R. astr. Soc.* **207**, 47.
- Bevington, P. R. & Robinson, D. K. (1992), *Data Reduction and Error Analysis for the Physical Sciences*, Mc Graw-Hill.
- Boella, G., Butler, R. C., Perola, G. C., Piro, L., Scarsi, L. & Bleeker, J. A. M. (1997), *Astr. Astrophys. Suppl.* **122**, 299–307.
- Boella, G., Chiappetti, L., Conti, G., Cusumano, G., del Sordo, S., La Rosa, G., Maccarone, M. C., Mineo, T., Molendi, S., Re, S., Sacco, B. & Tripiciano, M. (1997), *Astr. Astrophys. Suppl.* **122**, 327–340.
- Bohlin, R. C., Savage, B. D. & Drake, J. F. (1978), *Astrophys. J.* **224**, 132.
- Bookbinder, J., Cowie, L. L., Ostriker, J. P., Krolik, J. H. & Rees, M. (1980), *Astrophys. J.* **237**, 647–654.
- Bothun, G. D., Schmitz, M., Halpern, J. P., Lonsdale, C. J. & Impey, C. (1989), *Astrophys. J. Suppl.* **70**, 271–328.
- Boyle, B. J., Griffiths, R. E., Shanks, T., Stewart, G. C. & Georgantopoulos, I. (1993), *Mon. Not. R. astr. Soc.* **260**, 49–58.
- Boyle, B. J., Wilkes, B. J. & Elvis, M. (1997), *Mon. Not. R. astr. Soc.* **285**, 511–528.
- Brandt, W. N., Ward, M. J., Fabian, A. C. & Hodge, P. W. (1997), *Mon. Not. R. astr. Soc.* **291**, 709.
- Briel, U. G. et al. (1994), *The ROSAT User's Handbook*, MPE.
- Buat, V. & Xu, C. (1996), *Astr. Astrophys.* **306**, 61.
- Cappi, M., Persic, M., Bassani, L., Franceschini, A., Hunt, L. K., Molendi, S., Palazzi, E., Palumbo, G. G. C., Rephaeli, Y. & Salucci, P. (1999), *Astr. Astrophys.* **350**, 777–790.
- Cardelli, J. A., Clayton, G. C. & Mathis, J. S. (1989), *Astrophys. J.* **345**, 245–256.
- Casoli, F., Combes, F., Augarde, R., Figon, P. & Martin, J. M. (1989), *Astr. Astrophys.* **224**, 31.
- Charles, P.A. Seward, F. (1995), Cambridge University Press.

- Chen, L. W., Fabian, A. C. & Gendreau, K. C. (1997), *Mon. Not. R. astr. Soc.* **285**, 449–471.
- Chevalier, R. A. & Clegg, A. W. (1985), *Nature* **317**, 44.
- Comastri, A., Setti, G., Zamorani, G. & Hasinger, G. (1995), *Astr. Astrophys.* **296**, 1.
- Condon, J. J. (1987), *Astrophys. J. Suppl.* **65**, 485–541.
- Condon, J. J. (1992), *Ann. Rev. Astron. Astrophys.* **30**, 575–611.
- Condon, J. J., Anderson, M. L. & Helou, G. (1991), *Astrophys. J.* **376**, 95–103.
- Condon, J. J., Huang, Z. P., Yin, Q. F. & Thuan, T. X. (1991), *Astrophys. J.* **378**, 65–76.
- Connolly, A. J., Szalay, A. S., Dickinson, M., Subbarao, M. U. & Brunner, R. J. (1997), *Astrophys. J. Letts.* **486**, L11–.
- Cox, P., Kruegel, E. & Mezger, P. G. (1986), *Astr. Astrophys.* **155**, 380–396.
- Cox, P. & Mezger, P. G. (1989), *Astr. Astrophys. Review* **1**, 49–83.
- Coziol, R., Torres, C. A. O., Quast, G. R., Contini, T. & Davoust, E. (1998), *Astrophys. J. Suppl.* **119**, 239–253.
- Dahari, O. (1985), *Astrophys. J. Suppl.* **57**, 643–664.
- Dahlem, M. (1997), *Pub. Astr. Soc. Pacific.* **109**, 1298–1320.
- Dahlem, M., Parmar, A., Oosterbroek, T., Orr, A., Weaver, K. & Heckman, T. (2000), *astro/ph* **0003020**.
- Dahlem, M., Weaver, K. A. & Heckman, T. M. (1998), *Astrophys. J. Suppl.* **118**, 401–453.
- D’Antona, F. (1998), in G. Gilmore & D. Howell, eds, ‘The Stellar Initial Mass function, 38th Herstmonceux Conference’, Astronomical Society of the Pacific Conf. Series, p. 157.
- David, L. P., Jones, C. & Forman, W. (1992), *Astrophys. J.* **388**, 82–92.
- David, L. et al. (1997), *The ROSAT High Resolution Imager Calibration Report*, CfA.
- Davies, R. I., Alonso-Herrero, A. & Ward, M. J. (1997), *Mon. Not. R. astr. Soc.* **291**, 557+.
- Davies, R. I., Sugai, H. & Ward, M. J. (1998), *Mon. Not. R. astr. Soc.* **295**, 43.

- de Grijp, M. H. K., Keel, W. C., Miley, G. K., Goudfrooij, P. & Lub, J. (1992), *Astr. Astrophys. Suppl.* **96**, 389–428.
- de Vaucouleurs, G. H. (1991), *Third reference catalogue of bright galaxies*, New York : Springer-Verlag, c1991.
- Della Ceca, R., Griffiths, R. E. & Heckman, T. M. (1997), *Astrophys. J.* **485**, 581.
- Della Ceca, R., Griffiths, R. E., Heckman, T. M. & Mackenty, J. W. (1996), *Astrophys. J.* **469**, 662.
- Devereux, N. A. & Eales, S. A. (1989), *Astrophys. J.* **340**, 708–712.
- Devereux, N. A. & Hameed, S. (1997), *Astron. Journ.* **113**, 599.
- Devereux, N. A. & Young, J. S. (1990), *Astrophys. J. Letts.* **350**, L25–L28.
- Done, C. & Osborne, J. P. (1997), *Mon. Not. R. astr. Soc.* **288**, 649.
- Ehle, M., Pietsch, W. & Beck, R. (1995), *Astr. Astrophys.* **295**, 289.
- Elvis, M., Soltan, A. & Keel, W. C. (1984), *Astrophys. J.* **283**, 479.
- Fabbiano, G. (1988), *Astrophys. J.* **330**, 672–683.
- Fabbiano, G. (1989), *Ann. Rev. Astron. Astrophys.* **27**, 87.
- Fabbiano, G. (1995), in W. H. G. Lewin, J. van Paradijs & E. P. J. van den Heuvel, eds, ‘X-ray Binaries’, Cambridge University Press, Cambridge, p. 390.
- Fabbiano, G., Feigelson, E. & Zamorani, G. (1982), *Astrophys. J.* **256**, 397.
- Fabbiano, G., Gioia, I. M. & Trinchieri, G. (1988), *Astrophys. J.* **324**, 749.
- Fabbiano, G., Kim, D. W. & Trinchieri, G. (1992), *Astrophys. J. Suppl.* **80**, 531.
- Fabbiano, G., Schweizer, F. & Mackie, G. (1997), *Astrophys. J.* **478**, 542.
- Fabian, A. C., Barcons, X., Almaini, O. & Iwasawa, K. (1998), *Mon. Not. R. astr. Soc.* **297**, L11.
- Fabian, A. C. & Terlevich, R. (1996), *Mon. Not. R. astr. Soc.* **280**, L5–L8.
- Fabian, A. C. & Ward, M. J. (1993), *Mon. Not. R. astr. Soc.* **263**, L51.

- Fairall, A. P. (1981), *Mon. Not. R. astr. Soc.* **196**, 417–424.
- Filippenko, A. V. & Terlevich, R. (1992), *Astrophys. J. Letts.* **397**, L79–L82.
- Flores, H., Hammer, F., Thuan, T. X., Ceacut#sarsky, C., Desert, F. X., Omont, A., Lilly, S. J., Eales, S., Crampton, D. & Le Fegrave#vre, O. (1999), *Astrophys. J.* **517**, 148–167.
- Fourniol, N., Pakull, M. & Motch, C. (1996), in ‘Roentgenstrahlung from the Universe’, pp. 375–376.
- Franceschini, A., Hasinger, G., Miyaji, T. & Malquori, D. (1999), *Mon. Not. R. astr. Soc.* **310**, L5–L9.
- Friedman, S. D., Cohen, R. D., Jones, B. et al. (1987), *Astron. Journ.* **94**, 1480.
- Frontera, F., Costa, E., dal Fiume, D., Feroci, M., Nicastrò, L., Orlandini, M., Palazzi, E. & Zavattini, G. (1997), *Astr. Astrophys. Suppl.* **122**, 357–369.
- Fruscione, A. & Griffiths, R. E. (1991), *Astrophys. J. Letts.* **380**, L13–L16.
- Gallego, J., Zamorano, J., Aragon-Salamanca, A. & Rego, M. (1995), *Astrophys. J. Letts.* **455**, L1–.
- Gaskell, C. M. & Ferland, G. J. (1984), *Pub. Astr. Soc. Pacific.* **96**, 393–397.
- Gehrz, R. D., Sramek, R. A. & Weedman, D. W. (1983), *Astrophys. J.* **267**, 551.
- Gendreau, K. C. (1995), X-ray CCDS for space applications: Calibration, Radiation hardness, and use for measuring the spectrum of the cosmic X-ray background., PhD thesis, MIT.
- Georgantopoulos, I., Basilakos, S. & Plionis, M. (1999), *Mon. Not. R. astr. Soc.* **305**, L31–L34.
- Georgantopoulos, I., Stewart, G. C., Shanks, T. et al. (1996), *Mon. Not. R. astr. Soc.* **280**, 276.
- Giacconi, R., Branduardi, G., Briel, U., Epstein, A., Fabricant, D., Feigelson, E., Holt, S. S., Becker, R. H., Boldt, E. A. & Serlemitsos, P. J. (1979), *Astrophys. J.* **230**, 540–550.
- Giacconi, R., Gursky, H., Paolini, F. & Rossi, B. (1962), *Phys. Rev. Lett* **9**, 439–443.
- Glazebrook, K., Blake, C., Economou, F., Lilly, S. & Colless, M. (1999), *Mon. Not. R. astr. Soc.* **306**, 843–856.

- Goldader, J. D., Joseph, R. D., Doyon, R. & Sanders, D. B. (1997), *Astrophys. J.* **474**, 104+.
- Goldshmidt, O. & Rephaeli, Y. (1995), *Astrophys. J.* **444**, 113–118.
- Gordon, K. D., Calzetti, D. & Witt, A. N. (1997), *Astrophys. J.* **487**, 625.
- Green, P. J., Anderson, S. F. & Ward, M. J. (1992), *Mon. Not. R. Astr. Soc.* **254**, 30.
- Griffiths, R. E., Della Ceca, R., Georgantopoulos, I., Boyle, B. J., Stewart, G. C., Shanks, T. & Fruscione, A. (1996), *Mon. Not. R. astr. Soc.* **281**, 71–83.
- Griffiths, R. E. & Padovani, P. (1990), *Astrophys. J.* **360**, 483.
- Hasinger, G., Burg, R., Giacconi, R., Schmidt, M., Trumper, J. & Zamorani, G. (1998), *Astr. Astrophys.* **329**, 482–494.
- Hasinger, G., Turner, T., George, I. & Boese, G. (1992), *ROSAT PSPC : The on-axis Point Spread Function*, OGIP.
- Heckman, T. M. (1980), *Astr. Astrophys.* **87**, 152–164.
- Heckman, T. M., Armus, L. & Miley, G. K. (1990), *Astrophys. J. Suppl.* **74**, 833.
- Heckman, T. M., Dahlem, M., Lehnert, M. D., Fabbiano, G., Gilmore, D. & Waller, W. H. (1995), *Astrophys. J.* **448**, 98.
- Hensler, G., Dickow, R. & Junkes, N. (1997), *Revista Mexicana de Astronomia y Astrofisica Conference Series* **6**, 90.
- Hewitt, A. & Burbidge, G. (1991), *Astrophys. J. Suppl.* **75**, 297–356.
- Ho, L. C., Filippenko, A. V. & Sargent, W. L. (1995), *Astrophys. J. Suppl.* **98**, 477.
- Ho, L. C., Filippenko, A. V. & Sargent, W. L. W. (1997a), *Astrophys. J. Suppl.* **112**, 315.
- Ho, L. C., Filippenko, A. V. & Sargent, W. L. W. (1997b), *Astrophys. J.* **487**, 568.
- Ho, L. C., Filippenko, A. V., Sargent, W. L. W. & Peng, C. Y. (1997), *Astrophys. J. Suppl.* **112**, 391.
- Hodge, P., Strobel, N. V. & Kennicutt, R. C. (1994), *Pub. Astr. Soc. Pacific.* **106**, 309.
- Holmberg, E. (1958), *Meddelanden fran Lunds Astronomiska Observatorium Serie II* **136**, 1.

- Hook, I. M., McMahon, R. G., Irwin, M. J. & Hazard, C. (1996), *Mon. Not. R. astr. Soc.* **282**, 1274–1298.
- Hughes, D. H., Serjeant, S., Dunlop, J., Rowan-Robinson, M., Blain, A., Mann, R. G., Ivison, R., Peacock, J., Efstathiou, A., Gear, W., Oliver, S., Lawrence, A., Longair, M., Goldschmidt, P. & Jenness, T. (1998), *Nature* **394**, 241–247.
- Hughes, J. P. & Singh, K. P. (1994), *Astrophys. J.* **422**, 126.
- Hunter, D. A., Elmegreen, B. G. & Baker, A. L. (1998), *Astrophys. J.* **493**, 595.
- Iben, I., J., Tutukov, A. V. & Yungelson, L. R. (1995), *Astrophys. J. Suppl.* **100**, 233.
- Inoue, H. (1991), in T. Y. & K. Koyama, eds, ‘Frontiers of X-ray astronomy’, Universal Academy Press, Tokyo, p. 291.
- Isobe, T., Feigelson, E. D. & Nelson, P. I. (1986), *Astrophys. J.* **306**, 490–507.
- Kaastra, J. (1997), X-ray spectroscopic observations with asca and beposax, in J. van Paradijs & J. Bleeker, eds, ‘X-ray Spectroscopy in Astrophysics’, Springer Verlag, p. 269.
- Kaneda, H., Makishima, K., Yamauchi, S., Koyama, K., Matsuzaki, K. & Yamasaki, N. Y. (1997), *Astrophys. J.* **491**, 638.
- Kennicutt, R. C., J. (1998a), *Astrophys. J.* **498**, 541.
- Kennicutt, R. C., J. (1998b), *Ann. Rev. Astron. Astrophys.* **36**, 189–232.
- Kennicutt, R. C., J. & Kent, S. M. (1983), *Astron. Journ.* **88**, 1094–1107.
- Kewley, L. J., Heisler, C. A., Dopita, M. A., Sutherland, R., Norris, R. P., Reynolds, J. & Lumsden, S. (2000), *Astrophys. J.* **530**, 704–718.
- Kim, D. C. & Sanders, D. B. (1998), *Astrophys. J. Suppl.* **119**, 41–58.
- Kim, D. C., Sanders, D. B., Veilleux, S., Mazzarella, J. M. & Soifer, B. T. (1995), *Astrophys. J. Suppl.* **98**, 129.
- Kirhakos, S. D. & Steiner, J. E. (1990), *Astron. Journ.* **99**, 1722–1739.
- Komossa, S. & Schulz, H. (1998), *Astr. Astrophys.* **339**, 345–354.

- Kormendy, J. (1985), *Astrophys. J.* **295**, 73–79.
- Koyama, K., Makishima, K., Tanaka, Y. & Tsunemi, H. (1986), *Pub. Astr. Soc. Japan.* **38**, 121–131.
- Lavalley, M., Isobe, T. & Feigelson, E. (1992), Asurv: Astronomy survival analysis package, in ‘ASP Conf. Ser. 25: Astronomical Data Analysis Software and Systems I’, Vol. 1, p. 245.
- Lehmann, I., Hasinger, G., Schmidt, M., Gunn, J. E., Schneider, D. P., Giacconi, R., McCaughrean, M., Trumper, J. & Zamorani, G. (2000), *Astr. Astrophys.* **354**, 35–54.
- Leitherer, C. (1998), in G. Gilmore & D. Howell, eds, ‘The Stellar Initial Mass function, 38th Herstmonceux Conference’, Astronomical Society of the Pacific Conf. Series, p. 61.
- Leitherer, C., Robert, C. & Drissen, L. (1992), *Astrophys. J.* **401**, 596.
- Leitherer, C., Schaerer, D., Goldader, J. D., Delgado, R. M. G. l., Robert, C., Kune, D. F., de Mello, D. l. F., Devost, D. & Heckman, T. M. (1999), *Astrophys. J. Suppl.* **123**, 3–40.
- Lilly, S. J., Le Fevre, O., Hammer, F. & Crampton, D. (1996), *Astrophys. J. Letts.* **460**, L1–.
- Lira, P. (1999), Nuclear activity in a volume-limited sample of nearby galaxies, PhD thesis, University of Edinburgh.
- Liu, C. T. & Kennicutt, R. C., J. (1995), *Astrophys. J. Suppl.* **100**, 325+.
- Longair, M. (1992), *High Energy Astrophysics, vol 2*, Cambridge University Press.
- Longair, M. (1995), in B. Binggeli & R. Buser, eds, ‘The Deep Universe, Saas-Fee Advanced Course 23’, Springer Verlang, p. 317.
- Mac Low, M.-M. & McCray, R. (1988), *Astrophys. J.* **324**, 776.
- Madau, P., Pozzetti, L. & Dickinson, M. (1998), *Astrophys. J.* **498**, 106.
- Maiolino, R. & Rieke, G. H. (1995), *Astrophys. J.* **454**, 95+.
- Markarian, B. E. (1967), *Astrofizika* **3**, 24–38.
- Markarian, B. E., Lipovetskii, V. A. & Stepanian, D. A. (1981), *Astrofizika* **17**, 619–627.

- Marston, A. P., Elmegreen, D., Elmegreen, B., Forman, W., Jones, C. & Flanagan, K. (1995), *Astrophys. J.* **438**, 663.
- Masai, K. (1994), *Astrophys. J.* **437**, 770–780.
- Massey, P., Strobel, K., Barnes, J. V. & Anderson, E. (1988), *Astrophys. J.* **328**, 315–333.
- Mazzarella, J. M. & Balzano, V. A. (1986), *Astrophys. J. Suppl.* **62**, 751–819.
- Mazzarella, J. M. & Boroson, T. A. (1993), *Astrophys. J. Suppl.* **85**, 27–109.
- McHardy, I. M., Jones, L. R., Merrifield, M. R., Mason, K. O., Newsam, A. M., Abraham, R. G., Dalton, G. B., Carrera, F., Smith, P. J., Rowan-Robinson, M. & Abraham, R. G. (1998), *Mon. Not. R. astr. Soc.* **295**, 641.
- Miller, G. E. & Scalo, J. M. (1979), *Astrophys. J. Suppl.* **41**, 513–547.
- Miyauchi-Isobe, N. & Takase, B. (1988), *Vistas in Astronomy* **31**, 585–587.
- Moran, E. C., Halpern, J. P. & Helfand, D. J. (1996), *Astrophys. J. Suppl.* **106**, 341.
- Moran, E. C. & Lehnert, M. D. (1997), *Astrophys. J.* **478**, 172.
- Moran, E. C., Lehnert, M. D. & Helfand, D. J. (1999), *Astrophys. J.* **526**, 649–664.
- Moshir, M. (1991), *Journal of the British Interplanetary Society* **44**, 495–504.
- Mulder, P. S. & Van Driel, W. (1996), *Astr. Astrophys.* **309**, 403.
- Mushotzky, R., Cowie, L. I., Barger, A. J. & Arnaud, K. A. (2000), *astro/ph* **0002313**.
- Nagase, F., Zylstra, G., Sonobe, T., Kotani, T., Inoue, H. & Woo, J. (1994), *Astrophys. J. Letts.* **436**, L1–L4.
- Nakagawa, T., Nagata, T., Geballe, T. R., Okuda, H., Shibai, H. & Matsuhara, H. (1989), *Astrophys. J.* **340**, 729.
- Netzer, H. & Ferland, G. J. (1984), *Pub. Astr. Soc. Pacific.* **96**, 593–597.
- Niklas, S., Klein, U. & Wielebinski, R. (1997), *Astr. Astrophys.* **322**, 19.
- Noguchi, T., Maehara, H. & Kondo, M. (1980), *Annales of the Tokyo Astronomical Observatory* **18**, 55–70.

- Ohashi, T., Ebisawa, K., Fukazawa, Y., Hiyoshi, K. et al. (1996), *Pub. Astr. Soc. Japan.* **48**, 157.
- Ohashi, T., Makishima, K., Tsuru, T., Takano, S., Koyama, K. & Stewart, G. C. (1990), *Astrophys. J.* **365**, 180–185.
- Okada, K., Dotani, T., Makishima, K., Mitsuda, K. & Mihara, T. (1998), *Pub. Astr. Soc. Japan.* **50**, 25–30.
- Oke, J. B. (1990), *Astron. Journ.* **99**, 1621–1631.
- Osterbrock, D. E. & Martel, A. (1993), *Astrophys. J.* **414**, 552–562.
- Parmar, A. N., Martin, D. D. E., Bavdaz, M., Favata, F., Kuulkers, E., Vacanti, G., Lammers, U., Peacock, A. & Taylor, B. G. (1997), *Astr. Astrophys. Suppl.* **122**, 309–326.
- Pastoriza, M. G., Dottori, H. A., Terlevich, E. et al. (1993), *Mon. Not. R. astr. Soc.* **260**, 177.
- Pei, Y. C. & Fall, S. M. (1995), *Astrophys. J.* **454**, 69.
- Peterson, B. (1997), *An introduction to active galactic nuclei*, Cambridge University Press.
- Pettini, M., Kellogg, M., Steidel, C. C., Dickinson, M., Adelberger, K. L. & Giavalisco, M. (1998), *Astrophys. J.* **508**, 539–550.
- Pfeffermann, E. et al. (1987), *Proc. SPIE Int. Soc. Opt. Eng.* **733**, 519.
- Ptak, A. & Griffiths, R. (1999), *Astrophys. J. Letts.* **517**, L85–L89.
- Ptak, A., Serlemitsos, P., Yaqoob, T. & Mushotzky, R. (1999), *Astrophys. J. Suppl.* **120**, 179–208.
- Ptak, A., Serlemitsos, P., Yaqoob, T., Mushotzky, R. & Tsuru, T. (1997), *Astron. Journ.* **113**, 1286.
- Puche, D., Westpfahl, D., Brinks, E. & Roy, J.-R. (1992), *Astron. Journ.* **103**, 1841.
- Raymond, J. C. & Smith, B. W. (1977), *Astrophys. J. Suppl.* **35**, 419.
- Read, A. M., Ponman, T. J. & Strickland, D. K. (1997), *Mon. Not. R. astr. Soc.* **286**, 626.
- Rees, M. J. (1984), *Ann. Rev. Astron. Astrophys.* **22**, 471–506.
- Reeves, J. N., Turner, M. J. L., Ohashi, T. & Kii, T. (1997), *Mon. Not. R. astr. Soc.* **292**, 468.

- Reynolds, C. S., Loan, A. J., Fabian, A. C., Makishima, K., Brandt, W. N. & Mizuno, T. (1997), *Mon. Not. R. astr. Soc.* **286**, 349–357.
- Rigopoulou, D., Lutz, D., Genzel, R. et al. (1996), *Astr. Astrophys.* **315**, L125.
- Roberts, T. P. & Warwick (2000), *Mon. Not. R. astr. Soc.* **in press**.
- Rowan-Robinson, M. & Crawford, J. (1989), *Mon. Not. R. astr. Soc.* **238**, 523–558.
- Rush, B., Malkan, M. A. & Spinoglio, L. (1993), *Astrophys. J. Suppl.* **89**, 1.
- Salpeter, E. E. (1955), *Astrophys. J.* **121**, 161.
- Sanders, D. B. & Mirabel, I. F. (1985), *Astrophys. J. Letts.* **298**, L31.
- Sanders, D. B., Soifer, B. T., Elias, J. H., Neugebauer, G. & Matthews, K. (1988), *Astrophys. J. Letts.* **328**, L35–L39.
- Sansom, A. E., Dotani, T., Okada, K., Yamashita, A. & Fabbiano, G. (1996), *Mon. Not. R. astr. Soc.* **281**, 48.
- Scalo, J. M. (1986), *Fundamentals of Cosmic Physics* **11**, 1–278.
- Schaaf, R., Pietsch, W., Biermann, P. L., Kronberg, P. P. & Schmutzler, T. (1989), *Astrophys. J.* **336**, 722–733.
- Schaerer, D. (1999), *in* F.Hammer et al., eds, ‘‘Building the galaxies: From the primordial universe to the present’’, XIXth Monriond astrophysics meeting’.
- Schaerer, D., Contini, T. & Pindao, M. (1999), *Astr. Astrophys. Suppl.* **136**, 35–52.
- Schartel, N., Green, P. J., Anderson, S. F., Hewett, P. C., Foltz, C. B., Margon, B., Brinkmann, W., Fink, H. & Trumper, J. (1996), *Mon. Not. R. astr. Soc.* **283**, 1015–1026.
- Schmitt, H. R., Kinney, A. L., Calzetti, D. & Storchi Bergmann, T. (1997), *Astron. Journ.* **114**, 592–612.
- Schmitt, J. H. M. M. (1985), *Astrophys. J.* **293**, 178–191.
- Serlemitsos, P., Ptak, A. & Yaqoob, T. (1996), *in* ‘ASP Conf. Ser. 103: The Physics of Liners in View of Recent Observations’, p. 70.

- Simien, F. & de Vaucouleurs, G. (1986), *Astrophys. J.* **302**, 564–578.
- Snowden, S. L., McCammon, D., Burrows, D. N. & Mendenhall, J. A. (1994), *Astrophys. J.* **424**, 714–728.
- Soifer, B. T., Sanders, D. B., Madore, B. F. et al. (1987), *Astrophys. J.* **320**, 238.
- Stark, A. A., Gammie, C. F., Wilson, R. W., Bally, J., Linke, R. A., Heiles, C. & Hurwitz, M. (1992), *Astrophys. J. Suppl.* **79**, 77–104.
- Stevens, I. R. & Strickland, D. K. (1998), *Mon. Not. R. astr. Soc.* **294**, 523.
- Strauss, M. A., Huchra, J. P., Davis, M., Yahil, A., Fisher, K. B. & Tonry, J. (1992), *Astrophys. J. Suppl.* **83**, 29–63.
- Strickland, D. K. (1998), PhD thesis, University of Birmingham.
- Strickland, D. K., Ponman, T. J. & Stevens, I. R. (1997), *Astr. Astrophys.* **320**, 378.
- Strickland, D. K. & Stevens, I. R. (1998), *Mon. Not. R. astr. Soc.* **297**, 747.
- Strickland, D. K. & Stevens, I. R. (2000), *Mon. Not. R. astr. Soc.* **in press**.
- Suchkov, A. A., Berman, V. G., Heckman, T. M. & Balsara, D. S. (1996), *Astrophys. J.* **463**, 528.
- Takase, B. & Miyauchi-Isobe, N. (1984), *Annales of the Tokyo Astronomical Observatory* **19**, 595–638.
- Takase, B. & Miyauchi-Isobe, N. (1988), *Vistas in Astronomy* **31**, 589–594.
- Takase, B. & Miyauchi-Isobe, N. (1993), *Publications of the National Astronomical Observatory of Japan* **3**, 169–257.
- Takase, B., Noguchi, T. & Maehara, H. (1983), *Annales of the Tokyo Astronomical Observatory* **19**, 440–462.
- Tanaka, Y., Inoue, H. & Holt, S. S. (1994), *Pub. Astr. Soc. Japan.* **46**, L37.
- Telesco, C. M. & Gatley, I. (1984), *Astrophys. J.* **284**, 557.
- Terlevich, R., Tenorio-Tagle, G., Franco, J. & Melnick, J. (1992), *Mon. Not. R. astr. Soc.* **255**, 713–728.

- Tongue, T. D. & Westpfahl, D. J. (1995), *Astron. Journ.* **109**, 2462.
- Tresse, L. & Maddox, S. J. (1998), *Astrophys. J.* **495**, 691.
- Treyer, M. A., Ellis, R. S., Milliard, B., Donas, J. & Bridges, T. J. (1998), *Mon. Not. R. astr. Soc.* **300**, 303–314.
- Trumper, J. (1984), *Physica Scripta* **7**, 209.
- Tsuru, T. G., Awaki, H., Koyama, K. & Ptak, A. (1997), *Pub. Astr. Soc. Japan.* **49**, 619.
- Tsuru, T., Ohashi, T., Makishima, K., Mihara, T. & Kondo, H. (1990), *Pub. Astr. Soc. Japan.* **42**, L75.
- Turner, J. L., Ho, P. T. P. & Beck, S. (1987), *Astrophys. J.* **313**, 644.
- Ueda, Y., Takahashi, T., Inoue, H., Tsuru, T., Sakano, M., Ishisaki, Y., Ogasaka, Y., Makishima, K., Yamada, T. & Ohta, K. (1998), *Nature* **391**, 866.
- Vacca, W. D. & Conti, P. S. (1992), *Astrophys. J.* **401**, 543–558.
- Vaceli, M. S., Viegas, S. M., Gruenwald, R. & de Souza, R. E. (1997), *Astron. Journ.* **114**, 1345+.
- Vallee, J. P. (1993), *Mon. Not. R. astr. Soc.* **264**, 665.
- van Paradijs, J. & McClintock, J. (1995), in W. H. G. Lewin, J. van Paradijs & E. P. J. van den Heuvel, eds, ‘X-ray Binaries’, Cambridge University Press, Cambridge, p. 58.
- Veilleux, S., Kim, D. C. & Sanders, D. B. (1999), *Astrophys. J.* **522**, 113–138.
- Veilleux, S., Kim, D. C., Sanders, D. B., Mazzarella, J. M. & Soifer, B. T. (1995), *Astrophys. J. Suppl.* **98**, 171.
- Veilleux, S. & Osterbrock, D. E. (1987), *Astrophys. J. Suppl.* **63**, 295.
- Veilleux, S., Sanders, D. B. & Kim, D. C. (1999), *Astrophys. J.* **522**, 139–156.
- Veron-Cetty, M. P. & Veron, P. (1986), *Astr. Astrophys. Suppl.* **66**, 335–372.
- Veron, P., Goncalves, A. C. & Veron-Cetty, M. P. (1997), *Astr. Astrophys.* **319**, 52–66.

- Voges, W., Aschenbach, B., Boller, T., Braunschweiger, H., Briel, U., Burkert, W., Dennerl, K., Englhauser, J., Gruber, R., Haberl, F., Hartner, G., Hasinger, G., Kuntz, M., Pfeffermann, E., Pietsch, W., Predehl, P., Rosso, C., Schmitt, J. H. M. M., Trümper, J. & Zimmermann, H. U. (1999), *Astr. Astrophys.* **349**, 389–405.
- Ward, M. J., Wilson, A. S., Penston, M. V., Elvis, M., Maccacaro, T. & Tritton, K. P. (1978), *Astrophys. J.* **223**, 788–797.
- Watson, M. G. (1990), The milky way in x-rays, in G. J. Fabbiano & R. A., eds, ‘Windows on Galaxies’, Kluwer Academic Publishers, pp. 177–189.
- Watson, M. G., Stanger, V. & Griffiths, R. E. (1984), *Astrophys. J.* **286**, 144.
- Weedman, D. W., Feldman, F. R., Balzano, V. A., Ramsey, L. W., Sramek, R. A. & Wu, C. C. (1981), *Astrophys. J.* **248**, 105–112.
- White, N. E., Peacock, A., Hasinger, G., Mason, K. O., Manzo, G., Taylor, B. G. & Branduardi-Raymont, G. (1986), *Mon. Not. R. astr. Soc.* **218**, 129–138.
- Whittet, D. C. B. (1992), *Dust in the galactic environment*, Institute of Physics Publishing.
- Wynn-Williams, C. G., Hodapp, K. W., Joseph, R. D. et al. (1991), *Astrophys. J.* **377**, 426.
- Yamasaki, N. Y., Ohashi, T., Takahara, F., Yamauchi, S., Koyama, K., Kamae, T., Kaneda, H., Makishima, K., Sekimoto, Y., Hirayama, M., Takahashi, T., Yamagami, T., Gunji, S., Tamura, T., Miyazaki, S. & Nomachi, M. (1997), *Astrophys. J.* **481**, 821.
- Yaqoob, T. (1997), *The ASCA ABC Guide v2.0*, NASA GSFC.
- Yaqoob, T., Serlemitsos, P. J., Ptak, A., Mushotzky, R., Kunieda, H. & Terashima, Y. (1995), *Astrophys. J.* **455**, 508.
- Yokogawa, J., Imanishi, K., Tsujimoto, M., Koyama, K., Nagase, F. & Corbet, R. (2000), *astro/ph* **0002167**.
- Young, J. S., Allen, L., Kenney, J. D. P., Lesser, A. & Rownd, B. (1996), *Astron. Journ.* **112**, 1903.
- Young, S., Hough, J. H., Efstathiou, A., Wills, B. J., Bailey, J. A., Ward, M. J. & Axon, D. J. (1996), *Mon. Not. R. astr. Soc.* **281**, 1206–1242.

Zezas, A. L., Georgantopoulos, I. & Ward, M. J. (1999), *Mon. Not. R. astr. Soc.* **308**, 302–308.

Zhao, J.-H., Anantharamaiah, K. R., Goss, W. M. & Viallefond, F. (1997), *Astrophys. J.* **482**, 186.